Adsorption performance and cold plasma activation of biochar for on-site CH_4 storage and energy recovery in oil fields

Thesis submitted to the University of Ottawa
in partial fulfillment of the requirements for the degree of
Doctor of Philosophy in Chemical Engineering

Yoonhee Ko

Department of Chemical and Biological Engineering
Faculty of Engineering
University of Ottawa

Abstract

Routine flaring of associated petroleum gas (APG) remains a major source of greenhouse gas emissions in upstream oil production, particularly at remote or infrastructure-limited production sites where gas transportation and processing are uneconomic. Developing a field-deployable, integrated utilization pathway that captures methane (CH_4)-rich APG for on-site generation of electricity and heat at low cost could significantly reduce energy consumption and greenhouse gas (GHG) emissions across the oil industry. This thesis evaluates biochar as an adsorbent for capturing and storing CH_4 and cold plasma surface modification as a means of enhancing CH_4 adsorption, upgrading low-cost biomass-derived chars as effective adsorbents for such a system.

CH_4 adsorption performance was measured for four biochars and compared against that of three commercial activated carbons. While the pristine biochars exhibited adsorption capacities at least 50% lower than those of the tested activated carbons, they demonstrated more than twice the CH_4 storage capacity of compressed natural gas (CNG) at equivalent pressure and vessel volume (10-75 bar), demonstrating their potential to reduce compression requirements and avoid heavy high-pressure storage vessels in field applications. Adsorption thermodynamics and kinetics were analyzed to establish performance baselines and implications for adsorbed natural gas (ANG) storage.

To improve CH_4 storage performance of biochars, this work further investigated cold dielectric barrier discharge (DBD) plasma as a solvent-free, low-temperature surface modification technique. Three key findings emerged: the optimal plasma duration was 30 minutes; the initial volatile matter content of biochar directly governs plasma modification efficiency; and Ar plasma is the most

effective source gas, increasing CH_4 adsorption capacity by up to 73%. It was also demonstrated that O_2 in plasma gas (i.e., air or O_2/He) led to a reduction in plasma effectiveness. Results indicate that the enhancement is associated with an increase in the specific surface area of biochars driven by the development of ultramicropores (<0.68 nm), which is in turn associated with the removal of organic impurities from biochar surfaces. Evidence indicates that the morphology, especially the width of pore entrances, may govern the adsorption effectiveness of biochars.

Finally, the research evaluated the end-of-life utilization of spent biochars. Multicycle adsorption tests showed that the adsorption performance of biochars degraded with repeated cycles. However, the degraded biochars can still store more methane volumetrically than compressed gas vessels at low to medium pressures relevant to oil and gas fields. Spent biochars retained residual CH_4, which increased calorific value (e.g. from 13.88 to 18.62 kJ/g) and reduced ignition temperatures (e.g. from 320 °C to 250 °C), supporting their reuse as an enhanced solid fuel.

This work demonstrates a laboratory-scale proof-of-concept that integrates emission abatement, energy recovery, and circular material use. If future work achieves techno-economic optimization, multicomponent gas validation, and successful scale-up of plasma treatment, this approach could potentially contribute to reducing the lifecycle GHG footprint of remote oil field operations. Significant engineering and economic development remains before field deployment feasibility can be assessed.

Résumé

Le torchage routinier du gaz de pétrole associé (APG) demeure une source majeure d'émissions de gaz à effet de serre dans la production pétrolière en amont, en particulier sur les sites de production éloignés ou à infrastructure limitée où le transport et le traitement du gaz ne sont pas économiquement viables. Le développement d'une stratégie déployable sur le terrain et en boucle fermée, permettant de capter l'APG riche en méthane (CH_4) pour la production sur site d'électricité et de chaleur à faible coût, contribuerait à réduire de manière significative la consommation d'énergie et les émissions de gaz à effet de serre (GES) de l'industrie pétrolière. Cette thèse examine l'utilisation du biochar comme adsorbant pour capter et stocker le CH_4, ainsi que la modification de surface par plasma froid comme moyen d'améliorer l'adsorption du CH_4, afin de valoriser des biochars dérivés de biomasse à faible coût en tant qu'adsorbants efficaces pour un tel système.

Les performances d'adsorption du CH_4 ont été mesurées pour quatre biochars et comparées à celles de trois charbons actifs commerciaux. Bien que les biochars non modifiés aient présenté des capacités d'adsorption au moins 50 % inférieures à celles des charbons actifs testés, ils ont démontré une capacité de stockage du CH_4 plus de deux fois supérieure à celle du gaz naturel comprimé (GNC) à pression et volume de réservoir équivalents (10–75 bar), ce qui indique leur potentiel pour réduire les exigences de compression et éviter l'utilisation de réservoirs lourds à haute pression dans les applications sur le terrain. La thermodynamique et la cinétique d'adsorption ont été analysées afin d'établir des références de performance et d'évaluer les implications pour le stockage de gaz naturel adsorbé (ANG).

Afin d'améliorer les performances de stockage du CH_4 des biochars, ce travail a également étudié le plasma à décharge à barrière diélectrique (DBD) à froid comme technique de modification de surface sans solvant et à basse température. Trois résultats principaux ont été obtenus: la durée optimale du traitement plasma est de 30 minutes; la teneur initiale en matières volatiles du biochar influence directement l'efficacité de la modification par plasma; et le plasma d'argon (Ar) constitue le gaz source le plus efficace, augmentant la capacité d'adsorption du CH_4 jusqu'à 73 %. Il a également été démontré que la présence d'O_2 dans le gaz plasma (p. ex., air ou O_2/He) réduit l'efficacité du traitement plasma. Les résultats indiquent que l'amélioration est associée à une augmentation de la surface spécifique des biochars due au développement d'ultramicropores (< 0,68 nm), elle-même liée à l'élimination d'impuretés organiques à la surface du biochar. Les observations suggèrent également que la morphologie des pores, en particulier la largeur de l'entrée des pores, peut influencer l'efficacité d'adsorption des biochars.

Enfin, la recherche a évalué l'utilisation en fin de vie des biochars usagés. Des essais d'adsorption multi-cycles ont montré que les performances d'adsorption des biochars diminuent au cours des cycles répétés. Toutefois, même dégradés, les biochars peuvent encore stocker plus de méthane en termes de capacité volumétrique que les réservoirs de gaz comprimé aux pressions faibles à modérées typiques des champs pétroliers et gaziers. Les biochars usagés retiennent du CH_4 résiduel, ce qui augmente leur pouvoir calorifique (par exemple de 13,88 à 18,62 kJ/g) et abaisse leur température d'inflammation (par exemple de 320 °C à 250 °C), soutenant leur réutilisation comme combustible solide amélioré.

En combinant réduction des émissions, récupération d'énergie et utilisation circulaire des matériaux, ce travail met en évidence une voie pragmatique pour réduire l'empreinte des gaz à

effet de serre sur l'ensemble du cycle de vie (CO_2éq) des opérations pétrolières dans les sites éloignés. Cependant, les travaux futurs devraient aborder les interactions entre gaz multicomposants, la mise à l'échelle du procédé plasma et l'optimisation technico-économique, avant que le déploiement sur le terrain puisse être évalué.

Copyright Statement

Statement of Contributions of Collaborators

I declare that I am the sole author of this thesis. I was responsible for the conception of the research objectives, experimental design, execution of all laboratory work, data processing, analysis, and preparation of the manuscript text.

Scientific supervision, technical advice, and editorial feedback were provided by my supervisors, Drs. Christopher Lan and Jinsheng Wang. Contributions from collaborators in the form of academic discussion or manuscript review are acknowledged where appropriate, and individuals who meet authorship criteria are listed as co-authors in the corresponding journal publications.

Acknowledgments

This research benefited from the support, guidance, and collaboration of many individuals.

Sincere appreciation is extended to my supervisor, Dr. Christopher Lan, whose mentorship and constructive feedback were instrumental in navigating the research and publication process. Through his guidance, I have strengthened my scientific reasoning and gained the confidence to become an independent researcher. I feel truly fortunate to have had him as my mentor.

I am equally grateful to my co-advisor, Dr. Jinsheng Wang, for the original idea that gave rise to this study, for his expertise that helped establish the scientific and mathematical foundations of the adsorption studies, and for his readily available guidance throughout this research.

Valuable support was provided by my colleagues at CanmetENERGY-Ottawa and the Subsurface Energy Technology Group. The COVID-19 shutdown and subsequent roof repairs at CanmetENERGY-Ottawa presented significant delays and additional challenges. I am deeply thankful to David Ryan, my group leader, for his understanding and accommodation, which were essential to completing this work.

Exceptional expertise was shared by Dr. Vladimir Pankov at the National Research Council, one of the few plasma specialists in Canada, whose safety and grounding inspection of the laboratory, diagnosis of a critical RF reactor instrument issue, and thoughtful review of the manuscript were invaluable to the progress and quality of this thesis.

Deepest appreciation is reserved for my husband, Dr. Alexandre Martychenko, whose suggestion to explore plasma modification opened new directions in this thesis. His hands-on assistance

during the design and execution of the plasma experiments, including safety oversight during high-voltage operation, was indispensable. Beyond the laboratory, his constant care and steadfast belief kept me moving forward. For his love, his scientific insight, and his presence at every stage, I am forever grateful.

List of publications from the results of this project

Journal articles

A. **V.Y. Ko**, J. Wang, I. He, D. Ryan, X. Zhang, C. Lan, Adsorption of CH_4 on biochar for emission reduction in oil and gas fields, *Biochar* 5 (2023) 15, https://doi.org/10.1007/s42773-023-00209-x. **(Chapter 3).**

B. **V.Y. Ko**, J. Wang, C. Lan, D. Ryan, Enhanced CH_4 adsorption through ultramicropores development in cold plasma-activated biochar, *Chemical Engineering Journal* 524 (2025) 169286. https://doi.org/10.1016/j.cej.2025.169286. **(Chapter 4).**

C. **V.Y. Ko**, J. Wang, C. Lan, D. Ryan, Cold-plasma treated biochars and activated carbons for CH_4 adsorption: effects of plasma source gases, submitted to *Environmental Science and Technology* **(Chapter 5).**

D. **V.Y. Ko**, J. Wang, C. Lan, D. Ryan, Multicycle CH_4 adsorption-desorption in biochar: degradation analysis and value-added applications, to be submitted to a peer-reviewed journal **(Chapter 6).**

Conferences

A. **V.Y. Ko**, J. Wang, C. Lan, D. Ryan, CH_4 Capture in oil fields using biochar for energy recovery, women in STEM symposium 2020, on-line oral presentation, February 2020

B. **V.Y. Ko**, J. Wang, C. Lan, D. Ryan, Biochar for oil fields CH_4 storage and energy recovery, the 2020 Canadian Chemical Engineering Conference, on-line oral presentation, October 2020

C. **V.Y. Ko**, J. Wang, C. Lan, D. Ryan, CH_4 storage and energy recovery using biochar, 2023 Canada-Korea Conference on Science and Technology, oral presentation, Niagara Falls, June 2023

D. **V.Y. Ko**, J. Wang, C. Lan, D. Ryan, Advancing CH_4 mitigation in oil fields through enhanced CH_4 storage and energy recovery using cold plasma-activated biochar, CanCH_4 2025 Symposium, poster presentation, Ottawa, May 2025

E. **V.Y. Ko**, J. Wang, C. Lan, D. Ryan, Introducing CH_4 storage and energy recovery in oil fields using surface-modified biochar-cold plasma activation for improved adsorption and value-added product as a fuel or soil amendment, 3rd international conference on Net-Zero Built Environment, Net-Zero Future 2026, oral presentation, Germany, September 2026

Table of Contents

List of Figures

List of Tables

Abbreviations

AC	Activated Carbon
AC-CABOT	Activated Carbon - Cabot Corporation
AC-CS	Activated Carbon - Coconut Shell
AC-DC	Activated Carbon - Petroleum Coke
AC-FB	Activated Carbon – Fisher Brand
AC-FW	Activated Carbon - Fruit Wood
ANG	Adsorbed Natural Gas
APG	Associated Petroleum Gas
ARE	Average Relative Error
ASTM	American Society for Testing and Materials
AT	Alberta Tamarack
ATR	Attenuated Total Reflectance
ATR-FTIR	Attenuated Total Reflectance Fourier Transform Infrared Spectroscopy
BC	Biochar
BC-AT	Biochar – Air Terra
BC-BL	Biochar - Bella
BET	Brunauer-Emmett-Teller
BJH	Barrett-Joyner-Halenda
CNG	Compressed Natural Gas
COF	Covalent Organic Framework
DA	Dubinin-Astakhov
DBD	Dielectric Barrier Discharge
DFT	Density Functional Theory
DI	Deionized
DOE	US Department of Energy
DR	Dubinin-Radushkevich
DSC	Differential Scanning Calorimetry
EDF	Environmental Defense Fund
EOR	Enhanced Oil Recovery
EPA	U.S. Environmental Protection Agency
EWC	Expected Working Capacities
FTIR	Fourier Transform Infrared Spectroscopy
GCMC	Grand Canonical Monte Carlo
GHG	Greenhouse Gas

GWP	Global Warming Potential
HHV	High Heating Value
HK	Horvath-Kawazoe
IEA	International Energy Agency
IGA	Intelligent Gravimetric Analyzer
IUPAC	International Union of Pure and Applied Chemistry
LNG	Liquefied Natural Gas
MOF	Metal Organic Framework
NG	Natural Gas
NLDFT	Non-Local Density Functional Theory
NOx	Nitrogen Oxides
PCT	Pressure Concentration Temperature
POP	Porous Organic Polymer
PSA	Pressure Swing Adsorption
PSD	Pore Size Distribution
RF	Radio Frequency
SEM	Scanning Electron Microscopy
SSA	Specific Surface Area
STP	Standard Temperature and Pressure 0 °C and 1 atm.
TEM	Transmission Electron Microscopy
V/V	Volume per Volume
XPS	X-ray Photoelectron Spectroscopy
XRD	X-ray Diffraction
XRF	X-ray Fluorescence

Nomenclature

A	adsorbate cross sectional area (0.373 nm^2 for **CH_4**)
A_N	CH_4 adsorption at cycle, N (mmol/g)
Ar	residual activity
Ar	argon
B	adsorption parameter in adsorption models (Langmuir, Sips, and Toth)
B	Langmuir constant (bar^{-1})
B_0	adsorption coefficient in Toth adsorption model (bar^{-1})
B_t	value of B at a reference temperature (K)
C	BET constant (dimensionless)
CO_2 eq	carbon dioxide equivalent
eq	equilibrium
K	equilibrium constant (dimensionless)
k_1	pseudo 1st order rate constant (hr^{-1})
k_2	pseudo 2nd order rate constant $(mmol/g \cdot hr)^{-1}$
k_a	rate constant for adsorption $(bar \cdot hr)^{-1}$
k_d	rate constant for desorption (hr^{-1})
M	molecular weight of adsorbate
max	maximum value
N	weight of gas adsorbed (mg)
n	number of gas moles
n	dimensionless parameter in Toth model
N	total number of cycles
N	adsorption amount (mmol/g)
N_0	initial value of N (mmol/g)
N/N_m, θ	fraction of the adsorption sites
N∞	maximum adsorption capacity (mmol/g)
N_m	adsorption capacity (mmol/g)
N_{mt}	N_m value at a reference temperature (mg)
N_s	saturation adsorption capacity in Toth model (mmol/g)
N_{s0}	reference saturation adsorption capacity in Toth model (mmol/g)
P	gas pressure (bar)
P/P_0	Relative pressure to vaporization pressure (dimensionless)
Q	parameter in Toth model (dimensionless)
Q_e	amount of CH_4 adsorbed at equilibrium (mmol/g)

Q_t	amount of CH_4 adsorbed at time t, (mmol/g)
R	universal gas constant (8.314 J/mol·K)
R_{min}	minimum CH_4 residual (mmol/g)
t	parameter in Toth model (dimensionless)
t	time (hour)
t_0	heterogeneity parameter at reference temperature in Toth model (dimensionless)
T, T_0, T_a	temperature (K)
v/v	volume of gas delivered per volume of the storage container (cm^3/cm^3)
Wt%	weight percent

Greek symbols

α	Temperature dependence coefficient of Toth heterogeneity parameter t (dimensionless)
B	adsorption affinity parameter
Δ	change
θ	fraction of the adsorption sites occupied (N/N_m) (0-1)
θ_0	initial value of θ (0-1)
χ	Temperature dependence coefficient of Toth saturation capacity N_s (dimensionless)
η	plasma treatment effectiveness (%)
γ	surface concentration of CH_4 (mol/m^2)
ρ	density of adsorbed phase or bulk gas (g/ml)
ρ_a	density of the adsorbed phase (g/ml)
ρ_g	density of the gas phase (g/ml)

Chapter 1. Introduction

1.1 Motivation

Methane (CH_4) is both a valuable energy carrier and a highly potent greenhouse gas. Although its atmospheric lifetime is relatively short, approximately 12 years, CH_4 absorbs infrared radiation more effectively than carbon dioxide (CO_2) and promotes the formation of tropospheric ozone and stratospheric water vapor, resulting in a 100-year global warming potential more than 28 times greater than that of CO_2 [1]. Consequently, reducing CH_4 emissions offers substantial near-term climate benefits and has become a central focus of global mitigation strategies [2].

The oil and gas sector is a major source of CH_4 emissions, largely due to routine venting and flaring of associated petroleum gas (APG), a CH_4-dominant gas mixture co-produced with crude oil [3]. At a global scale, routine APG flaring releases an estimated 400 million tonnes of CO_2 equivalent annually, representing substantial and largely avoidable hydrocarbon emissions in the energy sector [4]. In many oil fields, particularly in remote locations or during early-stage developments, APG is flared because transportation or processing is uneconomic. In practice, flaring is therefore preferred to direct venting from a climate perspective because it converts CH_4 to CO_2. However, flaring remains environmentally detrimental, as it generates substantial CO_2 emissions and often releases fugitive CH_4 due to incomplete combustion and flare inefficiencies commonly referred to as CH_4 slip [5,6]. Beyond its environmental impact, flaring also represents a significant loss of a valuable energy resource.

Recognizing the environmental burden and energy losses associated with routine flaring, this work advances the concept of capturing and utilizing APG directly at the field site as a practical

alternative. APG can be recovered and converted to useful heat and power, reducing CH_4 emissions while partially displacing externally supplied fuels, such as diesel in remote oil field operations [7]. Furthermore, an integrated carbon and energy management system is considered in which CH_4 utilization is coupled with capture and reinjection of CO_2-rich exhaust streams for enhanced oil recovery (EOR) or geological sequestration, forming a closed carbon management loop. At the field level, such integration offers a structured pathway to reduce routine flaring through a modular and adaptable configuration that can operate in remote locations with limited gas transportation infrastructure.

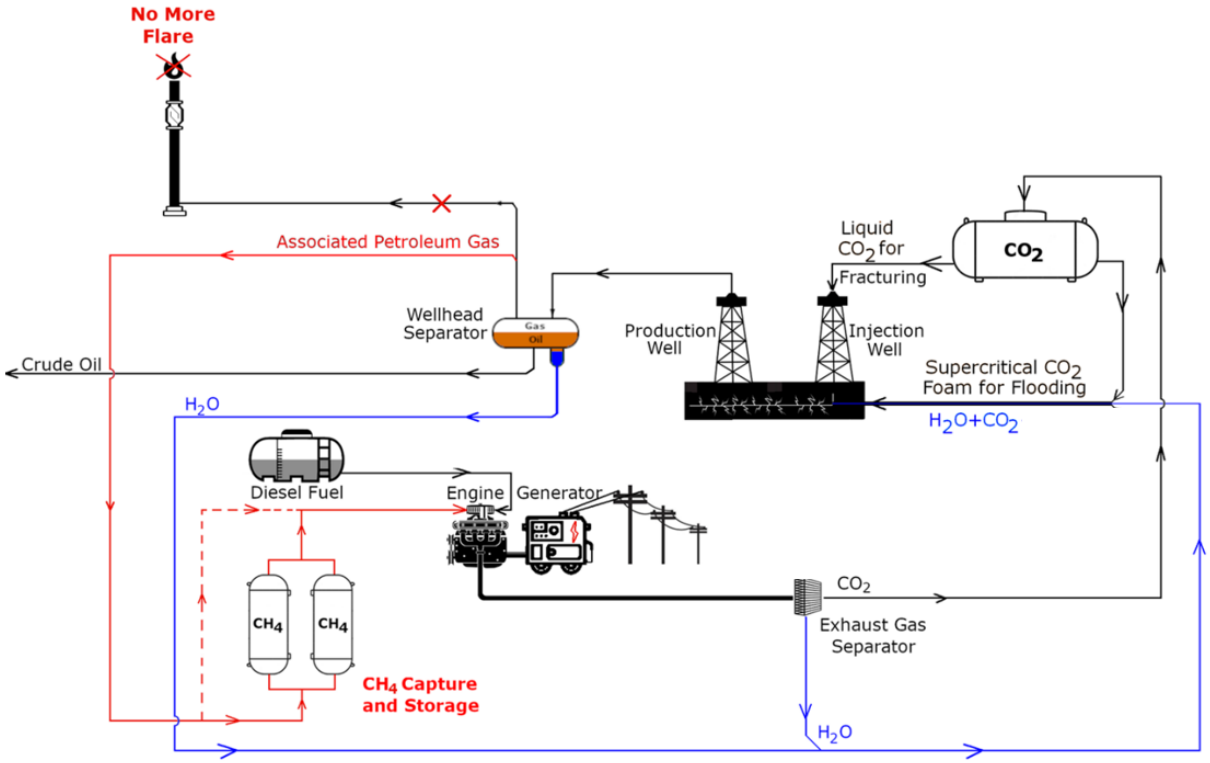

Fig. 1.1 Schematic of an exemplary process integrating biochar-based ANG system with on-site power generation and CO_2 reinjection in tight oil reservoirs

Fig. 1.1 illustrates the conceptual framework in which a biochar-based adsorbed natural gas (ANG) system with on-site power generation and subsequent CO_2 capture and reinjection in a tight oil

reservoir. APG separated from crude oil is routed to ANG vessels operated in a pressure-swing adsorption mode [8], where CH_4 is cyclically adsorbed at elevated pressure and desorbed on demand to fuel gas or dual-fuel engines for on-site heat and power generation. Engine exhaust, composed mainly of CO_2, N_2, and water vapor, can be directed to a separation unit to recover a concentrated CO_2 stream for potential on-site reinjection. Where reservoir conditions permit, the recovered CO_2 may be combined with produced water to generate CO_2-based foam for enhanced oil recovery, particularly in tight or heterogeneous formations to improve sweep efficiency and conformance [9]. CO_2 improves oil mobility while simultaneously enabling subsurface carbon storage.

A key technical requirement for such a system is reliable CH_4 storage to buffer variability in gas production and to provide a steady fuel supply. Conventional APG management options, such as liquefied natural gas (LNG) or compressed natural gas (CNG), require substantial infrastructure investment [10,11]. ANG offers a suitable alternative by storing CH_4 through physisorption on porous solids at moderate pressures and near ambient temperatures, enabling simpler operation and flexible deployment [12]. Adsorbent selection is therefore central to the ANG system. Established adsorbents such as activated carbon are costly and require complex manufacturing processes that limit their viability in remote field settings [13]. Biochar, produced through biomass pyrolysis, is an attractive adsorbent material in ANG due to its low cost, feedstock availability, and simple end-of-life handling [14].

However, enhancing biochar performance can further improve the technical and economic feasibility of ANG deployment. Common activation methods such as KOH impregnation or steam activation are effective but chemically intensive and energy demanding [15,16].

In this work, cold plasma treatment is employed as a low-temperature, solvent-free modification method capable of altering pore accessibility and surface properties without chemical reagents or high thermal input. Although plasma processing of carbon materials has attracted increasing attention, its application to biochar for CH_4 storage remains largely unexplored [17]. The present work therefore examines cold-plasma modification in detail, with emphasis on optimizing treatment parameters and elucidating the physicochemical changes responsible for enhanced CH_4 adsorption.

Beyond CH_4 capture and storage, this study adopts a life cycle perspective in which CO_2 generated during combustion is treated as a recoverable carbon stream for potential EOR or geological storage [9,18]. In addition, spent biochar retains value after adsorption service and can be repurposed as a soil amendment or as a solid fuel with increased heating value due to residual CH_4 within its pore structure, supporting a circular carbon-use strategy.

This research proposes a viable pathway to reduce emissions at oil production sites by converting APG into on-site energy using plasma-enhanced biochar-based ANG storage, integrated with CO_2 utilization and end-of-life biochar reuse.

1.2 Bridging the gap

This work identifies the central gap in APG management as the absence of adsorption systems that are compatible with the economic, operational, and lifecycle constraints of remote oil field deployment. To the author's knowledge, this thesis presents the first systematic investigation of biochar and plasma-modified biochar for high-pressure, cyclic CH_4 adsorption under oil field-relevant ANG conditions.

First, this research demonstrates that biochar can achieve meaningful CH_4 storage under ANG-relevant pressures while remaining scalable, low cost, and tolerant of field-relevant gas compositions. Through cold plasma modification, biochar performance is systematically enhanced without reliance on high temperatures, corrosive chemicals, or centralized manufacturing. This approach bridges the gap between laboratory adsorption performance and materials that can be produced and deployed near the point of gas generation.

Second, the work embeds ANG within a broader energy and carbon management framework. Integrating biochar-based ANG storage with on-site power generation and CO_2 capture and reinjection transforms APG from a flaring liability into a flexible energy buffer while enabling subsurface carbon storage. This integration closes the operational gap between CH_4 mitigation and CO_2 management using infrastructure already familiar to the oil and gas sector.

Third, the lifecycle perspective adopted here addresses a persistent limitation of solid adsorbents: end-of-life handling. Biochar uniquely enables a dual-use pathway in which spent adsorbents retain value as enhanced solid fuels, converting adsorbent degradation from a disposal burden into a resource recovery opportunity.

Collectively, these contributions position biochar-based ANG as a technically grounded and potentially field-deployable response to the APG flaring problem.

1.3 Research objectives

The present work investigates cold plasma activation of biochar as a strategy to enhance CH_4 adsorption performance for ANG-based APG utilization in remote oil field environments.

The following specific objectives are pursued:

1. **Establish the baseline CH_4 adsorption performance of raw biochar.**
   Quantify CH_4 adsorption on biochar through adsorption isotherms and kinetics, establishing baseline performance relevant to ANG deployment in oil and gas fields.

2. **Evaluate the effects of plasma treatment duration on biochar modification and CH_4 adsorption.**
   Investigate the physicochemical changes induced by cold plasma activation, particularly ultramicropore development through removal of surface-bound impurities and their effect on CH_4 uptake.

3. **Assess the effects of feedstock properties and plasma source gas composition on treatment efficiency.**
   Systematically examine how adsorbent volatile content and plasma gas identity govern the extent and nature of plasma-induced surface modification.

4. **Examine multicycle adsorption stability and spent biochar reuse.**
   Quantify capacity retention over repeated adsorption-desorption cycles and characterize spent biochar fuel properties through calorific value and ignition temperature measurements.

1.4 Thesis structure

This thesis is organized into seven chapters and three appendices.

Chapter 1 introduces the research motivation, context, objectives, and bridging gaps addressed by this work. **Chapter 2** establishes the research rationale, by examining APG flaring challenges, ANG storage as a field-deployable alternative, biochar as a low-cost adsorbent, surface modification strategies including cold plasma, and end-of-life valorization pathways. **Chapter 3** compares the isotherms and kinetics of the CH_4 adsorption of four biochars and three activated carbons and established biochars as a viable adsorbent for adsorbed natural gas system aiming for application in oil fields and the need to further improve their adsorption capacities. **Chapter 4** examines how plasma treatment duration drives pore structure evolution and translates into measurable gains in CH_4 adsorption capacity with a focus on the effects of plasma duration. **Chapter 5** extends this investigation to the role of feedstock properties, especially the initial volatile content, and the plasma gas in governing modification outcomes across biochar and activated carbon substrates. **Chapter 6** addresses multicycle adsorption-desorption stability and end-of-life characterization of spent biochar as a solid fuel. **Chapter 7** summarizes key findings, and outlines implications and future research directions. *Appendices A* and *B* provide supplementary material for Chapter 3 and *Appendix C* presents a poster contributed to the CanCH_4 Workshop.

References

[1] World Bank Group, How can we reduce methane emissions? World Bank. https://www.worldbank.org/en/programs/gasflaringreduction/methane-explained.

[2] US EPA, Methane Emissions Reduction Program, (2023). https://www.epa.gov/inflation-reduction-act/methane-emissions-reduction-program.

[3] X. Yang, E. Kuru, X. Zhang, S. Zhang, R. Wang, J. Ye, D. Yang, J.J. Klemeš, B. Wang, Direct measurement of methane emissions from the upstream oil and gas sector: Review of measurement results and technology advances (2018–2022), J. Clean. Prod. 414 (2023) 137693. https://doi.org/10.1016/j.jclepro.2023.137693.

[4] World Bank Group, What is Gas Flaring? World Bank. https://www.worldbank.org/en/programs/gasflaringreduction/gas-flaring-explained.

[5] G. Plant, E.A. Kort, A.R. Brandt, Y. Chen, G. Fordice, A.M. Gorchov Negron, S. Schwietzke, M. Smith, D. Zavala-Araiza, Inefficient and unlit natural gas flares both emit large quantities of methane, Science 377 (2022) 1566–1571. https://doi.org/10.1126/science.abq0385.

[6] D.T. Allen, D. Smith, V.M. Torres, F.C. Saldaña, Carbon dioxide, methane and black carbon emissions from upstream oil and gas flaring in the United States, Curr. Opin. Chem. Eng. 13 (2016) 119–123. https://doi.org/10.1016/j.coche.2016.08.014.

[7] V. Morenov, E. Leusheva, G. Buslaev, O.T. Gudmestad, System of Comprehensive Energy-Efficient Utilization of Associated Petroleum Gas with Reduced Carbon Footprint in the Field Conditions, Energies 13 (2020) 4921. https://doi.org/10.3390/en13184921.

[8] J. Romanos, T. Rash, S. Abou Dargham, M. Prosniewski, F. Barakat, P. Pfeifer, Cycling and Regeneration of Adsorbed Natural Gas in Microporous Materials, Energy Fuels 31 (2017) 14332–14337. https://doi.org/10.1021/acs.energyfuels.7b03119.

[9] S.H. Talebian, R. Masoudi, I. Mohd. Tan, P.L.J. Zitha, Foam assisted CO_2-EOR: A review of concept, challenges, and future prospects, J. Pet. Sci. Eng. 120 (2014) 202–215. https://doi.org/10.1016/j.petrol.2014.05.013.

[10] A. Sharafian, O.E. Herrera, W. Mérida, Performance analysis of liquefied natural gas storage tanks in refueling stations, J. Nat. Gas Sci. Eng. 36 (2016) 496–509. https://doi.org/10.1016/j.jngse.2016.10.062.

[11] Y. Ali, A. Younus, A.U. Khan, A.H. Alrefai, Compressed Natural Gas (CNG) as a fuel and the associated risks: A quantitative analysis in the scenario of a developing country, J. Saf. Sci. Resil. 5 (2024) 306–316. https://doi.org/10.1016/j.jnlssr.2024.05.001.

[12] J. Wegrzyn, M. Gurevich, Adsorbent storage of natural gas, Appl. Energy 55 (1996) 71–83. https://doi.org/10.1016/S0306-2619(96)00015-3.

[13] A.K. Vuppaladadiyam, M.K. Jena, I.G. Hakeem, S. Patel, G. Veluswamy, A.V. Thulasiraman, A. Surapaneni, K. Shah, A critical review of biochar versus hydrochar and their application for H_2S removal from biogas, Rev. Environ. Sci. Biotechnol. 23 (2024) 699–737. https://doi.org/10.1007/s11157-024-09700-8.

[14] F.R. Oliveira, A.K. Patel, D.P. Jaisi, S. Adhikari, H. Lu, S.K. Khanal, Environmental application of biochar: Current status and perspectives, Bioresour. Technol. 246 (2017) 110–122. https://doi.org/10.1016/j.biortech.2017.08.122.

[15] G.G. Stavropoulos, A.A. Zabaniotou, Minimizing activated carbons production cost, Fuel Process. Technol. 90 (2009) 952–957. https://doi.org/10.1016/j.fuproc.2009.04.002.

[16] J.Y. Lai, L.H. Ngu, Comparative laboratory cost analysis of various activated carbon activation process, IOP Conf. Ser. Mater. Sci. Eng. 1195 (2021) 012018. https://doi.org/10.1088/1757-899X/1195/1/012018.

[17] X. Sun, J. Bao, K. Li, M.D. Argyle, G. Tan, H. Adidharma, K. Zhang, M. Fan, P. Ning, Advance in Using Plasma Technology for Modification or Fabrication of Carbon-Based Materials and Their Applications in Environmental, Material, and Energy Fields, Adv. Funct. Mater. 31 (2021) 2006287. https://doi.org/10.1002/adfm.202006287.

[18] H. McLaughlin, A.A. Littlefield, M. Menefee, A. Kinzer, T. Hull, B.K. Sovacool, M.D. Bazilian, J. Kim, S. Griffiths, Carbon capture utilization and storage in review: Sociotechnical implications for a carbon reliant world, Renew. Sustain. Energy Rev. 177 (2023) 113215. https://doi.org/10.1016/j.rser.2023.113215.

Chapter 2. Research Rationale

2.1 CH_4 utilization in the oil industry

2.1.1 CH_4 emissions and APG challenges

Near-zero CH_4 emissions from oil and gas operations have been identified as a technical possibility [1–3]; however, achieving this at scale requires substantial infrastructure investment. Global estimates indicate that approximately USD 200 billion would be needed, largely to connect recovered CH_4 to existing pipeline networks and downstream markets [1,4].

APG is often treated as an unwanted by-product because its production is intermittent, geographically dispersed, and frequently remote from pipeline infrastructure, making conventional gas gathering and transport economically unattractive [5–7]. In addition, natural gas prices are highly volatile and location dependent; in areas lacking nearby consumers or pipeline access, the gas may have little or no market value [8]. Consequently, centralized gas-handling infrastructure is rarely justified, leaving a substantial fraction of APG unmanaged and routinely disposed of through venting or flaring for operational and safety reasons. According to the International Energy Agency, oil operations alone emitted approximately 45 Mt CH_4 in 2024, with natural gas operations contributing an additional 35 Mt CH_4 [9].

From a climate perspective, flaring is preferable to direct venting because it oxidizes CH_4 to CO_2, thereby lowering short-term radiative forcing given CH_4's much higher global warming potential (GWP) relative to CO_2 (GWP of 28 vs. 1, over 100 years). Nevertheless, flaring remains an inherently inefficient mitigation strategy, as it releases CO_2, black carbon, and products of incomplete combustion while permanently destroying a valuable energy resource. Globally, the

energy content of flared gas in 2024 was estimated to be equivalent to approximately 136 million tonnes of oil per year, highlighting flaring as both an environmental liability and a significant lost opportunity for energy recovery [10,11]. These limitations motivate a shift beyond mitigation toward strategies that retain the energetic value of APG.

2.1.2 From flare to fuel: CH_4 recovery

Realizing this potential requires decentralized, field-deployable solutions that prioritize capture and productive use of APG over disposal [12]. Routing APG into on-site utilization pathways, such as power generation or combined heat and power system, can deliver more durable emissions abatement while improving energy reliability and displacing diesel generation, which dominates many remote oil field operations [13,14]. This defines a coherent capture-store-use paradigm: APG is collected at the point of production, temporarily stored to buffer supply intermittency, and utilized on site, reducing CH_4 emissions without reliance on large-scale pipeline infrastructure [7,15,16]. The core technical question, therefore, is how to convert CH_4-rich APG into a storable and utilizable on-site fuel under field-relevant constraints. Solutions must tolerate variable flow rates and composition, operate at near ambient temperature, minimize safety risks, and remain cost-effective in decentralized environments [17].

Oil companies are increasingly paying attention to APG utilization, motivated not only by regulatory requirements but also by the potential for economic benefit [18]. Nevertheless, the prevailing industrial approach remains component separation, particularly through the recovery of C_2+ hydrocarbons, rather than direct utilization of the APG stream [19,20]. APG is primarily composed of CH_4, ethane, propane, and butane, making it a valuable feedstock for petrochemical processing. However, gas-to-liquids, gas-to-chemicals, and separation-based processing are

capital intensive and are often economically impractical for small-scale or remote oil fields. Table 2.1 presents the typical composition of APG.

Table 2.1 Typical composition of APG [21–23]

Component	Approximate range
CH_4	60-80 vol%
C_2H_6	5-15 vol%
C_3H_8	5-10 vol%
C_4+ (Butane, pentane, heavier natural gas components)	~10 vol%
N_2, CO_2, H_2S, inert/acid gases	trace to a few %

Despite growing interest, on-site APG utilization remains limited in practice. The primary barrier is supply intermittency: APG production fluctuates significantly with crude oil output, making a stable fuel supply difficult to maintain without intermediate storage [18]. The choice of storage technology is therefore a critical design consideration for field deployment.

2.1.3 Adsorbed natural gas (ANG) as a field-relevant alternative to compressed natural gas (CNG) and liquefied natural gas (LNG)

Neither conventional storage technology is well suited to remote oil field conditions. LNG requires cryogenic temperatures (-161 °C), complex refrigeration systems, and active boil-off management, making it capital-intensive and operationally burdensome at small scales [24]. CNG demands compression to 200-250 bar, resulting in high stored energy density, heavier vessels, and elevated safety and cost concerns in remote oil field environments [25].

ANG offers a promising alternative. By exploiting reversible physisorption in porous materials, ANG systems can store CH_4 at moderate pressures (typically 35–65 bar) and ambient temperatures [26]. This pressure range corresponds to a practical compromise between adsorption capacity and

deliverability, substantially reducing compression energy, vessel mass, and safety risks while enabling modular, lightweight storage compatible with on-site deployment [27]. ANG storage operates through reversible physisorption allowing gas molecules to accumulate near the surface without undergoing liquefaction [28], and thus avoids issues associated with cryogenic handling or high-pressure containment. Importantly, ANG operating conditions closely align with those of APG separation and downstream handling units (below 100 bar) [29], simplifying integration into existing field infrastructure. As a result, ANG is particularly attractive for small-to-medium-scale field deployment, where space is abundant, but reliability is paramount.

To benchmark ANG performance against established storage technologies, the U.S. Department of Energy (DOE) defined CH_4 storage targets in 2012 for LNG, CNG, and ANG in natural gas vehicle applications [30,31] as summarized in Table 2.2. Although developed for vehicular systems, these targets provide a useful reference for comparing the fundamental storage efficiency of different CH_4 storage technologies.

Table 2.2 DOE Target CH_4 storage capacities of LNG, CNG, and ANG [30,32,33]

Gas storage method	**LNG**	**CNG**	**ANG**
CH_4 Storage Capacity	600 v/v	230 v/v	263 v/v
@ Operation Conditions	@ -161 °C, 1 bar	@ 25 °C, 250 bar	@ 20-25 °C, 1-35 bar
v/v (cm^3(STP)/cm^3): volume of gas delivered per volume of the storage container			

It is acknowledged that LNG has a clear advantage in volumetric energy density (~22.2 MJ/L for LNG vs. ~5–9 MJ/L for ANG at 35 bar, depending on the adsorbent), and for applications involving bulk transport over long distances, LNG remains the established technology. However, the thesis targets a fundamentally different use case: on-site capture and utilization of stranded APG at remote, infrastructure-limited oil field locations, where the operational simplicity, low

capital cost, ambient-temperature operation, and modularity of ANG provide compelling advantages that outweigh the volumetric density penalty.

In vehicle applications, the volumetric energy density (deliverable or working capacity) is a critical parameter of CH_4 storage due to stringent space and weight constraints. In contrast, in oil production environments where surface footprint is less restrictive, storage volume becomes a secondary consideration [34]. Instead, system simplicity, safety, and compatibility with fluctuating gas supply dominate design requirements. Under these conditions, physisorption of natural gas on porous materials is well suited as a storage strategy [35].

This advantage is illustrated in Fig. 2.1, which reproduces reported data from an ANG tank developed at the University of Missouri. Experimental measurements conducted at 35–43 bar using a monolithic activated carbon adsorbent at 296 K are compared against compressed natural gas (CNG) storage at higher pressures, showing that ANG provides greater volumetric CH_4 storage than CNG below 250 bar [36]. Such pressure regimes are particularly relevant for buffering intermittent APG streams using pressure-swing adsorption and desorption cycles.

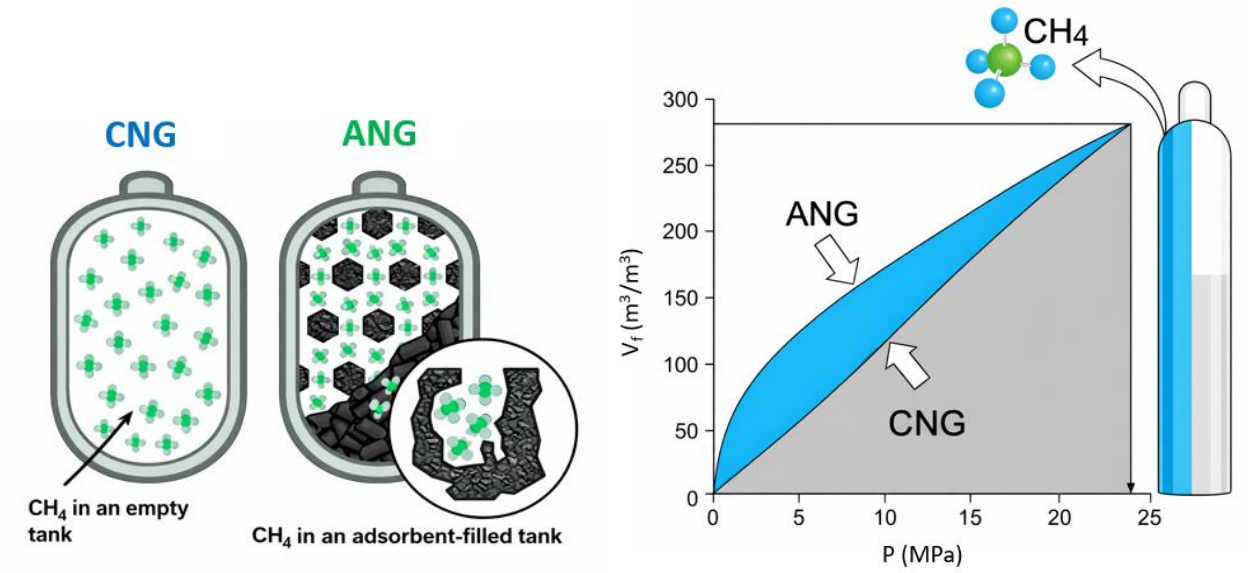

Fig. 2.1 Comparison of ANG and CNG [36,37]

Despite these technical advantages, dedicated design and engineering standards for integrating ANG storage into oil field operations have not yet been established, and the technology is not explicitly addressed in existing oil and gas codes and guidelines [38]. This regulatory gap contributes to the limited deployment of ANG systems in field environments. Nevertheless, techno-economic assessments indicate promising potential: a review of ANG applications in stationary emergency power systems concluded that, for a 500 kW generator, ANG storage could offer a lower-cost alternative to comparable CNG cylinder systems, with capital costs for the storage system estimated at approximately 55–80% of CNG while delivering equivalent power output [34].

Despite this economic potential, documented field applications remain scarce**.** Although pilot-scale stationary ANG systems have been reported, publicly available documentation of on-site ANG utilization of APG remains limited. For example, a technology provider describes an ongoing field test using more than 10 metric tons of activated carbon to fuel a grid-connected electric

generator [39]. However, grid-connected operation implies power export beyond the facility boundary and does not represent a self-contained, on-site APG utilization scenario. This gap highlights the need for field-ready ANG systems and adsorbent materials capable of delivering stable methane storage performance under realistic APG pressures, variable flow rates, and fluctuating gas compositions [39,40].

2.2 Adsorbent selection

The technical feasibility and economic viability of ANG-based APG utilization systems depend fundamentally on the choice of porous adsorbent. Several classes of porous materials, including activated carbons (ACs), metal organic frameworks (MOFs), porous organic polymers (POPs), and covalent organic frameworks (COFs), have been investigated for CH_4 storage [41,42]. However, many of these materials face challenges related to high production cost, limited scalability, and environmentally detrimental synthesis routes involving strong chemicals, organic solvents, or energy-intensive thermal treatments [43,44]. Consequently, despite strong laboratory performance, their real-world applicability in decentralized oil-field environments remains constrained [45]. To date, reported CH_4 adsorption studies are almost exclusively focused on ANG systems for vehicular applications, where performance is benchmarked against U.S. DOE targets that prioritize high adsorption at low pressure to ensure safety and compact storage volume under mobile constraints (Table 2.2).

The following sections review the general characteristics of each adsorbent class and critically assess their suitability for large-scale, low-cost ANG deployment in oil field environments.

2.2.1 Activated Carbons

Activated carbons represent the most mature and widely deployed class of physisorptive gas adsorbents, with extensive industrial use in gas separation and storage owing to their high microporosity and tunable pore size distributions [46,47]. They are typically produced via carbonization of organic feedstocks followed by physical activation with steam [48], or CO_2 at elevated temperatures (850–1000 °C) or chemical activation using reagents such as KOH, $ZnCl_2$ and H_3PO_4 [49]. These processes generate a high fraction of micropores (<2 nm), which are particularly effective for CH_4 adsorption [50].

When evaluated against the requirements of remote oil field ANG systems, however, several structural and economic limitations emerge:

- Energy and environmental intensity:

  Production of high-performance activated carbons is inherently energy-intensive, particularly for physically activated materials requiring sustained high-temperature operation. Chemical activation further generates acidic or alkaline waste streams requiring neutralization and disposal. As a result, reported life-cycle greenhouse gas emissions for activated carbon typically reach up to 11 kg CO_2eq per kg of product, which is substantially higher than those associated with biochar produced via low-temperature pyrolysis, where values are reported up to 1.5 kg CO_2eq per kg, [51–53] as summarized in Table 2.3.

- Cost at scale:

  Once activation, shaping, densification, and post-treatment are included, activated carbons are not commodity-priced materials. Specialty grades frequently exceed USD 10–20 per

kg [54,55], making large adsorbent inventories and replacement logistics economically challenging in remote oil field settings.

- Supply-chain misalignment:

  Activated carbon manufacturing is highly centralized and optimized for large industrial throughput, limiting flexibility for decentralized deployment. In contrast, oil field ANG systems benefit from materials that can be produced or replenished regionally using locally available resources [56,57].

2.2.2 Metal–organic frameworks (MOFs)

Metal–organic frameworks (MOFs), recognized by the 2025 Nobel Prize in Chemistry [58], represent the highest-performing class of porous materials for CH_4 storage under controlled laboratory conditions, owing to their crystalline architectures, extreme tunability, and exceptionally high surface areas [59]. MOFs constructed from metal nodes (i.e., Zn^{2+}, Cu^{2+}, Ni^{2+}) and organic linkers routinely achieve surface areas of 3000–5000 m^2/g, with gravimetric and working CH_4 capacities exceeding those of activated carbons under ANG-relevant pressures [60–63].

These performance advantages, however, do not directly translate to oil field ANG deployment for the reasons outlined below:

- Synthesis intensity and environmental burden:

  Most MOFs are synthesized via solvothermal routes involving toxic organic solvents, surfactants, and multistep purification, generating substantial chemical waste and environmental impact [64–66].

- Cost and scalability constraints:

  Commercial MOFs are sold at prices far above commodity sorbents, often hundreds to thousands of USD/kg for specialty grades, and manufacturing remains limited to kg-ton scales, well below the volumes required for field deployment [45,64,67–69].

- Mechanical and chemical fragility:

  Pelletization and densification frequently lead to framework collapse and loss of volumetric performance [70–72], and many MOFs exhibit poor stability in the presence of moisture, CO_2, H_2S, and heavier hydrocarbons common in APG streams [73–76].

- Moisture sensitivity:

  Carboxylate-based MOFs are particularly vulnerable to water; even trace moisture can hydrolyze metal–ligand bonds, leading to framework degradation and loss of accessible porosity [74,77].

2.2.3 Porous organic polymers (POPs) and covalent organic frameworks (COFs)

Porous organic polymers (POPs) and their subclass, covalent organic frameworks (COFs) are metal-free porous adsorbents composed primarily of light elements (C, H, N, O, B) [78–80]. The absence of metal-ligand bonds offers improved resistance to hydrolysis and chemical attack compared with many MOFs, making POPs and COFs attractive candidates for CH_4 adsorption under hydrocarbon containing conditions [81]. POPs are typically amorphous networks formed via irreversible covalent linkages [82,83], whereas COFs are crystalline materials assembled through reversible covalent chemistry [84], yielding ordered pore architectures. Both exhibit high surface areas, often exceeding 2000 m^2/g and tunable pore environments that enable competitive CH_4 uptake under laboratory conditions [85–87].

For field-scale ANG operation, several challenges remain:

- Mechanical robustness and densification:

  Practical ANG systems require pelletized or packed-bed configurations to achieve adequate volumetric performance. Many POPs and COFs are mechanically fragile, with densification often leading to pore collapse and loss of working capacity [88].

- Chemical stability under cycling:

  Although generally more moisture-tolerant than MOFs, some COFs rely on reversible covalent linkages that degrade over extended cycling [89], especially in the presence of trace water, CO_2, or acid gases common in APG streams.

- Technology readiness and cost:

  POPs and COFs are typically synthesized via multi-step organic reactions using specialty monomers and solvents, resulting in batch-scale production, modest yields, and high material cost. Their technology readiness level for ANG deployment remains low (TRL 3-5) relative to biochar [90,91].

2.2.4 Biochar as a cost-effective CH_4 adsorbent

Biochar is a porous carbonaceous, chemically robust material produced by pyrolysis of biomass feedstocks such as agricultural residues, forestry waste, or manure at 300–700 °C under oxygen-limited conditions [92]. The process converts biomass into a porous, charcoal-like carbon matrix while retaining a substantial fraction of the original carbon in a stable form [93]. While historically used as a soil amendment, its porous structure, chemical robustness, and carbon stability have prompted growing interest in gas storage and separation applications [94].

In contrast to engineered porous materials, biochar aligns closely with the operational realities of oil field ANG systems:

- Cost effectiveness and feedstock availability:

  Biochar can be produced from abundant, low-value biomass wastes, with bulk prices typically in the range of USD 0.15–0.19 per kg [52]. This cost advantage becomes decisive for large adsorbent inventories and periodic replacement. Continued market growth to approximately USD 6.7 billion by 2033 [95], supported by carbon removal policies such as the EU Carbon Farming Initiative and the US Inflation Reduction Act, further indicates scalability and commercial maturity [96].

- Low energy demand and favorable environmental footprint:

  Biochar production requires 0.84-16 MJ/kg, far lower than activated carbon, and often exhibits net negative life cycle GHG emissions due to long-term carbon sequestration [52]. Table 2.3 summarizes these contrasts.

Table 2.3 Environmental performance comparison of biochar and activated carbon [52,97–105]

Parameter	**Biochar**	**Activated Carbon**
Energy Consumption (MJ/kg)	0.84 -16	79.8 -170
GWP (kg CO_2 eq/kg)	(-) 3.5 - (+)1.5	1.2 -11 (coal-AC: up to 18.3)
Carbon Sequestration Potential (% of biomass C)	50 -80	Negligible
Primary CO_2 emission sources	Feedstock transport: pyrolysis energy input (offset by sequestered C)	Activation energy (steam/CO_2 at 800–1000 °C); chemical reagent production; waste stream treatment
Biogenic carbon credit	Yes — converts fast-cycle biomass C to stable aromatic C (>100 yr residence)	Limited — biomass-derived AC retains C but activation step releases 40–60% as CO_2
Typical Feedstock	Biomass wastes	Coal/wood (often fossil-derived)

- Operational compatibility with ANG systems:

  ANG systems typically operate at 35–65 bar [26], enabling CH_4 adsorption, storage, and controlled desorption for on-site heat and power generation without cryogenic handling or extreme compression.

- Favorable end of life management:

  Spent biochar retains value as a solid fuel or soil amendment, enabling circular material usage rather than disposal. This lifecycle flexibility is discussed further in Section 2.4.

To place the CH_4 storage performance and material cost of biochar in context, representative CH_4 uptakes and indicative prices for common porous adsorbents reported in the literature are summarized in Table 2.4.

Table 2.4 CH_4 storage performances and costs of different adsorbents

Material Class	**Representative Materials**	**CH_4 Uptake (mmol/g, 35–65 bar)**	**CH_4 Uptake References**	**Cost (USD/kg)**	**General Pricing References**
MOFs	HKUST-1 (Cu-BTC), MOF-5 (IRMOF-1), MIL-101(Cr)	6–12	[60,106–108]	13–55	[44,67,68,109]
POPs	PPNs, HCPs, PAF-type networks, flexible PANs	5–18	[110]	1–15	[110]
COFs	2D & 3D COFs, crystalline, lab scale	7–10	[81,111]	69	[112]
ACs	Optimized commercial, tailored microporous carbons	2.6–3.2	[113–115]	0.34–22	[52,116,117]
BCs	Commercial, hardwood	0.05-0.87 (<0.01bar)	[115]	0.05–8.3	[52,118]
	Commercial, spruce wood	1.4 (126 bar)	[119]		

Crucially, as summarized in Table 2.4, peer-reviewed studies reporting CH_4 adsorption on biochar under ANG-relevant conditions (35–65 bar) remain extremely limited. Although a small number of studies have examined biochar at higher pressures (e.g., up to 126 bar), these studies do not address storage feasibility under practical field constraints. In contrast, extensive CH_4 uptake data

exist for MOFs, POPs, COFs, and activated carbons within the ANG pressure range, leaving biochar underexplored despite its low cost, scalability, and environmental advantages. The table indicates that biochars (BCs) exhibit substantially lower reported CH_4 uptake than activated carbons (ACs); however, this apparent underperformance cannot be directly interpreted because AC values were measured at high pressures (35–65 bar), whereas the available BC data were obtained at very low pressure (<0.01 bar), and high-pressure adsorption studies for BCs remain scarce in the literature. This gap reflects the historical role of BCs in agricultural soil amendment and landfill cover applications, rather than high-pressure stationary applications such as oil field gas management. Accordingly, the high-pressure CH_4 adsorption behavior, cyclic durability, and practical feasibility of biochar as an ANG adsorbent remain unexplored in the open literature.

2.3 CH_4 adsorption performance

2.3.1 CH_4 adsorption isotherms

To address this knowledge gap, quantitative evaluation of CH_4 adsorption performance is required under ANG-relevant operating conditions. Adsorption isotherm analysis is central to quantifying CH_4 storage capacity, interpreting experimental uptake behavior, and enabling meaningful comparison across adsorbent materials. Isotherm models describe the relationship between adsorbed amount and gas pressure at constant temperature, thereby providing insight into adsorbent–adsorbate interaction strength, pore accessibility, and the role of microporous structures [120]. In this work, commonly used isotherm models, including Langmuir, BET, Freundlich, Sips, and Toth, are employed to evaluate and benchmark CH_4 adsorption performance across unmodified and plasma-modified biochars and commercial activated carbons under ANG-relevant operating conditions.

The Langmuir model is widely used because it is theoretically derived for monolayer adsorption on uniform sites and provides physically interpretable parameters [121]. The BET model assumes multilayer adsorption approaching condensation (P_0), which is not applicable to methane at ambient temperature because CH_4 is supercritical (Tc=190.6 K, Pc=45.99 bar) [122]. In this work, the Freundlich, Sips, and Toth models provide good statistical fits to the experimental CH_4 adsorption data; however, their empirical nature limits mechanistic interpretation and reliable extrapolation [121]. By contrast, the Langmuir model offers a physically interpretable framework with a well-defined saturation capacity and adsorption affinity constant, enabling thermodynamic interpretation of adsorption behavior. For this reason, the Langmuir model is adopted as the primary basis for discussion and comparison of CH_4 adsorption behavior throughout this study, and to extrapolate adsorption behavior beyond the experimentally investigated temperatures:

$$N = \frac{N_m * BP}{1 + BP} \tag{2.1}$$

where N is the adsorbed amount (mmol/g), Nm is the monolayer adsorption capacity (mmol/g), B is the Langmuir affinity constant (bar^{-1}), and p is the gas pressure (bar). The fractional surface coverage is defined as $\theta = N/N_m$. Langmuir constant B reflects the affinity between adsorbent and adsorbate. A larger value of B indicates stronger affinity between adsorbent and adsorbate.

2.3.2 CH_4 adsorption kinetics

To investigate adsorption mechanisms and identify rate-controlling steps, kinetic models are applied to the experimental CH_4 uptake data for biochars and activated carbons. Kinetic analysis provides insight into mass-transfer limitations, surface interaction rates, and the time scales required to reach equilibrium under ANG-relevant pressures.

Empirical pseudo-first order and pseudo-second-order kinetic models are commonly used to describe adsorption processes [123–126]. These models are expressed as:

$$\frac{dQ_t}{dt} = k_1(Q_e - Q_t) \tag{2.2}$$

$$\ln(Q_e - Q_t) = \ln Q_e - k_1 t \tag{2.3}$$

$$\frac{dQ_t}{dt} = k_2(Q_e - Q_t)^2 \tag{2.4}$$

$$\frac{t}{Q_t} = \frac{1}{k_2 {Q_e}^2} + \frac{t}{Q_e} \tag{2.5}$$

where Q_t is the amount of CH_4 adsorbed at time t on the adsorbent, Q_e is the amount of CH_4 adsorbed at equilibrium, and k_1 and k_2 are the rate constants of the respective models. Q_e varies strongly with pressure, making the kinetic parameters pressure dependent and limiting the physical interpretability of these models for high-pressure CH_4 adsorption. In this study, to address this limitation, adsorption kinetics are formulated directly from the Langmuir adsorption mechanism:

$$N = \frac{N_m BP}{1 + BP}\left[1 - e^{-k_d(1+BP)(t-t_0)}\right] + N_0 e^{-k_d(1+BP)(t-t_0)} \qquad [127] \tag{2.6}$$

where N_m is the Langmuir saturation capacity, B is the Langmuir affinity constant, k_d is the desorption rate constant, and N_0 is the initial adsorption amount. At sufficiently long times, Eq. 2.6 converges to the Langmuir equilibrium isotherm (Eq. 2.1).

The full derivation of the governing equations and their application to experimental CH_4 adsorption data are presented in Chapter 3.

2.3.3 Physicochemical basis of CH_4 adsorption on carbon surfaces

Although CH_4 is chemically inert, it adsorbs onto surfaces through London dispersion forces, attractive interactions arising from correlated electron density fluctuations between the adsorbate molecule and the surface. The strength of this interaction scales with the polarizability of both interacting molecules. CH_4 has zero permanent dipole and quadrupole moments due to its tetrahedral symmetry (Table 2.5), eliminating any electrostatic contribution to adsorption. However, its polarizability (25.9×10^{-25} cm^3) is substantially higher than N_2 (17.4), CO (19.5), and Ar (16.4), explaining its higher adsorption capacity on porous materials despite the absence of an electrostatic handle [128]. Phani et al. confirmed on an aluminum terephthalate MOF that the adsorption capacities of CO_2, CH_4, CO, N_2, Ar, and O_2 are governed primarily by polarizability rather than quadrupole moment [129]. CH_4 also possesses a non-zero octupole moment ($0.47–0.88 \times 10^{-24}$ esu·cm^2) [130], which may provide a weak secondary electrostatic contribution; this motivated the use of zeta potential measurements in Chapters 4 and 5 to assess whether surface charge plays any role alongside London dispersion.

Table 2.5 Molecular properties of common adsorbate gases [130–132]

Molecular properties	**CH_4**	**CO_2**	**N_2**	**CO**	**Ar**
Boiling point (K)	109.0	194.7	77.4	81.7	87.3
Molecular configuration	Tetrahedral				
Kinetic diameter (pm)	382	330-390	364-380	376	340
Polarizability ($\times 10^{-25}$ cm^3)	25.9	29.1	17.4	19.5	16.4
dipole moment ($\times 10^{-18}$ statcoulomb-cm)	0	0	0	0	0
quadrupole moment ($\times 10^{-26}$ esu cm^2)	0.00	4.30	1.52	2.50	0
Octupole moment, ($\times 10^{-24}$ esu cm^2)	0.47-0.88	0	0	NA	0
NA: data not available					

Since London dispersion force strength depends equally on the polarizability of the adsorbent surface, the carbon surface chemistry matters as much as the adsorbate properties. Carbon surfaces rich in graphitic character provide stronger dispersion interactions with CH_4 than surfaces dominated by amorphous carbon or oxygenated functional groups, which also introduce competitive water adsorption and reduce effective CH_4 capacity [133,134].

Beyond surface chemistry, pore geometry provides a separate and equally important contribution through confinement energy. When pore widths approach the CH_4 molecular diameter, simultaneous interaction with opposing pore walls amplifies the total adsorption energy relative to an open surface, making ultramicropore volume a stronger predictor of CH_4 capacity than total surface area alone [135,136].

The target adsorbent profile for effective CH_4 storage therefore combines a well-developed ultramicropore network to maximize confinement energy and a graphitic surface with low oxygenated functional group content to maximize London dispersion interactions — the properties quantified by the characterization framework described in Section 2.3.4.

2.3.4 Characterization of pore structure and surface chemistry

Adsorption performance is strongly governed by pore structure, particularly the presence of micropores. Pore morphology and surface structural changes are examined by scanning electron microscopy (SEM), while surface area and pore size distributions are quantified by gas physisorption. N_2 adsorption at 77 K is the widely used standard method for Brunauer–Emmett–Teller (BET) surface area but underestimates accessible area in ultramicroporous materials due to

kinetic diffusion limitations at 77 K in pores below ~0.7 nm [137], and its quadrupole moment introduces a surface chemistry bias on polar sites. CO_2 adsorption at 273 K is therefore employed to resolve the ultramicropore regime, which play a dominant role in CH_4 confinement [128]. Pore size distributions are derived using density functional theory (DFT) or grand canonical Monte Carlo (GCMC) analysis with a slit pore kernel; Barrett–Joyner–Halenda (BJH) is not applied because its capillary condensation assumptions break down below 2 nm. Where both datasets are available, N_2 and CO_2 physisorption are treated as complementary probes of different pore size regimes.

Beyond pore structure, surface chemical properties influence CH_4 adsorption by modifying adsorption energetics and tolerance to coexisting gas species. Surface functional groups are commonly characterized using Fourier-transform infrared spectroscopy (FTIR), X-ray photoelectron spectroscopy (XPS), and Boehm titration. Oxygen-containing groups, including carboxyls and phenols, increase surface polarity and hydrophilicity, which can reduce CH_4 affinity. Biochars typically retain higher oxygen content than activated carbons unless chemically or physically modified, making surface chemistry characterization particularly important for evaluating their suitability as CH_4 adsorbents.

In this study, attenuated total reflectance Fourier-transform infrared (ATR-FTIR) spectroscopy is employed to provide semi-quantitative directional information about changes in surface functional group concentrations and aromatic character before and after treatment. Measurements of pH and zeta potential provide complementary insight into surface acid–base properties and interfacial charge behavior, reflecting protonation–deprotonation equilibria and associated changes in surface polarity. While polarizability was not directly measured, these combined observations allow qualitative inference of changes in surface polarizability relevant to CH_4 adsorption.

For oil field ANG applications, competitive adsorption in the presence of moisture, CO_2, and heavier hydrocarbons requires careful investigation [115], as these species can alter pore accessibility and surface polarity, promote pore blockage, and reduce effective CH_4 storage capacity under realistic gas compositions.

2.4 Surface modification

Although biochar offers advantages such as low cost, scalability, and environmental sustainability, its native pore structure and surface chemistry are not always optimal for high-pressure CH_4 storage. Baseline adsorption measurements can reveal limitations in pore accessibility and adsorption performance, indicating the need for material modification. The target properties for effective CH_4 adsorption are: (i) ultramicropore width of 0.55–0.70 nm, where overlapping wall potentials from opposing pore surfaces maximize confinement energy and adsorption enthalpy [135]; (ii) a surface with high instantaneous polarizability, characteristic of sp^2 graphitic domains, to maximize London dispersion interactions with the non-polar, non-quadrupolar CH_4 molecule; and (iii) minimal oxygenated functional groups to reduce competitive water adsorption and preserve the π-electron density of the carbon framework. A wide range of modification strategies has therefore been investigated to enhance adsorption performance, particularly through increasing microporosity, opening blocked pore networks, or tuning surface chemistry [138]. These approaches can be broadly categorized as physical, chemical, or plasma-based methods, each operating through distinct mechanisms and carrying different implications for performance and environmental impact.

2.4.1 Physical modification methods

Physical modification methods employ thermal energy, radiation, or reactive gases to restructure biochar porosity without introducing liquid-phase chemicals [139]. These approaches are generally considered environmentally benign and scalable, but they typically require elevated temperatures and multiple processing steps, leading to higher energy consumption [140].

- Steam activation:

  Involves exposing pyrolyzed biochar to steam at 700-900 °C, where endothermic gasification reactions ($C + H_2O \rightarrow CO + H_2$) selectively remove carbon atoms and generate microporosity. Recent optimizations using superheated steam (up to 1000 °C) and controlled flow rates have yielded specific surface area (SSA) of 800-1500 m^2/g from wood-based biochars, with micropore volumes increasing to 0.4-0.6 cm^3/g [141]. For CH_4 storage, steam activation increases the fraction of narrow micropores (0.5-1.2 nm), which strengthens CH_4 confinement and can improve deliverable capacity in ANG pressure-swing operation [33].

- Microwave-assisted pyrolysis:

  Utilizes microwave irradiation (2.45 GHz, 500-1000 W) for rapid, volumetric heating, producing biochar with uniform pores in minutes versus in hours for conventional pyrolysis [142]. Recent studies use dielectric susceptors (e.g., SiC) to improve heating efficiency and uniformity [143], enabling high surface areas up to 1200 m^2/g [144,145]. Microwave processing can also increase carbon aromaticity and ordering, which is beneficial for electrochemical applications [146].

- Gas purging:

Employs inert (N_2, Ar) or reactive gases (CO_2) at high temperatures (600-1000 °C) to remove volatiles and widen pores. CO_2 purging, a mild activation, increases SSA by 50-200% with minimal structural damage, recently optimized for selective micropore development in algal biochars [147].

2.4.2 Chemical modification methods

Chemical modifications introduce reactive reagents or dopants to alter surface polarity, charge distribution, and functional groups, often enhancing adsorption selectivity and reactivity. However, they typically involve corrosive chemicals and multistep washing procedures, which can limit environmental compatibility and scalability [148].

- Acid/base modification:

  Acids (e.g., HNO_3, H_2SO_4, H_3PO_4) protonate surfaces, increasing carboxylic and phenolic groups [149], whereas bases (e.g., KOH, NaOH) deprotonate and etch pores [150].
- Functional group modification:

  Involves grafting amines, thiols, or polymers (e.g., polyethyleneimine) to target specific pollutants [151,152].
- Impregnation with mineral oxides:

  Doping with metals (e.g., Fe/Ca, Zn, Mg, Cu/Co oxides) via co-precipitation or sol-gel methods creates magnetic or catalytic sites [153,154]. Recent studies report that Fe-modified biochars increased adsorption capabilities (up to 891 mg/g) for contaminant degradation (tetracycline) [155].

2.4.3 Cold plasma modification

In addition to physical and chemical treatments, plasma-based methods have emerged as an alternative for modifying carbon materials [156]. Cold plasma, also referred to as non-thermal plasma, is a partially ionized gas in which energetic electrons coexist with ions, radicals, and neutral species while the bulk gas remains near ambient temperature [157]. Unlike thermal plasmas, where all species are in thermal equilibrium, cold plasma is characterized by electron temperatures on the order of several electron volts (equivalent to approximately 10^4 K), while the gas and solid surfaces remain only slightly heated. These energetic electrons drive ionization, excitation, and dissociation of the working gas, producing a diverse mixture of reactive species such as radicals, metastables, and ions that interact with material surfaces. As a result, cold plasma enables highly energetic chemical and physical processes to occur without exposing the treated material to high bulk temperatures [158].

This nonequilibrium nature makes cold plasma an environmentally attractive and versatile surface modification method. Plasma treatments can alter surface chemistry, remove contaminants, and restructure pore networks without the use of solvents, acids, or other hazardous reagents, and without generating liquid waste streams [159]. Because reactions are confined to the surface and driven by short lived reactive species, treatment times are short and material loss is minimal. Cold plasma has therefore been widely applied to polymers, carbons, catalysts, membranes, and biomedical substrates to tailor wettability, adhesion, reactivity and porosity [160]. In porous carbons, cold plasma provides an effective route for modifying surface accessibility and functionality while preserving the bulk structure, offering a low energy and field alternative to conventional thermal or chemical activation methods [159].

Plasma performance is governed by several control variables including gas composition (e.g., Ar, N_2, CO_2, O_2, air), electrical power, and exposure time, and gas-solid contacting mode (fixed bed or moving bed). To date, plasma-modified biochars have been most extensively studied for gas-phase mercury capture [161,162], aqueous-phase adsorption of metals and dyes [163–165], and CO_2 capture [166].

Cold plasma is typically implemented through specific plasma reactor configurations, including:

- Dielectric barrier discharge (DBD) plasma:

  Operates at atmospheric pressure using high voltage AC excitation across a dielectric barrier, producing spatially uniform discharge suitable for treating powders in fixed beds or moving beds [167]. DBD can increase metal-adsorption rate and a 40% higher maximum adsorption capacity of heavy metal ion Pb2+ [168].
- Radio frequency (RF) plasma:

  Typically operated at reduced pressure with RF excitation, enabling more stable plasmas and finer control of ion energy and treatment intensity [169]. RF plasma is well suited for reproducible surface etching and mild functionalization with lower thermal load [170]. By optimizing discharge parameters such as power and pressure, allows precise introduction of functional groups onto carbon nanotubes while maintaining structural integrity by avoiding excessive chemical etching [171].
- Microwave plasma:

  Uses microwave excitation to generate high density plasmas with strong radical production. Microwave plasmas can provide rapid treatment and high throughput when designed with effective gas solid contacting [172]. Depending on the gas chemistry, microwave plasmas can emphasize pore carving, surface cleaning, or heteroatom

incorporation, but reactor design is more complex than DBD due to field distribution and coupling constraints [173].

- Glow discharge and corona plasma:

  Glow discharge is used to improve polymer adhesivity [174] and to decompose N_2O [175].

  Corona discharge is efficient in decomposition of CO_2 and formation of CO [176].

Across these reactor types, reported outcomes vary with discharge characteristics and operating conditions.

To narrow the focus to biochar modification relevant to adsorption applications, Table 2.6 summarizes representative cold-plasma treatments and their reported effects on surface properties and adsorption performance.

Table 2.6 Cold plasma modification on biochar surface properties and adsorption performance

Plasma Gas	Treatment Conditions	Improvement	Key Changes	Ref.
CH_4, CO_2, H_2, Ar	13.56 MHz and 90 W; ~2 Torr; treatment time 10 min, reaching 200 °C (RF plasma), biochar synthesized from coconut initially activated by steam	SSA increase (Ar: 5.2%, H_2: 2.6%, CO_2: 5.5%, CH_4: 8.9%), micropore volume increase (Ar: 8.7%, H_2: 6.5%, CO_2: 10.9%, CH_4: 13.0%)	Increase in micropore volume, SSA and specific capacitance	[177]
O_2/He	O_2/He DBD plasma modification of sawdust biochar	+23.5% aniline adsorption capacity	Surface etching/pits; increased oxygen content and oxygenated functional groups	[178]
Cl_2	DBD in Cl_2 gas on straw-derived biochar	Hg^0 removal efficiency 8% → 80% and 36× higher Hg^0 adsorption capacity	Increased C-Cl active sites; surface functional group changes	[179]
Air/He	60-Hz 6.50-kV; corona discharge. Wood chips	pH decreases from 5.79 to 4.79	pH and FTIR confirm introduction of O_2/N_2 functional groups	[180]
O_2	RF-DBD, <150 °C, yellow pine biochar	Capacitance: 60.4 →171.4 F/g (+184%)	Broad pore size distribution; larger SSA	[181]
H_2O vapor	60 kV, 1% H_2O; corn straw biochar	Pb^{2+} removal 90.94% with adsorption capacity 87.2 mg/g	C-OH groups increase; ZnO active sites; $Pb(OH)_2$ and $PbCO_3$ formation	[182]

As summarized in Table 2.6, cold plasma treatment has been applied to biochar using a range of plasma gases and reactor configurations, generally resulting in increased surface area, enhanced pore development, and greater functional group density, which translate to improved adsorption performance for a variety of target compounds. However, none of the reported studies have examined CH_4 adsorption, indicating that plasma-modified biochar has not yet been evaluated for methane storage applications.

To address this gap, the present study investigates cold plasma treatment as a surface modification strategy for biochar adsorbents used in CH_4 storage applications. Three plasma reactor

configurations, i.e., DBD, fluidized bed coupled DBD (FB-DBD), and RF systems, were evaluated for biochar surface modification. Among these approaches, FB-DBD-driven cold plasma treatment of biochar was explored as a novel modification strategy. Preliminary results indicated promising surface modification effects, and the approach was considered for potential intellectual property protection, although the process was not pursued further due to administrative constraints.

The reactor selection process and the resulting surface modification outcomes were presented at the CanCH_4 Symposium (Ottawa, 2025); supporting material is provided in *Appendix C.*

2.4.4 Activation methods overview

Table 2.7 summarizes representative surface modification and activation techniques reported in the literature, highlighting their typical effects on specific surface area, CH_4 adsorption capacity, and practical advantages and limitations.

Table 2.7 Activation methods for CH_4 adsorption enhancement

Method category	Technique example	SSA (m^2/g)	Adsorption capacity (mmol/g)	Pros	Cons	Refs
Physical	Steam Activation	1,583	0.1-0.5 (25 °C, 1 bar)	Strong micropore development; scalable	High temperature; yield loss	[183,184]
Chemical	H_3PO_4 wet Pyrolysis	520-1,441	3-6 (25 °C, 35-70 bar)	High SSA; tunable micro/mesoporosity	Acid handling and washing requirements	[185]
	KOH Activation	2,372	5-12 (25 °C, 35 bar)	Very high SSA; strong microporosity	Corrosive reagents	[186]
		995-2,609	0.6-3.4 (0 °C, 1 bar)			[187]
		1,000	6.2-6.4 (25 °C, 65 bar)			[188]
	NaOH Activation	3,290	22.5 (20 °C, 35 bar)	High SSA	Corrosive reagents	[189]
Cold plasma	No CH_4 adsorption enhancement studies identified (ANG-relevant pressures).					

As shown in Table 2.7, reported CH_4 adsorption enhancement studies predominantly focus on high-temperature or chemically intensive treatments. While these approaches can substantially increase surface area and adsorption capacity, they impose high energy demands, corrosive reagents, and complex post-treatment steps, which are poorly aligned with decentralized oil field ANG deployment.

To the author's knowledge, no peer-reviewed studies have reported enhancement of CH_4 adsorption using cold plasma modification, despite plasma treatments being explored for applications such as contaminant removal and CO_2 capture. This gap motivates the present study. While surface modification governs initial CH_4 storage performance, long-term ANG deployment depends on adsorbent durability under repeated cycling and practical end-of-life pathways. These

considerations motivate the following section, which examines how spent biochar adsorbents can be repurposed as value-added products within a closed-loop carbon management strategy.

2.5 Multicycle operations and end-of-life adsorbent as value-added products

2.5.1 Multicycle adsorption–desorption tests and empirical degradation analysis

During ANG operation, CH_4 is repeatedly adsorbed for storage and subsequently desorbed for on-site power or heat generation. Complete recovery of the initial adsorption capacity after each cycle is not expected, as a fraction of CH_4 remains confined within ultramicropores or becomes weakly trapped at partially blocked adsorption sites. As cycling proceeds, this residual CH_4 progressively reduces the number of available adsorption sites, leading to gradual performance degradation rather than abrupt structural failure.

To evaluate the practical durability of biochar adsorbents under ANG-relevant conditions, multicycle CH_4 adsorption-desorption tests were performed using pressure swing adsorption (PSA) between 0 and 75 bar at 298 K. These experiments were designed to represent field-relevant ANG operation and to provide a basis for estimating sorbent longevity, replacement frequency, and end-of-life utilization.

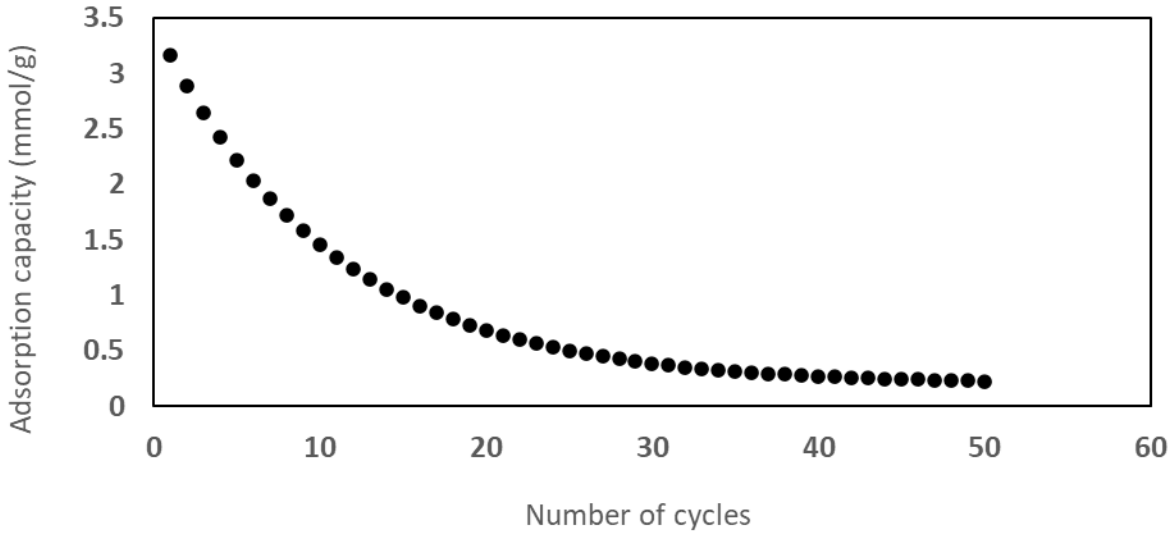

Fig. 2.2 Representative decline in adsorption capacity over number of cycles [190]

Fig. 2.2 illustrates a representative degradation trend for biochar adsorption capacity as a function of cycle number. Adsorbent activity, A_N is defined as the ratio of the adsorption capacity at cycle N to the initial adsorption capacity. To describe the observed degradation trend, an empirical decay relation reported in previous studies was used to fit the experimental data:

$$A_N = A_{N-1} - k(A_{N-1} - A_r) \qquad [190] \quad (2.7)$$

where k is a degradation constant reflecting the rate of capacity loss per cycle, and A_r is a residual activity representing the asymptotic lower bound of adsorption capacity that does not diminish further with continued cycling. Once sufficient experimental cycling data are available, the parameters k and A_r can be fitted to enable quantitative lifetime prediction and inform ANG system design.

With increasing cycle number, the calorific value of biochar increases, indicating that residual CH_4 retained within the pore structure contributes to enhanced fuel value. At the same time, the exothermic onset temperature decreases slightly, consistent with confined CH_4 lowering the

ignition threshold without compromising thermal stability. These trends confirm that spent biochar adsorbents remain suitable for secondary energy recovery after ANG service. Detailed multicycle data analysis and empirical curve fitting describing the evolution of adsorption capacity with cycle number are presented in Chapter 6.

2.5.2 Methanotrophic soil amendment and CH_4 mitigation

Based on the broader soil science literature, spent biochar holds potential as a soil amendment; this pathway is proposed here as a future valorization route rather than an experimentally validated outcome of this work.

After extended service in ANG applications, biochar adsorbents gradually accumulate residual CH_4 within ultramicropores as a result of incomplete desorption. Once adsorption capacity declines below an economic threshold for further gas storage, the material can be considered end-of-life from an ANG perspective. Unlike conventional engineered adsorbents, however, spent biochar retains substantial secondary value and can be repurposed rather than discarded.

When applied as a soil amendment, trace CH_4 retained in spent biochar does not pose an environmental hazard. Weakly physisorbed CH_4 is rapidly released under ambient soil conditions and can be oxidized by methanotrophic microorganisms [191]. Numerous soil studies report that biochar amendments enhance CH_4 oxidation and reduce net CH_4 emissions by improving soil aeration [192], providing microbial habitats [193], and adsorbing compounds that inhibit methanotrophy [194]. As a result, biochar-amended soils often exhibit reduced net CH_4 emissions rather than increased release, even when biochar contains sorbed gases [195].

Biochar incorporated into soils improves water retention, nutrient holding capacity, and microbial activity while sequestering carbon over long time scales. Importantly, the carbon matrix of biochar is highly recalcitrant, with mean residence times ranging from decades to centuries, depending on feedstock and pyrolysis conditions. This stability ensures that repurposing spent biochar for land application contributes to long-term carbon storage rather than rapid mineralization.

The presence of residual hydrocarbons can further enhance the agronomic and environmental value of spent biochar [196]. Low levels of adsorbed CH_4 and heavier hydrocarbons marginally increase the energy content of the material and may stimulate specific microbial communities upon soil incorporation [197]. Experimental studies on hydrocarbon-impacted biochars indicate that such materials do not inhibit plant growth when applied at agronomically relevant rates and, in some cases, improve soil microbial diversity and activity by serving as a slow-release carbon source [198].

From a life-cycle perspective, diverting spent biochar from disposal to soil application strengthens the circularity of the ANG system. Biomass-derived carbon is first used to capture and store CH_4, mitigating flaring and enabling energy recovery. After its service life, the same material is returned to the land, where it continues to deliver environmental benefits through carbon sequestration, soil improvement, and indirect CH_4 mitigation. This dual use contrasts sharply with conventional adsorbents such as activated carbon or MOFs, which typically require energy-intensive regeneration or disposal as industrial waste. Comprehensive experimental results and quantitative analysis of adsorbent aging and end-of-life utilization are provided in Chapter 6.

2.5.3 Biofuels of enhanced heat content

Once adsorption performance falls below an economic threshold, continued use of the material for ANG storage becomes impractical. At this point, spent biochar adsorbents retain an additional utilization pathway as solid biofuels. When residual CH_4 content exceeds thresholds suitable for soil amendment [199], thermal utilization through combustion or co-firing becomes the preferred route, enabling recovery of the remaining chemical energy rather than treating the adsorbent as waste.

Residual CH_4 retained within the pore structure after depressurization contributes directly to the higher heating value (HHV) of the spent biochar. Experimental results in this study show that this retained CH_4 increases calorific value by approximately 5-15%, effectively upgrading the material into a heating-value-enhanced biofuel [200].

This dual end-of-life flexibility is a key advantage of biochar over alternative ANG adsorbents. In contrast to many engineered materials, such as chemically impregnated activated carbons or metal organic frameworks, that face challenges related to toxicity, thermal stability, or disposal, plasma treated biochar can be safely combusted, co-fired, or gasified using existing infrastructure. Accordingly, biochar provides two viable end-of-life pathways: soil amendment supporting methanotrophic CH_4 mitigation, or conversion to a value-added solid fuel when residual CH_4 content is higher.

2.6 Closing the carbon loop: CO_2 exhaust for EOR and sequestration

While biochar-based ANG storage enables capture and utilization of CH_4-dominant APG that would otherwise be flared, on-site combustion of the recovered CH_4 inevitably generates CO_2

[201]. Therefore, an APG utilization strategy that only converts CH_4 to CO_2 remains incomplete from a life-cycle perspective. A more integrated pathway is to treat engine exhaust CO_2 as a secondary recoverable carbon stream and evaluate whether it can be captured and reinjected for subsurface storage, with EOR as a potential co-benefit.

Following the integrated configuration introduced in Fig. 1.1 (Chapter 1), the engine exhaust can be routed to a post-combustion separation unit. Among post-combustion CO_2 capture technologies [202], adsorption-based capture may be considered due to its conceptual compatibility with ANG and its modular deployment potential.

Once separated, the captured CO_2 stream can be directed to EOR with concurrent storage or geological sequestration [203], depending on reservoir suitability and injection infrastructure availability [204]. CO_2 quality requirements depend on the target application: miscible CO_2-EOR commonly requires approximately 90-98% CO_2, foam-injection studies frequently employ 70% or more CO_2 streams to ensure surfactant stability and controllable foam quality [205]. Foam-assisted EOR is a site-dependent integration option for single remote pads, as CO_2 supply is typically limited and uptime can be constrained by downtime and logistics.

Overall, incorporating CO_2 capture and reinjection into an APG utilization framework extends CH_4 mitigation by coupling flare avoidance with subsurface CO_2 handling. This closed-loop framing is used in this thesis to motivate why a field-deployable ANG approach can be more than a storage technology, and it can serve as an enabling platform for broader carbon management, while detailed capture energy penalties, compression requirements, and corrosion/water-management design are outside the scope of the present work.

References

[1] G. Szarek, N. Sharma, P. Gargett, The true cost of methane abatement | McKinsey, (2024). https://www.mckinsey.com/industries/oil-and-gas/our-insights/the-true-cost-of-methane-abatement-a-crucial-step-in-oil-and-gas-decarbonization.

[2] A. Dewar, B. Sudmeijer, G. Moss, Toward Near-Zero Methane Emissions in Oil and Gas, BCG Glob. (2024). https://www.bcg.com/publications/2024/toward-near-zero-methane-emissions.

[3] C. Beck, S. Rashidbeigi, O. Roelofsen, E. Speelman, The future of oil and gas is now: How companies can decarbonize | McKinsey, (n.d.). https://www.mckinsey.com/industries/oil-and-gas/our-insights/the-future-is-now-how-oil-and-gas-companies-can-decarbonize.

[4] J.E. Aldy, F. Reinhardt, R.N. Stavins, Methane Abatement Costs in the Oil and Gas Industry: Survey and Synthesis | The Belfer Center for Science and International Affairs, (2025). https://www.belfercenter.org/research-analysis/methane-abatement-costs-oil-and-gas-industry-survey-and-synthesis.

[5] A. Vorobev, E. Shchesnyak, Associated Petroleum Gas Flaring: The Problem and Possible Solution, in: S. Glagolev (Ed.), 14th Int. Congr. Appl. Mineral. ICAM2019, Springer International Publishing, Cham, 2019: pp. 227–230. https://doi.org/10.1007/978-3-030-22974-0_55.

[6] W. Wakil, Minimize Flaring in Oil and Gas Facilities, (2022). https://www.aiche.org/resources/publications/cep/2023/january/minimize-flaring-oil-and-gas-facilities.

[7] IEA, Key findings – Global Methane Tracker 2025 – Analysis, IEA (n.d.). https://www.iea.org/reports/global-methane-tracker-2025/key-findings.

[8] Y. Chen, S. Dong, S. Qian, K. Chung, Impact of oil price volatility and economic policy uncertainty on business investment - Insights from the energy sector, Heliyon 10 (2024) e26533. https://doi.org/10.1016/j.heliyon.2024.e26533.

[9] IEA, Understanding methane emissions – Global Methane Tracker 2025 – Analysis, IEA (n.d.). https://www.iea.org/reports/global-methane-tracker-2025/understanding-methane-emissions).

[10] C.D. Elvidge, M.D. Bazilian, M. Zhizhin, T. Ghosh, K. Baugh, F.-C. Hsu, The potential role of natural gas flaring in meeting greenhouse gas mitigation targets, Energy Strategy Rev. 20 (2018) 156–162. https://doi.org/10.1016/j.esr.2017.12.012.

[11] J. Motte, R.A.F. Alvarenga, J.W. Thybaut, J. Dewulf, Quantification of the global and regional impacts of gas flaring on human health via spatial differentiation, Environ. Pollut. 291 (2021) 118213. https://doi.org/10.1016/j.envpol.2021.118213.

[12] E. Ibrahim Mustafa, H. Hassan, Utilizing associated gas to generate electrical power to replace the traditional crude/diesel fuel as a source of energy for oil and gas fields, Int. J. Eng. Appl. Sci. Technol. 5 (2021). https://doi.org/10.33564/IJEAST.2021.v05i09.015.

[13] Trent Jacobs, Displacing Diesel: The Rising Use of Natural Gas by Onshore Operators, J. Pet. Technol. (2013). https://jpt.spe.org/displacing-diesel-rising-use-natural-gas-onshore-operators.

[14] R.D. Trevizan, A.J. Headley, R. Geer, S. Atcitty, I. Gyuk, Integration of energy storage with diesel generation in remote communities, MRS Energy Sustain. 8 (2021) 57–74. https://doi.org/10.1557/s43581-021-00013-9.

[15] IPIECA, Global Flaring and Methane Reduction Partnership (GFMR)Homepage, World Bank (n.d.). https://www.worldbank.org/en/programs/gasflaringreduction.

[16] World Bank, 2025 Global Gas Flaring Tracker Report, World Bank (n.d.). https://www.worldbank.org/en/programs/gasflaringreduction/publication/2025-global-gas-flaring-tracker-report.

[17] WorldBank, International Development, Poverty and Sustainability, (n.d.). https://www.worldbank.org/ext/en/home.

[18] Carbon Limits AS, Improving Utilization of Associated Gas in US Tight Oil Fields, (n.d.). https://www.carbonlimits.no/projects/improving-utilization-of-associated-gas-in-us-tight-oil-fields-kshpa.

[19] E.A. Emam, Gas Flaring in Industry: An Overview, Pet. Coal ISSN 1337-7027 (2015) 24.

[20] A. Khalili-Garakani, M. Nezhadfard, M. Iravaninia, Enviro-economic investigation of various flare gas recovery and utilization technologies in upstream and downstream of oil and gas industries, J. Clean. Prod. 346 (2022) 131218. https://doi.org/10.1016/j.jclepro.2022.131218.

[21] C.M. Reddy, J.S. Arey, J.S. Seewald, S.P. Sylva, K.L. Lemkau, R.K. Nelson, C.A. Carmichael, C.P. McIntyre, J. Fenwick, G.T. Ventura, B.A.S. Van Mooy, R. Camilli, Composition and fate of gas and oil released to the water column during the Deepwater Horizon oil spill, Proc. Natl. Acad. Sci. 109 (2012) 20229–20234. https://doi.org/10.1073/pnas.1101242108.

[22] M.R. Johnson, A.R. Coderre, Compositions and greenhouse gas emission factors of flared and vented gas in the Western Canadian Sedimentary Basin, J. Air Waste Manag. Assoc. 62 (2012) 992–1002. https://doi.org/10.1080/10962247.2012.676954.

[23] M.M. Zyryanova, P.V. Snytnikov, Yu.I. Amosov, V.D. Belyaev, V.V. Kireenkov, N.A. Kuzin, M.V. Vernikovskaya, V.A. Kirillov, V.A. Sobyanin, Upgrading of associated petroleum gas into methane-rich gas for power plant feeding applications. Technological and economic benefits, Fuel 108 (2013) 282–291. https://doi.org/10.1016/j.fuel.2013.02.047.

[24] M. Deymi-Dashtebayaz, M. Farzaneh-Gord, H. Reza Rahbari, Simultaneous thermodynamic simulation of CNG filling process, Green Sci. 16 (2014) 7–14. https://doi.org/10.2478/pjct-2014-0002.

[25] I. Cetiner, A. Coskun, Cost based optimization of industrial bulk CNG filling facility operations, Therm. Sci. 25 (2020) 206–206. https://doi.org/10.2298/TSCI200430206C.

[26] A. Chaudhary, S. Sahoo, Performance enhancement of an adsorbed natural gas storage system using various nanofluids: A heat and mass transfer approach, AIP Conf. Proc. 2960 (2024) 040001. https://doi.org/10.1063/5.0185360.

[27] E.M. Strizhenov, S.S. Chugaev, I.D. Shelyakin, A.V. Shkolin, I.E. Men'shchikov, A.A. Zherdev, Numerical modeling of heat and mass transfer in an adsorbed natural gas storage tank with monolithic active carbon during charging and discharging processes, Heat Mass Transf. 60 (2024) 1931–1944. https://doi.org/10.1007/s00231-022-03272-5.

[28] M. Sabat, H. Hassan, R. Roukos, S.A. Dargham, J. Romanos, Long-term degradation of adsorbed natural gas storage in the MOF Basolite C300 due to Cn≥2 alkanes accumulation, Sci. Rep. 15 (2025) 33054. https://doi.org/10.1038/s41598-025-10131-w.

[29] H. Devold, Oil and gas production handbook, ABB Libr. https://doi.org/ISBN%2520978-82-997886-0-1.

[30] US Department of Energy, Methane Opportunities for Vehicular Energy, (2012). https://arpa-e.energy.gov/?q=arpa-e-programs/move.

[31] MOVE | ARPA-E, (n.d.). https://arpa-e.energy.gov/programs-and-initiatives/view-all-programs/move.

[32] Z. Nie, Y. Lin, X. Jin, Research on the theory and application of adsorbed natural gas used in new energy vehicles: A review, Front. Mech. Eng. 11 (2016) 258–274. https://doi.org/10.1007/s11465-016-0381-2.

[33] E. Mahmoud, Evolution of the Design of CH_4 Adsorbents, Surfaces 3 (2020) 433–466. https://doi.org/10.3390/surfaces3030032.

[34] M. Hainzl, Commercialization of Adsorbed Natural Gas Storage Technology for Use in Stationary Emergency Power Systems, (2017). https://doi.org/10.13140/RG.2.2.11235.96801.

[35] P. Bénard, R. Chahine, 10 - Carbon nanostructures for hydrogen storage, in: G. Walker (Ed.), Solid-State Hydrog. Storage, Woodhead Publishing, 2008: pp. 261–287. https://doi.org/10.1533/9781845694944.3.261.

[36] M.J. Prosniewski, T.A. Rash, E.W. Knight, A.K. Gillespie, D. Stalla, C.J. Schulz, P. Pfeifer, Controlled charge and discharge of a 40-L monolithic adsorbed natural gas tank, Adsorption 24 (2018) 541–550. https://doi.org/10.1007/s10450-018-9961-2.

[37] A.Yu. Tsivadze, O.E. Aksyutin, A.G. Ishkov, I.E. Men'shchikov, A.A. Fomkin, A.V. Shkolin, E.V. Khozina, V.A. Grachev, Porous carbon-based adsorption systems for natural gas (methane) storage, Russ. Chem. Rev. 87 (2018) 950–983. https://doi.org/10.1070/RCR4807.

[38] I. Driscoll, R. Facey, K.J. Kowalishen, B. Moore, Codes and Standards for Renewable Gas Pathways, CSA Group (2022).

[39] Ingevity Corporation - Adsorbed Natural Gas for Flare Gas Recovery and Utilization, (n.d.). https://www.globalmethane.org/challenge/ingevity.html.

[40] World Bank Document, (n.d.). https://documents1.worldbank.org/curated/en/305891644478108245/pdf/Report-on-Small-scale-Technologies-for-Utilization-of-Associated-Gas.pdf.

[41] T.A. Makal, J.-R. Li, W. Lu, H.-C. Zhou, Methane storage in advanced porous materials, Chem. Soc. Rev. 41 (2012) 7761–7779. https://doi.org/10.1039/C2CS35251F.

[42] J.L. Mendoza-Cortes, T.A. Pascal, W.A.I. Goddard, Design of Covalent Organic Frameworks for Methane Storage, J. Phys. Chem. A 115 (2011) 13852–13857. https://doi.org/10.1021/jp209541e.

[43] S. Ge, K. Wei, W. Peng, R. Huang, E. Akinlabi, H. Xia, M. Wakil Shahzad, X. Zhang, B. Bin Xu, J. Jiang, A comprehensive review of covalent organic frameworks (COFs) and their derivatives in environmental pollution control, Chem. Soc. Rev. 53 (2024) 11259–11302. https://doi.org/10.1039/D4CS00521J.

[44] A.M. Metawea, G. Walker, Continuous manufacturing and scale up of metal organic materials (MOM): Current situation, challenges and future direction, J. Ind. Eng. Chem. 148 (2025) 150–173. https://doi.org/10.1016/j.jiec.2025.01.020.

[45] W.L. Teo, W. Zhou, C. Qian, Y. Zhao, Industrializing metal–organic frameworks: Scalable synthetic means and their transformation into functional materials, Mater. Today 47 (2021) 170–186. https://doi.org/10.1016/j.mattod.2021.01.010.

[46] A.S. Mestre, C. Freire, J. Pires, A.P. Carvalho, M.L. Pinto, High performance microspherical activated carbons for methane storage and landfill gas or biogas upgrade, J Mater Chem A 2 (2014) 15337–15344. https://doi.org/10.1039/C4TA03242J.

[47] Gautam, S. Sahoo, Experimental investigation on different activated carbons as adsorbents for CO_2 capture, Therm. Sci. Eng. Prog. 33 (2022) 101339. https://doi.org/10.1016/j.tsep.2022.101339.

[48] M.A. Nazem, M.H. Zare, S. Shirazian, Preparation and optimization of activated nano-carbon production using physical activation by water steam from agricultural wastes, RSC Adv. 10 (2020) 1463–1475. https://doi.org/10.1039/C9RA07409K.

[49] S. Kundu, T. Khandaker, M.A.-A.M. Anik, M.K. Hasan, P.K. Dhar, S.K. Dutta, M.A. Latif, M.S. Hossain, A comprehensive review of enhanced CO_2 capture using activated carbon derived from biomass feedstock, RSC Adv. 14 (2024) 29693–29736. https://doi.org/10.1039/D4RA04537H.

[50] J. Alcañiz-Monge, D. Lozano-Castelló, D. Cazorla-Amorós, A. Linares-Solano, Fundamentals of methane adsorption in microporous carbons, Microporous Mesoporous Mater. 124 (2009) 110–116. https://doi.org/10.1016/j.micromeso.2009.04.041.

[51] J. Saleem, Z.K.B. Moghal, F. Tahir, T. Al-Ansari, A.I. Osman, G. McKay, Life cycle assessment of high value activated carbon production based on mass and functional performance metrics, Sci. Rep. 15 (2025) 1–15. https://doi.org/10.1038/s41598-025-16300-1.

[52] H.A. Alhashimi, C.B. Aktas, Life cycle environmental and economic performance of biochar compared with activated carbon: A meta-analysis, Resour. Conserv. Recycl. 118 (2017) 13–26. https://doi.org/10.1016/j.resconrec.2016.11.016.

[53] A. Vilén, P. Laurell, R. Vahala, Comparative life cycle assessment of activated carbon production from various raw materials, J. Environ. Manage. 324 (2022) 116356. https://doi.org/10.1016/j.jenvman.2022.116356.

[54] M. Nematian, C. Keske, J.N. Ng'ombe, A techno-economic analysis of biochar production and the bioeconomy for orchard biomass, Waste Manag. 135 (2021) 467–477. https://doi.org/10.1016/j.wasman.2021.09.014.

[55] J.O. Ighalo, F.O. Omoarukhe, V.E. Ojukwu, K.O. Iwuozor, C.A. Igwegbe, Cost of adsorbent preparation and usage in wastewater treatment: A review, Clean. Chem. Eng. 3 (2022) 100042. https://doi.org/10.1016/j.clce.2022.100042.

[56] D. Zilberman, D. Laird, C. Rainey, J. Song, G. Kahn, Biochar supply-chain and challenges to commercialization, GCB Bioenergy 15 (2023) 7–23. https://doi.org/10.1111/gcbb.12952.

[57] T. Banerjee, J. Bravo, C.E. Romero, T. Lowe, G. Driscoll, B. Kreglow, H. Schobert, Z. Yao, Process design and techno-economic analysis of activated carbon derived from anthracite coal, J. Environ. Manage. 355 (2024) 120525. https://doi.org/10.1016/j.jenvman.2024.120525.

[58] Science Advisor, The 2025 Nobel Prize in Chemistry: Metal-Organic Frameworks | Science | AAAS, (n.d.). https://doi.org/10.1126/science.

[59] D. Ursueguía, E. Díaz, S. Ordóñez, Metal-Organic Frameworks (MOFs) as methane adsorbents: From storage to diluted coal mining streams concentration, Sci. Total Environ. 790 (2021) 148211. https://doi.org/10.1016/j.scitotenv.2021.148211.

[60] Y. Peng, V. Krungleviciute, I. Eryazici, J.T. Hupp, O.K. Farha, T. Yildirim, Methane Storage in Metal–Organic Frameworks: Current Records, Surprise Findings, and

Challenges, J. Am. Chem. Soc. 135 (2013) 11887–11894. https://doi.org/10.1021/ja4045289.

[61] S. Ghaedi, H. Rajabi, M. Hadi Mosleh, M. Sedighi, MOF biochar composites for environmental protection and pollution control, Bioresour. Technol. 418 (2025) 131982. https://doi.org/10.1016/j.biortech.2024.131982.

[62] O.K. Farha, I. Eryazici, N.C. Jeong, B.G. Hauser, C.E. Wilmer, A.A. Sarjeant, R.Q. Snurr, S.T. Nguyen, A.Ö. Yazaydın, J.T. Hupp, Metal–Organic Framework Materials with Ultrahigh Surface Areas: Is the Sky the Limit?, J. Am. Chem. Soc. 134 (2012) 15016–15021. https://doi.org/10.1021/ja3055639.

[63] A. Tomczyk, Z. Sokołowska, P. Boguta, Biochar physicochemical properties: pyrolysis temperature and feedstock kind effects, Rev. Environ. Sci. Biotechnol. 19 (2020) 191–215. https://doi.org/10.1007/s11157-020-09523-3.

[64] T.J. Azbell, T.A. Pitt, R.T. Jerozal, R.M. Mandel, P.J. Milner, Simplifying the Synthesis of Metal-Organic Frameworks, Acc. Mater. Res. 4 (2023) 867–878. https://doi.org/10.1021/accountsmr.3c00121.

[65] V.F. Yusuf, N.I. Malek, S.K. Kailasa, Review on Metal–Organic Framework Classification, Synthetic Approaches, and Influencing Factors: Applications in Energy, Drug Delivery, and Wastewater Treatment, ACS Omega 7 (2022) 44507–44531. https://doi.org/10.1021/acsomega.2c05310.

[66] H. Rastin, D. Dell'Angelo, A. Sayede, M. Badawi, S. Habibzadeh, Green and sustainable metal-organic frameworks (MOFs) in wastewater treatment: A review, Environ. Res. 282 (2025) 122087. https://doi.org/10.1016/j.envres.2025.122087.

[67] D. DeSantis, J.A. Mason, B.D. James, C. Houchins, J.R. Long, M. Veenstra, Techno-economic Analysis of Metal–Organic Frameworks for Hydrogen and Natural Gas Storage, Energy Fuels 31 (2017) 2024–2032. https://doi.org/10.1021/acs.energyfuels.6b02510.

[68] M.I. Severino, E. Gkaniatsou, F. Nouar, M.L. Pinto, C. Serre, MOFs industrialization: a complete assessment of production costs, Faraday Discuss. 231 (2021) 326–341. https://doi.org/10.1039/D1FD00018G.

[69] D. Chakraborty, A. Yurdusen, G. Mouchaham, F. Nouar, C. Serre, Large-Scale Production of Metal–Organic Frameworks, Adv. Funct. Mater. 34 (2024) 2309089. https://doi.org/10.1002/adfm.202309089.

[70] B. Yeskendir, J.-P. Dacquin, Y. Lorgouilloux, C. Courtois, S. Royer, J. Dhainaut, From metal–organic framework powders to shaped solids: recent developments and challenges, Mater. Adv. 2 (2021) 7139–7186. https://doi.org/10.1039/D1MA00630D.

[71] B.M. Connolly, M. Aragones-Anglada, J. Gandara-Loe, N.A. Danaf, D.C. Lamb, J.P. Mehta, D. Vulpe, S. Wuttke, J. Silvestre-Albero, P.Z. Moghadam, A.E.H. Wheatley, D. Fairen-Jimenez, Tuning porosity in macroscopic monolithic metal-organic frameworks for

exceptional natural gas storage, Nat. Commun. 10 (2019). https://doi.org/10.1038/s41467-019-10185-1.

[72] M. Nazari, F. Zadehahmadi, M.M. Sadiq, A.L. Sutton, H. Mahdavi, M.R. Hill, Challenges and solutions to the scale-up of porous materials, Commun. Mater. 5 (2024) 1–9. https://doi.org/10.1038/s43246-024-00608-y.

[73] H. Li, K. Wang, Y. Sun, C.T. Lollar, J. Li, H.-C. Zhou, Recent advances in gas storage and separation using metal–organic frameworks, Mater. Today 21 (2018) 108–121. https://doi.org/10.1016/j.mattod.2017.07.006.

[74] K. Tan, N. Nijem, P. Canepa, Q. Gong, J. Li, T. Thonhauser, Y.J. Chabal, Stability and Hydrolyzation of Metal Organic Frameworks with Paddle-Wheel SBUs upon Hydration, Chem. Mater. 24 (2012) 3153–3167. https://doi.org/10.1021/cm301427w.

[75] P. Lyu, G. Maurin, H_2S Stability of Metal–Organic Frameworks: A Computational Assessment, ACS Appl. Mater. Interfaces 13 (2021) 4813–4822. https://doi.org/10.1021/acsami.0c21285.

[76] J.N. Joshi, G. Zhu, J.J. Lee, E.A. Carter, C.W. Jones, R.P. Lively, K.S. Walton, Probing Metal–Organic Framework Design for Adsorptive Natural Gas Purification, Langmuir 34 (2018) 8443–8450. https://doi.org/10.1021/acs.langmuir.8b00889.

[77] N.C. Burtch, H. Jasuja, K.S. Walton, Water Stability and Adsorption in Metal–Organic Frameworks, Chem. Rev. 114 (2014) 10575–10612. https://doi.org/10.1021/cr5002589.

[78] X. Hong, Y. Fang, D. Chao, A metal–free porous organic polymer with high CO_2 adsorption for robust aqueous CO_2 photoreduction via molecular regulation, Mol. Catal. 549 (2023) 113476. https://doi.org/10.1016/j.mcat.2023.113476.

[79] M. Debruyne, N. Raeymackers, H. Vrielinck, S. Radhakrishnan, E. Breynaert, M. Delaey, A. Laemont, K. Leus, J. Everaert, H. Rijckaert, D. Poelman, R. Morent, N. De Geyter, P. Van Der Voort, V. Van Speybroeck, C.V. Stevens, T.S.A. Heugebaert, Development of Porous Organic Polymers as Metal-Free Photocatalysts for the Aromatization of N-Heterocycles, ChemCatChem 16 (2024) e202301205. https://doi.org/10.1002/cctc.202301205.

[80] R. Liu, K.T. Tan, Y. Gong, Y. Chen, Z. Li, S. Xie, T. He, Z. Lu, H. Yang, D. Jiang, Covalent organic frameworks: an ideal platform for designing ordered materials and advanced applications, Chem. Soc. Rev. 50 (2021) 120–242. https://doi.org/10.1039/D0CS00620C.

[81] Y. Yin, Y. Zhang, X. Zhou, B. Gui, W. Wang, W. Jiang, Y.-B. Zhang, J. Sun, C. Wang, Ultrahigh–surface area covalent organic frameworks for methane adsorption, Science 386 (2024) 693–696. https://doi.org/10.1126/science.adr0936.

[82] B.-H. Han, Porous organic polymers, J. Polym. Sci. 62 (2024) 1491–1492. https://doi.org/10.1002/pol.20240193.

[83] W. Liu, Y. Yang, L. Guo, J. Di, C. Hon Lau, M.V. Bermeshev, L. Shao, Recent advances in porous organic polymers for sustainable gas separations, Chem. Eng. J. 498 (2024) 155569. https://doi.org/10.1016/j.cej.2024.155569.

[84] A. Shahbaz, K. Ahmad, K. Qureshi, H. Majeed, I. Arshad, T. Tabinda, T. Iftikhar, K. Khair, M. Ashfaq, H.U.R. Shah, M. Ahmad, S. Lee, Porous materials: Covalent Organic Frameworks (COFs) as game-changers in practical applications, a review, Rev. Inorg. Chem. 44 (2023). https://doi.org/10.1515/revic-2023-0018.

[85] D.W. Burke, Z. Jiang, A.G. Livingston, W.R. Dichtel, 2D Covalent Organic Framework Membranes for Liquid-Phase Molecular Separations: State of the Field, Common Pitfalls, and Future Opportunities, Adv. Mater. 36 (2024) 2300525. https://doi.org/10.1002/adma.202300525.

[86] S. Zhuang, Y. Liu, J. Wang, Covalent organic frameworks as efficient adsorbent for sulfamerazine removal from aqueous solution, J. Hazard. Mater. 383 (2020) 121126. https://doi.org/10.1016/j.jhazmat.2019.121126.

[87] S. Chakraborty, Y. Colón, R. Snurr, S. Nguyen, Hierarchically Porous Organic Polymers: Highly Enhanced Gas Uptake and Transport through Templated Synthesis, Chem Sci 6 (2014). https://doi.org/10.1039/C4SC02502D.

[88] D. Zhu, J.-J. Zhang, X. Wu, Q. Yan, F. Liu, Y. Zhu, X. Gao, M.M. Rahman, B.I. Yakobson, P.M. Ajayan, R. Verduzco, Understanding fragility and engineering activation stability in two-dimensional covalent organic frameworks, Chem. Sci. 13 (2022) 9655–9667. https://doi.org/10.1039/D2SC03489A.

[89] Y. Zhao, Emerging Applications of Metal–Organic Frameworks and Covalent Organic Frameworks, Chem. Mater. 28 (2016) 8079–8081. https://doi.org/10.1021/acs.chemmater.6b04677.

[90] L. Guo, Q.Y. Zhang, Z. Yu, R. Krishna, F. Luo, Minute and Large-Scale Synthesis of Covalent-Organic Frameworks in Water at Room Temperature by a Two-Step Dissolution–Precipitation Method, Chem. Mater. 35 (2023) 5648–5656. https://doi.org/10.1021/acs.chemmater.3c01220.

[91] D. Gamaralalage, S. Rodgers, A. Gill, W. Meredith, T. Bott, H. West, J. Alce, C. Snape, J. McKechnie, Biowaste to biochar: a techno-economic and life cycle assessment of biochar production from food-waste digestate and its agricultural field application, Biochar 7 (2025) 50. https://doi.org/10.1007/s42773-025-00456-0.

[92] J.A. Ippolito, L. Cui, C. Kammann, N. Wrage-Mönnig, J.M. Estavillo, T. Fuertes-Mendizabal, M.L. Cayuela, G. Sigua, J. Novak, K. Spokas, N. Borchard, Feedstock choice, pyrolysis temperature and type influence biochar characteristics: a comprehensive meta-data analysis review, Biochar 2 (2020) 421–438. https://doi.org/10.1007/s42773-020-00067-x.

[93] F. Amalina, A.S.A. Razak, S. Krishnan, H. Sulaiman, A.W. Zularisam, M. Nasrullah, Biochar production techniques utilizing biomass waste-derived materials and environmental applications – A review, J. Hazard. Mater. Adv. 7 (2022) 100134. https://doi.org/10.1016/j.hazadv.2022.100134.

[94] A.I. Osman, S. Fawzy, M. Farghali, M. El-Azazy, A.M. Elgarahy, R.A. Fahim, M.I.A.A. Maksoud, A.A. Ajlan, M. Yousry, Y. Saleem, D.W. Rooney, Biochar for agronomy, animal farming, anaerobic digestion, composting, water treatment, soil remediation, construction, energy storage, and carbon sequestration: a review, Environ. Chem. Lett. 20 (2022) 2385–2485. https://doi.org/10.1007/s10311-022-01424-x.

[95] Pheonix Research, Global Biochar Market Size and Share Analysis 2025-2033, Pheonix Res. (n.d.). https://www.pheonixresearch.com/press-release/global-biochar-market-2025-2033.

[96] S.J. Johannes Lehmann, Char and Carbon Materials Derived from Biomass, Elsevier, 2019. https://doi.org/10.1016/C2017-0-02406-0.

[97] G.F. Arfasa, Z.A. Tilahun, Life-Cycle impacts of biochar, MOFs, and biomass adsorbents: A meta-analysis for wastewater and carbon management, Environ. Chall. 21 (2025) 101331. https://doi.org/10.1016/j.envc.2025.101331.

[98] H.A. Alhashimi, C.B. Aktas, Life cycle environmental and economic performance of biochar compared with activated carbon: A meta-analysis, Resour. Conserv. Recycl. 118 (2017) 13–26. https://doi.org/10.1016/j.resconrec.2016.11.016.

[99] J. Shaheen, Y.H. Fseha, B. Sizirici, Performance, life cycle assessment, and economic comparison between date palm waste biochar and activated carbon derived from woody biomass, Heliyon 8 (2022) e12388. https://doi.org/10.1016/j.heliyon.2022.e12388.

[100] X. Deng, F. Teng, M. Chen, Z. Du, B. Wang, R. Li, P. Wang, Exploring negative emission potential of biochar to achieve carbon neutrality goal in China, Nat. Commun. 15 (2024) 1085. https://doi.org/10.1038/s41467-024-45314-y.

[101] R.C. Canatoy, S.J.C. Galgo, Greenhouse Gas Mitigation and Carbon Sequestration Potential of Biochar Derived from Plant and Animal Biomasses Under Submerged Soil Condition, Agric. Res. (2025). https://doi.org/10.1007/s40003-025-00860-9.

[102] L. Rodrigues, A. Budai, L. Elsgaard, B. Hardy, S.G. Keel, C. Mondini, C. Plaza, J. Leifeld, The importance of biochar quality and pyrolysis yield for soil carbon sequestration in practice, Eur. J. Soil Sci. 74 (2023) e13396. https://doi.org/10.1111/ejss.13396.

[103] S.K. Karan, D. Woolf, E.S. Azzi, C. Sundberg, S.A. Wood, Potential for biochar carbon sequestration from crop residues: A global spatially explicit assessment, GCB Bioenergy 15 (2023) 1424–1436. https://doi.org/10.1111/gcbb.13102.

[104] J. Lehmann, J. Gaunt, M. Rondon, Bio-char Sequestration in Terrestrial Ecosystems – A Review, Mitig. Adapt. Strateg. Glob. Change 11 (2006) 395–419. https://doi.org/10.1007/s11027-005-9006-5.

[105] J. Lehmann, A. Cowie, C.A. Masiello, C. Kammann, D. Woolf, J.E. Amonette, M.L. Cayuela, M. Camps-Arbestain, T. Whitman, Biochar in climate change mitigation, Nat. Geosci. 14 (2021) 883–892. https://doi.org/10.1038/s41561-021-00852-8.

[106] I. Senkovska, S. Kaskel, High pressure methane adsorption in the metal-organic frameworks Cu3(btc)2, Zn2(bdc)2dabco, and $Cr_3F(H_2O)_2O$(bdc)3, Microporous Mesoporous Mater. 112 (2008) 108–115. https://doi.org/10.1016/j.micromeso.2007.09.016.

[107] M. Gallo, D. Glossman-Mitnik, Fuel Gas Storage and Separations by Metal−Organic Frameworks: Simulated Adsorption Isotherms for H2 and CH_4 and Their Equimolar Mixture, J. Phys. Chem. C 113 (2009) 6634–6642. https://doi.org/10.1021/jp809539w.

[108] S. Kayal, B. Sun, A. Chakraborty, Study of metal-organic framework MIL-101(Cr) for natural gas (methane) storage and compare with other MOFs (metal-organic frameworks), Energy 91 (2015) 772–781. https://doi.org/10.1016/j.energy.2015.08.096.

[109] M. Karimi, C. Janiak, The metal–organic framework MIL-160: comprehensive insights into synthesis and applications, Chem. Commun. 61 (2025) 18742–18755. https://doi.org/10.1039/D5CC04626B.

[110] S. Bracco, D. Piga, I. Bassanetti, J. Perego, A. Comotti, P. Sozzani, Porous 3D polymers for high pressure methane storage and carbon dioxide capture, J. Mater. Chem. A 5 (2017) 10328–10337. https://doi.org/10.1039/C7TA00934H.

[111] J.L. Mendoza-Cortés, S.S. Han, H. Furukawa, O.M. Yaghi, W.A.I. Goddard, Adsorption Mechanism and Uptake of Methane in Covalent Organic Frameworks: Theory and Experiment, J. Phys. Chem. A 114 (2010) 10824–10833. https://doi.org/10.1021/jp1044139.

[112] Z. Wang, Y. Zhang, Kilogram-Scale Fabrication of a Robust Olefin-Linked Covalent Organic Framework for Separating Ethylene from a Ternary C2 Hydrocarbon Mixture | Journal of the American Chemical Society, https://doi.org/10.1021/jacs.3c07224.

[113] A. Policicchio, E. Maccallini, R.G. Agostino, F. Ciuchi, A. Aloise, G. Giordano, Higher methane storage at low pressure and room temperature in new easily scalable large-scale production activated carbon for static and vehicular applications, Fuel 104 (2013) 813–821. https://doi.org/10.1016/j.fuel.2012.07.035.

[114] J. Romanos, S.A. Dargham, M. Prosniewski, R. Roukos, F. Barakat, P. Pfeifer, Structure–Function Relations for Gravimetric and Volumetric Methane Storage Capacities in Activated Carbon, ACS Omega 3 (2018) 15119–15124. https://doi.org/10.1021/acsomega.8b02233.

[115] B.Y. Sadasivam, K.R. Reddy, Adsorption and transport of methane in biochars derived from waste wood, Waste Manag. 43 (2015) 218–229. https://doi.org/10.1016/j.wasman.2015.04.025.

[116] Business Analytiq, Activated carbon prices, Businessanalytiq (2023). https://businessanalytiq.com/procurementanalytics/index/activated-carbon-prices.

[117] imarc, Activated Carbon Prices, Chart, Index and Forecast, (n.d.). https://www.imarcgroup.com/activated-carbon-pricing-report.

[118] M. Nematian, C. Keske, J.N. Ng'ombe, A techno-economic analysis of biochar production and the bioeconomy for orchard biomass, Waste Manag. 135 (2021) 467–477. https://doi.org/10.1016/j.wasman.2021.09.014.

[119] M. Lutyński, J. Kielar, D. Gajda, M. Mikeska, J. Najser, High-Pressure Adsorption of CO_2 and CH_4 on Biochar—A Cost-Effective Sorbent for In Situ Applications, Materials 16 (2023) 1266. https://doi.org/10.3390/ma16031266.

[120] M. Bastos-Neto, A.E.B. Torres, D.C.S. Azevedo, C.L. Cavalcante, A Theoretical and Experimental Study of Charge and Discharge Cycles in a Storage Vessel for Adsorbed Natural Gas, Adsorption 11 (2005) 147–157. https://doi.org/10.1007/s10450-005-4906-y.

[121] M. Mozaffari Majd, V. Kordzadeh-Kermani, V. Ghalandari, A. Askari, M. Sillanpää, Adsorption isotherm models: A comprehensive and systematic review (2010−2020), Sci. Total Environ. 812 (2022) 151334. https://doi.org/10.1016/j.scitotenv.2021.151334.

[122] M. Thommes, K. Kaneko, A.V. Neimark, J.P. Olivier, F. Rodriguez-Reinoso, J. Rouquerol, K.S.W. Sing, Physisorption of gases, with special reference to the evaluation of surface area and pore size distribution (IUPAC Technical Report), Pure Appl. Chem. 87 (2015) 1051–1069. https://doi.org/10.1515/pac-2014-1117.

[123] H.M. Jang, S. Yoo, Y.-K. Choi, S. Park, E. Kan, Adsorption isotherm, kinetic modeling and mechanism of tetracycline on Pinus taeda-derived activated biochar, Bioresour. Technol. 259 (2018) 24–31. https://doi.org/10.1016/j.biortech.2018.03.013.

[124] Y.S. Ho, G. McKay, Pseudo-second order model for sorption processes, Process Biochem. 34 (1999) 451–465. https://doi.org/10.1016/S0032-9592(98)00112-5.

[125] Y.S. Ho, G. McKay, A Comparison of Chemisorption Kinetic Models Applied to Pollutant Removal on Various Sorbents, Process Saf. Environ. Prot. 76 (1998) 332–340. https://doi.org/10.1205/095758298529696.

[126] G. William Kajjumba, S. Emik, A. Öngen, H. Kurtulus Özcan, S. Aydın, Modelling of Adsorption Kinetic Processes—Errors, Theory and Application, in: S. Edebali (Ed.), Adv. Sorpt. Process Appl., IntechOpen, 2019. https://doi.org/10.5772/intechopen.80495.

[127] J. Wang, D. Ryan, H. Samara, P. Jaeger, Interactions of CO_2 with Hydrocarbon Liquid Observed from Adsorption of CO_2 in Organic-Rich Shale, Energy Fuels 34 (2020) 14476–14482. https://doi.org/10.1021/acs.energyfuels.0c02774.

[128] F.A. Abdul Kareem, A.M. Shariff, S. Ullah, N. Mellon, L.K. Keong, Adsorption of pure and predicted binary (CO_2:CH_4) mixtures on 13X-Zeolite: Equilibrium and kinetic properties at offshore conditions, Microporous Mesoporous Mater. 267 (2018) 221–234. https://doi.org/10.1016/j.micromeso.2018.04.007.

[129] P. Rallapalli, K.P. Prasanth, D. Patil, R.S. Somani, R.V. Jasra, H.C. Bajaj, Sorption studies of CO_2, CH_4, N_2, CO, O_2 and Ar on nanoporous aluminum terephthalate [MIL-53(Al)], J. Porous Mater. 18 (2011) 205–210. https://doi.org/10.1007/s10934-010-9371-7.

[130] S. Sircar, Basic Research Needs for Design of Adsorptive Gas Separation Processes, Ind. Eng. Chem. Res. 45 (2006) 5435–5448. https://doi.org/10.1021/ie051056a.

[131] G. Sethia, R.S. Somani, H.C. Bajaj, Adsorption of carbon monoxide, methane and nitrogen on alkaline earth metal ion exchanged zeolite-X: structure, cation position and adsorption relationship, RSC Adv. 5 (2015) 12773–12781. https://doi.org/10.1039/C4RA11511B.

[132] N. Heymans, B. Alban, S. Moreau, G. De Weireld, Experimental and theoretical study of the adsorption of pure molecules and binary systems containing methane, carbon monoxide, carbon dioxide and nitrogen. Application to the syngas generation, Chem. Eng. Sci. 66 (2011) 3850–3858. https://doi.org/10.1016/j.ces.2011.05.018.

[133] D. Hernández-Monje, L. Giraldo, J.C. Moreno-Piraján, Interaction between Hydrocarbons C6 and Modified Activated Carbons: Correlation between Adsorption Isotherms and Immersion Enthalpies, ACS Omega 4 (2019) 19595–19604. https://doi.org/10.1021/acsomega.9b02062.

[134] X. Song, L. Wang, J. Gong, X. Zhan, Y. Zeng, Exploring a New Method to Study the Effects of Surface Functional Groups on Adsorption of CO_2 and CH_4 on Activated Carbons, Langmuir 36 (2020) 3862–3870. https://doi.org/10.1021/acs.langmuir.9b03475.

[135] P. Kowalczyk, H. Tanaka, K. Kaneko, A. P. Terzyk, D. D. Do, Grand Canonical Monte Carlo Simulation Study of Methane Adsorption at an Open Graphite Surface and in Slitlike Carbon Pores at 273 K | Langmuir 21 (2005) 5639–5646, https://doi.org/10.1021/la050126f.

[136] M.M. Dubinin, Fundamentals of the theory of adsorption in micropores of carbon adsorbents: Characteristics of their adsorption properties and microporous structures, Carbon 27 (1989) 457–467. https://doi.org/10.1016/0008-6223(89)90078-X.

[137] R.V.R.A. Rios, J. Silvestre-Albero, A. Sepúlveda-Escribano, M. Molina-Sabio, F. Rodríguez-Reinoso, Kinetic Restrictions in the Characterization of Narrow Microporosity in Carbon Materials, J. Phys. Chem. C 111 (2007) 3803–3805. https://doi.org/10.1021/jp0701486.

[138] Y. Zhang, H. Chen, S. Islam, Advances in biochar modification for environmental remediation with emphasis on iron functionalization, (n.d.). https://www.maxapress.com/article/doi/10.48130/bchax-0025-0010.

[139] B. Sajjadi, W.-Y. Chen, N.O. Egiebor, A comprehensive review on physical activation of biochar for energy and environmental applications, Rev. Chem. Eng. 35 (2019) 735–776. https://doi.org/10.1515/revce-2017-0113.

[140] G. Greco, R.L.S. Canevesi, C. Di Stasi, A. Celzard, V. Fierro, J.J. Manyà, Biomass-derived carbons physically activated in one or two steps for CH_4/CO_2 separation, Renew. Energy 191 (2022) 122–133. https://doi.org/10.1016/j.renene.2022.04.035.

[141] K. Adlak, R. Chandra, V.K. Vijay, K.K. Pant, Physicochemical activation and palletisation of *Azadirachta indica* wood carbons for increased biomethane adsorbed energy storage, J. Anal. Appl. Pyrolysis 155 (2021) 105102. https://doi.org/10.1016/j.jaap.2021.105102.

[142] Y.F. Huang, W.H. Kuan, S.L. Lo, C.F. Lin, Total recovery of resources and energy from rice straw using microwave-induced pyrolysis, Bioresour. Technol. 99 (2008) 8252–8258. https://doi.org/10.1016/j.biortech.2008.03.026.

[143] A. Amini, M. Latifi, J. Chaouki, Electrification of materials processing via microwave irradiation: A review of mechanism and applications, Appl. Therm. Eng. 193 (2021) 117003. https://doi.org/10.1016/j.applthermaleng.2021.117003.

[144] Y.P.N. Yuh, L.R. Keey, O.M. Shahril, W.C. Chung, L.S. Shiung, Microwave pyrolysis using self-generated pyrolysis gas as activating agent: An innovative single-step approach to convert waste palm shell into activated carbon, E3S Web Conf. 22 (2017) 00195. https://doi.org/10.1051/e3sconf/20172200195.

[145] C. Liu, W. Chen, M. Li, S. Hong, W. Li, M. Pan, Q. Wu, C. Mei, Rapid microwave activation of waste palm into hierarchical porous carbons for supercapacitors using biochars from different carbonization temperatures as catalysts, RSC Adv. 9 (2019) 19441–19449. https://doi.org/10.1039/D6RA02117D.

[146] S. Allende, Y. Liu, M.A. Zafar, M.V. Jacob, Nitrite sensor using activated biochar synthesised by microwave-assisted pyrolysis, Waste Dispos. Sustain. Energy 5 (2023) 1–11. https://doi.org/10.1007/s42768-022-00120-4.

[147] A.U. Rajapaksha, S.S. Chen, D.C.W. Tsang, M. Zhang, M. Vithanage, S. Mandal, B. Gao, N.S. Bolan, Y.S. Ok, Engineered/designer biochar for contaminant removal/immobilization from soil and water: Potential and implication of biochar modification, Chemosphere 148 (2016) 276–291. https://doi.org/10.1016/j.chemosphere.2016.01.043.

[148] L. Wang, Y.S. Ok, D.C.W. Tsang, D.S. Alessi, J. Rinklebe, H. Wang, O. Mašek, R. Hou, D. O'Connor, D. Hou, New trends in biochar pyrolysis and modification strategies: feedstock, pyrolysis conditions, sustainability concerns and implications for soil amendment, Soil Use Manag. 36 (2020) 358–386. https://doi.org/10.1111/sum.12592.

[149] J. Ouyang, J. Chen, W. Chen, L. Zhou, D. Cai, C. Ren, H3PO4 activated biochars derived from different agricultural biomasses for the removal of ciprofloxacin from aqueous solution, Particuology 75 (2023) 217–227. https://doi.org/10.1016/j.partic.2022.07.016.

[150] L. Deng, J. Shi, Y. Zhao, D. Feng, W. Zhang, Y. Yu, S. Sun, Straw-based biochar prepared from multi-step KOH activation and its structure-effect relationship of CO_2 capture under atmospheric/pressurized conditions via experimental analysis and MD/DFT calculations, Chem. Eng. J. 495 (2024) 153403. https://doi.org/10.1016/j.cej.2024.153403.

[151] P. Zhang, W. Duan, H. Peng, B. Pan, B. Xing, Functional Biochar and Its Balanced Design, ACS Environ. Au 2 (2022) 115–127. https://doi.org/10.1021/acsenvironau.1c00032.

[152] M. Drobota, S. Ursache, M. Aflori, Surface Functionalities of Polymers for Biomaterial Applications, Polymers 14 (2022) 2307. https://doi.org/10.3390/polym14122307.

[153] L. Liu, X. Sun, C. Nie, M. Chen, Y. Wang, Q. Zhang, Y. Xu, Salts-activated synthesis of Cu/Co co-doped biochar for efficient removal of elemental mercury from coal combustion flue gas, Chem. Eng. J. 499 (2024) 156174. https://doi.org/10.1016/j.cej.2024.156174.

[154] A. Hu, Y. Jiang, J. An, Novel Fe/Ca oxide co-embedded coconut shell biochar for phosphorus recovery from agricultural return flows - RSC Advances (RSC Publishing) DOI:10.1039/D4RA04795H.

[155] A. Sun, S. Bian, L. Li, Z. Guo, W. Li, J. Li, S. Xu, P.-D. Liu, Preparation of highly adsorptive biochar by sequential iron impregnation under refluxing and pyrolysis at low temperature for removal of tetracycline, Environ. Pollut. 348 (2024) 123886. https://doi.org/10.1016/j.envpol.2024.123886.

[156] C. Tendero, C. Tixier, P. Tristant, J. Desmaison, P. Leprince, Atmospheric pressure plasmas: A review, Spectrochim. Acta Part B At. Spectrosc. 61 (2006) 2–30. https://doi.org/10.1016/j.sab.2005.10.003.

[157] L. Bárdos, H. Baránková, Cold atmospheric plasma: Sources, processes, and applications, Thin Solid Films 518 (2010) 6705–6713. https://doi.org/10.1016/j.tsf.2010.07.044.

[158] M.A. Lieberman, A.J. Lightenberg, Principles of Plasma Discharges and Materials Processing, 1st ed., John Wiley & Sons, Ltd, 2005. https://doi.org/10.1002/0471724254.

[159] Y. Vadikkeettil, Y. Subramaniam, R. Murugan, P.V. Ananthapadmanabhan, J. Mostaghimi, L. Pershin, C. Batiot-Dupeyrat, Y. Kobayashi, Plasma assisted decomposition and reforming of greenhouse gases: A review of current status and emerging trends, Renew. Sustain. Energy Rev. 161 (2022) 112343. https://doi.org/10.1016/j.rser.2022.112343.

[160] A. Bogaerts, E. Neyts, R. Gijbels, J. van der Mullen, Gas discharge plasmas and their applications, Spectrochim. Acta Part B At. Spectrosc. 57 (2002) 609–658. https://doi.org/10.1016/S0584-8547(01)00406-2.

[161] Q. Niu, J. Luo, Y. Xia, S. Sun, Q. Chen, Surface modification of bio-char by dielectric barrier discharge plasma for Hg0 removal, Fuel Process. Technol. 156 (2017) 310–316. https://doi.org/10.1016/j.fuproc.2016.09.013.

[162] M. Cun, K. Wang, Z. Yin, J. Guo, T. Wang, S. Yang, G. Liu, Y. Zhang, Q. Feng, L. Liu, Y. Chen, Research progress on elemental mercury (Hg0) removal in flue gas using non-thermal plasma technology, Environ. Pollut. 361 (2024) 124806. https://doi.org/10.1016/j.envpol.2024.124806.

[163] D.R. Kandel, H.-J. Kim, J.-M. Lim, M.B. Poudel, M. Cho, H.-W. Kim, B.-T. Oh, C. Nah, S.H. Lee, B. Dahal, J. Lee, Cold plasma-assisted regeneration of biochar for dye adsorption, Chemosphere 309 (2022) 136638. https://doi.org/10.1016/j.chemosphere.2022.136638.

[164] R. Waghmare, Cold plasma technology for fruit based beverages: A review, Trends Food Sci. Technol. 114 (2021) 60–69. https://doi.org/10.1016/j.tifs.2021.05.018.

[165] M. LIM, A.Z.S. ZULKIFLI, Investigation of biomass surface modification using non-thermal plasma treatment, Plasma Sci. Technol. 20 (2018) 115502. https://doi.org/10.1088/2058-6272/aac819.

[166] S.S. Senadheera, X. Yuan, B. Yi, S.K. Im, Y.S. Ok, Plasma-modified biochar for energy and environmental sustainability, Curr. Opin. Chem. Eng. 49 (2025) 101166. https://doi.org/10.1016/j.coche.2025.101166.

[167] H. Bamdad, K. Hawboldt, Comparative study between physicochemical characterization of biochar and metal organic frameworks (MOFs) as gas adsorbents, Can. J. Chem. Eng. 94 (2016) 2114–2120. https://doi.org/10.1002/cjce.22595.

[168] R. Zhou, X. Wang, R. Zhou, J. Weerasinghe, T. Zhang, Y. Xin, H. Wang, P. Cullen, H. Wang, K.K. Ostrikov, Non-thermal plasma enhances performances of biochar in wastewater treatment and energy storage applications, Front. Chem. Sci. Eng. 16 (2022) 475–483. https://doi.org/10.1007/s11705-021-2070-x.

[169] M. Dhayal, D. Forder, K.L. Parry, R.D. Short, J.W. Bradley, Using an afterglow plasma to modify polystyrene surfaces in pulsed radio frequency (RF) argon discharges, Surf. Coat. Technol. 174–175 (2003) 872–876. https://doi.org/10.1016/S0257-8972(03)00562-0.

[170] G.V. Latag, M.R. Vasquez Jr., Effects of RF plasma modification on the thermal and mechanical properties of electrospun chitosan/poly(vinyl alcohol) nanofiber mats, J. Vac. Sci. Technol. B 36 (2018) 04I101. https://doi.org/10.1116/1.5030507.

[171] A. Felten, C. Bittencourt, J.J. Pireaux, G. Van Lier, J.C. Charlier, Radio-frequency plasma functionalization of carbon nanotubes surface O_2, NH_3, and CF_4 treatments, J. Appl. Phys. 98 (2005) 074308. https://doi.org/10.1063/1.2071455.

[172] H. Zhu, Y. Huang, S. Yin, W. Zhang, Microwave plasma setups for CO_2 conversion: A mini-review, Green Energy Resour. 2 (2024) 100061. https://doi.org/10.1016/j.gerr.2024.100061.

[173] R. Johnson, M.A. Zafar, S. Thomas, M.V. Jacob, A critical review on vacuum and atmospheric microwave plasma-based graphene synthesis, FlatChem 50 (2025) 100812. https://doi.org/10.1016/j.flatc.2025.100812.

[174] J.F. Friedrich, P. Rohrer, W. Saur, Th. Gross, A. Lippitz, W. Unger, Improvement in polymer adhesivity by low and normal pressure plasma surface modification, Surf. Coat. Technol. 59 (1993) 371–378. https://doi.org/10.1016/0257-8972(93)90115-5.

[175] J.M. Austin, A.L.S. Smith, Decomposition of N_2O in a glow discharge, J. Phys. Appl. Phys. 6 (1973) 2236. https://doi.org/10.1088/0022-3727/6/18/308.

[176] I. Maezono, J.-S. Chang, Reduction of CO/sub 2/ from combustion gases by DC corona torches, IEEE Trans. Ind. Appl. 26 (1990) 651–655. https://doi.org/10.1109/28.55989.

[177] E. Adhamash, R. Pathak, K. Chen, M.T. Rahman, A. El-Magrous, Z. Gu, S. Lu, Q. Qiao, Y. Zhou, High-energy plasma activation of renewable carbon for enhanced capacitive performance of supercapacitor electrode, Electrochimica Acta 362 (2020) 137148. https://doi.org/10.1016/j.electacta.2020.137148.

[178] H. Zhang, J. Yu, J. Wang, Non-Thermal Oxygen-Helium Plasma Modification and Regeneration of Sawdust Biochar to Promote Aniline Removal, ES Energy Environ. Volume 15 (March 2022) (2022) 15–27.

[179] T. Wang, J. Liu, Y. Zhang, H. Zhang, W.-Y. Chen, P. Norris, W.-P. Pan, Use of a non-thermal plasma technique to increase the number of chlorine active sites on biochar for improved mercury removal, Chem. Eng. J. 331 (2018) 536–544. https://doi.org/10.1016/j.cej.2017.09.017.

[180] S. Xie, P.D. Pedrow, K.R. Englund, Cold Plasma Processing of Biochar Using Corona Discharge in Atmospheric Pressure Dry Air and Helium, IEEE Trans. Plasma Sci. 48 (2020) 2457–2463. https://doi.org/10.1109/TPS.2020.2998436.

[181] R.K. Gupta, M. Dubey, P. Kharel, Z. Gu, Q.H. Fan, Biochar activated by oxygen plasma for supercapacitors, J. Power Sources 274 (2015) 1300–1305. https://doi.org/10.1016/j.jpowsour.2014.10.169.

[182] J. Zhang, H. Zhang, F. Li, H. Wang, Synthesis of porous functional biochar through template method and plasma modification for Pb2+ removal: Performance and mechanism, Energy 312 (2024) 133549. https://doi.org/10.1016/j.energy.2024.133549.

[183] V. Gargiulo, A. Gomis-Berenguer, P. Giudicianni, C.O. Ania, R. Ragucci, M. Alfè, Assessing the Potential of Biochars Prepared by Steam-Assisted Slow Pyrolysis for CO_2 Adsorption and Separation, Energy Fuels 32 (2018) 10218–10227. https://doi.org/10.1021/acs.energyfuels.8b01058.

[184] S. Rong, Y. He, L. Ni, Q. Gao, X. Feng, S. Liu, Y. Zhong, Y. Li, Z. Liu, Steam-activated biochar for efficient removal of sulfamethoxazole from water: Activation temperature-

mediated differences, J. Water Process Eng. 72 (2025) 107462. https://doi.org/10.1016/j.jwpe.2025.107462.

[185] R. Rios, F. Miranda da Silva, A. Torres, D. Azevedo, C. Cavalcante Jr, Adsorption of Methane in Activated Carbons Obtained from Coconut Shells Using H3PO4 Chemical Activation, Adsorpt.-J. Int. Adsorpt. Soc. - Adsorpt. 15 (2009) 271–277. https://doi.org/10.1007/s10450-009-9174-9.

[186] A. Altwala, R. Mokaya, Predictable and targeted activation of biomass to carbons with high surface area density and enhanced methane storage capacity, Energy Environ. Sci. 13 (2020) 2967–2978. https://doi.org/10.1039/D0EE01340D.

[187] Y. Li, T. Ben, B. Zhang, Y. Fu, S. Qiu, Ultrahigh gas storage both at low and high pressures in KOH-activated carbonized porous aromatic frameworks, Sci. Rep. 3 (2013) 2420. https://doi.org/10.1038/srep02420.

[188] L. Scott Blankenship, R. Mokaya, Modulating the porosity of carbons for improved adsorption of hydrogen, carbon dioxide, and methane: a review, Mater. Adv. 3 (2022) 1905–1930. https://doi.org/10.1039/D1MA00911G.

[189] A. Perrin, A. Celzard, A. Albiniak, J. Kaczmarczyk, J.F. Marêché, G. Furdin, NaOH activation of anthracites: effect of temperature on pore textures and methane storage ability, Carbon 42 (2004) 2855–2866. https://doi.org/10.1016/j.carbon.2004.06.030.

[190] J. Wang, Edward J. Anthony, A common decay behavior in cyclic processes, Chem. Eng. Commun. 194 (2007) 1409–1420. https://doi.org/10.1080/00986440701401594.

[191] J. Le Mer, P. Roger, Production, oxidation, emission and consumption of methane by soils: A review, Eur. J. Soil Biol. 37 (2001) 25–50. https://doi.org/10.1016/S1164-5563(01)01067-6.

[192] B.Y. Sadasivam, K.R. Reddy, Landfill methane oxidation in soil and bio-based cover systems: a review, Rev. Environ. Sci. Biotechnol. 13 (2014) 79–107. https://doi.org/10.1007/s11157-013-9325-z.

[193] C. Scheutz, P. Kjeldsen, J.E. Bogner, A. De Visscher, J. Gebert, H.A. Hilger, M. Huber-Humer, K. Spokas, Microbial methane oxidation processes and technologies for mitigation of landfill gas emissions, Waste Manag. Res. 27 (2009) 409–455. https://doi.org/10.1177/0734242X09339325.

[194] A. De Visscher, O.V. Cleemput, Induction of enhanced CH_4 oxidation in soils: NH4+ inhibition patterns, Soil Biol. Biochem. 35 (2003) 907–913. https://doi.org/10.1016/S0038-0717(03)00122-6.

[195] K.R. Reddy, E.N. Yargicoglu, D. Yue, P. Yaghoubi, Enhanced Microbial Methane Oxidation in Landfill Cover Soil Amended with Biochar, J. Geotech. Geoenvironmental Eng. 140 (2014) 04014047. https://doi.org/10.1061/(ASCE)GT.1943-5606.0001148.

[196] D. He, R. Yang, Y. Fu, B. Zhu, Superior properties of biochar contribute to soil carbon sequestration and climate change mitigation, J. Environ. Chem. Eng. 13 (2025) 116936. https://doi.org/10.1016/j.jece.2025.116936.

[197] X. Gui, X. Xu, Z. Zhang, L. Hu, W. Huang, L. Zhao, X. Cao, Biochar-amended soil can further sorb atmospheric CO_2 for more carbon sequestration, Commun. Earth Environ. 6 (2025) 5. https://doi.org/10.1038/s43247-024-01985-5.

[198] W. Han, Y. Lai, H. Ji, Biochar-driven soil carbon sequestration: priming effects and emission reduction, Environ. Sci. Process. Impacts 27 (2025) 3725–3745. https://doi.org/10.1039/D5EM00500K.

[199] A. Pertiwiningrum, Heating Value Enhancement by Biogas Purification using Natural Zeolite and Rice Straw-Based Biochar, Int. J. GEOMATE 16 (2019). https://doi.org/10.21660/2019.55.4715.

[200] Y. Dai, N. Zhang, C. Xing, Q. Cui, Q. Sun, The adsorption, regeneration and engineering applications of biochar for removal organic pollutants: A review, Chemosphere 223 (2019) 12–27. https://doi.org/10.1016/j.chemosphere.2019.01.161.

[201] Dylan Brown et al., Capturing Value From Natural Gas: Mitigating the Flaring of Natural Gas in North Dakota-A comprehensive report on pathways for mitigation of natural gas flaring, (n.d.).

[202] E. Pancione, A. Erto, F. Di Natale, A. Lancia, M. Balsamo, A comprehensive review of post-combustion CO_2 capture technologies for applications in the maritime sector: A focus on adsorbent materials, J. CO_2 Util. 89 (2024) 102955. https://doi.org/10.1016/j.jcou.2024.102955.

[203] M. Al-Shargabi, S. Davoodi, D.A. Wood, V.S. Rukavishnikov, K.M. Minaev, Carbon Dioxide Applications for Enhanced Oil Recovery Assisted by Nanoparticles: Recent Developments, ACS Omega 7 (2022) 9984–9994. https://doi.org/10.1021/acsomega.1c07123.

[204] L. Yang, W. Rui, Z. Qingmin, Z. Yuanlong, F. Xin, X. Zhaojie, CO_2-enhanced oil recovery with CO_2 utilization and storage: Progress and practical applications in China, Unconv. Resour. 4 (2024) 100096. https://doi.org/10.1016/j.uncres.2024.100096.

[205] A. Sæle, A. Graue, Z. Alcorn, Unsteady-state CO_2 foam injection for increasing enhanced oil recovery and carbon storage potential, Adv. GEO-ENERGY Res. 6 (2022) 472–481. https://doi.org/10.46690/ager.2022.06.04.

Chapter 3. Adsorption of CH_4 on biochar for emission reduction in oil and gas fields[1]

Part of this chapter has been published in the *Journal of Biochar.*

Graphical Abstract:

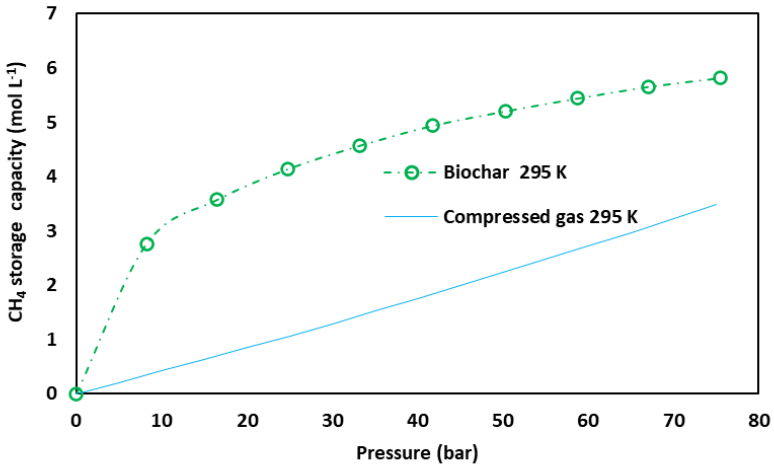

[1]V. Y. Ko, J. Wang, I. He, D. Ryan, X. Zhang, and C. Lan, "Adsorption of methane on biochar for emission reduction in oil and gas fields," Biochar, vol. 5, no. 1, p. 15, Mar. 2023, https://doi.org/10.1007/s42773-023-00209-x.

Abstract

The capture and storage of CH_4 using low-cost biochar as adsorbents under oil and gas fields conditions is investigated in an effort to reduce methane (CH_4) emissions. This chapter presents results of CH_4 adsorption on four biochars made from forestry wastes in comparison with the results of three commercial activated carbons. Although the adsorption capacity of the biochars is lower by over 50% than that of the activated carbons, the low cost and potential environmental benefits provide the incentive to the investigation. Moreover, biochar can store more CH_4 than compressed gas vessels up to the pressure of 75 bar, suggesting the possibility of avoiding high-pressure gas compression and heavy vessels for cost savings in oil and gas fields. The thermodynamic and kinetic behaviors of the adsorption are studied and implications for the targeted application are discussed.

Keywords:

Biochar, Adsorbent, CH_4 emissions, Greenhouse gas reduction, Adsorption behavior.

Highlights:

- Biochar stores more CH_4 per unit volume than compressed gas at pressures up to 75 bar.
- CH_4 adsorption increases with decreasing temperature (303–295 K). Linear van't Hoff plots of the Langmuir constant enable extrapolation to other temperatures.
- CH_4 adsorption equilibrium is reached within 2 minutes, demonstrating rapid adsorption kinetics.

3.1 Introduction

Global warming driven by greenhouse gas emissions is progressing at an alarming pace. CH_4 has been recognized as a greenhouse gas with high global warming potential [1]. Meanwhile, large quantities of CH_4 have been emitted into the atmosphere, which is responsible for one-quarter of the warming that we experience today [2]. CH_4 concentrations in the atmosphere have reached a record high level in 2021, which is nearly three times the pre-industrial levels [3]. The United States leads the global effort of mitigating CH_4 emissions. A large source of CH_4 emissions is the oil and gas industry. Canada aims to reduce CH_4 emissions from the oil and gas industry to at least 25% of 2012 levels by 2030 [4,5].

In oil and gas industry, gas venting (releasing to atmosphere) and flaring (burning) are increasingly adding to the global emission problem. Natural gas is a by-product of oil fields and is vented or flared when it is uneconomical to collect and sell. CH_4 is the main component of vented natural gas. Each ton of CH_4 contributes over 70 times more to global warming (over 20 years) than a ton of CO_2 [6]. Flaring can reduce the global warming effect, but the resultant CO_2 is still a greenhouse gas. Moreover, CH_4 is a clean and valuable energy source that should not be wasted.

We have been exploring the collection and storage of natural gas as an alternative to venting and flaring, using the gas as on-site fuel. Gas engines, diesel engines, and dual fuel engines can all work with CH_4. However, for a steady gas supply to the engines, an efficient and cost-effective means of storage is needed. Adsorbed natural gas (ANG) can be a competitive technology for fuel storage in natural gas vehicles [7] and would be more economical compared to liquefied natural gas (LNG) or compressed natural gas (CNG) for oil and gas fields. Biochars can serve as low-cost adsorbents [8–12]. Such adsorbents may store natural gas at ambient temperature and

moderate pressure and eliminate the need for high-pressure compression and the associated large compressors. This would be particularly attractive to small and medium-sized oil and gas producers for cost savings. Moreover, adsorbed gas can be moved easily to where it will be used, without the need for pipelines. This is another benefit because pipelines are typically not equipped in oil fields for transporting gas [13].

While numerous studies examine CH_4 adsorbents including activated carbons for vehicle applications, biochar offers greater cost-effectiveness for oil and gas field deployment. Biochar is cheap and widely available. It has been forecasted that the world's biochar market will double by 2026 [14]. Biochar adsorbents for greenhouse gases including CH_4 have been actively studied [15–24], although not for oil and gas field applications. There are abundant forestry and agricultural wastes which can be used to make biochar adsorbents. Biochar may have lower CH_4 adsorption capacity than activated carbons do, and hence a larger volume of biochar is needed to store the same quantity of CH_4. However, compared to vehicle applications, cost could be more important than volume or space for oil and gas fields. Besides, the spent biochar adsorbents may be used for combustion and soil amendment. Thus, the overall advantage of using biochar for CH_4 capture and storage can be significant.

In this work, we study CH_4 adsorption behavior of biochars that are produced from forestry wastes and discuss the effectiveness of the biochars as adsorbents for the targeted application in oil and gas fields.

3.2 Experimental

3.2.1 Adsorption measurement

Adsorption was measured using a volumetric method. A commercial sorption analyzer PCT-Pro manufactured by Setaram Inc. is used for adsorption experiments. The analyzer can measure adsorption under pressure up to 200 bar, with sample size up to 5 ml. The PCT-Pro is a Sievert-type analyzer. A schematic of the measurement system is shown in Fig. 3.1.

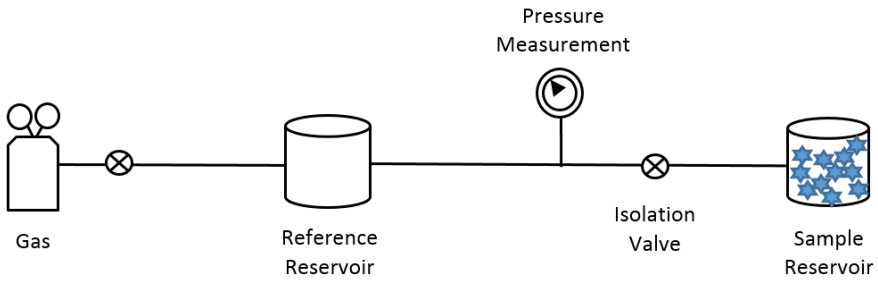

Fig. 3.1 A schematic of the Sievert measurement system

The free volume of the sample reservoir is calibrated with helium at the experimental temperature for each adsorbent sample. CH_4 is pressurized in the reference reservoir, then released into the sample reservoir containing the adsorbent sample for adsorption to take place. The amount of CH_4 adsorption is calculated by the difference between the equilibrium pressure before and after gas injection into the sample reservoir. To obtain an adsorption isotherm, the pressure can be increased stepwise automatically through a computer program of the analyzer.

The molar amount of gas admitted into the reference reservoir and the molar amount of gas remaining at the adsorption equilibrium are determined by pressure-volume-temperature relations before and after adsorption using non-ideal gas equations incorporated in the computer program.

The difference of CH_4 adsorbed at each pressure step in the sample is calculated by the computer program from the pressure difference between the equilibrium adsorptions. The pressure decrease of CH_4 gas in the sample reservoir corresponds to the adsorption to the sample. The quantity of gas is related to pressure by the gas law. Gas compressibility factor is determined for different pressure and temperature conditions using the National Institute of Standards and Technology (NIST) database Thermophysical Properties of Fluid Systems.

3.2.2 Materials

Four biochars are studied in this work. Three activated carbons are also studied for comparison. Physical properties of these materials are shown in Table 3.1, where BET surface area, pore volume and average pore width are determined using a porosimetry analyzer (Micromeritics, ASAP2020), particle size determined by sieve analysis, bulk density determined using a sample cell with a known volume, and skeletal density determined by a pycnometer (Micromeritics, Accupyc II 1340). Compositional analyses including proximate analysis (moisture, ash, volatile matter, fixed carbon), ultimate analysis (C, H, N, O, S) and X-ray fluorescence (XRF) metal oxides analyses are shown in Table 3.2.

Table 3.1 Properties of adsorbent materials

Sample*	Type	BET Surface Area ($m^2 g^{-1}$)	Pore volume ($cm^3 g^{-1}$)	Average Pore width (nm)	Particle Size (mm)	Bulk Density ($g\ ml^{-1}$)	Skeletal Density ($g\ ml^{-1}$)
BC-Ash	**Non-commercial**	**490**	**0.25**	**1.998**	**1.18 - 1.70**	**0.06**	**2.00**
BC-Birch	**Lab-made**	**34**	**0.02**	**2.407**	**1.18 - 3.36**	**0.10**	**-**
BC-Biocarb	**Commercial**	**525**	**0.29**	**2.226**	**1.70 - 3.36**	**0.13**	**1.86**
BC-Elkem	**Commercial**	**3.72**	**0.06**	**64.64**	**1.18 - 1.70**	**0.16**	**1.42**
AC-FW	**Commercial**	**970**	**0.65**	**2.666**	**1.18 - 1.70**	**0.06**	**2.05**
AC-CABOT*	**Commercial**	**551**	**0.54**	**3.944**	**1.18 - 1.70**	**0.40**	**2.06**
AC-F400	**Commercial**	**907**	**0.52**	**2.280**	**1.18 - 1.70**	**0.59**	**2.14**

*BC denotes biochar and AC denotes activated carbon.

Table 3.2 Compositional analysis of adsorbent materials (wt%)

Sample	Moisture	Ash	VM[a]	FC[b]	C	H	N	S	O	SiO_2	Al_2O_3	Fe_2O_3	TiO_2	P_2O_5	CaO	MgO	SO_3	Na_2O	K_2O
BC-Ash	**8.68**	**12.0**	**12.9**	**66.4**	**71.8**	**0.64**	**0.31**	**<0.05**	**6.56**	**14**	**4.4**	**2.7**	**0.2**	**1.8**	**28**	**4.3**	**14**	**3.4**	**13**
BC-Birch	**4.54**	**5.00**	**n/a**	**n/a**	**73.1**	**1.98**	**0.55**	**0.20**	**14.5**	**n/a**	**n/a**	**n/a**	**n/a**	**n/a**	**n/a**	**n/a**	**n/a**	**n/a**	**n/a**
BC-Biocarb	**6.31**	**6.21**	**6.01**	**87.8**	**89.2**	**0.85**	**0.51**	**0.00**	**3.19**	**42**	**7.3**	**15**	**15**	**0.9**	**13**	**3.1**	**0.9**	**1.9**	**7.3**
BC-Elkem	**3.32**	**1.43**	**26.6**	**72.0**	**79.9**	**3.80**	**0.29**	**0.00**	**14.6**	**7.2**	**2.4**	**2.1**	**0.1**	**1.5**	**35**	**5.4**	**1.0**	**0.3**	**11**
AC-FW	**1.92**	**2.25**	**2.46**	**93.4**	**92.3**	**0.44**	**0.68**	**<0.05**	**2.39**	**1.9**	**1.5**	**1.5**	**<0.03**	**3.4**	**30**	**5.8**	**31**	**0.3**	**14**
AC-CABOT	**7.77**	**19.57**	**5.15**	**67.5**	**67.7**	**0.49**	**0.63**	**0.72**	**3.14**	**70**	**16**	**1.4**	**2.3**	**0.1**	**1.4**	**1.0**	**2.4**	**2.8**	**1.3**
AC-F400	**3.93**	**5.94**	**2.98**	**87.2**	**86.9**	**0.19**	**0.84**	**0.64**	**1.56**	**n/a**	**n/a**	**n/a**	**n/a**	**n/a**	**n/a**	**n/a**	**n/a**	**n/a**	**n/a**

[a]VM denotes Volatile Matter; [b] FC denotes Fixed Carbon

In the above materials BC refers to biochar and AC refers to activated carbon. The biochars are all from forestry wastes which are abundant. BC-Ash is an ash residue collected from a waste-wood boiler by FPInnovations, a not-for-profit R&D organization. BC-Biocarb and BC-Elkem are commercial biochar products for metallurgic uses. BC-Birch is prepared in the laboratory of CanmetENERGY-Ottawa by pyrolyzing a wood (birch) residue with a heating rate of 5 ℃ min^{-1} up to 600℃ and holding for 3 hours in argon. AC-FW, AC-F400 and AC-CABOT are commercial activated carbons.

3.3 Results and discussions

3.3.1 Adsorption capacity

Experimental results for adsorption of CH_4 on the biochars are shown in Fig. 3.2. All the four biochars show similar patterns of adsorption. It is clear that the amount of adsorption increases with pressure generally and decreases with temperature. BC-Biocarb shows the highest adsorption capacity, followed by BC-Ash. The other two biochars show lower adsorption capacity. It is worth noting that CH_4 adsorption by BC-Elkem at 303 K (30 °C) increases with pressure first but after a maximum value it decreases with pressure and approaches zero adsorption. BC-Biocarb and BC-Birch also show a trend of decreasing adsorption with increasing pressure after a maximum value at 303 K. Such pressure dependence has been reported for CH_4 adsorption on coal and shale and could be described in terms of excess adsorption [25,26]. This will be discussed in the *Appendix A*.

The results for adsorption of CH_4 on the three activated carbons are also shown in Fig. 3.2 for comparison. AC-FW shows the highest adsorption capacity, which is over twice of that of the biochars. AC-CABOT shows the lowest adsorption capacity. Its capacity at 295 K is higher than that of BC-Biocarb and BC-Ash biochars by only a small degree. However, unlike the case of the biochars, the capacity of AC-CABOT does not depend strongly on temperature. The weak temperature dependence is also exhibited by the other two activated carbons. This suggests that the activated carbons could give more stable performance in ambient temperature range. By contrast, the adsorption capacities of the biochars decrease substantially as the temperature increases from 295 K to 303 K.

The applicability of the Langmuir monolayer assumption to CH_4 adsorption on biochar can be understood through micropore filling theory. In ultramicropores (< 0.7 nm), the pore width approaches the kinetic diameter of CH_4 (0.38 nm), accommodating at most one molecule across the pore width. Adsorption in such confined spaces proceeds not by progressive layer-by-layer surface coverage as described by BET, but by volume filling of the pore space, where each molecule simultaneously interacts with both opposing pore walls [27,28]. The Langmuir monolayer assumption is therefore consistent with this filling mechanism: the micropore geometry itself imposes a single-molecule occupancy constraint per pore cross-section. Furthermore, CH_4 is supercritical at all measurement temperatures (295–303 K, well above Tc = 190.6 K), meaning condensation into a liquid phase is physically impossible and multilayer formation cannot occur [29]. The assumption of negligible adsorbate–adsorbate interactions is reasonable within this framework: in narrow micropores, wall–adsorbate interactions dominate over lateral adsorbate–adsorbate interactions; in wider pores and at elevated pressures, adsorbate–adsorbate interactions become increasingly significant [30], and adsorption is better described as a collective filling of the pore space governed by the local adsorption potential rather than occupation of independent sites. Lateral interactions between molecules in adjacent pores are negligible compared to the dominant adsorbent–adsorbate interaction. At high pressures approaching 75 bar, where fractional coverage increases, some adsorbate–adsorbate interactions within wider pores become non-negligible; their effects are absorbed into the effective N_m and B parameters without compromising the overall thermodynamic consistency of the analysis.

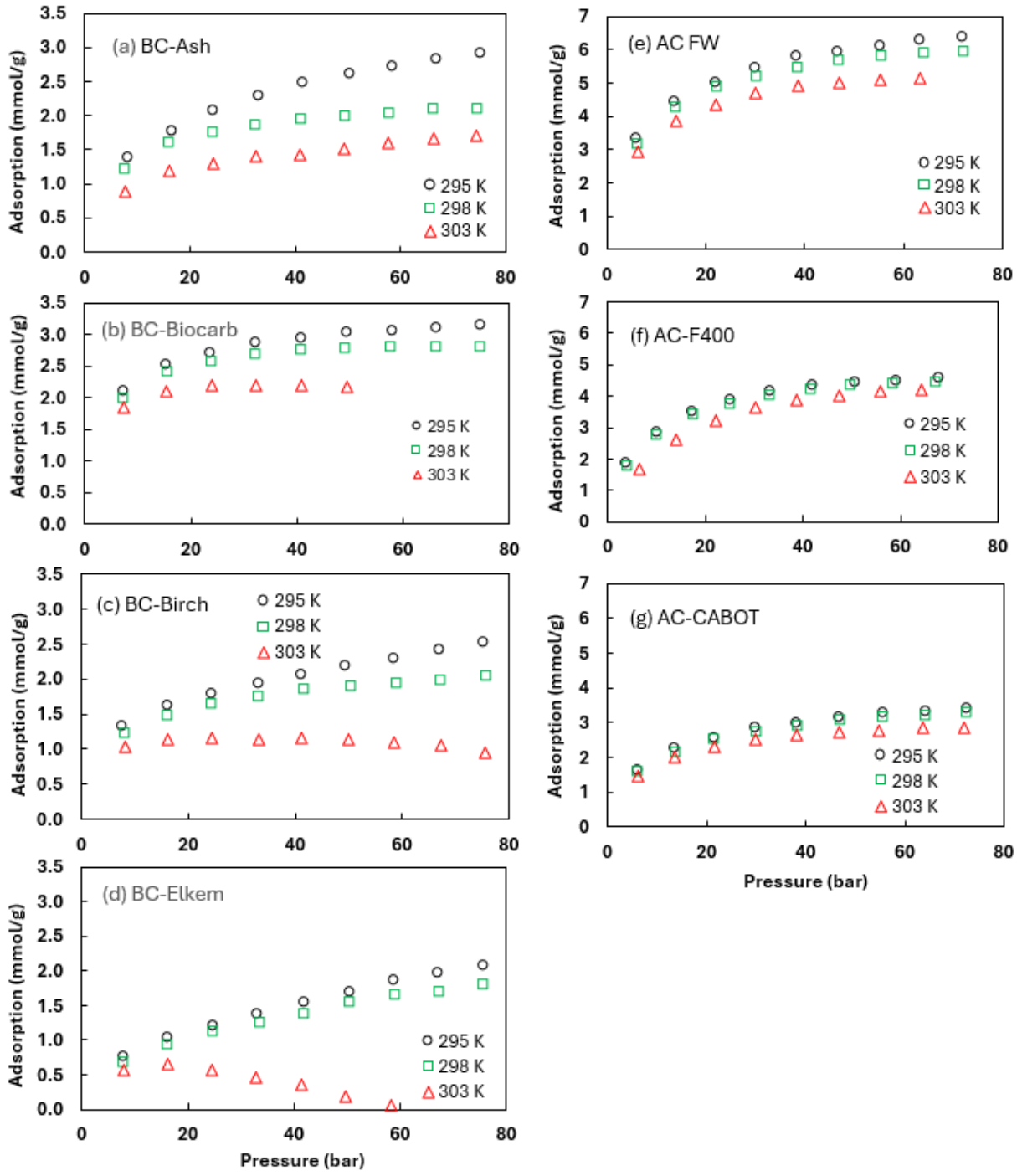

Fig. 3.2 Adsorption of CH_4 on biochars and activated carbons as a function of pressure. Biochars are on the left: (a) BC-Ash; (b) BC-Biocarb; (c) BC-Birch; (d) BC-Elkem; activated carbons are on the right: (e) AC-FW; (f) AC-F400; (g) AC-CABOT

For Canadian oil and gas fields, the temperature could be below 295 K and biochars could have considerable CH_4 adsorption capacity (the temperature effect is discussed in more detail later). Moreover, activated carbon would cost at least several hundred dollars per ton whereas some biochar wastes, such as BC-Ash, would have zero or negative cost because the cost for disposal is avoided. Considering the cost issue, there is incentive to explore using biochars for CH_4 capture and storage.

Among the four biochars studied in this work, BC-Biocarb has the highest CH_4 adsorption capacity, followed by BC-Ash. However, in the discussion hereafter we focus on BC-Ash instead of BC-Biocarb, because BC-Ash has lower cost. BC-Ash is a waste material obtained from combustion ash of waste wood, which otherwise requires disposal. It also has a reasonable adsorption capacity. This material has a high skeletal density of nearly 2 g cm^{-3}. With this density the adsorption capacity in terms of the volume that the solid portion occupies (i.e., the excess adsorption per skeletal volume) is calculated and compared with the volume of compressed CH_4 under the same pressure, as shown in Fig. 3.3. As can be seen, the capacity for accommodating CH_4 by the skeletal volume of this biochar is considerably higher than compressed CH_4 that occupies the same volume in the pressure range up to 75 bar. This suggests that, with the same volume, the biochar would be able to store more CH_4 than compressed CH_4 in our targeted application for oil and gas fields. The storage capacity of biochar is increasingly higher with decreasing pressure and temperature than compressed gas. By contrast, the capacity for compressed gas is essentially independent of temperature at ambient conditions, as suggested by Fig. 3.3.

In Canadian oil and gas fields, the temperature can be below 295 K. To adsorb gas at low to medium pressure, large compressors and thick-walled vessels which are necessary for compressed

natural gas (CNG) are not required [31]. Higher storage capacity of biochar adsorbents than that of CNG with lower pressure would allow smaller and light-walled vessels, and, because of lower pressure, reduce leaking potential and explosion risk. In consequence, the advantage of adsorbed natural gas (ANG) with biochar adsorbents over CNG would be more significant for Canadian oil and gas fields. It should be noted that there is no evidence suggesting that BC-Ash would be the most promising biochar for CH_4 capture and storage. Other low-cost biochar materials, which give better performance in adsorption of CH_4, may exist. Alternatively, the performance of the current biochar may be improved, through surface modification, for example.

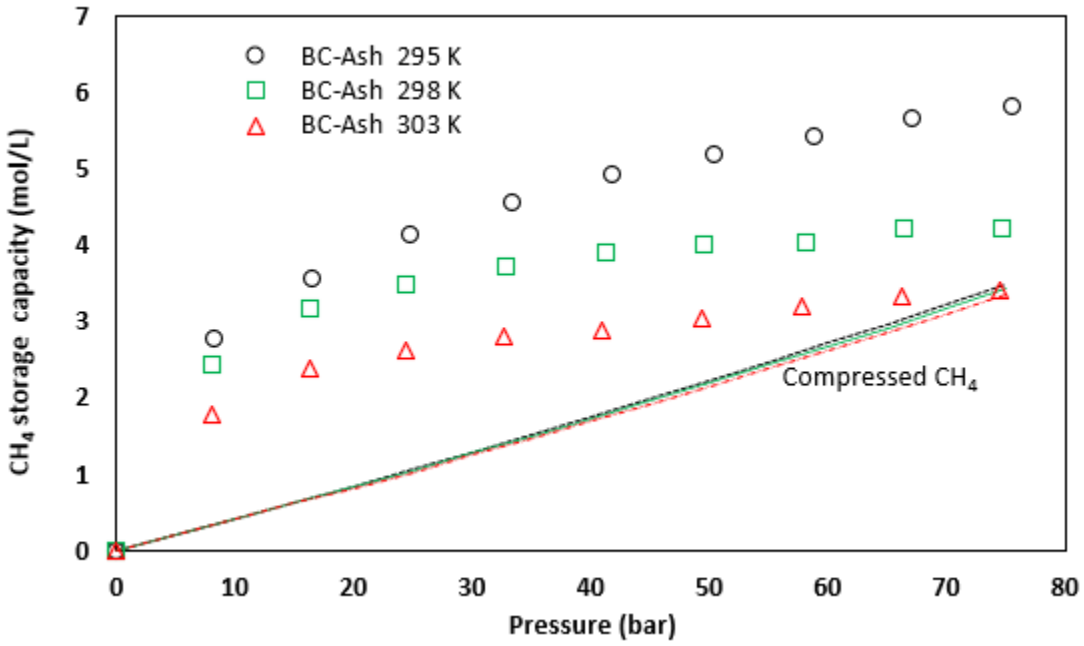

Fig. 3.3 Comparison of storage capacity for biochar BC-Ash and compressed gas. The lines represent the storage capacity of vessels for pressurized CH_4 at 295 K, 298 K, and 303 K. The three lines at these temperatures essentially overlap each other

To describe the CH_4 adsorption behavior, we have examined several common adsorption isotherm models including Langmuir, Freundlich, Sips, BET and Toth models (shown in *Appendix B*). The Langmuir model is the most widely used adsorption isotherm model for activated carbons and can

be derived theoretically for monolayer adsorption. BET model is applicable for multilayer adsorption, but only below critical temperature of adsorbates. Hence, it is not applicable for CH_4 under the conditions of our study. Freundlich model, which is empirical, can be used for non-uniform surface adsorption. Sips model is a combination of Langmuir and Freundlich models. Toth model is a temperature dependent isotherm model which has six parameters. Freundlich, Sips and Toth models fit our experimental data well. However, they are empirical models; thus, the results could not provide insights to the behavior or be extrapolated beyond the range of the experiment conditions. Moreover, these models describe our experimental data only slightly better than the Langmuir model does, as illustrated in Fig. 3.4. The Langmuir model is useful for our study not only for describing the adsorption data but also for predicting adsorption capacity at other temperatures. In this work we use Langmuir model as the basis for discussion of the adsorption data.

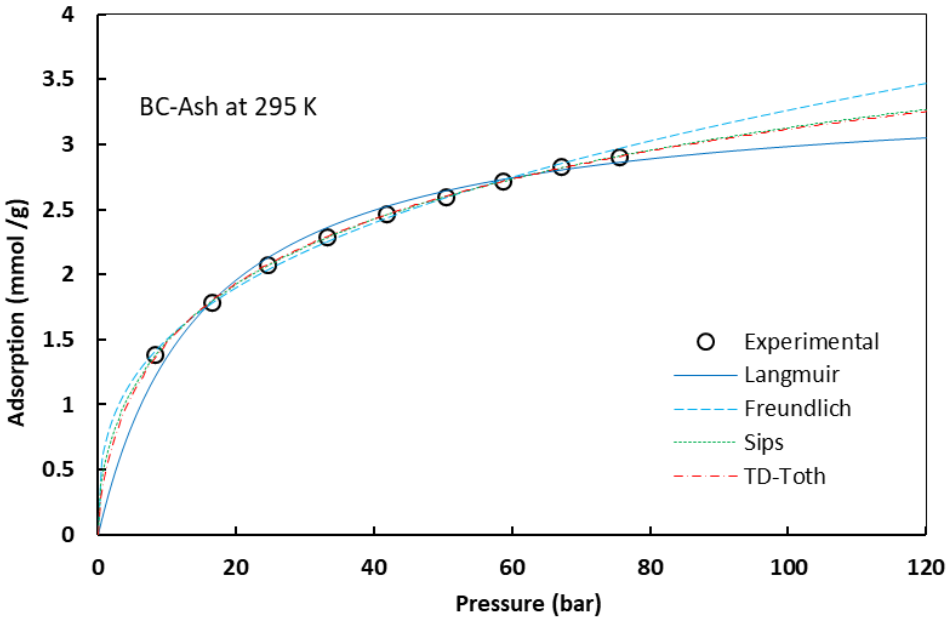

Fig. 3.4 CH_4 adsorption isotherms of 4 different models for biochar BC-Ash at 295 K

With the Langmuir model, the pressure dependence is given by

$$N = \frac{N_m BP}{1+BP} \tag{3.1}$$

where N is the amount of adsorbed gas molecules. P is gas pressure. N_m and B are Langmuir capacity and Langmuir constant, respectively, which are independent of gas pressure. The Langmuir constant B is regarded as an equilibrium constant, which depends on temperature in the following way [32]:

$$B = B_0 \exp\left(\frac{-\Delta H}{RT}\right) \tag{3.2}$$

where T is absolute temperature. B_0 is the value of B at a reference temperature. ΔH is the enthalpy change of gas molecules due to adsorption. R is the gas constant. For the temperature dependence of the Langmuir capacity N_m, the temperature dependence of Langmuir capacity N is treated differently in the literature. Some studies treat it as independent of temperature [32], whereas other studies treat it as dependent on temperature [33]. For BC-Ash, we have evaluated the two parameters assuming both temperature independence and temperature dependence for N_m, as shown by Figs. 3.5 and 3.6, respectively. As can be seen, with a temperature-dependent N_m, the Langmuir model describes better the adsorption behavior of CH_4 on the biochar. This can also be understood from inspection of the adsorption data. Eq. 3.1 can be rearranged into

$$P/N = 1/(N_m B) + P/N_m \tag{3.3}$$

If the Langmuir equation describes the adsorption data, a plot of P/N against p should yield a straight line. Such plots for the isotherms at the three temperatures are shown in Fig. 3.6. The plots

are approximately linear at all temperatures. However, their slopes suggest that N_m is not constant, but decreases with increasing temperature, according to Eq. 3.3.

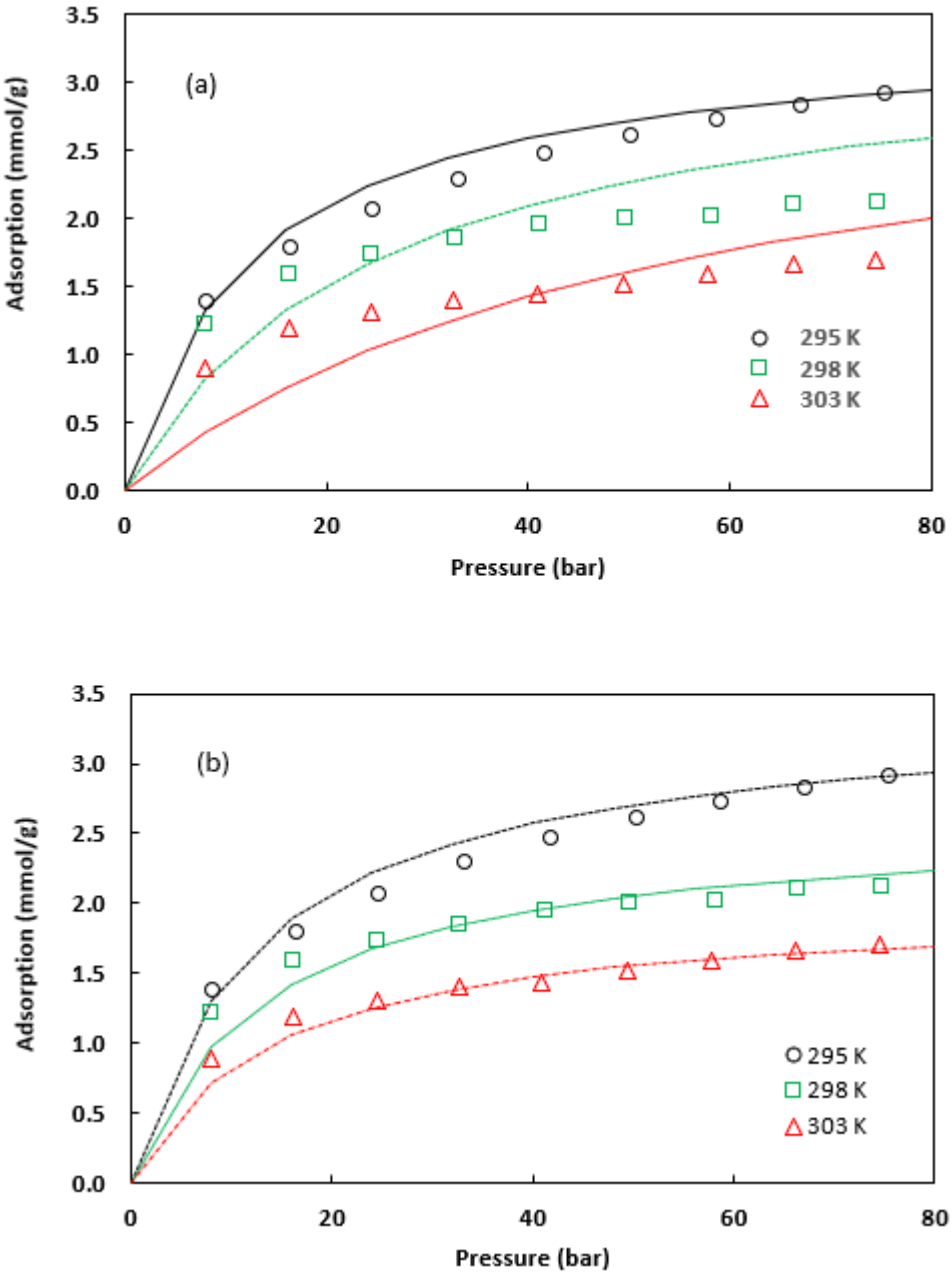

Fig. 3.5 Description of adsorption behavior by the Langmuir model for biochar BC-Ash at 295 K, 298 K, and 303 K, respectively. (**a**) with temperature-independent N_m; (**b**) with temperature-dependent N_m.

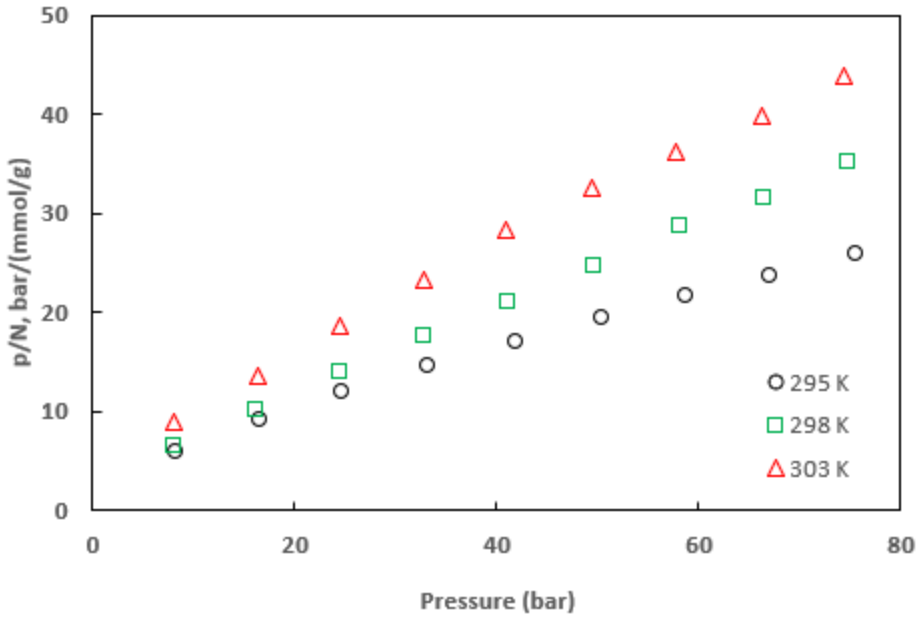

Fig. 3.6 Description of the adsorption behavior with temperature-dependent N_m for biochar BC-Ash at 295 K, 298 K and 303 K, respectively

Fig. 3.7 shows van't Hoff plots for Langmuir constant B with temperature-independent and temperature-dependent Langmuir capacity cases, respectively. The plots are approximately linear in both cases, which may be used for extrapolation for other temperatures.

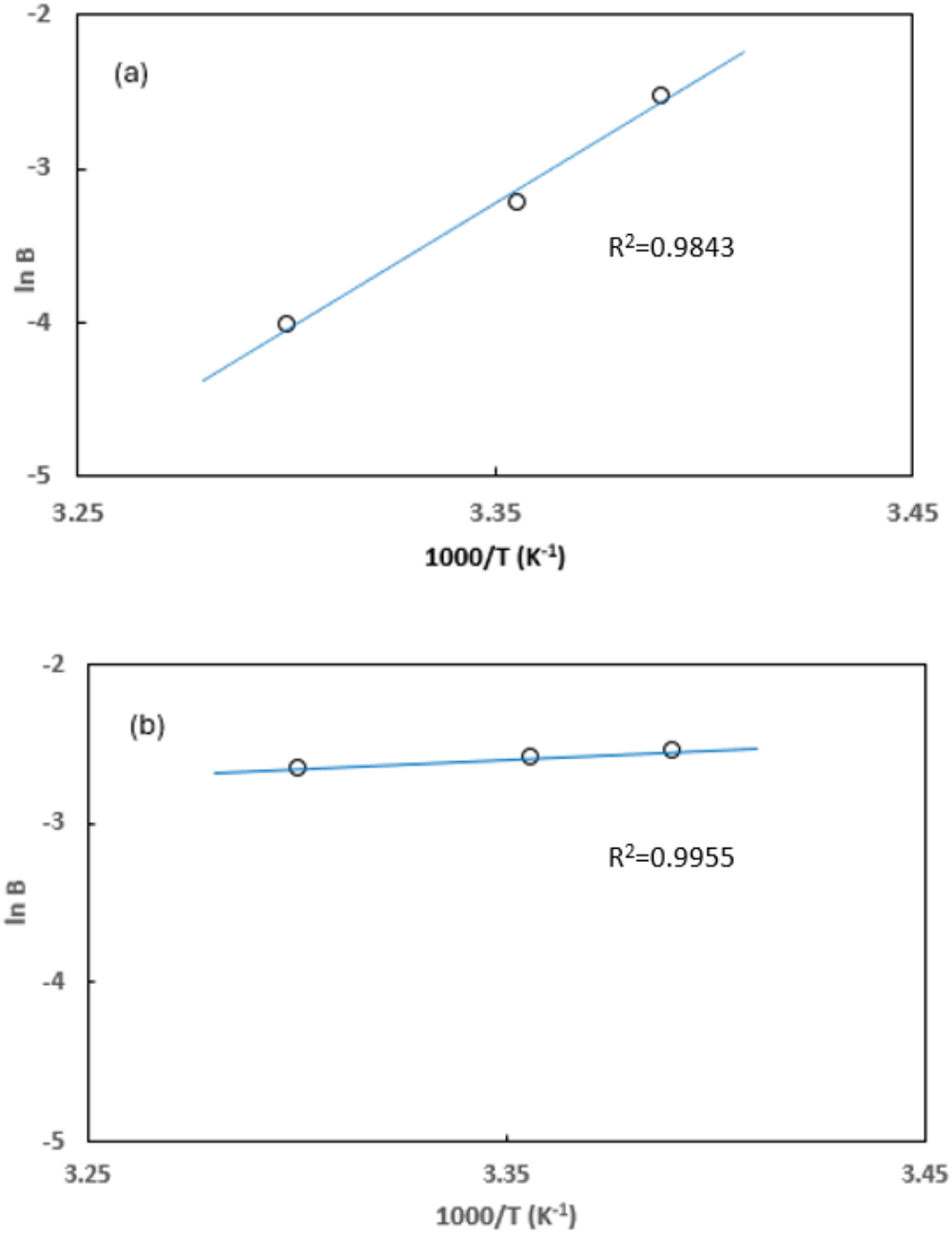

Fig. 3.7 Van't Hoff plots for *B* obtained from Fig. 3.5 for biochar BC-Ash. a with temperature-independent N_m; b with temperature-dependent N_m

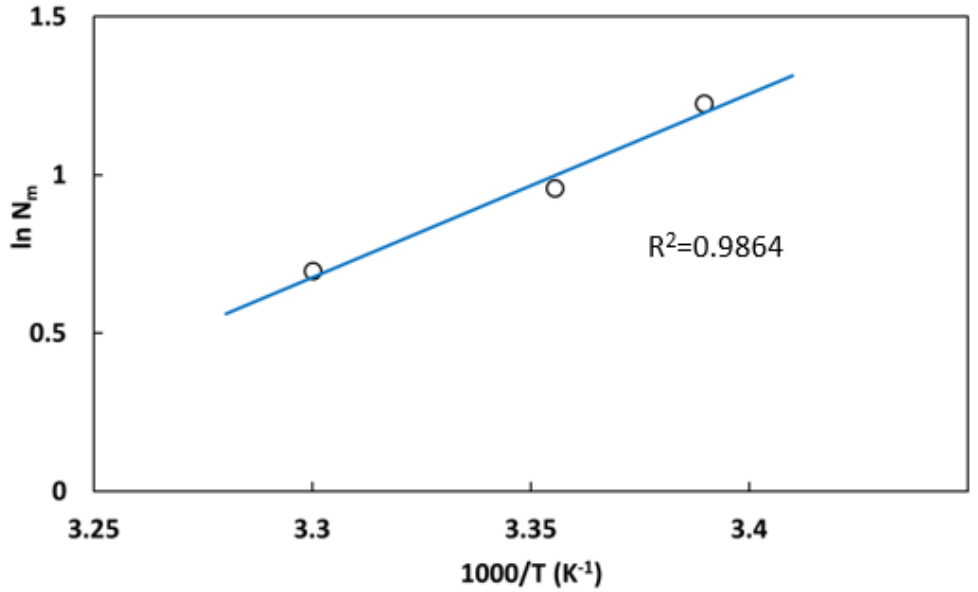

Fig. 3.8 Plot for Nm in terms of Eq. 3.5 ($\ln N_m = \ln N_{m0} + \chi/T$) for biochar BC-Ash

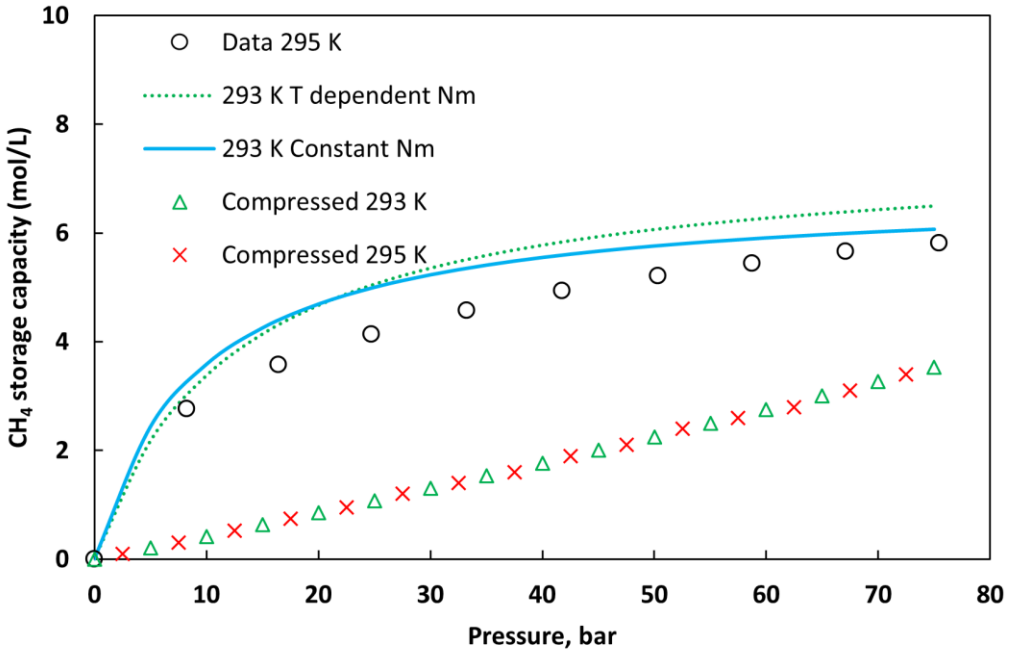

Fig. 3.9 Comparison of predicted storage capacity at 293 K for adsorbed CH_4 on Biochar BC-Ash and compressed CH_4. The open circle represents experimental data at 295 K. The two curves represent the prediction in terms of constant Langmuir capacity and temperature-dependent Langmuir capacity, respectively. The triangle and cross symbols near the bottom represent the molar density of compressed CH_4 at 293 K and 295 K, respectively.

The temperature dependence of N_m obtained from Fig. 3.5 may be expressed by

$$\mathrm{N_m} = \mathrm{N_{m0}} \exp\left(\chi/\mathrm{T}\right) \tag{3.4}$$

where N_{m0} is the N_m value at a reference temperature. χ is a parameter which is independent of temperature. This expression has also been used for Langmuir model by others for adsorption of CH_4 in shale [33].

Eq. 3.4 can be rearranged into

$$\ln\mathrm{N_m} = \ln\mathrm{N_{m0}} + \chi/\mathrm{T} \tag{3.5}$$

A plot for N_m in terms of Eq. 3.5 is shown in Fig. 3.8. This plot is approximately linear and may be used to estimate $N_m$values at other temperatures.

As an application of the above analyses of the temperature dependence, Fig. 3.9 shows predicted CH_4 adsorption capacity for BC-Ash at 293 K (20 °C) based on both temperature-independent and temperature-dependent Langmuir capacity, in comparison to the capacity of compressed CH_4. The two treatments yield somewhat different pressure dependencies. However, the important point is that in both cases an appreciable increase in the adsorption capacity is predicted as a result of a temperature decrease of a mere 2 degrees. By contrast, the change in the capacity of the compressed CH_4 by the same degrees of temperature change is hardly observable. If the temperature decreases to below 20 °C, which is quite possible for Canadian oil and gas fields, the storage capacity of biochar for CH_4 would be even higher than that of compressed gas.

3.3.2 Adsorption kinetics

The time dependence of CH_4 uptake is used to evaluate the rate of the adsorption process.

Pseudo-first-order model (Eq. 3.6 and 3.7) and pseudo-second-order model (Eq. 3.8 and 3.9) have been used for analyzing adsorption kinetics of other adsorbent-adsorbate systems [34–36]:

$$\frac{dQ_t}{dt} = k_1(Q_e - Q_t) \tag{3.6}$$

$$\ln(Q_e - Q_t) = \ln Q_e - k_1 t \tag{3.7}$$

$$\frac{dQ_t}{dt} = k(Q_e - Q_t)^2 \tag{3.8}$$

$$\frac{t}{Q_t} = \frac{1}{k_2 {Q_e}^2} + \frac{t}{Q_e} \tag{3.9}$$

where Q_t is the amount of adsorbate at time t on the adsorbent, and Q_e is the amount of adsorbate at equilibrium. The disadvantage of such models for CH_4 adsorption is that the degree of adsorption is not related to gas pressure. Moreover, the parameter C_e would depend on the pressure, with higher pressures giving higher Q_e values.

The Langmuir adsorption model, which we have used to describe adsorption equilibria, could also be used to study adsorption kinetics [37]. The Langmuir model is derived with the assumption of equilibrium between adsorption and the reverse process desorption:

$$k_a P(1 - \theta) = k_d \theta \tag{3.10}$$

where θ is the fraction of adsorption sites occupied by adsorbed molecules; k_a is the rate constant for adsorption; k_d is the rate constant for desorption; P is gas pressure.

Rearranging Eq. 3.10 into

$$\theta = \frac{k_a P}{k_a P + k_d} \tag{3.11}$$

leads to Eq. 3.1, the Langmuir equation,

$$N = \frac{N_m B P}{1 + B P} \tag{3.1}$$

where $N/N_m = \theta$ and $B = k_a/k_d$.

Eq. 3.10 can be expressed as

$$\frac{d\theta}{dt} = k_a P(1 - \theta) - k_d \theta \tag{3.12}$$

For constant CH_4 pressure P,

$$\frac{d\theta}{k_a P - (k_a P + k_d)\theta} = dt \tag{3.13}$$

$$\frac{d\ln[k_a P - (k_a P + k_d)\theta]}{[k_a P - (k_a P + k_d)\theta]} = -(k_a P + k_d)dt \tag{3.14}$$

$$\ln\frac{[k_aP-(k_aP+k_d)\theta]}{[k_aP-(k_aP+k_d)\theta_0]}=-(k_aP+k_d)(t-t_0) \tag{3.15}$$

where θ_0 is the initial value of θ.

From Eq. 3.15,

$$\theta=\frac{k_aP}{k_aP+k_d}\left[1-e^{-(k_aP+k_d)(t-t_0)}\right]+\theta_0 e^{-(k_aP+k_d)(t-t_0)}$$

$$=\frac{BP}{1+BP}\left[1-e^{-k_d(1+BP)(t-t_0)}\right]+\theta_0 e^{-k_d(1+BP)(t-t_0)} \tag{3.16}$$

$$N=\frac{N_mBP}{1+BP}\left[1-e^{-k_d(1+BP)(t-t_0)}\right]+N_0 e^{-k_d(1+BP)(t-t_0)} \tag{3.17}$$

where N_m is the Langmuir capacity and N_0 is the initial value of N. With a sufficiently long-time t, Eq. 3.17 becomes Eq. 3.1.

Unlike the pseudo-first and second order models, Eq. 3.17 explicitly relates the adsorption to pressure, and the parameters are independent of pressure.

Our sorption analyzer uses a computer program to determine adsorption as a function of time automatically. The pressure is increased stepwise and the adsorption is calculated from the pressure of the sample holder, which is connected to the reservoir. In principle, we could apply the equation to the real time data and evaluate the values of the parameters. However, there is a problem associated with the analyzer. Each step of pressure increase starts with a transient peak in pressure signal, as shown in Fig. 3.10. The corresponding adsorption reading generated by the computer program exhibits a negative peak shown in Fig. 3.10. Such values are clearly not true values of adsorption. Thus, the time evolution from the start of the pressure increase is not known.

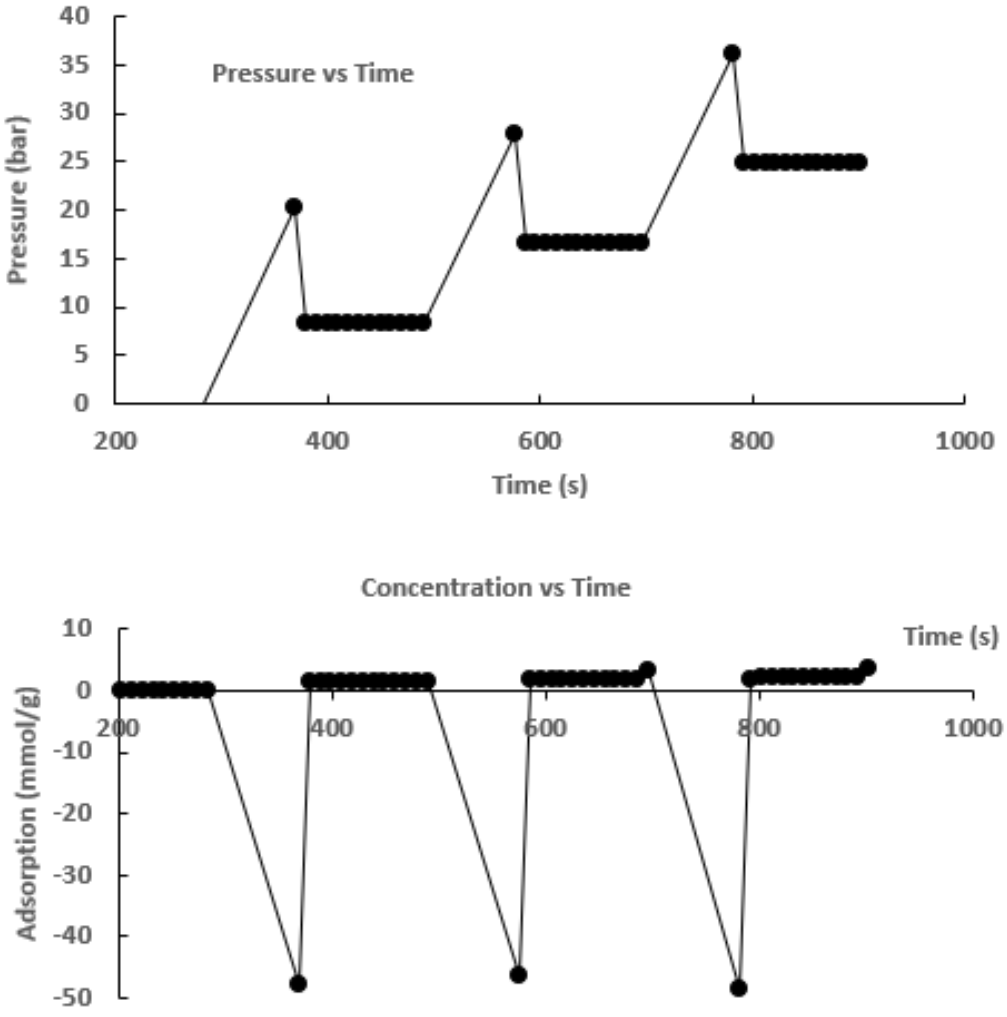

Fig. 3.10 Time evolution of pressure (upper) and adsorption (lower) during kinetic measurement for biochar BC-Ash

We can fit the equation to the data by adjusting the starting time t_0 and an example is shown in Fig. 3.11 for 16 bar. Whereas Eq. 3.17 can be seen to give a reasonable description of the data, the parameter values would not have high certainty. On the other hand, although it is difficult to study the kinetics from the data, the equilibrium adsorption values can be determined despite the transient peaks. Regarding the kinetics, our concern is whether the adsorption occurs too slowly. As the data reveal, the adsorption is quite fast and reaches equilibrium within two minutes. Thus, for the present biochar, the kinetic behavior is not as important as the adsorption capacity.

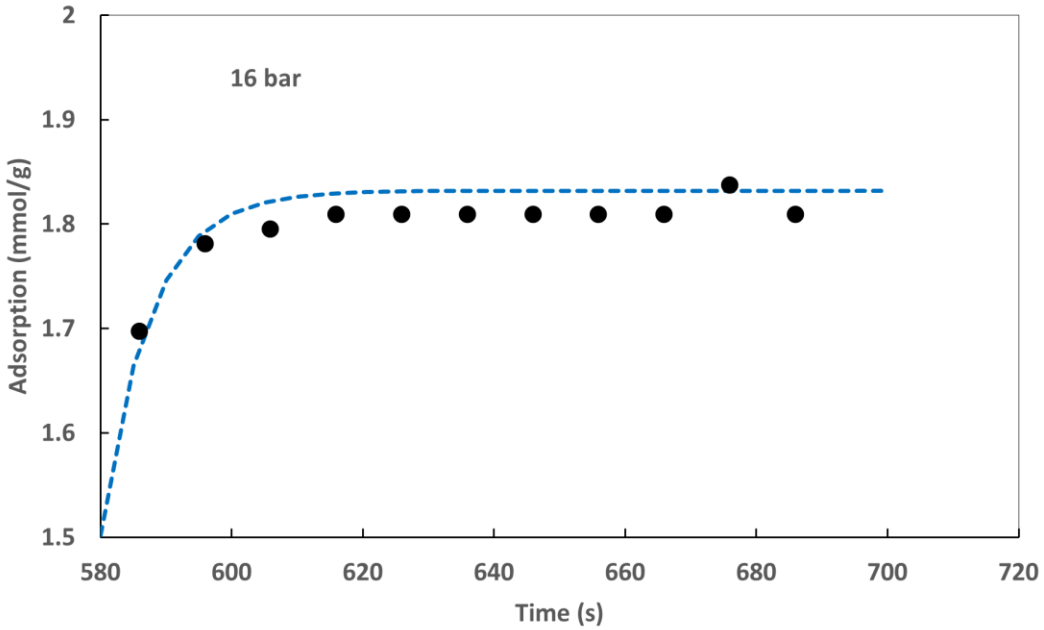

Fig. 3.11 Description of the time evolution of CH_4 adsorption for biochar BC-Ash at 16 bar in terms of the Langmuir model

3.4 Conclusions

Biochar from forestry wastes shows promise for capture and storage of CH_4 to contribute to the efforts in CH_4 emission reduction from oil and gas industry. In particular, biochar BC-Ash, which is a combustion ash residue, showed a reasonable adsorption capacity and rapid CH_4 take-up.

Although the adsorption capacity is more than 50% lower than that of activated carbon in the studied temperature range 295 - 303 K, it could increase faster with decreasing temperature. Moreover, the anticipated storage capacity in terms of volume can be higher than that of compressed CH_4 for the targeted pressure and temperature conditions in the oil and gas fields, suggesting significant cost advantages. This work aims to motivate further investigation into this topic and contribute to the mitigation of CH_4 emissions.

Acknowledgements

The authors are thankful to Ms. Maria Abbassi, Dr. Xianai Huang and Dr. Lia Kouchachvili of CanmetENERGY-Ottawa, Natural Resources Canada, who have provided biochar and activated carbon samples along with various advice.

Author contributions

All authors contributed to this work. All authors read and approved the final manuscript.

Funding

This work is supported by the Program of Energy Research Development of Canada.

Availability of data and materials All related data are included in this article or available upon request.

Declarations

Competing interests:

The authors have no competing interests to declare that are relevant to the content of this article.

References

[1] US EPA, Understanding Global Warming Potentials, US EPA (2016). https://www.epa.gov/ghgemissions/understanding-global-warming-potentials.

[2] Environmental Defense Fund, The Five Keys for Oil & Gas Companies to Establish Credible Methane Reduction Targets, Environmental Defense Fund (2020). https://www.edf.org/media/five-keys-oil-gas-companies-establish-credible-methane-reduction-targets.

[3] US department of commerce, Increase in atmospheric methane set another record during 2021 | National Oceanic and Atmospheric Administration, (n.d.). https://www.noaa.gov/news-release/increase-in-atmospheric-methane-set-another-record-during-2021.

[4] Environment and Climate Change Canada, Canada publishes progress report towards 2025 methane emissions reduction target and launches consultations on 2030 target, (2021). https://www.canada.ca/en/environment-climate-change/news/2021/12/canada-publishes-progress-report-towards-2025-methane-emissions-reduction-target-and-launches-consultations-on-2030-target.html.

[5] A. Schummer, Key points from Canada's plan to hit 2030 climate target, Reuters (2022). https://www.reuters.com/business/environment/key-points-canadas-plan-hit-2030-climate-target-2022-03-29.

[6] P. Forster, R. Venkatachalam, Changes in Atmospheric Constituents and in Radiative Forcing, Cambridge University Press, Cambridge, United Kingdom and New York, NY, USA Chapter 2 (2007).

[7] S. Alhasan, R. Carriveau, D. S.-K. Ting, A review of adsorbed natural gas storage technologies, International Journal of Environmental Studies 73 (2016) 343–356. https://doi.org/10.1080/00207233.2016.1165476.

[8] H. Bamdad, K. Hawboldt, S. MacQuarrie, A review on common adsorbents for acid gases removal: Focus on biochar, Renewable and Sustainable Energy Reviews 81 (2018) 1705–1720. https://doi.org/10.1016/j.rser.2017.05.261.

[9] P.D. Dissanayake, S. You, A.D. Igalavithana, Y. Xia, A. Bhatnagar, S. Gupta, H.W. Kua, S. Kim, J.-H. Kwon, D.C.W. Tsang, Y.S. Ok, Biochar-based adsorbents for carbon dioxide capture: A critical review, Renewable and Sustainable Energy Reviews 119 (2020) 109582. https://doi.org/10.1016/j.rser.2019.109582.

[10] H. La, J.P.A. Hettiaratchi, G. Achari, The influence of biochar and compost mixtures, water content, and gas flow rate, on the continuous adsorption of methane in a fixed bed column, Journal of Environmental Management 233 (2019) 175–183. https://doi.org/10.1016/j.jenvman.2018.12.015.

[11] S. Nanda, A.K. Dalai, F. Berruti, J.A. Kozinski, Biochar as an Exceptional Bioresource for Energy, Agronomy, Carbon Sequestration, Activated Carbon and Specialty Materials, Waste Biomass Valor 7 (2016) 201–235. https://doi.org/10.1007/s12649-015-9459-z.

[12] C. Zhang, G. Zeng, D. Huang, C. Lai, M. Chen, M. Cheng, W. Tang, L. Tang, H. Dong, B. Huang, X. Tan, R. Wang, Biochar for environmental management: Mitigating greenhouse gas emissions, contaminant treatment, and potential negative impacts, Chemical Engineering Journal 373 (2019) 902–922. https://doi.org/10.1016/j.cej.2019.05.139.

[13] R.C.B.N.R.A.-H.B. News, Flaring, or Why So Much Gas Is Going Up in Flames: QuickTake, (2019). https://news.bloomberglaw.com/environment-and-energy/flaring-or-why-so-much-gas-is-going-up-in-flames-quicktake-1.

[14] G.I.A. Inc, Global Industry Analysts Predicts the World Biochar Market to Reach $2 Billion by 2026, (n.d.). https://www.prnewswire.com/news-releases/global-industry-analysts-predicts-the-world-biochar-market-to-reach-2-billion-by-2026-301485134.html.

[15] B. Delgado, D. López González, S. Godbout, R. Lagacé, A. Giroir-Fendler, A. Avalos Ramirez, A study of torrefied cardboard characterization and applications: Composition, oxidation kinetics and methane adsorption, Science of The Total Environment 593–594 (2017) 406–417. https://doi.org/10.1016/j.scitotenv.2017.03.119.

[16] M. Dicko, M. Guilmont, F. Lamari, Adsorption and Biomass: Current Interconnections and Future Challenges, Curr Sustainable Renewable Energy Rep 5 (2018) 247–256. https://doi.org/10.1007/s40518-018-0116-6.

[17] G. Durán-Jiménez, E.T. Kostas, L.A. Stevens, W. Meredith, M. Erans, V. Hernández-Montoya, A. Buttress, C.N. Uguna, E. Binner, Green and simple approach for low-cost bioproducts preparation and CO_2 capture, Chemosphere 279 (2021) 130512. https://doi.org/10.1016/j.chemosphere.2021.130512.

[18] V. Gargiulo, A. Gomis-Berenguer, P. Giudicianni, C.O. Ania, R. Ragucci, M. Alfè, Assessing the Potential of Biochars Prepared by Steam-Assisted Slow Pyrolysis for CO_2 Adsorption and Separation, Energy Fuels 32 (2018) 10218–10227. https://doi.org/10.1021/acs.energyfuels.8b01058.

[19] G. Greco, R.L.S. Canevesi, C. Di Stasi, A. Celzard, V. Fierro, J.J. Manyà, Biomass-derived carbons physically activated in one or two steps for CH_4/CO_2 separation, Renewable Energy 191 (2022) 122–133. https://doi.org/10.1016/j.renene.2022.04.035.

[20] B.Y. Sadasivam, K.R. Reddy, Quantifying the Effects of Moisture Content on Transport and Adsorption of Methane through Biochar in Landfills, (2014) 191–200. https://doi.org/10.1061/9780784413432.020.

[21] B.Y. Sadasivam, K.R. Reddy, Adsorption and transport of methane in biochars derived from waste wood, Waste Management 43 (2015) 218–229. https://doi.org/10.1016/j.wasman.2015.04.025.

[22] B.Y. Sadasivam, K.R. Reddy, Adsorption and transport of methane in landfill cover soil amended with waste-wood biochars, Journal of Environmental Management 158 (2015) 11–23. https://doi.org/10.1016/j.jenvman.2015.04.032.

[23] B.Y. Sadasivam, K.R. Reddy, Influence of Physico-Chemical Properties of Different Biochars on Landfill Methane Adsorption, (2015) 2647–2656. https://doi.org/10.1061/9780784479087.246.

[24] A.N. Shafawi, A.R. Mohamed, P. Lahijani, M. Mohammadi, Recent advances in developing engineered biochar for CO_2 capture: An insight into the biochar modification approaches, Journal of Environmental Chemical Engineering 9 (2021) 106869. https://doi.org/10.1016/j.jece.2021.106869.

[25] K. Hu, H. Mischo, Absolute adsorption and adsorbed volume modeling for supercritical methane adsorption on shale, Adsorption 28 (2022) 27–39. https://doi.org/10.1007/s10450-021-00350-8.

[26] K. Mosher, J. He, Y. Liu, E. Rupp, J. Wilcox, Molecular simulation of methane adsorption in micro- and mesoporous carbons with applications to coal and gas shale systems, International Journal of Coal Geology 109–110 (2013) 36–44. https://doi.org/10.1016/j.coal.2013.01.001.

[27] M.M. Dubinin, V.A. Astakhov, Development of the concepts of volume filling of micropores in the adsorption of gases and vapors by microporous adsorbents, Russ Chem Bull 20 (1971) 8–12. https://doi.org/10.1007/BF00849308.

[28] K. Kaneko, K. Murata, An analytical method of micropore filling of a supercritical gas, Adsorption 3 (1997) 197–208. https://doi.org/10.1007/BF01650131.

[29] A. Malek, S. Farooq, Comparison of isotherm models for hydrocarbon adsorption on activated carbon, AIChE Journal 42 (1996) 3191–3201. https://doi.org/10.1002/aic.690421120.

[30] F. Zhu, J. Li, M. Zhu, L. Kang, Effect of Oxygen-Containing Group on the Catalytic Performance of Zn/C Catalyst for Acetylene Acetoxylation, Nanomaterials 11 (2021) 1174. https://doi.org/10.3390/nano11051174.

[31] K.V. Kumar, K. Preuss, M.-M. Titirici, F. Rodríguez-Reinoso, Nanoporous Materials for the Onboard Storage of Natural Gas, Chem. Rev. 117 (2017) 1796–1825. https://doi.org/10.1021/acs.chemrev.6b00505.

[32] D. M. Ruthven, Principles of adsorption & adsorption processes, John Wiley & Sons, 1984, xxiv + 433 pp - Helfferich - 1985 - AIChE Journal - Wiley Online Library, ISBN: 0471866067, ISBN: 9780471866060, OCLC: (OCoLC)9919072

[33] J. Fianu, J. Gholinezhad, M. Hassan, Comparison of Temperature-Dependent Gas Adsorption Models and Their Application to Shale Gas Reservoirs, Energy Fuels 32 (2018) 4763–4771. https://doi.org/10.1021/acs.energyfuels.8b00017.

[34] Y.S. Ho, G. McKay, A Comparison of Chemisorption Kinetic Models Applied to Pollutant Removal on Various Sorbents, Process Safety and Environmental Protection 76 (1998) 332–340. https://doi.org/10.1205/095758298529696.

[35] Y.S. Ho, G. McKay, Pseudo-second order model for sorption processes, Process Biochemistry 34 (1999) 451–465. https://doi.org/10.1016/S0032-9592(98)00112-5.

[36] H.M. Jang, S. Yoo, Y.-K. Choi, S. Park, E. Kan, Adsorption isotherm, kinetic modeling and mechanism of tetracycline on *Pinus taeda*-derived activated biochar, Bioresource Technology 259 (2018) 24–31. https://doi.org/10.1016/j.biortech.2018.03.013.

[37] J. Wang, D. Ryan, H. Samara, P. Jaeger, Interactions of CO_2 with Hydrocarbon Liquid Observed from Adsorption of CO_2 in Organic-Rich Shale, Energy Fuels 34 (2020) 14476–14482. https://doi.org/10.1021/acs.energyfuels.0c02774.

Chapter 4. Enhanced CH_4 adsorption through the development of ultramicropores in cold plasma-activated biochar[2]

Part of this chapter has been published in the *Chemical Engineering Journal*, 2025.

Graphic abstract:

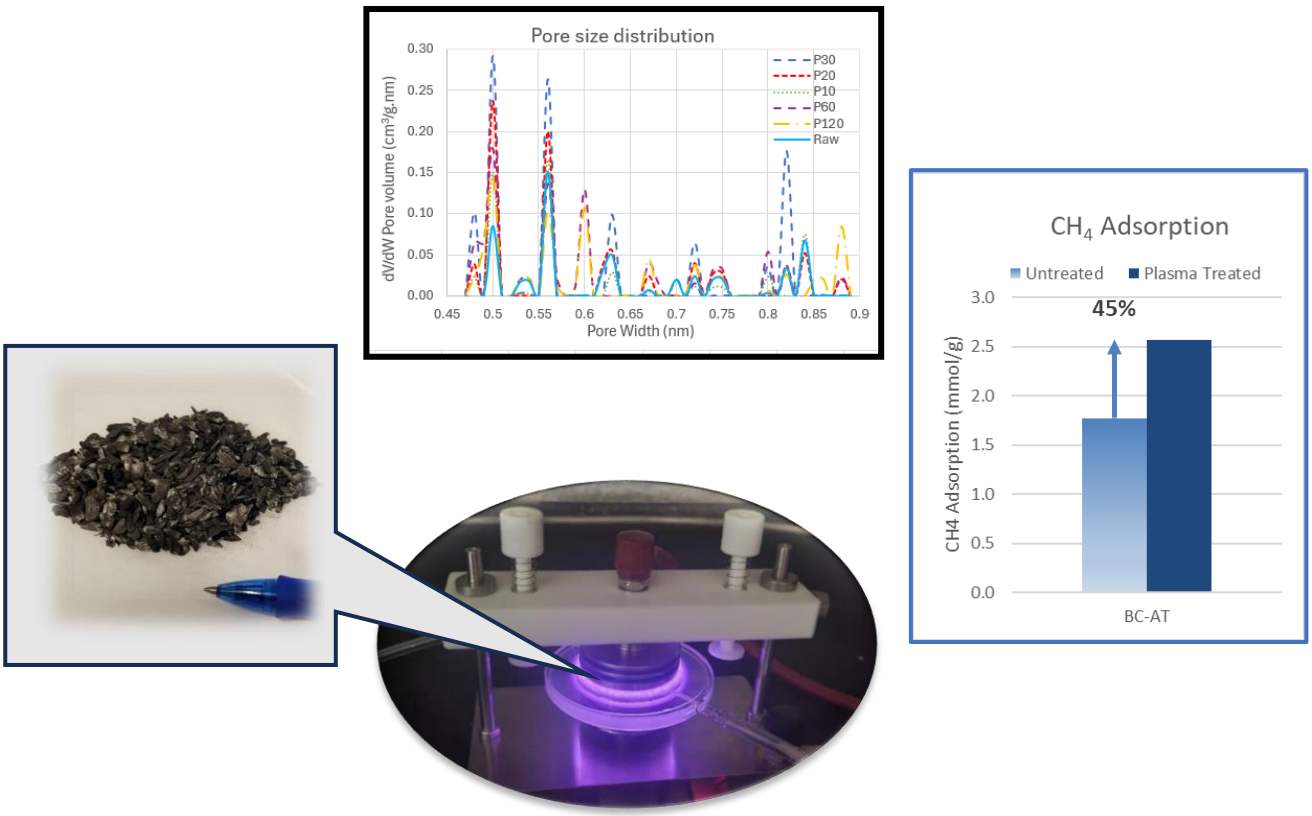

[2] V. Y. Ko, J. Wang, C. Lan, and D. Ryan, "Enhanced CH4 Adsorption Through the Development of Ultramicropores in Cold Plasma-Activated Biochar" *Chemical Engineering Journal* 524 (2025) 169286, https://doi.org/10.1016/j.cej.2025.169286.

Abstract

This study investigates methane (CH_4) adsorption on biochars activated by cold dielectric barrier discharge (DBD) plasma at pressures up to 75 bar, targeting waste natural gas recovery in oil and gas fields. A commercial biochar was treated with argon plasma at 500 ml/min for various durations, achieving up to a 45% improvement in CH_4 adsorption capacity. Characterization using Brunauer–Emmett–Teller (BET) CO_2/N_2 physisorption, scanning electron microscopy (SEM), attenuated total reflectance Fourier-transform infrared spectroscopy (ATR-FTIR), pH, and zeta potential analysis revealed that CH_4 adsorption capacity increased almost linearly with plasma treatment up to 30 minutes. This enhancement was associated with growth in specific surface area, formation of ultramicropores (≤0.68 nm), and surface impurity removal, as evidenced by elevated pH and zeta potential, along with FTIR-confirmed reductions in C-H, O-H, C-O, C-N, and C=O groups, which likely increased biochar hydrophobicity and promoted CH_4 uptake. Beyond 30 minutes, extended treatment reduced specific surface area and surface concentration of CH_4 (γ) due to pore enlargement and coalescence, diminishing adsorption sites, while pH and zeta potential stabilized, suggesting that over-treatment mainly affects pore structure rather than surface chemistry.

Keywords:

methane (CH_4) adsorption; natural gas storage; oil and gas industry; biochar; cold plasma; ultramicropores

Highlights:

- Cold plasma treatment enhanced CH_4 adsorption by increasing the specific surface area of biochars.
- Formation of ultramicropores (0.47–0.68 nm) contributed to the enhanced CH_4 adsorption.
- Removal of inorganic and organic impurities from pores and surfaces increased accessible adsorption sites.
- Excessive plasma treatment (>30 min) caused partial pore collapse and reduced CH_4 adsorption capacity.

4.1 Introduction

Methane (CH_4) is a clean energy source but also a powerful greenhouse gas [1,2]. While it has a shorter lifespan in the atmosphere than carbon dioxide, CH_4 is over 28 times more effective at trapping heat [3,4]. Reducing CH_4 emissions could significantly impact atmospheric warming [5,6]. Natural gases are typically produced from gas fields. There are nonetheless large volumes of natural gases produced alongside crude oil, which are referred to as associated gases. Despite the large volume of associated gases, their volumes are usually not large enough to justify the construction of pipelines for delivery to markets, especially from remote oil fields. They are therefore often vented or flared during oil extractions, due to potential explosion hazards owing to their explosive nature and potent GHG effect [7]. However, this is a waste of precious energy [8–10]. If a cost-effective approach for on-site storage of CH_4 is available, the associated gases can be utilized for on-site heat and power generation.

Conventional storage technologies such as compressed natural gas (CNG) and liquefied natural gas (LNG) are widely deployed for commercial natural gas products but face notable technical and economic limitations. CNG requires high pressures (200-300 bar), which demands costly heavy cylindrical tanks, considerable energy input for compression (~0.25 kWh/kg), and raises safety concerns [11–13]. LNG depends on cryogenic storage at -162 °C requiring the use of expensive vacuum-insulated tanks and costly liquefaction processes [14,15]. Adsorbed Natural Gas (ANG), on the other hand, offers a promising alternative by employing porous adsorbents such as activated carbons, metal organic frameworks (MOFs), and advanced polymers to achieve high CH_4 uptake at moderate pressures (35-50 bar) and ambient temperatures. ANG systems can reach storage capacities of ~267 cm^3 gas /cm^3 adsorbent (at STP) [16], approaching or even surpassing those of CNG at much higher pressures, i.e., ~230-250 V/V at 250 bar [17], while avoiding the cryogenic requirements of LNG (~600 V/V at -162 °C) [18,19]. The performance of ANG systems depends critically on the choice of adsorbent, which must balance capacity, scalability, and cost [20].

The associated natural gas, which is produced alongside crude oil, is separated at surface facilities where operational pressures generally range from 100 to 1,000 psi (7-70 bar), depending on the separator design and field conditions. In high-pressure offshore operations, first-stage separators may operate at pressures up to 124 bar. Subsequent processing stages and pipeline transportation often involve pressure reductions to levels between 7 and 35 bar to meet downstream requirements [21,22]. Since ANG operates at moderate pressures of 35 bar or less and ambient temperatures, we can use lightweight and inexpensive conformable tanks with negligible compression energy, which is also convenient and safe to handle compared to the high-pressure CNG and cryogenic LNG systems.

Activated carbon has been extensively studied for CH_4 adsorption in vehicle applications [23,24]. However, its potential for on-site utilization of associated gases has received little attention. While vehicle applications are volume sensitive and demand a high degree of compactness and therefore large adsorption capacities, the potential applications in oil and gas fields requires large quantities of adsorbents and is therefore sensitive to adsorbent cost while being able to afford relatively large footprints. To this end, biochar presents itself as a competitive alternative adsorbent for ANG for on-site associated gas applications. On-site storage and utilization of associated gases in oil fields benefit from the extensive space available for adsorbent storage, a key advantage over space-constrained vehicle applications. Despite the biochar's lower adsorption capacity compared to the activated carbon, a significantly lower cost and a renewable nature of biochar enhance its feasibility for its large-scale oil field deployment, where space constraints are minimal.

Biochar is a carbon-rich material produced by pyrolyzing organic materials, such as plant or animal waste [25,26]. Compared to activated carbon ($1.20–$6.40/kg), biochar is more cost-effective at $0.8–$1.6/kg, with a lower environmental impact-global warming potential (GWP) of 1.53 kg CO_2 eq/kg and cumulative energy demand of 20.3 MJ/kg versus 8.6–18.28 kg CO_2 eq/kg and 119.5 MJ/kg for activated carbon [27]. Furthermore, its production from abundant forestry and agricultural waste aligns with sustainability goals [28]. Although biochar's CH_4 adsorption capacity may be lower than that of other adsorbents such as activated carbon and therefore require larger volumes for the same storage capacities, its low-cost and environmental friendliness can outweigh this drawback in the oil and gas field application, where space is of lesser concern. Additionally, the used biochar can then be repurposed for combustion, enhancing its overall value proposition.

Earlier studies examined biochar's CH_4 adsorption capabilities [29,30] with many of them focused on its potential for mitigating greenhouse gas emissions [31,32] from landfills [33,34], and soil [35]. These applications, however, typically operate under atmospheric pressure, which differs significantly from the high-pressure conditions required for capturing and storing associated gases in oil fields.

Our previous study [36] demonstrated that, at the same pressure of 75 bar and temperature of 25 °C, biochar can store 1.4 times more CH_4 per unit volume (mol/l) than the compressed CH_4, highlighting its potential as an efficient storage medium for oil and gas field applications. However, our results also showed that the CH_4 adsorption capacities of biochars were generally lower than those of activated carbons, hypothetically due to their less developed pore structures and smaller surface areas. It is therefore of great theoretical and practical interest to identify surface treatments capable of improving biochar CH_4 adsorption capacity and their underlying mechanisms.

The known modification processes typically involve development of the porous structure further refined through activation. Conventional activation methods such as physical activation with steam or chemical activation with KOH are effective but often involve high temperatures, corrosive chemicals, and produce environmentally harmful byproducts [37–39]. In recent years, cold plasma treatment has become increasingly popular for modifying the surface of carbon materials [40–42], as it effectively creates the desired physical and chemical alterations without altering the material's bulk properties and avoids using solvents or introducing chemical contaminants [43–45]. Cold plasma treatments can further enhance biochar's performance by increasing micropore volume, etching microstructures, and introducing functional groups, thereby improving adsorption capacities for CH_4 [46–48].

Cold plasma, also referred to as non-thermal or non-equilibrium plasma, is a partially ionized gas in which the electrons reach temperatures around 10,000 K while the bulk gas remains near ambient temperature [49,50]. This property allows plasma to selectively modify surface functionalities for a variety of different applications without compromising the structural integrity of the bulk material [40,50–52]. Cold plasma can be generated through various methods, including radio frequency [53,54], microwave [55], and Dielectric Barrier Discharge (DBD) excitation [56,57]. DBD is generated by applying high voltage between two electrodes separated by a dielectric barrier and a small gap, filled with gas at atmospheric pressure [58]. DBD plasmas find applications in various fields including ozone generation and surface treatment [59,60].

Recent studies show that cold plasma could modify biochar surfaces, leading to 40% higher adsorption capacities for Pb^{2+} as a model metal pollutant and faster adsorption kinetics [61]. In another research, cold oxygen plasma treatment on vinasse biochar for 3 minutes maximized specific surface area to 307 m^2/g, achieving Pb (II) adsorption capacity of 714 mg/g through improved pore accessibility [62].

In this research we investigated the potential of cold plasma treatment to modify biochar surfaces aimed at enhancing their CH_4 adsorption capacity. The study focused on the effects of plasma exposure time (plasma treatment duration) on the biochar's CH_4 adsorption capacity and the underlying mechanisms. To the best of our knowledge, this is the first study to apply DBD plasma for biochar treatment specifically aimed at improving CH_4 adsorption, and the first to provide an in-depth investigation of the role of nanopores generated by the cold plasma treatment in the enhancement of the biochar surface adsorption capacity.

4.2 Materials and methods

4.2.1 Materials

A commercial biochar from AirTerra Inc., derived from beetle-infested pinewood waste, was used as an adsorbent in this study. The sample underwent drying at 120 °C under vacuum prior to experimentation. Physical properties were measured to characterize the raw materials prior to plasma treatment. Particle size (1.18–3.36 mm) was defined by sieve mesh size. Skeletal density was obtained using a helium pycnometer (Accupyc II 1340, Micromeritics), while bulk density (g/ml) was measured using a 5 ml sample reservoir.

The argon gas (99.999 vol% purity) was provided by Air Liquide Ltd. (Ottawa, Canada).

4.2.2 Plasma treatment

A parallel plate-type Dielectric Barrier Discharge plasma reactor (CTP-2000K, ACS Material LLC) was employed to irradiate the biochar adsorbents. As illustrated in Fig. 4.1a and 4.1b, the high voltage power supply generated a high voltage sine wave, leading to the ionization of gas within the DBD reactor, resulting in the formation of cold plasma. To measure the applied voltage amplitude, frequency, and current, an oscilloscope probe was connected to the test port. The DBD reactor consisted of two quartz glass discs with an inner diameter of 90 mm and a thickness of 1 mm. An 8 mm gap is present between two such discs. Plasma generation occurred at a discharge voltage of 9–12 kV and a frequency of 9 kHz produced by a step-up voltage transformer and a variable voltage controller. The power consumption of the reactor was approximately 200 W, as measured by an oscilloscope (Tektronix TBS1102C-NEW) and a passive high-voltage probe (P6015A-NEW). The Ar gas flow rate was set at 500 ml/min.

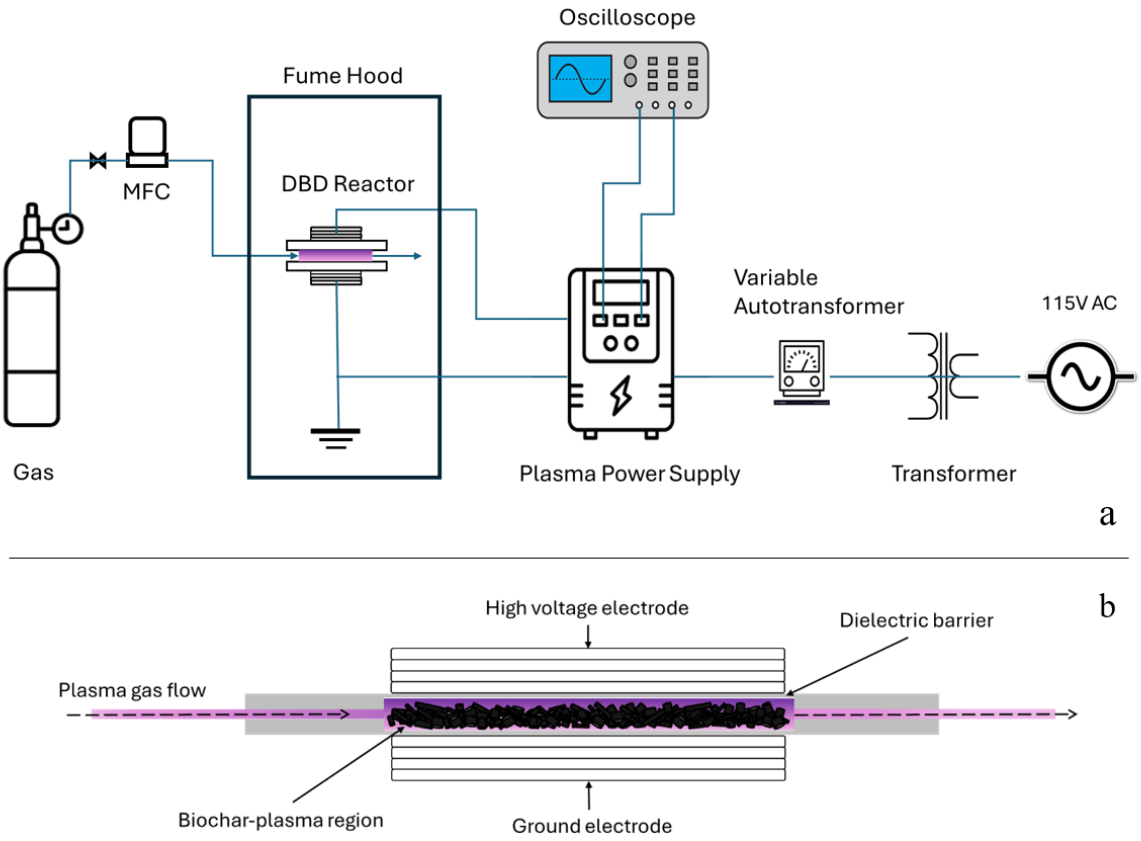

Fig. 4.1 Schematic diagram of the dielectric barrier discharge experimental device for biochar modification (a) and the dielectric barrier discharge reactor (b)

The experiment was conducted in the fume hood to prevent exposure to toxic gases such as O_3 and NO, which could be generated during plasma reactions with residual atmospheric gases. A 2.8-3.4 g sample was loaded into the reactor, which had an internal volume of 51 mL, for surface modification (see Fig. 4.1b). Prior to the test, the loaded reactor was purged for 5 minutes with the plasma gas Ar to remove air. Once the discharge stabilized, the plasma discharge voltage and current frequency were fine-tuned to 11 kV and 8.2 kHz, respectively and the samples underwent treatment for different durations of 10, 20, 30, 60, and 120 minutes (the corresponding samples were designated as Raw, P10, P20, P30, P60, and P120, respectively).

4.2.3 CH_4 adsorption experiments

A volumetric gas adsorption method was used to determine adsorption capacities, employing a commercial sorption Sievert-type analyzer PCT-Pro, by Setaram Inc. CH_4 was delivered to a 5 mL reactor in predefined pressure increments up to 75 bar, and adsorption experiments were carried out at a controlled temperature of 25 ± 0.5 °C. The basic principle of the instrument is illustrated in Fig. 4.2.

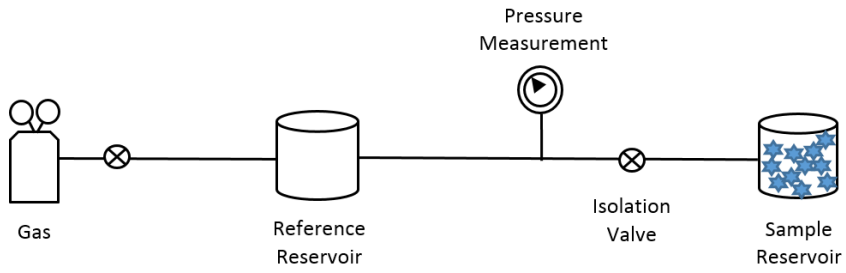

Fig. 4.2 A schematic of the Sievert measurement system

The sample reservoir's free volume was calibrated using helium at the experimental temperature for each adsorbent sample. Subsequently, CH_4 was pressurized in the reference reservoir and released into the sample reservoir, where adsorption took place. The amount of CH_4 adsorbed is determined by calculating the difference between the equilibrium pressure before and after gas injection into the sample reservoir. The molar amount of gas admitted into the reference reservoir and the molar amount of gas remaining at adsorption equilibrium were determined by applying pressure-volume-temperature relations, using non-ideal gas equations within the computer program. The computer program calculated the difference in adsorptions at each pressure step.

The Langmuir isotherm model was used to analyze the adsorption isotherms and to determine the adsorption capacities of different adsorbents [63].

$$N = \frac{N_m * BP}{1 + BP} \quad (4.1)$$

N (mmol/g) represents the amount of adsorbed gas molecules, p (bar) is the gas pressure, and N_m (mmol/g) and B (bar $^{-1}$) are the adsorption capacity and Langmuir constant, respectively. These parameters are independent of gas pressure. The Langmuir constant is considered an equilibrium constant, which is determined by the affinity of CH_4 to the surface of biochars at a given temperature.

4.2.4 Plasma treatment effectiveness (η) and surface concentration of CH_4 (γ)

To characterise the effects of plasma treatment on the biochar properties including its CH_4 adsorption, we introduced two parameters: plasma effectiveness (η) and surface concentration of CH_4 (γ). Plasma effectiveness (%) was defined as the percentage change of CH_4 adsorption capacity of biochar before and after the plasma treatment of a certain duration and the surface concentration of CH_4 (mmol/m^2) was defined as the maximum mass of CH_4 adsorbed by unit surface area of biochar.

The CH_4 plasma treatment effectiveness was calculated by the following equation,

$$\eta\ (\%) = \frac{A - A_0}{A_0} * 100 \quad (4.2)$$

where η is the plasma treatment effectiveness (%), A (mmol/g) is the CH_4 adsorption capacity of plasma-treated biochar (mmol/g), and A_o is that of the untreated (raw) biochar.

The surface concentration of CH_4 (γ) on untreated or treated biochar samples was calculated by the following equation,

$$\gamma = \frac{\mathrm{CH_4\ Adsorption\ capacity}\ \left(\frac{\mathrm{mmol}}{\mathrm{g}}\right)}{\mathrm{Specific\ surface\ area}\left(\frac{\mathrm{m^2}}{\mathrm{g}}\right)} * 1000 \quad (4.3)$$

where the specific surface area (m^2/g) is the surface area per unit mass biochar sample.

4.2.5 Pore structure and size distribution

The specific surface area, pore volume, and average pore width of each biochar sample were determined using CO_2 adsorption at 273 K with a Brunauer–Emmett–Teller (BET) apparatus (ASAP2020 V3.00G, Micromeritics, USA). Prior to BET analysis, all samples (0.2–0.3 g) were degassed under vacuum at 300 °C for 10 hours to remove residual moisture and gases confined within micropores.

N_2 is commonly used for BET analysis but cannot effectively access nanoscale pores at 77 K due to kinetic limitations [64–66]. To address this limitation, CO_2 was selected due to its smaller kinetic diameter, higher diffusivity, and ability to access nanopores [67–70]. CO_2 adsorption measurements were conducted at 273 K within a relative pressure range of P/P_0 = 0.001–0.03, where P is the equilibrium pressure of CO_2 and P_0 is the saturation vapor pressure. The improved diffusion of CO_2 operating at a higher temperature (273 K) enhanced the accuracy of surface area, pore volume, and average pore width measurements (<2 nm) [71–74]. These characteristics enable more accurate characterization of nanoscale pores (<1 nm), which are of particular interest in this study.

Pore structure analysis focused on the nanoscale region. The Horváth–Kawazoe (H-K) model [75] was applied to the CO_2 isotherms to estimate the median pore width and maximum pore volume for pores <1 nm. For sub-nanopore surface area estimation (0.47-0.87 nm), the Dubinin–Astakhov (D-A) model was employed. The D-A model [76] was selected for its suitability in describing

heterogeneous microporous materials and its greater accuracy compared to conventional Langmuir and BET approaches [77–80].

To resolve the pore size distributions (PSDs) in the 0.47–0.87 nm range, Grand Canonical Monte Carlo (GCMC) simulations were employed, while pores larger than 1.0 nm were analyzed using non-local density functional theory (NLDFT), all implemented through the MicroActive v7 software package (Micromeritics Ltd.). The built-in GCMC model [81–83] provided detailed characterization by fitting experimental isotherms through least-squares regression, minimizing deviations between observed and theoretical data. NLDFT is widely recognized as a reliable method for analyzing gas adsorption in heterogeneous porous materials, as it accounts for fluid–solid and fluid–fluid interactions at the molecular level, providing more accurate PSDs compared to classical methods such as Barrett- Joyner-Halenda (BJH) method [84,85]. This approach offers a more accurate representation of adsorption behavior across a range of pore sizes.

4.2.6 Scanning electron microscopy (SEM) analysis

Scanning electron microscopy (SEM) using a Hitachi 2500S (USA) and a Gemini500 SEM was employed to investigate surface morphology of biochar specimens. Samples were mounted on conductive adhesive for analysis. Initial observations were conducted with the Hitachi 2500S microscope at 1,000x magnification utilizing a secondary electron detector, a 10 mm working distance, and a 20 kV accelerating voltage. To identify nanoscale pores and achieve enhanced resolution, the Gemini500 SEM was operated at higher magnifications of 100,000x and 150,000x, with an accelerating voltage of 8 kV.

4.2.7 pH measurement

pH measurements were conducted on adsorbent samples before and after plasma treatment to assess chemical changes, particularly shifts in acidity or alkalinity in water, which indicate modifications to surface chemistry, such as the introduction or alteration of functional groups (e.g., carboxyl, hydroxyl, or carbonyl groups). These measurements serve as an indirect indicator of surface functional group modifications induced by plasma treatment. 0.02 g of the sampled biochar material was ground to a particle size of less than 250 μm and suspended in 20 mL of deionized (DI) water, achieving a static point, then the result was reported. A pH/electrochemistry meter from Thermo Fisher Scientific company (model: Orion Star) was used for the pH measurements. The pH readings were considered stable when they did not change more than 0.1 units over 1 minute. All pH measurements were performed in duplicate.

4.2.8 Zeta potential analysis

Electrokinetic potential was measured to find if plasma activation brings any differences in electrical charge. Zeta potentials are often used as an important parameter in analyzing the electrostatic surface interaction in adsorption [86]. In this study, it brings detailed insight into the causes of diffusion, and the affinity of CH_4 adsorption. To estimate the zeta potential, 0.01 g of each biochar sample was ground into powder (< 250 μm) and suspended in 10 mL of deionized (DI) water. The suspension was sonicated for 12 hours to ensure uniform dispersion, and then the samples were taken from the supernatants and used for zeta potential analysis. Prior to zeta potential measurement, the pH value of the sample in each of the vials was adjusted to 6.7 with 0.001 M HCl, and no background electrolyte was added to the sample. A zeta potential analyzer (Malvern Panalytical, UK) was used in the study. Triplicate measurements were recorded for accuracy.

4.2.9 Attenuated total reflectance (ATR) Fourier transform infrared spectroscopy (FTIR) analysis

Attenuated Total Reflectance Fourier Transform Infrared (ATR-FTIR) spectroscopy was utilized to reveal changes in the chemical and molecular properties of biochars induced by plasma treatment as a function of exposure time, and identify salts, oxides, or by-products generated during plasma activation. A benchtop single-reflection ATR (Cary 630 FTIR spectrometer, Agilent, USA) was used in the study. Samples were prepared by crushing and grinding biochar to a 60-mesh size (approximately 250 μm) using a mortar and pestle to ensure uniform particle size and effective contact with the ATR crystal (Internal Reflection Element, IRE). Diamond, a commonly used IRE with a refractive index of approximately 2.4, was initially used but introduced spectral interference due to its optical similarity to biochar. To address this, Germanium (Ge), with a higher refractive index of about 4.0, was selected to enhance spectral contrast and minimize optical overlap. The FTIR spectra were acquired across a wavenumber range of 4,000 to 650 cm^{-1} in the mid-infrared region, enabling the detection of characteristic vibrational modes of the biochar samples.

4.2.10 Plasma effluent gas analysis

Gas-phase products exiting the DBD reactor during plasma exposure of biochar samples were collected at three-time points: at the beginning, in the middle, and at the end of the run using a gas sampling bag. The collected gases were then analyzed using a refinery gas analyzer (RGA-FID/TCD) equipped with both flame ionization and thermal conductivity detectors on an Agilent 7890 GC system (Agilent Technologies).

4.3 Results and Discussions

4.3.1 Physicochemical properties of raw biochar

Table 4.1 presents the physical properties of the raw biochar (BC-AT), and Table 4.2 summarizes its proximate and ultimate analyses.

Table 4.1 Properties of raw biochar (BC-AT)

Sample	**BC-AT**
Specific Surface Area (m^2/g)	319
Maximum Pore volume	0.085
Average Pore width (nm)	0.62
Particle Size (mm)	1.18 - 3.36
Bulk Density (g/ml)	0.16
Skeletal Density (g/ml)	1.73

Table 4.2 Proximate and ultimate analyses of raw biochar (BC-AT) (wt%)

Proximate analysis				**Ultimate analysis**				
Moisture	Ash	Volatile Matter	Fixed Carbon	C	H	N	S	O
8.52	4.56	11.38	75.54	82.1	1.33	0.44	<0.05	3.38

BC-AT has a specific surface area of 319 m^2/g, an average pore width of 0.62 nm, and a pore volume of 0.085 cm^3/g (Table 4.1), confirming a microporous structure. Proximate and ultimate analyses (Table 4.2) show low ash (4.56 wt%) and moisture (8.52 wt%), high fixed carbon (75.54

wt%) and carbon content (82.1 wt%), and minor elements (H 1.33 wt%, N 0.44 wt%, S <0.05 wt%, O 3.38 wt%), indicating a carbon-rich, largely hydrophobic material.

4.3.2 CH_4 adsorption capacity before and after plasma treatment

Fig. 4.3 illustrates the CH_4 adsorption isotherms for the raw biochar and plasma-treated samples (labeled as P10, P20, P30, P60, and P120) measured at room temperature over a pressure range of 0 to 75 bar. All isotherms exhibit a Type I behavior according to the IUPAC classification [65], characterized by a steep initial uptake at low pressures followed by a gradual approach to saturation at higher pressures, indicative of microporous adsorbents where monolayer adsorption predominates. As shown in Table 4.3, the square of the regression coefficient (R^2) for the fitting of experimental isothermal data with the Langmuir model was all between 0.9958 and 0.9997, further confirm that the adsorption was indeed predominantly monolayer. It should be noted that the raw biochar displays the lowest adsorption capacity, and the plasma treatment enhanced the CH_4 uptake across all samples, with the capacities increasing in the order of Raw < P10 < P20 ~ P120 < P60 < P30 at 75 bar. The P30 sample achieves the highest adsorption capacity, representing a 45 % improvement over the raw biochar.

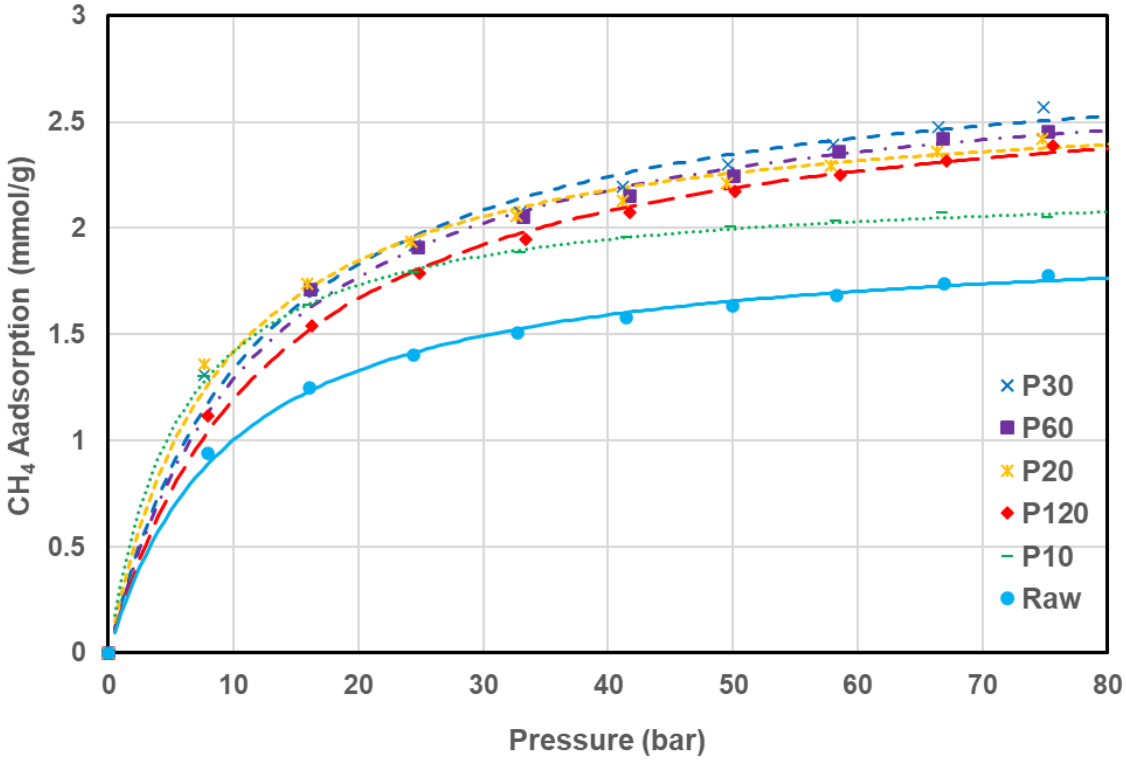

Fig. 4.3 CH_4 adsorption isotherms (Langmuir model) for biochar samples before (Raw) and after plasma treatment (P10, P20, P30, P60, and P120)

Table 4.3 Langmuir adsorption isotherm parameters of CH_4

	Raw	P10	P20	P30	P60	P120
R^2	0.9991	0.9997	0.9980	0.9958	0.9981	0.9986
N_m (mmol/g)	1.9794	2.2227	2.6553	2.8952	2.8289	2.7655
B (bar^{-1})	0.1026	0.1765	0.1141	0.0859	0.0836	0.0760

4.3.3 Effect of plasma treatment on surface area and CH_4 adsorption

Fig. 4.4 demonstrates the dependence of the CH_4 adsorption capacity on the specific surface area of the raw biochar and those subjected to different durations of plasma treatments. Plasma treatment appears to increase both the specific surface area and CH_4 adsorption compared to the untreated sample. While linear relationships were established between the specific surface area and the adsorption capacity of all the biochars with different plasma treatment durations, the data form two distinct groups according to the slope of the linear curves. The first group (blue squares),

consisting of Raw, P10, and P20 (0, 10, and 20 minutes), shows a linear increase in adsorption with a slope of 0.0054 mmol/m². The second group (orange triangles), including P30, P60, and P120 (30, 60, and 120 minutes), exhibits a smaller slope of 0.0019 mmol/m², which is less than 1/3 (32.08%) of that of the first group. It also shows that the specific surface area and CH_4 adsorption capacity of the biochar samples increased from 319 m²/g and 1.77 mmol/g for Raw to 527 m²/g and 2.57 mmol/g for P30, respectively, but decreased beyond 30 minutes plasma duration to 484 m²/g and 2.46 mmol/g for P60 and 434 m²/g and 2.39 mmol/g for P120. These data indicate that the plasma treatment duration affected not only the specific surface area of the biochar but also its other properties contributing to the biochar CH_4 adsorption capacity, which will be discussed more in detail later.

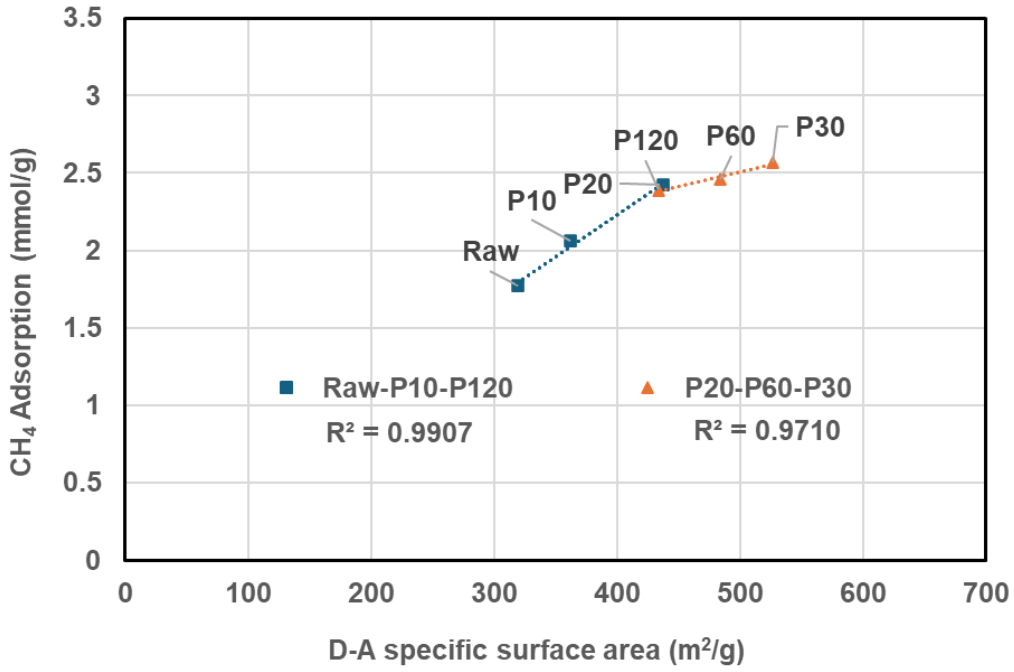

Fig. 4.4 Dependence of CH_4 adsorption on specific surface area of biochar

4.3.4 Plasma treatment effectiveness (η) and surface concentration of CH_4 (γ)

The dependence of plasma effectiveness (η) and surface concentration of CH_4 (γ) on biochars as a function of plasma treatment duration are presented in Fig. 4.5.

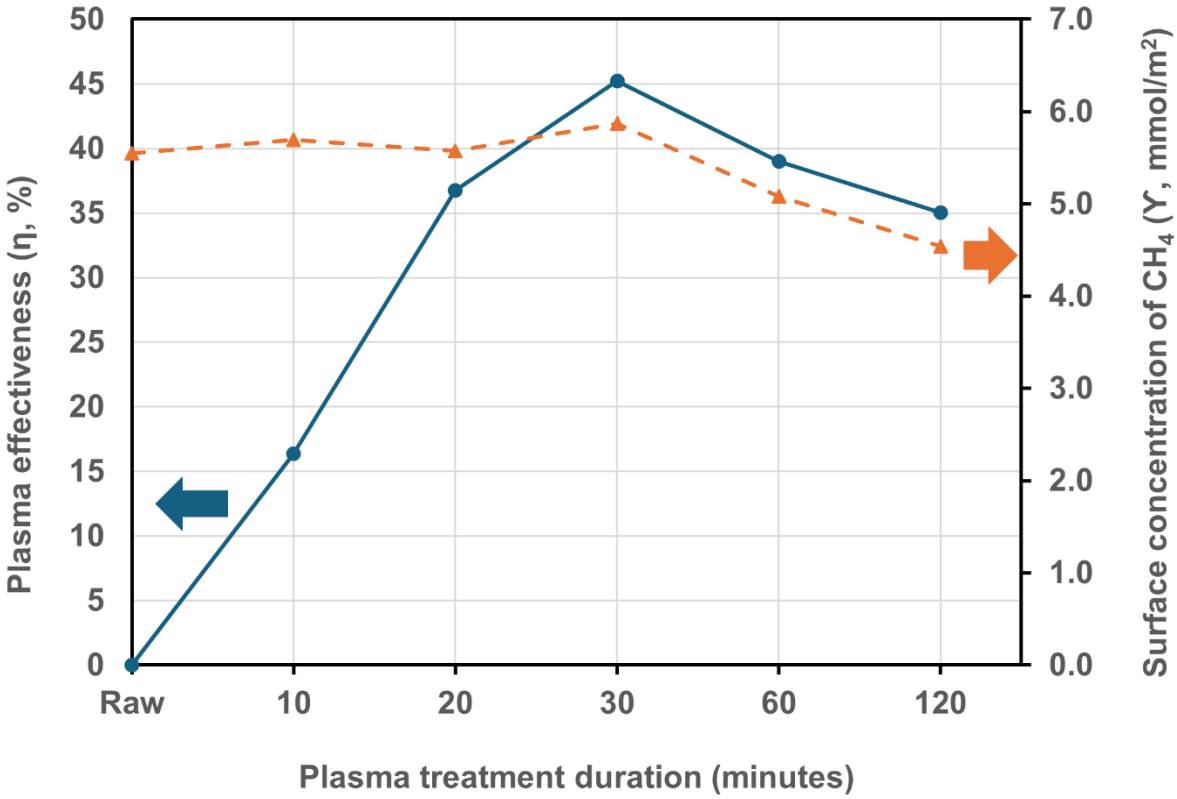

Fig. 4.5 Plasma effectiveness (η) and surface concentration of CH_4 (γ) of plasma-untreated (Raw) and plasma-treated biochars with different plasma treatment durations

As shown in Fig. 4.5, the plasma treatment effectiveness (η) increased almost linearly from 0% for the raw biochar (0 minutes plasma treatment duration) to 37% after 20 minutes plasma treatment, reaching 45% at 30 minutes, although with a reduced slope. For longer treatment durations (>30 min), η declined. In contrast, the CH_4 surface concentration (γ) remained nearly constant between up to 30 minutes, suggesting that adsorption sites per unit surface area remained fully accessible during this period, but decreased steadily for longer treatment durations.

These trends indicate that plasma treatment enhanced CH_4 adsorption primarily by increasing the specific surface area (Fig. 4.4) while maintaining uniform accessibility of adsorption sites up to 30 minutes. Beyond this optimal duration i.e., 60 and 120 minutes, both η and γ decreased, suggesting that over-treatment reduced the effective adsorption surface.

4.3.5 Pore structure evolution induced by plasma treatment

4.3.5.1 N_2 and CO_2 adsorption isotherms and pore accessibility

Fig. 4.6 presents the N_2 adsorption–desorption isotherms at 77 K for the raw biochar and the P30 sample. P30 shows notably higher N_2 uptake compared to the raw material, indicating that plasma treatment enhanced the accessible surface area and/or pore volume. A key observation is the low-pressure hysteresis observed, where the desorption branch failed to converge with the adsorption branch with a much larger residual adsorbed N_2 per unit mass of adsorbents than the equilibrium adsorption of N_2 at the same pressure. Such N_2 retention suggests either slow diffusion through nanopores or very narrow entrances of pore networks which limited accessibility [68,87]. This low-pressure hysteresis is a common phenomenon in biochars and microporous carbons creating "ink-bottles" with narrow entrances and larger cavities or very narrow slit shaped pores [64,88]

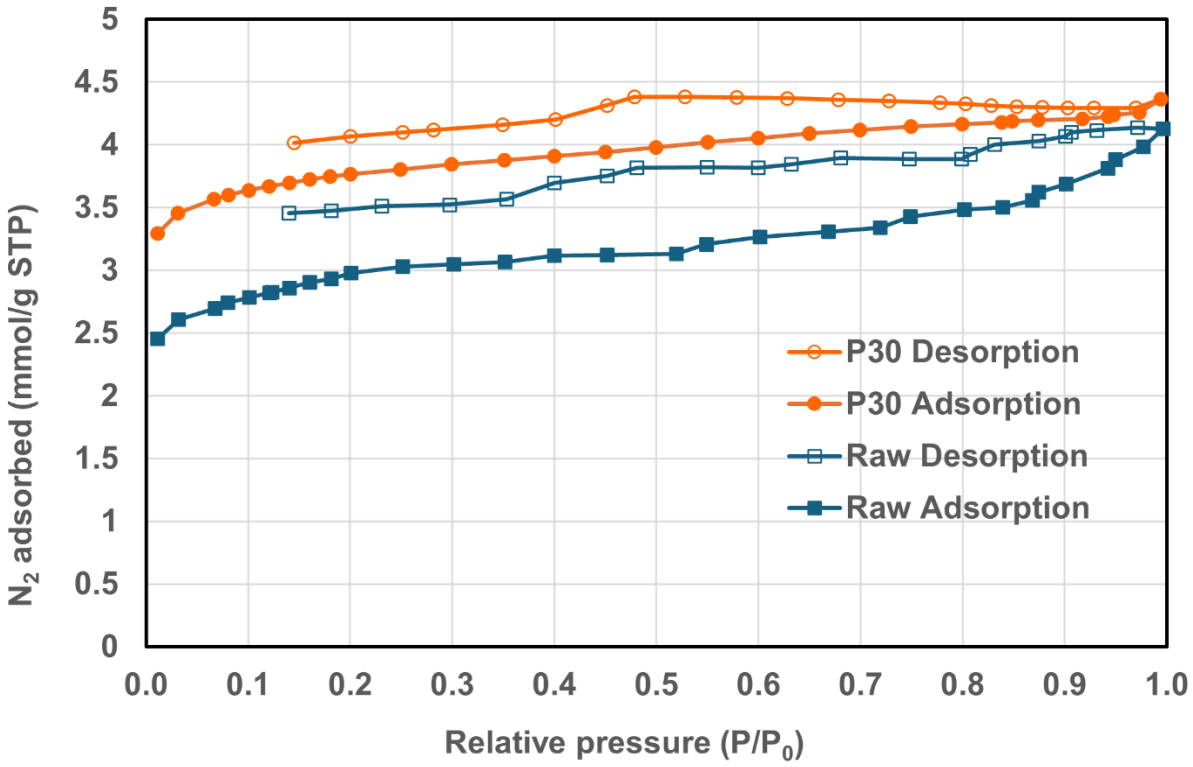

Fig. 4.6 N_2 adsorption-desorption isotherms exhibiting hysteresis for raw and plasma-treated with 30 minute duration (P30) samples

Interestingly, plasma treatment with 30 minutes duration appears to have mitigated this phenomenon significantly: the hysteresis loop narrowed, and residual uptake decreases. This could be due to plasma-induced widening of pore entrances, smoothing of internal pore walls, or reduced tortuosity, which reduced the retention effects cumulatively or synergistically. The characteristic abrupt desorption step at $P/P_0 \approx 0.42$-0.45, known as the tensile strength effect, was absent which is likely masked by broader pore heterogeneity typical of these materials [89]. Due to kinetic restrictions at cryogenic temperature, N_2 (kinetic diameter 0.364 nm) is unable to efficiently diffuse into nanopores smaller than 1.0 nm which can lead to underestimation of specific surface area and pore volume [90]. In contrast, CO_2 can access pores smaller than 1 nm due to smaller

kinetic diameter (0.330 nm), stronger quadrupolar interactions and its faster diffusivity at 273 K [91].

CO_2 adsorption isotherms at 273 K (Fig. 7) show a Type I profile, with CO_2 uptake at low relative pressures ($P/P_0 < 0.005$) indicating strong micropore filling. The observed adsorption capacities follow the order: Raw < P10 < P120 < P20 < P60 < P30, differing from the indistinguishable distinctions between P20 and P120 in the CH_4 isotherms as noted in Fig. 4.7 and Table 4.4. The CO_2 hysteresis was negligible (data not shown) with the adsorption and desorption profiles overlapping almost completely, which is consistent with literature reports on microporous materials [65]. The adsorption capacities of biochars all followed the trends of Raw<P10<P20<P30 and P30>P60>P120 for both CO_2 and N_2, consistent with the trend of the adsorption of CH_4.

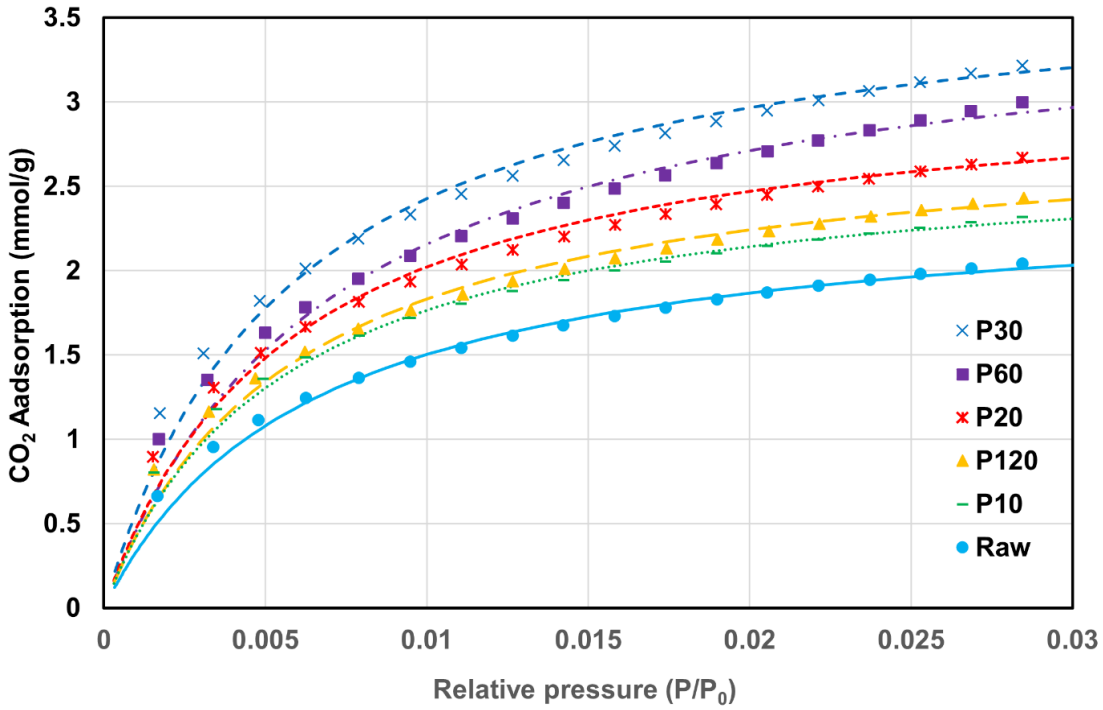

Fig. 4.7 CO_2 adsorption isotherms (Langmuir model) for biochar samples plasma-untreated (Raw) and plasma-treated samples (P10, P20, P30, P60, and P120)

Table 4.4 Langmuir adsorption isotherm parameters of CO_2

	Raw	P10	P20	P30	P60	P120
R^2	0.9977	0.9984	0.9974	0.9973	0.9953	0.9976
N_m (mmol/g)	2.4655	2.7270	3.1776	3.8153	3.6536	2.8893
B (bar^{-1})	156	183	175	175	144	173

4.3.5.2 Pore size distributions (PSDs) by CO_2 and N_2 physisorption

Fig. 4.8a presents the pore volume–weighted PSDs derived from CO_2 (273 K) and N_2 (77 K) physisorption for the Raw and P30 samples, analyzed using the NLDFT. CO_2 and N_2 provide complementary information: CO_2 at 273 K primarily resolves ultramicropores (< 0.7 nm) and partially supermicropores (0.7–2 nm), whereas N_2 at 77 K characterizes supermicropores and mesopores (≥ 2 nm) through multilayer adsorption and capillary condensation [92,93].

CO_2 is preferred for ultramicropore analysis because its higher measurement temperature (273 K) enhances molecular mobility and minimizes diffusion limitations that hinder N_2 at 77 K in pores < 1 nm. Consequently, CO_2 fills ultramicropores rapidly at low relative pressures, yielding sharp isotherm steps that can be interpreted using NLDFT and GCMC. In contrast, N_2 underestimates ultramicropore volume because of slow equilibration at cryogenic temperature (77K) in narrow pores, making long equilibration times impractical. Additionally, N_2 adsorption relies on multilayer formation and capillary condensation, which do not occur in ultramicropores too narrow for a liquid-like phase. N_2 remains essential for pores ≥ 1 nm, where these mechanisms apply effectively. However, at 273K, CO_2 adsorption is limited to pores smaller than approximately ~1 nm, as multilayer adsorption begins only near 10 bar (≈ 0.3 p/p_0) and capillary condensation occurs at 27–31 bar (≈ 0.8–0.9 p/p_0), close to the saturation pressure of 33–34 bar, and well above typical experimental conditions of 1 bar. Extending CO_2 analysis beyond 1 nm would therefore require near-saturation pressures or supercritical conditions (> 31 °C and

> 73.8 bar) [94,95]. Therefore, combining N_2 adsorption at 77 K and CO_2 adsorption at 273 K provides complementary information on the full micropore spectrum.

Fig. 4.8b compares GCMC and NLDFT for P30 using CO_2 adsorption, showing that GCMC provides sharper resolution and a lower detectable pore size limit. GCMC is generally more reliable for CO_2 adsorption isotherms because its better accounts for specific interaction effects and deviations from ideal adsorption behavior arising from the quadrupolar nature of CO_2 molecules [96,97].

The PSDs analysis (Fig. 4.9) indicates the development of pores ≤1 nm, encompassing part of the ultramicropore region (< 0.7 nm) as defined by IUPAC [65]. Due to instrumental limitations, pores smaller than 0.47 nm could not be resolved; therefore, the presence of smaller ultramicropores (0.3–0.47 nm) cannot be confirmed in this study.

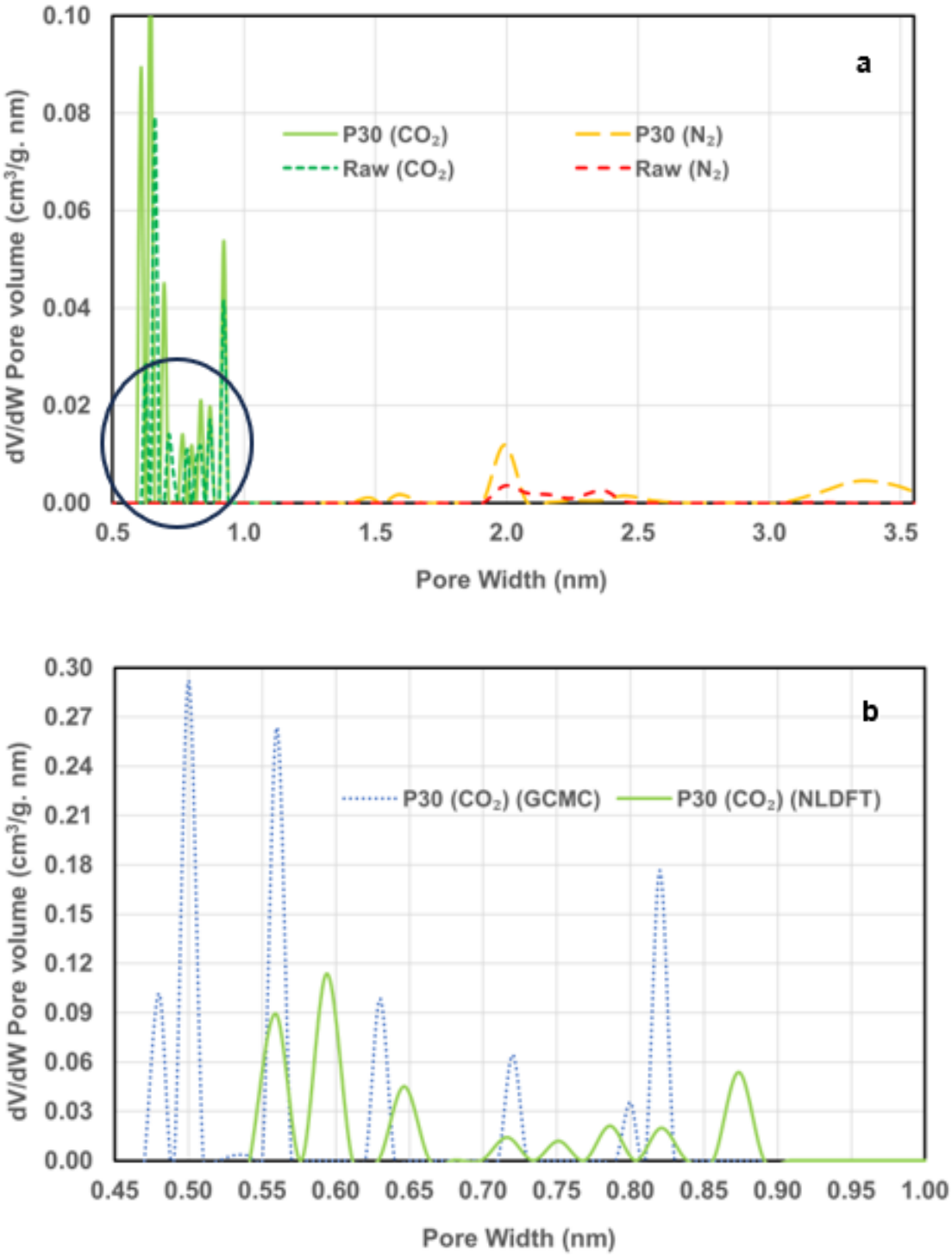

Fig. 4.8 a) NLDFT-derived PSDs from CO_2 (273 K) and N_2 (77 K) physisorption for Raw and P30 samples; b) Comparison of GCMC and NLDFT models for PSDs < 1 nm from CO_2 adsorption in P30

To examine the effect of plasma treatment in detail, Fig. 4.9 presents PSDs in the 0.47–0.89 nm range obtained from CO_2 adsorption at 273 K using GCMC, highlighting structural changes as a function of treatment duration.

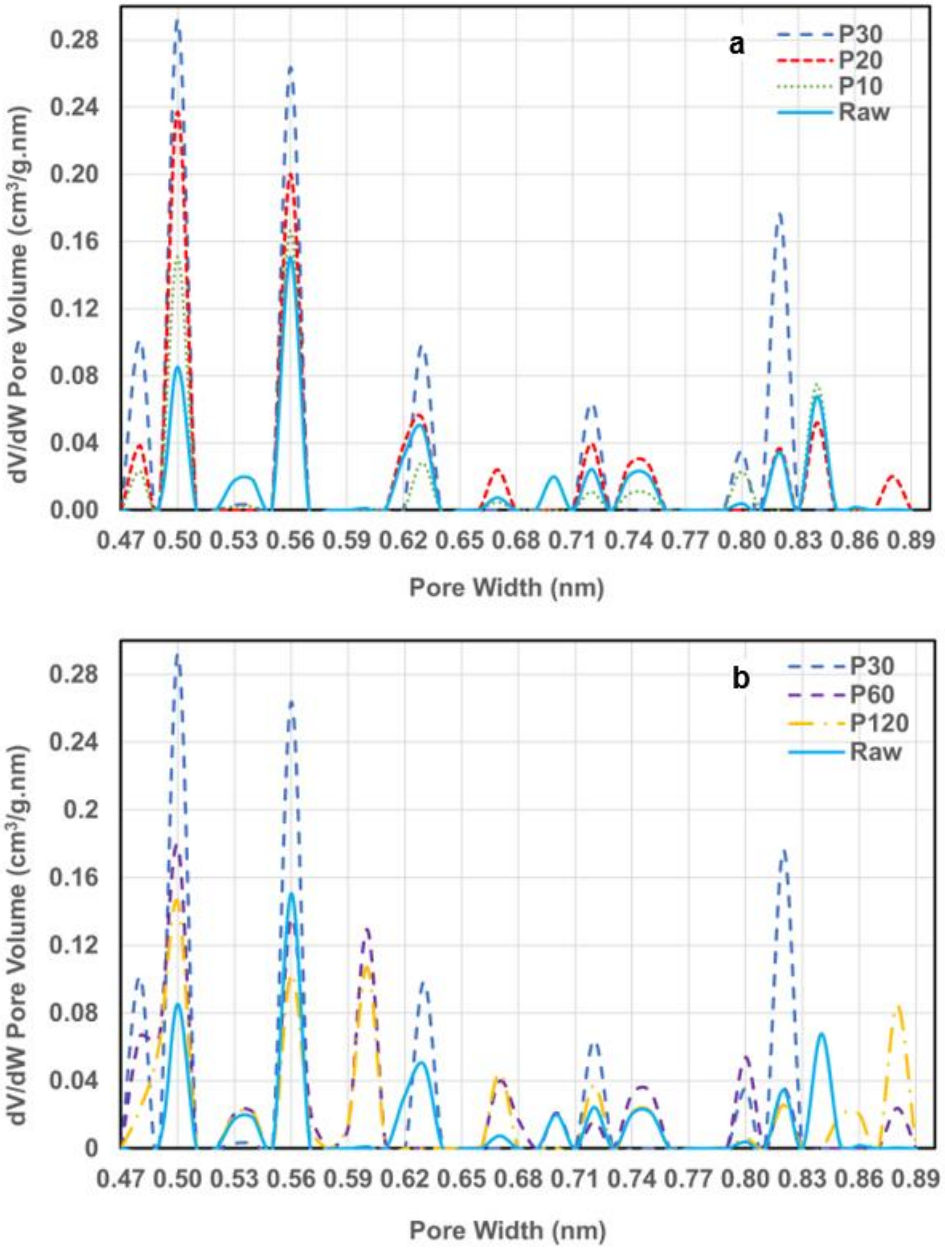

Fig. 4.9 PSDs derived by GCMC from CO_2 (273K) physisorption for the biochar with different plasma treatment durations: a) Raw, P10, P20, and P30; b) Raw, P30, P60, and P120

Fig. 4.9a and 4.9b show the PSDs of biochar with different plasma treatment durations ranging from 0 (Raw) to 120 minutes (P120). For clarity, Raw, P10, P20, and P30 are presented on Fig. 4.9a, and Raw, P30, P60, and P120 are presented on Fig.4.9b. As shown on Fig.4.9a, the Raw has two major peaks at 0.50 nm and 0.56 nm and both these two peaks increased with plasma treatment duration, following an order of P30>P20>P10>Raw. In addition, a new peak at 0.48 nm was detected for the plasma-treated biochars with peak values following the same order of P30>P20>P10. However, Fig.9b shows an opposite trend with both the peaks at 0.5 and 0.56 nm decreasing with plasma treatment duration in the order of P30>P60>P120. At 0.56 nm, the peak intensity for P120 decreased below that of the Raw sample. Furthermore, the additional peak at 0.48 nm of P60 was smaller than that of P30 but not nonexistent as that with P120 and the raw biochar. The consistent trends of these three peaks at 0.48, 0.50, and 0.56 nm, which all increased with plasma duration before reaching 30 minutes but reversed to a declining trend beyond it, might explain the similar trends of the dependence of the specific area of biochar on the plasma duration. There are a few other peaks in the range of 0.65-0.9 nm, which generally follow the same trends but with exceptions. These pores, however, contributed only a small portion of the ultramicropore surfaces of biomass as shown in Fig. 4.10a and 10b.

4.3.5.3 Surface area changes

Fig. 4.10a displays the GCMC simulated-cumulative specific surface area, and Fig. 4.10b presents the normalized cumulative specific surface area as functions of pore width for various plasma-treated biochar samples, including Raw, P10, P20, P30, P60, and P120. The vertical dashed lines represent pore widths corresponding to 1.5 and 2 times the molecular kinetic diameters of CH_4. The kinetic diameter of CH_4 is 0.380 nm. The cumulative specific surface area demonstrates a distinct trend of increase as the plasma treatment duration extends from 0 minutes (Raw) to 30

minutes (P30) in all pore width ranges, i.e., Raw<P10<P20<P30 (Fig. 4.10a). However, prolonged treatment, i.e., 60 minutes (P60) and 120 minutes (P120), resulted in a clear reversal, with a decline in the cumulative surface area observed throughout the pore width range, i.e., P30>P60>P120.

Fig. 4.10b presents the normalized cumulative specific surface area, expressed as a percentage of the total specific surface area, plotted against pore width. A significant portion of the surface area in plasma treated biochars is attributed to pores with a width of 0.48 nm, which did not exist in the raw biochar.

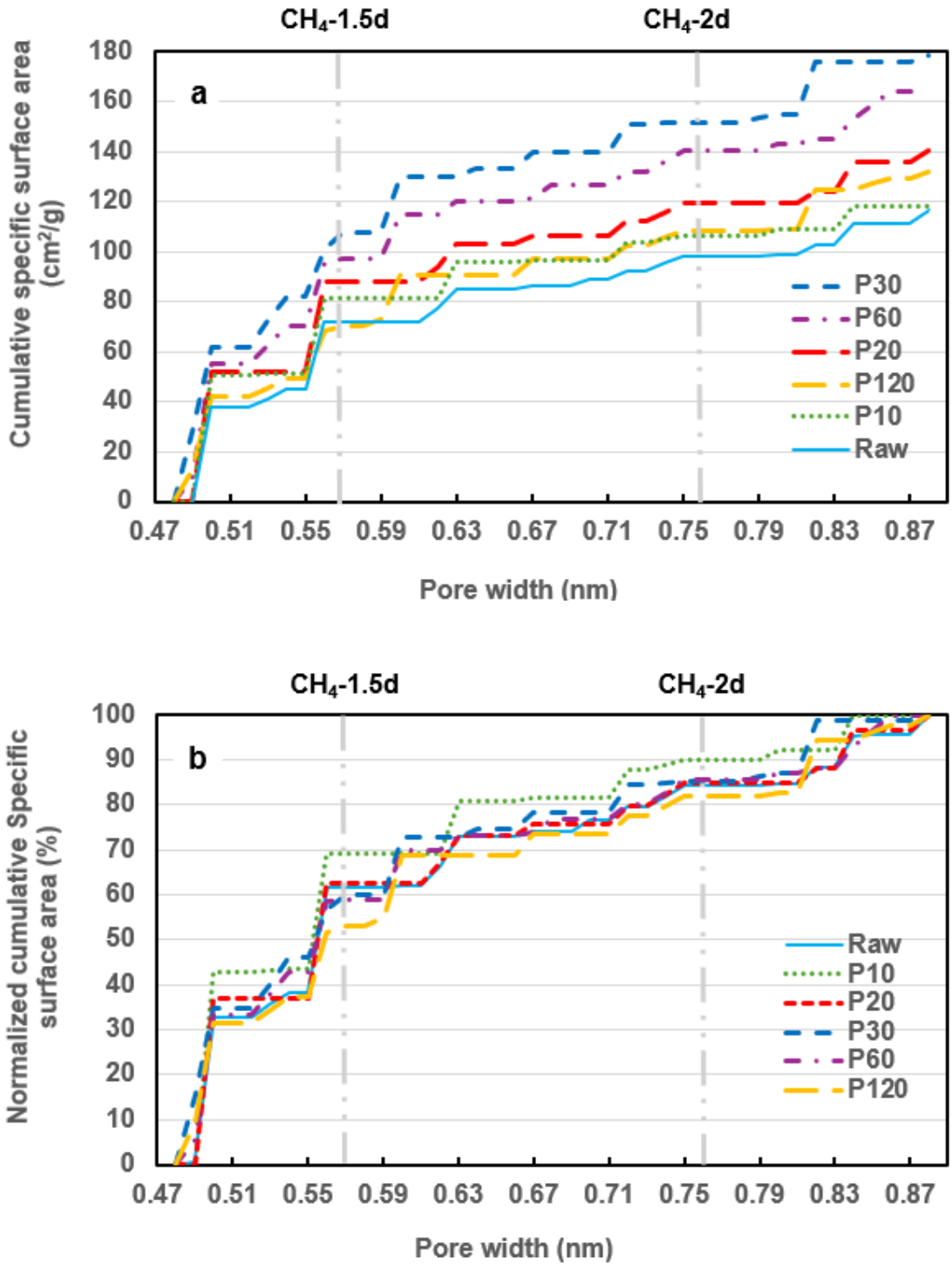

Fig. 4.10 GCMC simulated-cumulative specific surface area (a), and normalized cumulative specific surface area (b) against pore width of Raw, P10, P20, P30, P60, and P120. Vertical lines are the benchmarks of 1.5×, 2× of the kinetic diameter (d) of the CH_4 molecule.

It is evident from Fig. 4.10a that the ultramicropores primarily fall within the 0.48-0.57 nm width range (52-70%). Given that the kinetic diameter of CH_4 is 0.380 nm, these pores should be accessible for CH_4 adsorption. Variations in pore size can affect the accessibility for adsorption. Smaller pores may restrict the diffusion of larger molecules due to spatial constraints, while larger pores may not provide sufficient interaction energy for effective adsorption due to the absence of overlapping wall potentials, where the adsorbate molecule is too far from the opposing pore wall to benefit from confinement-enhanced interaction. This suggests that the collapse of existing pores or their enlargement of pores may lead to ineffective adsorption. This understanding is well aligned with other reported studies showing that surface roughness and pore morphology significantly

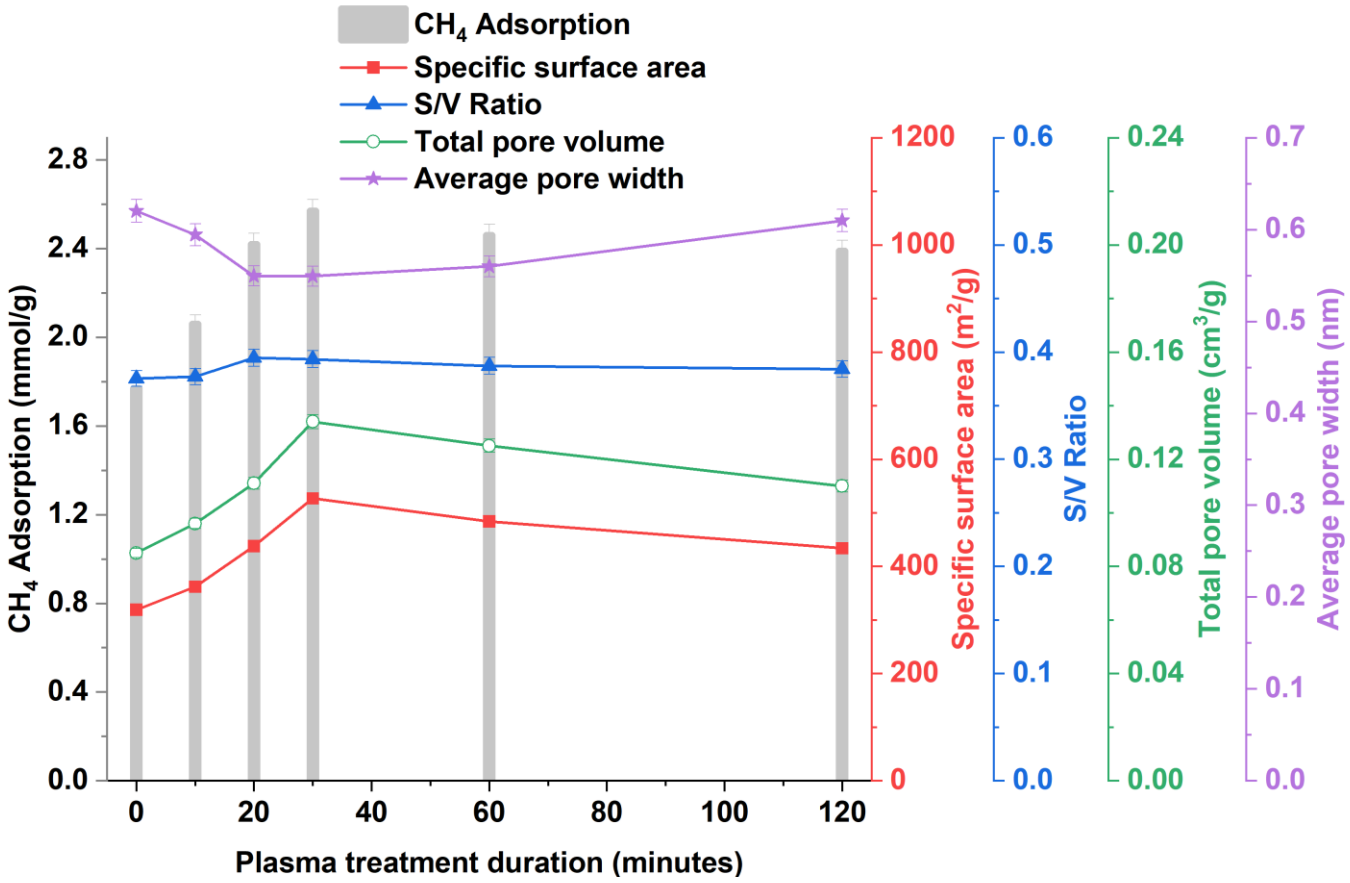

Fig. 4.11 CH_4 adsorption capacity and D-A specific surface area, total pore volume, average pore width of biochars of different plasma treatment durations

influence the surface adsorption behavior and that the optimum pore size can maximize the specimen's adsorption capacity [98].

Fig. 4.11 presents the CH_4 adsorption capacities of biochars subjected to different plasma treatment durations, derived from the Langmuir isotherms in Fig. 4.3, alongside key material properties. CH_4 adsorption capacity increased almost linearly with treatment time, from 1.77 mmol/g for the untreated biochar to 2.60 mmol/g after 30 minutes of plasma treatment. However, it decreased slightly with the treatment duration beyond 30 minutes to 2.4 mmol/g for 120 minute-plasma treatment. These results indicate that there is an optimum plasma treatment duration in terms of achieving the maximum adsorption capacity. While the D-A specific surface area and total pore volume had peaks at 30 minutes of plasma treatment duration as the turning point, the average pore width exhibited a valley at this point. Interestingly, the specific surface area/specific volume (S/V) ratio first increased slightly with plasma treatment duration up to 20 minutes and then remained essentially constant afterward. The S/V ratio represents the surface area available per unit pore volume. A higher S/V ratio indicates greater biochar surface exposure for a given volume, which can affect the biochar plasma activation process. The S/V ratio slightly increases with plasma treatment duration up to 30 minutes and then decreases.

4.3.5.4 Surface morphological changes

Fig. 4.12 presents SEM images of untreated biochar (Raw), 30-minute plasma-treated biochar (P30), and 120-minute plasma-treated biochar (P120) at different magnifications. A comparison of the SEM images revealed that plasma treatment induced changes in the surface morphology.

A micrograph of the Raw specimen (Fig. 4.12a) displays a well-preserved honeycomb-like structure with smooth inner walls and minimal surface roughness. An image of the P30 sample

(Fig. 4.12b) reveals damage to the walls, and an increased exposure of pores on internal surfaces. An image of the P120 sample (Fig. 4.12c) shows a more pronounced surface erosion, pore coalescence, and signs of partial structural collapse, which corresponds to a reduction of the biochar surface area.

At higher magnifications, the 30-minute plasma-treated biochar exhibits the existence of nanopores on its surface at 150,000× magnification (Fig. 4.12e), whereas the untreated biochar shows no visible pores at 100,000× (Fig. 4.12d). Fig. 4.12f of the P120 sample displays a stressed, rough surface that seems to have partially obscured the underlying pores, adding complexity to the biochar's nanoscale morphology. These surface changes can be attributed to the bombardment of the biochar by highly energized particles, such as electrons, ions, and neutral species, during the plasma treatment process.

However, the development of nanoscale pores below 1 nm could not be observed due to challenges in sample preparation, particularly the difficulty in achieving a flat surface, which limited the resolution of the SEM analysis.

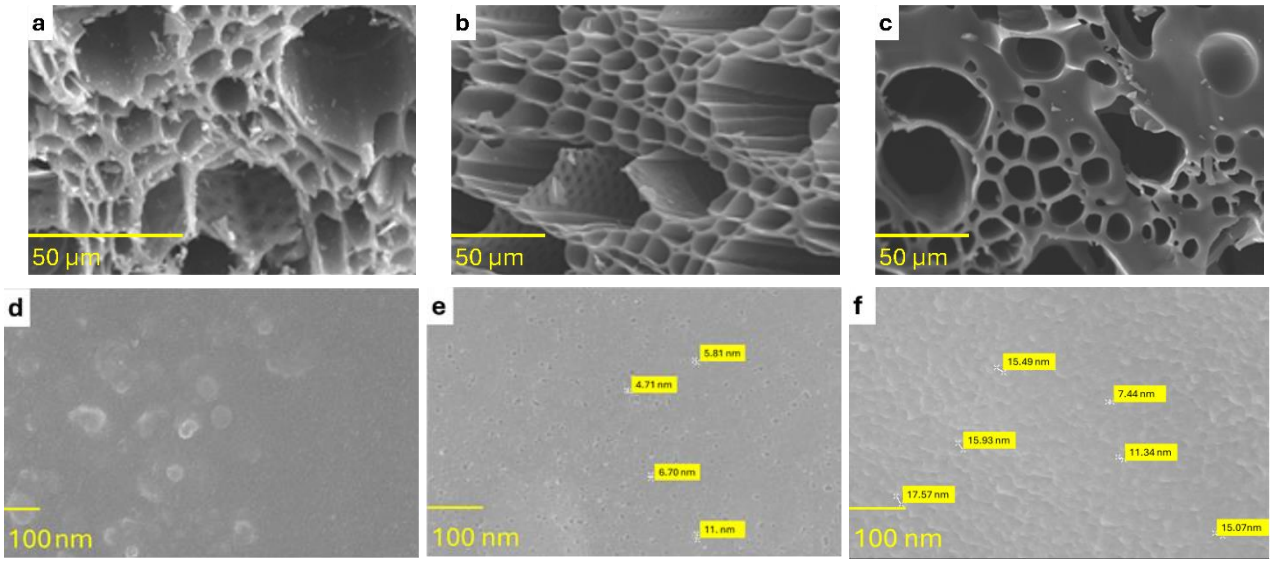

Fig. 4.12 SEM images of biochars, (a) Raw (1000×), (b) P30 (600×), (c) P120 (500×), (d) Raw (100,000×), (e) P30 (150,000×) and (f) P120 (100,000×)

4.3.6 Surface chemical modifications from plasma treatment

4.3.6.1 pH changes

The pH of biochars suspended in deionized water is an indicator of the protonation capacity of the biochar surface and therefore an indirect measurement of the abundance of carboxylate groups at biochar surfaces. Fig. 4.13 shows that the untreated biochar (Raw) had a pH of 9.05, which increased with plasma treatment duration until peaking at 30 minutes (P30) with a pH of 9.73 (ΔpH = +0.68). This enhancement is attributed to the removal of organic impurities including oxygen-containing groups, as supported by the zeta potential changes and ATR-FTIR data (reduced O-H, C=O peaks) to be discussed in the following sections. It is worth noting that prolonged plasma beyond 30 minutes showed a decline of pH, i.e., pH 9.77 (ΔpH = +0.72) and pH 9.57 (ΔpH = +0.52) for P60 and P120, respectively. This turning of trends coincides with that of the specific surface area, the CH_4 adsorption capacity, and the surface concentration of CH_4 on the treated

biochar. We therefore hypothesize that the creation of new nanoscale pores in the specimen treated with plasma for up to 30 minutes was primarily due to removal of organic impurities that originally filled these pores.

4.3.6.2 Zeta potential changes

As shown in Fig. 4.13, the zeta potential of the biochar, measured at a fixed pH of 6.7, increased with increased plasma treatment duration up to 20 minutes and then showed no further increase beyond. Since carbon is electrically neutral, the reduction of the negative zeta potential confirms the aforementioned hypothesis that the plasma treatment resulted in the removal of the organic impurities containing negatively charged functional groups from the biochar surface while the extent of that removal increased with a plasma treatment duration.

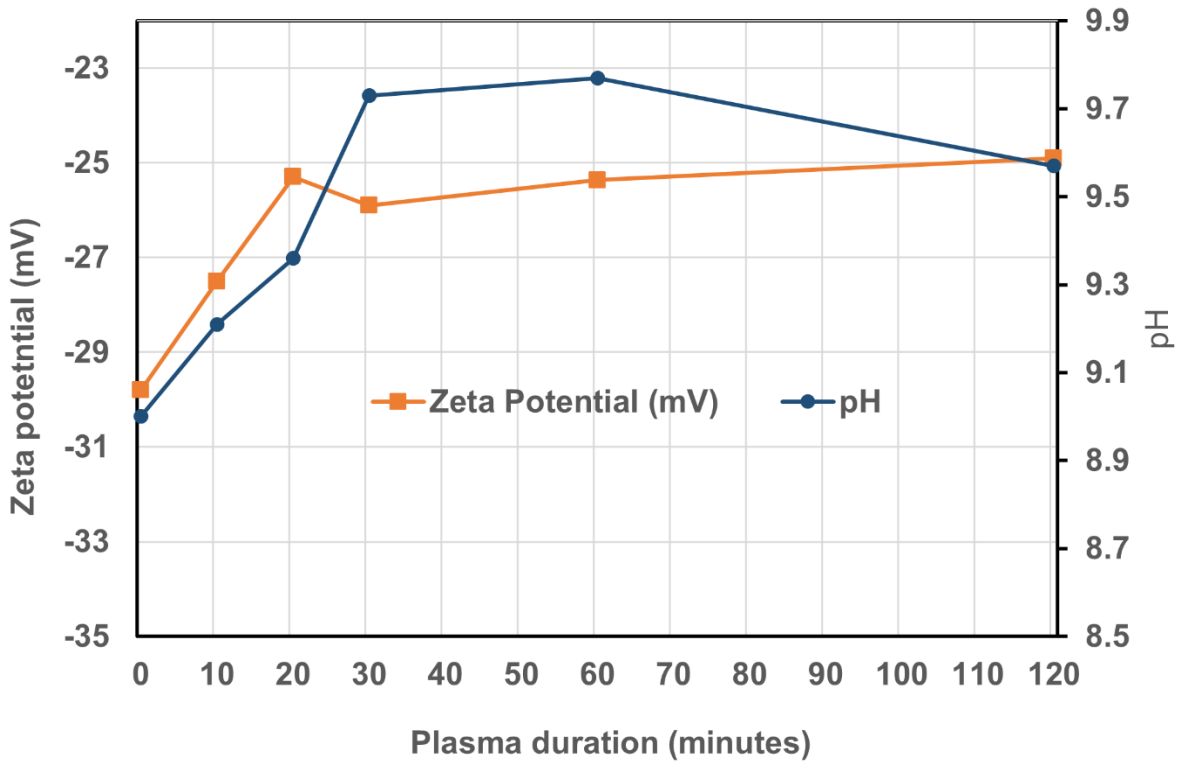

Fig. 4.13 Effect of plasma duration on the zeta potential of biochar

Furthermore, the pH of biochar suspension in deionized water increased with plasma treatment duration of up to 30 minutes and then ceased to rise. This trend of pH change confirms that organic impurities containing negatively charged functional groups, which are typically acidic and capable of releasing protons upon dissociation, were removed during the plasma treatment. These data also indicate that the impurities removal peaked at a plasma treatment duration of 30 minutes.

Similarly, the zeta potential became less negative with plasma exposure, reflecting the reduction of oxygen-containing functional groups, such as hydroxyl and carboxyl groups, which contribute to surface acidity. This shift confirms that plasma treatment altered the biochar surface chemistry, likely by partially removing these groups and decreasing the density of dissociable protons. The observed changes in protonation capacity and zeta potential are consistent with the results of previous studies. For instance, it has been reported that the zeta potential of biochar surfaces decreases due to the loss of oxygen-containing groups [99]. Additionally, the pH and zeta potential of biochars treated with plasma of 30 minutes or longer remained largely unchanged, suggesting that the removal of organic impurities from the biochar surfaces had reached its maximum and that extended plasma treatment does not further alter the surface chemistry. Notably, the continued removal of organic impurities, as indicated by rising pH and zeta potential, coincided with a stable surface concentration of CH_4 (Υ) during the first 30 minutes, whereas surface concentration declined beyond 30 minutes (Fig. 4.5). The steady pH and zeta potential after 30 minutes, reflecting completed impurity removal, partially explain this decrease in CH_4 adsorption. However, the further decline in adsorption beyond 30 minutes, despite constant surface chemistry, suggests that additional factors govern CH_4 uptake. This aligns with the observed increase in average pore size and decrease in specific surface area (Fig. 4.11). Over-treatment likely causes pore enlargement or partial collapse, reducing micropore surface area and, consequently, CH_4

adsorption due to the loss of adsorption sites, while pH and zeta potential remain largely unchanged.

4.3.6.3 Attenuated total reflectance-Fourier transform infrared spectroscopy (ATR-FTIR)

To further confirm the chemical modification of the biochar surfaces due to plasma treatment, we utilized ATR-FTIR spectroscopy by examining the functional groups on the biochar (see Fig. 4.14).

Although peak deconvolution was not performed, baseline subtraction and normalization were conducted using OriginPro software. Baseline correction was applied using the asymmetric least squares (ALS) method, followed by both peak height and area normalization. The peak heights and areas for each spectrum are provided in a table accompanying the spectra. These processed spectra were used to qualitatively assess relative changes in the C-H, O-H, C=O, and C-N bands. While no quantitative correlation was performed to directly relate these spectral changes to the observed increases in surface area or CH_4 uptake, the qualitative trends provide insight into the chemical modifications induced by treatment.

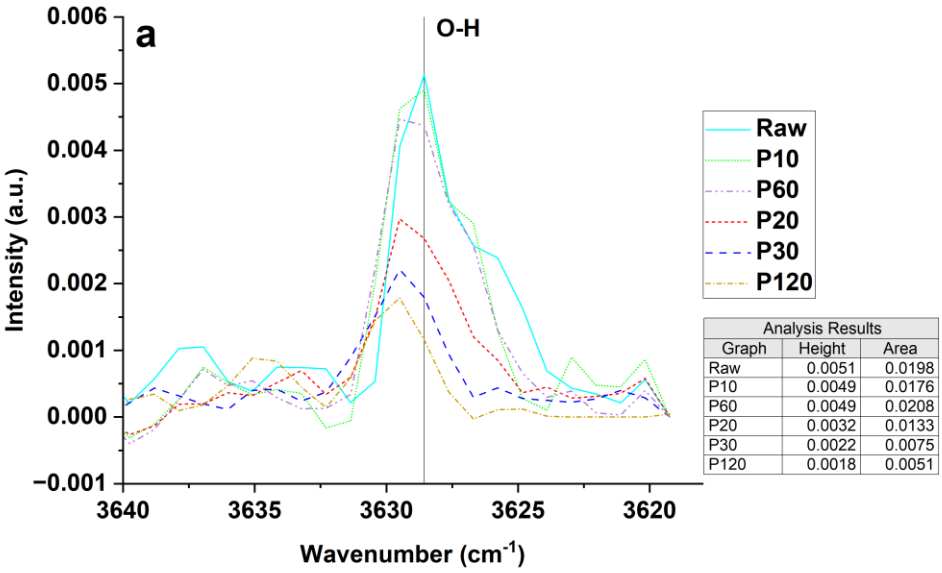

Analysis Results		
Graph	Height	Area
Raw	0.0051	0.0198
P10	0.0049	0.0176
P60	0.0049	0.0208
P20	0.0032	0.0133
P30	0.0022	0.0075
P120	0.0018	0.0051

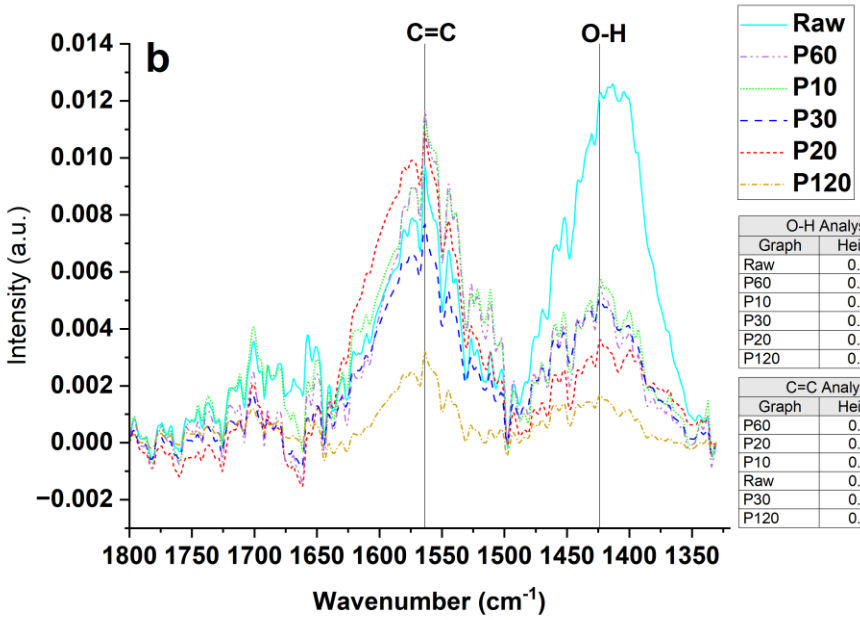

O-H Analysis Results		
Graph	Height	Area
Raw	0.0131	1.0923
P60	0.0069	0.6187
P10	0.0065	0.5503
P30	0.0059	0.5461
P20	0.0051	0.5479
P120	0.0023	0.2027

C=C Analysis Results		
Graph	Height	Area
P60	0.0131	0.964
P20	0.0124	1.0611
P10	0.0122	0.9269
Raw	0.0102	0.7256
P30	0.0086	0.6614
P120	0.0038	0.2352

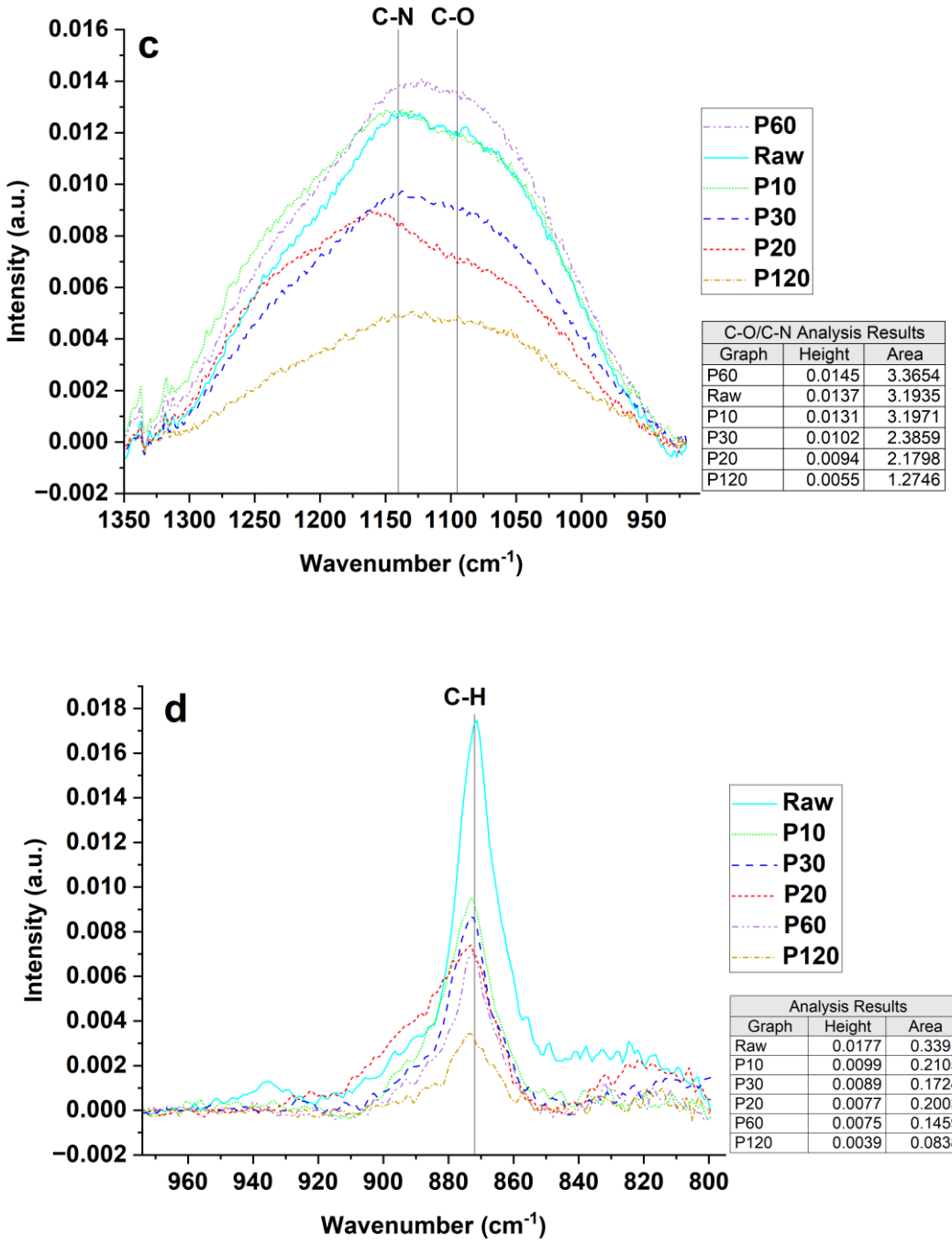

Fig. 4.14 Identified functional groups on ATR-FTIR spectra: a) O-H, b) C=C, O-H, c) C-N, C-O, d) C-H

Fig. 4.14 presents the ATR-FTIR spectra of biochar surfaces highlighting the peaks corresponding to commonly found organic bonds. Biochars with different plasma treatment durations, i.e., P10,

20, 30, 60, 120 exhibited ATR-FTIR spectral patterns similar to that of Raw, but of different peak values. With increasing plasma exposure duration from 10 to 120 minutes, a reduction was observed in key characteristic bands, at 3628-3629 cm^{-1} and 1423 cm^{-1} corresponding to O-H stretching and bending vibrations of oxygen-containing groups, as well as 873 cm^{-1} associated with C-H bond deformation. Plasma treatment resulted in a reduction in the intensity of the 1575 cm^{-1} band, corresponding to C=C bending vibrations. The peak shown in Fig. 14c could be C-O in alcohol (1087-1124 cm^{-1}) (see Table 4.5), or C-N stretching vibration in amines (1020-1250 cm^{-1}), which decreased when comparing the untreated (Raw), P10, P20, P30, and P120 biochar specimens.

Table 4.5 Surface functional groups as identified by ATR-FTIR spectra

FTIR Wavenumber (cm^{-1})	**Group**	**Class**	**Indicator**	**References**
3580-3650	O-H stretching	hydroxyl groups	surface polarity and hydrophilicity	[100,103–106]
1566-1650	C=C Stretching	aromatic structures	biochar's carbon framework	[100–103]
1395-1440	O-H bending	carboxylic acid	surface polarity and hydrophilicity	[104,107]
1087-1124	C-O stretching	Alcohol, carboxylic acid	surface polarity and hydrophilicity	[100,103,104,108]
1020-1250	C-N stretching	Aliphatic amine	hydrophilicity	[109,110]
750-900	C-H bending, stretching	1,2,4-trisubstituted, 1,3-disubstituted, aliphatic or aromatic benzene rings	hydrophobicity	[104,106,111,112]

With an inert plasma generating gas such as Ar, plasma-induced chemical bond formation is not expected, however reactive species such as C-H, C=C, and O-H can be effectively removed. On the other hand, extended exposure of biochar surface to inert gas plasmas can induce ion etching and generation of surface defects. These effects can additionally impact the biochar adsorption ability by generating new or destroying the existing pores, thereby affecting the structural integrity

and surface functionality of the biochar. Ar plasma treatment can cause physical etching of the material's surface due to the ion bombardment and the presence of energetic particles bombarding the biochar surface. This can break down unsaturated bonds, such as C=C bonds, induce radical formation and bond scission. Thus, the Ar plasma treatment may reduce the density of C=C bonds on the biochar surface. The surface can undergo reorganization, where highly reactive species (like C• radicals) may cause bond breakage or rearrangement, further reducing the concentration of C=C bonds on the surface. Plasma can also reduce the surface concentration of C-H, O-H, C-O, C-N, and C=O groups leading potentially higher biochar hydrophobicity. Ar plasma treatment does not introduce any polar or ionizable groups (such as –OH or –COOH). As a result, the zeta potential becomes less negative due to the lack of ionizable polar groups that would otherwise contribute to negative charges. This can increase the relative proportion of hydrophobic, nonpolar sites on the biochar surface. As the concentration of oxygen-containing functional groups decrease, the content of effective adsorption sites increases, leading to the enhancement of the biochar CH_4 adsorption capacity. Although the 750-900 cm^{-1} band could arise from the rocking vibrations of C–H groups [112], the absence of the 2850–3000 cm^{-1} band, which corresponds to the stretching vibration of saturated aliphatic C–H, suggests the absence of saturated aliphatic C-H bonds. The 750-900 cm^{-1} bands have therefore most likely arisen from the aromatic C-H bond. The lack of aliphatic C-H from all the biochar samples, one of the most abundant structural moieties in wood, was likely due to the loss of them during the pyrolysis process for the production of the raw biochars.

4.3.6.4 Plasma effluent gas

To investigate the interactions between the Ar plasma and biochar and study the removal of volatile compounds or functional groups such as O-H, C=C, C-H, moisture, or impurities during the biochar plasma treatment, the composition of effluent gases released from the plasma reactor were

analyzed. Table 4.2 presents the compositions of raw biochar, including proximate analysis (moisture, ash, volatile matter, fixed carbon), and ultimate analysis (C, H, N, O, S). Since the biochar contained much more O element (3.38 wt%) than N (0.44 wt%), it is reasonable to hypothesize that the peak in Fig. 4.14 is more likely attributable to C-O in alcohol than C-N in amine.

Table 4.6 indicates that H_2, N_2, CO_2, and CO were generated during the biochar plasma treatment. The plasma gas was pure Ar. The only source of these gases in the effluent would be the adsorbed atmospheric gas molecules and organic impurities embedded on the biochar surfaces, which can include elements H, O, N, and C. This again confirms that the plasma treatment induces chemical surface modifications leading to the breakdown of and desorption of organic impurities and atmospheric gases. This observation aligns with the composition of the raw biochar (Table 4.2), which contained 11.38 wt% volatile matter, indicating the presence of volatile organic compounds (VOCs) prior to plasma treatment. After 30 minutes of plasma treatment, the effluent gas contained 0.16 mol% N_2 and a total of 0.17 mol% oxygen atoms from CO_2 (0.03 mol%), CO (0.01 mol%), and O_2 (estimated at 0.05 mol%). This corresponds to an N/O atomic ratio of approximately 1.88, which is lower than the atmospheric N/O ratio of 3.73, suggesting an enrichment of oxygen-containing species in the effluent. Given that the raw biochar initially contained substantially more oxygen (3.38 wt%) than nitrogen (0.44 wt%) (Table 4.2), converting to molar quantities (O: 3.38/16.00 = 0.211 mol; N: 0.44/14.01 = 0.031 mol) yields an N/O atomic ratio of 0.15, these results support the conclusion that both nitrogen and oxygen in the effluent originated, at least in part, from the decomposition of organic impurities during plasma treatment.

Table 4.6 Compositions of effluent gas after plasma treatment with argon (99.9999 %) as a plasma source gas for a 30-minute duration (P30)

Gas Detected	Amount [mol %]
H_2	0.04
He	< 0.1
CO_2	0.03
Ar	99.77
O_2	< 0.1
N_2	0.16
CO	0.01
VOCs C_1-C_5/C_6+	Trace
Sum	100

VOCs: volatile organic compounds

In summary, the surface chemistry data, including zeta potential, pH, FTIR spectra, and effluent gas composition, all point to a substantial chemical modification of the biochar surfaces caused by plasma treatment. These data also suggest that the chemical modification was primarily attributed to the removal of organic impurities that contained H, C, O, and N as well as negatively charged carboxylate groups. Furthermore, the impacts of plasma treatment duration on the extent of the chemical modification showed the turning point at 30 minutes, coinciding with the observed changes in both the amount of nanoscale pores and removal of organic impurities from the biochar surfaces, which might be one of the main mechanisms responsible for the observed enhancement of the CH_4 biochar adsorption capacity caused by the employed plasma treatment.

Cold plasma treatment initiates physical etching through the bombardment of biochar surfaces by high-energy ions, electrons, and radicals generated in the discharge, such as atomic oxygen (O•) and ozone (O_3). We hypothesize that this process selectively removes volatile carbon fragments and organic impurities, generating new super- and ultramicropores (~0.48 nm) while

simultaneously enlarging existing pore structures. The reactive species penetrate the carbon matrix, preferentially attacking defect sites and leading to the volatilization of carbonaceous residues as CO or CO_2, thereby generating finer pores without significant bulk degradation.

4.3.6.5 Interpretation of plasma effects on CH_4 adsorption

To provide an overall view, Fig. 4.15 shows the general trends of CH_4 adsorption capacity, plasma treatment efficiency (η), CH_4 surface concentration (γ), and surface chemistry parameters (pH and zeta potential) as functions of plasma treatment duration, irrespective of their absolute values.

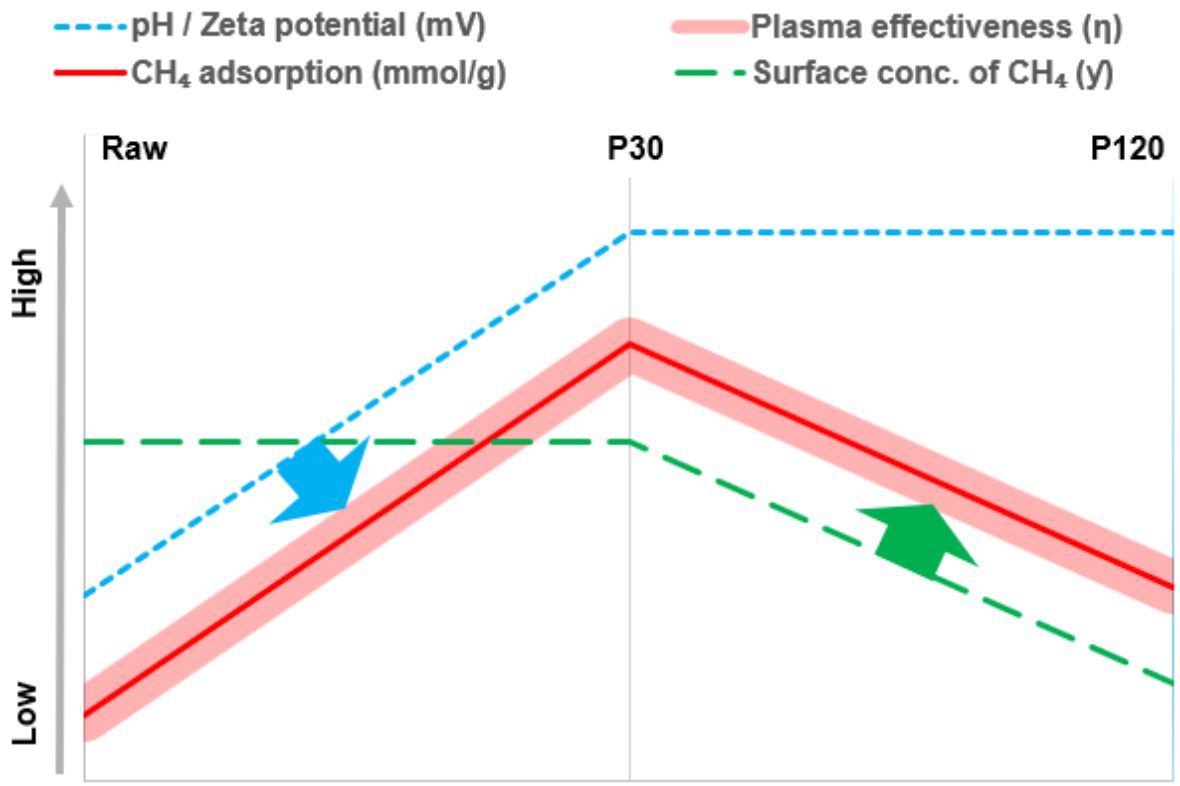

Fig. 4.15 Simplified trends of CH_4 adsorption, plasma effectiveness (η), surface concentration of CH_4 (γ), and pH/Zeta potential as functions of plasma treatment duration

Up to 30 minutes of plasma treatment, CH_4 adsorption capacity, plasma treatment effectiveness (η), and pH/zeta potential increase together, while the surface concentration of CH_4 (γ) remains

essentially constant. This indicates that the improvement in CH_4 uptake is governed primarily by micropore formation and greater accessibility of adsorption sites, as evidenced by the rising pH and zeta potential, which reflect effective removal of surface impurities, rather than by enhanced adsorption affinity (which would alter γ).

Beyond 30 minutes of plasma exposure, γ, η, and CH_4 adsorption capacity begin to decline, suggesting that excessive treatment causes surface morphological changes such as pore widening and coalescence that reduce the number of available micropore adsorption sites. An increase in average pore size and a decrease in specific surface area (Fig. 4.11), together with the widening of pore entrances (Fig. 4.6) and other structural alterations, were evident in SEM and BET (CO_2 and N_2) analyses, which showed enlarged pores and reduced micropore surface area. Meanwhile, pH and zeta potential stabilize, indicating that impurity removal has reached completion and no longer contributes to further adsorption improvement.

4.4 Conclusions

Cold plasma treatment significantly improved the CH_4 adsorption capacity of biochars, primarily through an increase in specific surface area associated with the development of ultramicropores, particularly in the 0.47–0.68 nm range. The plasma treatment effectiveness (η) and adsorption capacity of CH_4 were mainly governed by ultramicropore formation and the increased availability of adsorption sites resulting from impurity removal, as indicated by rising pH and zeta potential, along with FTIR evidence showing reductions in surface concentrations of C-H, O-H, C-O, C-N, and C=O groups, which may increase biochar hydrophobicity and contribute to higher CH_4 uptake. Excessive plasma exposure beyond the optimal duration of 30 minutes, however, reduced specific surface area, plasma treatment efficiency (η), and surface concentration of CH_4 (γ), while

causing minimal additional changes in pH or zeta potential. This constant pH/zeta potential values and declines in γ and η support the conclusion that at extended treatment durations, CH_4 adsorption is governed mainly by structural properties rather than surface chemistry. FTIR analysis, together with plasma effluent gas composition evaluated against the elemental composition of raw biochar, confirms impurity removal during plasma treatment and provide evidence of plasma-induced chemical modification of the biochar surface.

CRediT authorship contribution statement

Vivien Yoonhee Ko: Writing – original draft, Visualization, Validation, Resources, Project administration, Methodology, Investigation, Formal analysis, Data curation, Conceptualization. Jinsheng Wang: Supervision, Resources, Project administration, Conceptualization. Christopher Lan: Writing – review & editing, Supervision. David Ryan: Supervision, Resources, Project administration, Funding acquisition.

Declaration of Competing Interest

The authors declare that they have no known competing financial interests or personal relationships that could have appeared to influence the work reported in this paper.

Funding

This work is supported by the Program of Energy Research Development of Canada.

Acknowledgment

The authors gratefully acknowledge the Characterization Laboratory at CanmetENERGY Ottawa, Natural Resources Canada, for providing the ATR-FTIR spectra and valuable analytical insights. We also extend our appreciation to the NanoFab facility at the University of Ottawa for enabling high-resolution scanning electron microscopy (SEM) imaging of nanoporous structures, which was instrumental in this study.

References

[1] M.E. Malerba, T. de Kluyver, N. Wright, L. Schuster, P.I. Macreadie, Methane emissions from agricultural ponds are underestimated in national greenhouse gas inventories, Commun. Earth Environ. 3 (2022) 1–7. https://doi.org/10.1038/s43247-022-00638-9.

[2] UNEP, Facts about Methane | UNEP - UN Environment Programme, (2021). https://www.unep.org/explore-topics/energy/facts-about-methane.

[3] O. US EPA, Overview of Greenhouse Gases, (2015). https://www.epa.gov/ghgemissions/overview-greenhouse-gases.

[4] O. US EPA, Understanding Global Warming Potentials, US EPA (2016). https://www.epa.gov/ghgemissions/understanding-global-warming-potentials.

[5] Global Warming Potential, http://large.stanford.edu/courses/2016/ph240/jadhav1/

[6] U.S.E. Singapore, Fact Sheet: President Biden Tackles Methane Emissions, Spurs Innovations, and Supports Sustainable Agriculture, U.S. Embassy in Singapore (2021). https://sg.usembassy.gov/president-biden-tackles-methane-emissions-and-more/

[7] US EPA, Importance of Methane, (2016). https://www.epa.gov/gmi/importance-methane.

[8] World Bank Group, Global Gas Flaring Data, https://www.worldbank.org/en/programs/gasflaringreduction/global-flaring-data.

[9] World Bank Group, Global Gas Flaring Reduction Partnership (GGFR), World Bank. https://www.worldbank.org/en/programs/gasflaringreduction.

[10] Gas Flaring - Energy System - IEA, https://www.iea.org/energy-system/fossil-fuels/gas-flaring.

[11] B.P. Prajwal, K.G. Ayappa, Evaluating methane storage targets: from powder samples to onboard storage systems, Adsorption 20 (2014) 769–776. https://doi.org/10.1007/s10450-014-9620-1.

[12] K.V. Kumar, K. Preuss, M.-M. Titirici, F. Rodríguez-Reinoso, Nanoporous Materials for the Onboard Storage of Natural Gas, Chem. Rev. 117 (2017) 1796–1825. https://doi.org/10.1021/acs.chemrev.6b00505.

[13] A. Arora, A. Bachle, Storage of Natural Gas by Adsorption Process, in: SPEIATMI Asia Pac. Oil Gas Conf. Exhib., Society of Petroleum Engineers, Nusa Dua, Bali, Indonesia, 2015. https://doi.org/10.2118/176129-MS.

[14] B. Shingan, N. Banerjee, M. Kumawat, P. Mitra, V. Parthasarthy, V. Singh, Liquefied Natural Gas Value Chain: A Comprehensive Review and Analysis, Chem. Eng. Technol. 47 (2024) 430–447. https://doi.org/10.1002/ceat.202300304.

[15] J. Park, H. Mun, J. Kim, I. Lee, Advanced natural gas liquefaction process on LNG supply chain with liquid air: From design to thermodynamic and techno-economic analyses, Energy Convers. Manag. 252 (2022) 115107. https://doi.org/10.1016/j.enconman.2021.115107.

[16] S. Himeno, K. Ata, Porous Material Densification While Maintaining Its Pore Structure, Energy Fuels 39 (2025) 8601–8611. https://doi.org/10.1021/acs.energyfuels.4c06191.

[17] J.R. Rugarabamu, D. Zhao, S. Li, R. Diao, K. Song, Structure modeling of activated carbons used for simulating methane adsorption – A review, Pet. Res. 8 (2023) 103–117. https://doi.org/10.1016/j.ptlrs.2022.06.004.

[18] E.M. Strizhenov, A.V. Shkolin, S.S. Chugaev, I.E. Men'shchikov, O.V. Solovtsova, A.A. Shiryaev, M.S. Nickolsky, Adsorbed natural gas storage facility based on activated carbon of wood waste origin, Adsorption 29 (2023) 291–307. https://doi.org/10.1007/s10450-022-00372-w.

[19] S.S. Chugaev, A.A. Fomkin, I.E. Men'shchikov, E.M. Strizhenov, A.V. Shkolin, Adsorption Accumulation of Liquefied Natural Gas Vapors, Prot. Met. Phys. Chem. Surf. 56 (2020) 897–903. https://doi.org/10.1134/S2070205120050081.

[20] M. Vashishtha, S. Gadipelli, K.V. Kumar, Deliverable Capacity of Methane: Required Material Property Levels for the Ideal "Holy Grail" Adsorbent, Chem Bio Eng. 2 (2024) 64–67. https://doi.org/10.1021/cbe.4c00127.

[21] C. Beal, The Viscosity of Air, Water, Natural Gas, Crude Oil and Its Associated Gases at Oil Field Temperatures and Pressures, Trans. AIME 165 (1946) 94–115. https://doi.org/10.2118/946094-G.

[22] P. Alexander, S. Al-Obaidi, Influence of Temperature And Pressure Of Incoming Oil-Containing Liquid from Field Wells On The Gas Separation Process, 3 (2001) 20–24. https://doi.org/10.31224/osf.io/2vdyw.

[23] Z. Nie, Y. Lin, X. Jin, Research on the theory and application of adsorbed natural gas used in new energy vehicles: A review, Front. Mech. Eng. 11 (2016) 258–274. https://doi.org/10.1007/s11465-016-0381-2.

[24] Assessment of Fuel Economy Technologies for Light-Duty Vehicles, National Academies Press, Washington, D.C., 2011. https://doi.org/10.17226/12924.

[25] M. Ahmad, A.U. Rajapaksha, J.E. Lim, M. Zhang, N. Bolan, D. Mohan, M. Vithanage, S.S. Lee, Y.S. Ok, Biochar as a sorbent for contaminant management in soil and water: A review, Chemosphere 99 (2014) 19–33. https://doi.org/10.1016/j.chemosphere.2013.10.071.

[26] M. Belhachemi, B. Khiari, M. Jeguirim, A. Sepúlveda-Escribano, 3 - Characterization of biomass-derived chars, in: M. Jeguirim, L. Limousy (Eds.), Char Carbon Mater. Deriv. Biomass, Elsevier, 2019: pp. 69–108. https://doi.org/10.1016/B978-0-12-814893-8.00003-1.

[27] J. Shaheen, Y.H. Fseha, B. Sizirici, Performance, life cycle assessment, and economic comparison between date palm waste biochar and activated carbon derived from woody biomass, Heliyon 8 (2022) e12388. https://doi.org/10.1016/j.heliyon.2022.e12388.

[28] B. Glaser, M. Parr, C. Braun, G. Kopolo, Biochar is carbon negative, Nat. Geosci. 2 (2009) 2–2. https://doi.org/10.1038/ngeo395.

[29] B.Y. Sadasivam, K.R. Reddy, Adsorption and transport of methane in biochars derived from waste wood, Waste Manag. 43 (2015) 218–229. https://doi.org/10.1016/j.wasman.2015.04.025.

[30] Adsorption of Carbon Dioxide, Methane, and Their Mixtures in Porous Carbons: Effect of Surface Chemistry, Water Content, and Pore Disorder | Langmuir, https://pubs.acs.org/doi/10.1021/la3048938.

[31] X. Yang, D. Jiang, X. Cheng, C. Yuan, S. Wang, Z. He, S. Esakkimuthu, Adsorption properties of seaweed-based biochar with the greenhouse gases (CO_2, CH_4, N_2O) through density functional theory (DFT), Biomass Bioenergy 163 (2022) 106519. https://doi.org/10.1016/j.biombioe.2022.106519.

[32] S. Sethupathi, M. Zhang, A. Rajapaksha, S. Lee, N. Mohamad Nor, A. Mohamed, M. Al-Wabel, S. Lee, Y. Ok, Biochars as Potential Adsorbers of CH_4, CO_2 and H_2S, Sustainability 9 (2017) 121. https://doi.org/10.3390/su9010121.

[33] B.Y. Sadasivam, K.R. Reddy, Adsorption and transport of methane in landfill cover soil amended with waste-wood biochars, J. Environ. Manage. 158 (2015) 11–23. https://doi.org/10.1016/j.jenvman.2015.04.032.

[34] B.Y. Sadasivam, K.R. Reddy, Study of Methane Adsorption by Biochar in Landfill Cover, Department of Civil and Materials Engineering, University of Illinois at Chicago, Chicago, IL 60607, U.S.A (2014) 12982.

[35] Y. Lu, Q. Liu, L. Fu, Y. Hu, L. Zhong, S. Zhang, Q. Liu, Q. Xie, The effect of modified biochar on methane emission and succession of methanogenic archaeal community in paddy soil, Chemosphere 304 (2022) 135288. https://doi.org/10.1016/j.chemosphere.2022.135288.

[36] V.Y. Ko, J. Wang, I. He, D. Ryan, X. Zhang, C. Lan, Adsorption of methane on biochar for emission reduction in oil and gas fields, Biochar 5 (2023) 15. https://doi.org/10.1007/s42773-023-00209-x.

[37] R. Azargohar, A. Dalai, Steam and KOH activation of biochar: Experimental and modeling studies, Microporous Mesoporous Mater. 110 (2008) 413–421. https://doi.org/10.1016/j.micromeso.2007.06.047.

[38] E.M. Mistar, T. Alfatah, M.D. Supardan, Synthesis and characterization of activated carbon from Bambusa vulgaris striata using two-step KOH activation, J. Mater. Res. Technol. 9 (2020) 6278–6286. https://doi.org/10.1016/j.jmrt.2020.03.041.

[39] C. Moreno-Castilla, F. Carrasco-Marın, M.V. Lopez-Ramon, M.A. Alvarez-Merino, Chemical and physical activation of olive-mill waste water to produce activated carbons, (2001).

[40] L. Hui, S.F. Kong, Y.S. Liu, H. Zeng, Application of Plasma Technology in Surface Modification of Carbon Materials, Appl. Mech. Mater. 319 (2013) 102–106. https://doi.org/10.4028/www.scientific.net/AMM.319.102.

[41] R.K. Gupta, M. Dubey, P. Kharel, Z. Gu, Q.H. Fan, Biochar activated by oxygen plasma for supercapacitors, J. Power Sources 274 (2015) 1300–1305. https://doi.org/10.1016/j.jpowsour.2014.10.169.

[42] S. Corujeira-Gallo, H. Dong, Effect of microstructure on the plasma surface treatment of carbon fibres, J. Compos. Mater. 51 (2017) 3239–3256. https://doi.org/10.1177/0021998316684935.

[43] M.M. Cherif, I. Assadi, L. Khezami, N. Ben Hamadi, A.A. Assadi, W. Elfalleh, Review on Recent Applications of Cold Plasma for Safe and Sustainable Food Production: Principles, Implementation, and Application Limits, Appl. Sci. 13 (2023) 2381. https://doi.org/10.3390/app13042381.

[44] S. Jayasinghe, D. Pasan Siriwardena, I. Munaweera, C. Perera, N. Kottegoda, Sustainable Synthesis of Highly Functionalized Activated Carbon using Plasma Technology, ChemPlusChem 87 (2022). https://doi.org/10.1002/cplu.202200202.

[45] J. Fennila, K.A. Vijayalakshmi, Renewable cold plasma exposed activated carbon-derived eucalyptus leaves (EL) as electrode in fabricating low-cost energy storage devices, Energy Sources Part Recovery Util. Environ. Eff. 46 (2024) 6743–6760. https://doi.org/10.1080/15567036.2024.2353179.

[46] D.R. Kandel, H.-J. Kim, J.-M. Lim, M.B. Poudel, M. Cho, H.-W. Kim, B.-T. Oh, C. Nah, S.H. Lee, B. Dahal, J. Lee, Cold plasma-assisted regeneration of biochar for dye adsorption, Chemosphere 309 (2022) 136638. https://doi.org/10.1016/j.chemosphere.2022.136638.

[47] R. Zhou, X. Wang, R. Zhou, J. Weerasinghe, T. Zhang, Y. Xin, H. Wang, P. Cullen, H. Wang, K.K. Ostrikov, Non-thermal plasma enhances performances of biochar in wastewater treatment and energy storage applications, Front. Chem. Sci. Eng. 16 (2022) 475–483. https://doi.org/10.1007/s11705-021-2070-x.

[48] O. Kazak, A. Tor, Characteristics and mechanisms for highly efficient adsorption of Pb (II) from aqueous solutions by engineered vinasse biochar with cold oxygen plasma process, Chem. Eng. Process. - Process Intensif. 171 (2022) 108766. https://doi.org/10.1016/j.cep.2021.108766.

[49] M. Mozetič, A. Vesel, G. Primc, R. Zaplotnik, Introduction to Plasma and Plasma Diagnostics, in: Non-Therm. Plasma Technol. Polym. Mater., Elsevier, 2019: pp. 23–65. https://doi.org/10.1016/B978-0-12-813152-7.00002-0.

[50] A. Arpanaei, B. Winther-Jensen, E. Theodosiou, P. Kingshott, T.J. Hobley, O.R.T. Thomas, Surface modification of chromatography adsorbents by low temperature low pressure plasma, J. Chromatogr. A 1217 (2010) 6905–6916. https://doi.org/10.1016/j.chroma.2010.08.069.

[51] D. Thiry, A. Chauvin, A.-A. El Mel, C. Cardinaud, J. Hamon, E. Gautron, N. Stephant, A. Granier, P.-Y. Tessier, Tailoring the chemistry and the nano-architecture of organic thin films using cold plasma processes, Plasma Process. Polym. 14 (2017) 1700042. https://doi.org/10.1002/ppap.201700042.

[52] S. Mujin, H. Baorong, W. Yisheng, T. Ying, H. Weiqiu, D. Youxian, The surface of carbon fibres continuously treated by cold plasma, Compos. Sci. Technol. 34 (1989) 353–364. https://doi.org/10.1016/0266-3538(89)90004-3.

[53] Z. Karoly, L. Romanszki, G. Weltz, M. Mohai, J. Moczo, Sz. Klebert, Comparison of dielectric barrier discharge and radio-frequency plasma processing of carbon fibers, Express Polym. Lett. 15 (2021) 1004–1017. https://doi.org/10.3144/expresspolymlett.2021.80.

[54] Y. Huang, Q. Yu, M. Li, S. Sun, H. Zhao, S. Jin, J. Fan, J. Wang, An overview of low-temperature plasma surface modification of carbon materials for removal of pollutants from liquid and gas phases, Plasma Process. Polym. 18 (2021) 2000171. https://doi.org/10.1002/ppap.202000171.

[55] B.K. Barnes, H. Ouro-Koura, J. Derickson, S. Lebarty, J. Omidokun, N. Bane, O. Suleiman, E. Omagamre, M.J. Fotouhi, A. Ogunmolasuyi, A. Dominguez, L. Gonick, K.S. Das, Plasma generation by household microwave oven for surface modification and other emerging applications, Am. J. Phys. 89 (2021) 372–382. https://doi.org/10.1119/10.0002706.

[56] M. Pitto, H. Fiedler, N.K. Kim, C.J.R. Verbeek, T.D. Allen, S. Bickerton, Carbon fibre surface modification by plasma for enhanced polymeric composite performance: A review, Compos. Part Appl. Sci. Manuf. 180 (2024) 108087. https://doi.org/10.1016/j.compositesa.2024.108087.

[57] S.U. Kang, C. Kim, S. You, D.-Y. Lee, Y.-K. Kim, S.-J. Kim, C.-K. Kim, H.-K. Kim, Plasma Surface Modification of 3Y-TZP at Low and Atmospheric Pressures with Different Treatment Times, Int. J. Mol. Sci. 24 (2023) 7663. https://doi.org/10.3390/ijms24087663.

[58] S. Chaple, C. Sarangapani, J. Jones, E. Carey, L. Causeret, A. Genson, B. Duffy, P. Bourke, Effect of atmospheric cold plasma on the functional properties of whole wheat (Triticum aestivum L.) grain and wheat flour, Innov. Food Sci. Emerg. Technol. 66 (2020) 102529. https://doi.org/10.1016/j.ifset.2020.102529.

[59] V. Damideh, O.H. Chin, H.A. Gabbar, S.J. Ch'ng, C.Y. Tan, Study of ozone concentration from CO_2 decomposition in a water cooled coaxial dielectric barrier discharge, Vacuum 177 (2020) 109370. https://doi.org/10.1016/j.vacuum.2020.109370.

[60] P.S. De Velasco-Maldonado, V. Hernández-Montoya, M.A. Montes-Morán, N.A.-R. Vázquez, Ma.A. Pérez-Cruz, Surface modification of a natural zeolite by treatment with cold oxygen plasma: Characterization and application in water treatment, Appl. Surf. Sci. 434 (2018) 1193–1199. https://doi.org/10.1016/j.apsusc.2017.11.023.

[61] R. Zhou, X. Wang, R. Zhou, J. Weerasinghe, T. Zhang, Y. Xin, H. Wang, P. Cullen, H. Wang, K.K. Ostrikov, Non-thermal plasma enhances performances of biochar in wastewater treatment and energy storage applications, Front. Chem. Sci. Eng. 16 (2022) 475–483. https://doi.org/10.1007/s11705-021-2070-x.

[62] O. Kazak, A. Tor, Characteristics and mechanisms for highly efficient adsorption of Pb(II) from aqueous solutions by engineered vinasse biochar with cold oxygen plasma process, Chem. Eng. Process. - Process Intensif. 171 (2022) 108766. https://doi.org/10.1016/j.cep.2021.108766.

[63] I. Langmuir, THE ADSORPTION OF GASES ON PLANE SURFACES OF GLASS, MICA AND PLATINUM., J. Am. Chem. Soc. 40 (1918) 1361–1403. https://doi.org/10.1021/ja02242a004.

[64] P. Maziarka, C. Wurzer, P.J. Arauzo, A. Dieguez-Alonso, O. Mašek, F. Ronsse, Do you BET on routine? The reliability of N_2 physisorption for the quantitative assessment of biochar's surface area, Chem. Eng. J. 418 (2021) 129234. https://doi.org/10.1016/j.cej.2021.129234.

[65] M. Thommes, K. Kaneko, A.V. Neimark, J.P. Olivier, F. Rodriguez-Reinoso, J. Rouquerol, K.S.W. Sing, Physisorption of gases, with special reference to the evaluation of surface area and pore size distribution (IUPAC Technical Report), Pure Appl. Chem. 87 (2015) 1051–1069. https://doi.org/10.1515/pac-2014-1117.

[66] K.C. Kim, T.-U. Yoon, Y.-S. Bae, Applicability of using CO_2 adsorption isotherms to determine BET surface areas of microporous materials, Microporous Mesoporous Mater. 224 (2016) 294–301. https://doi.org/10.1016/j.micromeso.2016.01.003.

[67] M. Thommes, K.A. Cychosz, Physical adsorption characterization of nanoporous materials: progress and challenges, (2014).

[68] Y. Tian, C. Yan, Z. Jin, Characterization of Methane Excess and Absolute Adsorption in Various Clay Nanopores from Molecular Simulation, Sci. Rep. 7 (2017) 12040. https://doi.org/10.1038/s41598-017-12123-x.

[69] G. Sigmund, T. Hüffer, T. Hofmann, M. Kah, Biochar total surface area and total pore volume determined by N_2 and CO_2 physisorption are strongly influenced by degassing temperature, Sci. Total Environ. 580 (2017) 770–775. https://doi.org/10.1016/j.scitotenv.2016.12.023.

[70] K.A. Cychosz, M. Thommes, Progress in the Physisorption Characterization of Nanoporous Gas Storage Materials, Engineering 4 (2018) 559–566. https://doi.org/10.1016/j.eng.2018.06.001.

[71] D. Lozano-Castelló, D. Cazorla-Amorós, A. Linares-Solano, Usefulness of CO_2 adsorption at 273 K for the characterization of porous carbons, Carbon 42 (2004) 1233–1242. https://doi.org/10.1016/j.carbon.2004.01.037.

[72] D. Cazorla-Amorós, J. Alcañiz-Monge, M.A. de la Casa-Lillo, A. Linares-Solano, CO_2 As an Adsorptive To Characterize Carbon Molecular Sieves and Activated Carbons, Langmuir 14 (1998) 4589–4596. https://doi.org/10.1021/la980198p.

[73] A. Mukhtar, N. Mellon, S. Saqib, S.-P. Lee, M.A. Bustam, Extension of BET theory to CO_2 adsorption isotherms for ultra-microporosity of covalent organic polymers, SN Appl. Sci. 2 (2020) 1–4. https://doi.org/10.1007/s42452-020-2968-9.

[74] A. Aleghafouri, M. Mohsen-Nia, A. Mohajeri, M. Mahdyarfar, M. Asghari, Micropore Size Analysis of Activated Carbons Using Nitrogen, Carbon Dioxide and Methane Adsorption Isotherms: Experimental and Theoretical Studies, Adsorpt. Sci. Technol. 30 (2012) 307–316. https://doi.org/10.1260/0263-6174.30.4.307.

[75] C.M. Lastoskie, A Modified Horvath-Kawazoe Method for Micropore Size Analysis, in: K.K. Unger, G. Kreysa, J.P. Baselt (Eds.), Stud. Surf. Sci. Catal., Elsevier, 2000: pp. 475–484. https://doi.org/10.1016/S0167-2991(00)80053-1.

[76] Y. Sun, S. Li, R. Sun, S. Yang, X. Liu, Modified Dubinin–Astakhov Model for the Accurate Estimation of Supercritical Methane Sorption on Shales, ACS Omega 5 (2020) 16189–16199. https://doi.org/10.1021/acsomega.0c01675.

[77] S.G. Chen, R.T. Yang, Theoretical Basis for the Potential Theory Adsorption Isotherms. The Dubinin-Radushkevich and Dubinin-Astakhov Equations, Langmuir 10 (1994) 4244–4249. https://doi.org/10.1021/la00023a054.

[78] N. Saeidi, M. Parvini, Accuracy of Dubinin-Astakhov and Dubinin-Radushkevich Adsorption Isotherm Models in Evaluating Micropore Volume of Bentonite, Period. Polytech. Chem. Eng. 60 (2016) 123–129. https://doi.org/10.3311/PPch.8374.

[79] T.S. Jakubov, D.E. Mainwaring, Modified Dubinin–Radushkevich/Dubinin–Astakhov Adsorption Equations, J. Colloid Interface Sci. 252 (2002) 263–268. https://doi.org/10.1006/jcis.2002.8498.

[80] A. Gil, S.A. Korili, G.Yu. Cherkashinin, Extension of the Dubinin–Astakhov equation for evaluating the micropore size distribution of a modified carbon molecular sieve, J. Colloid Interface Sci. 262 (2003) 603–607. https://doi.org/10.1016/S0021-9797(03)00066-3.

[81] M.W. Maddox, J.P. Olivier, K.E. Gubbins, Characterization of MCM-41 Using Molecular Simulation: Heterogeneity Effects, Langmuir 13 (1997) 1737–1745. https://doi.org/10.1021/la961068o.

[82] B. Sun, S. Kayal, A. Chakraborty, Study of HKUST (Copper benzene-1,3,5-tricarboxylate, Cu-BTC MOF)-1 metal organic frameworks for CH_4 adsorption: An experimental

Investigation with GCMC (grand canonical Monte-carlo) simulation, Energy 76 (2014) 419–427. https://doi.org/10.1016/j.energy.2014.08.033.

[83] P.A. Gauden, A.P. Terzyk, S. Furmaniak, P. Kowalczyk, Adsorption potential distributions for carbons having defined pore structure—GCMC simulations of the effect of heterogeneity, Adsorption 15 (2009) 99–113. https://doi.org/10.1007/s10450-009-9158-9.

[84] J. Jagiello, C. Ania, J.B. Parra, C. Cook, Dual gas analysis of microporous carbons using 2D-NLDFT heterogeneous surface model and combined adsorption data of N_2 and CO_2, Carbon 91 (2015) 330–337. https://doi.org/10.1016/j.carbon.2015.05.004.

[85] C. Weidenthaler, Pitfalls in the characterization of nanoporous and nanosized materials, Nanoscale 3 (2011) 792–810. https://doi.org/10.1039/C0NR00561D.

[86] B. Salopek, D. Krasi, S. Filipovi, measurement and application of zeta potential.

[87] C. Schlumberger, M. Thommes, Characterization of Hierarchically Ordered Porous Materials by Physisorption and Mercury Porosimetry—A Tutorial Review, Adv. Mater. Interfaces 8 (2021) 2002181. https://doi.org/10.1002/admi.202002181.

[88] J. Serafin, K. Kiełbasa, B. Michalkiewicz, The new tailored nanoporous carbons from the common polypody (Polypodium vulgare): The role of textural properties for enhanced CO_2 adsorption, Chem. Eng. J. 429 (2022) 131751. https://doi.org/10.1016/j.cej.2021.131751.

[89] A.M. Silvestre-Albero, J.M. Juárez-Galán, J. Silvestre-Albero, F. Rodríguez-Reinoso, Low-Pressure Hysteresis in Adsorption: An Artifact?, J. Phys. Chem. C 116 (2012) 16652–16655. https://doi.org/10.1021/jp305358y.

[90] T. Zelenka, Adsorption and desorption of nitrogen at 77 K on micro- and meso- porous materials: Study of transport kinetics, Microporous Mesoporous Mater. 227 (2016) 202–209. https://doi.org/10.1016/j.micromeso.2016.03.009.

[91] J. Jagiello, M. Thommes, Comparison of DFT characterization methods based on N_2, Ar, CO_2, and H_2 adsorption applied to carbons with various pore size distributions, Carbon 42 (2004) 1227–1232. https://doi.org/10.1016/j.carbon.2004.01.022.

[92] K.A. Cychosz, M. Thommes, Progress in the Physisorption Characterization of Nanoporous Gas Storage Materials, Engineering 4 (2018) 559–566. https://doi.org/10.1016/j.eng.2018.06.001.

[93] J. Jagiello, M. Thommes, Comparison of DFT characterization methods based on N_2, Ar, CO_2, and H_2 adsorption applied to carbons with various pore size distributions, Carbon 42 (2004) 1227–1232. https://doi.org/10.1016/j.carbon.2004.01.022.

[94] S. Dantas, K.C. Struckhoff, M. Thommes, A.V. Neimark, Pore size characterization of micro-mesoporous carbons using CO_2 adsorption, Carbon 173 (2021) 842–848. https://doi.org/10.1016/j.carbon.2020.11.059.

[95] H. Ansari, L. Joss, J. Hwang, J.P.M. Trusler, G. Maitland, R. Pini, Supercritical adsorption in micro- and meso-porous carbons and its utilisation for textural characterisation, Microporous Mesoporous Mater. 308 (2020) 110537. https://doi.org/10.1016/j.micromeso.2020.110537.

[96] P.I. Ravikovitch, A. Vishnyakov, R. Russo, A.V. Neimark, Unified Approach to Pore Size Characterization of Microporous Carbonaceous Materials from N_2, Ar, and CO_2 Adsorption Isotherms, Langmuir 16 (2000) 2311–2320. https://doi.org/10.1021/la991011c.

[97] C. Weidenthaler, Pitfalls in the characterization of nanoporous and nanosized materials, Nanoscale 3 (2011) 792–810. https://doi.org/10.1039/C0NR00561D.

[98] W. Xu, M. Fayaz Torshizi, E. Müller, Effect of surface roughness and morphology on the adsorption and transport of CH_4/CO_2 mixtures in nanoporous carbons, J. CO_2 Util. 79 (2024) 102649. https://doi.org/10.1016/j.jcou.2023.102649.

[99] M. Hong, L. Zhang, Z. Tan, Q. Huang, Effect mechanism of biochar's zeta potential on farmland soil's cadmium immobilization, Environ. Sci. Pollut. Res. 26 (2019) 19738–19748. https://doi.org/10.1007/s11356-019-05298-5.

[100] K.A. Vijayalakshmi, K.C. Sowmiya, High capacitance sustainable low-cost cold plasma exposed activated carbon electrode derived from orange peel waste to eco-friendly technique, Carbon Lett. 34 (2024) 1737–1754. https://doi.org/10.1007/s42823-024-00722-4.

[101] C. Saka, Overview on the Surface Functionalization Mechanism and Determination of Surface Functional Groups of Plasma Treated Carbon Nanotubes, Crit. Rev. Anal. Chem. 48 (2018) 1–14. https://doi.org/10.1080/10408347.2017.1356699.

[102] A. Memetova, I. Tyagi, R. Rao Karri, Suhas, N. Memetov, A. Zelenin, R. Stolyarov, A. Babkin, V. Yagubov, I. Burmistrov, A. Tkachev, V. Bogoslovskiy, G. Shigabaeva, E. Galunin, High-Density Nanoporous carbon materials as storage material for Methane: A value-added solution, Chem. Eng. J. 433 (2022) 134608. https://doi.org/10.1016/j.cej.2022.134608.

[103] M.C. Almazán-Almazán, M. Pérez-Mendoza, M. Domingo-García, I. Fernández-Morales, F. del Rey-Bueno, A. García-Rodríguez, F.J. López-Garzón, The role of the porosity and oxygen groups on the adsorption of n-alkanes, benzene, trichloroethylene and 1,2-dichloroethane on active carbons at zero surface coverage, Carbon 45 (2007) 1777–1785. https://doi.org/10.1016/j.carbon.2007.05.003.

[104] M. Keiluweit, P.S. Nico, M.G. Johnson, M. Kleber, Dynamic Molecular Structure of Plant Biomass-Derived Black Carbon (Biochar), Environ. Sci. Technol. 44 (2010) 1247–1253. https://doi.org/10.1021/es9031419.

[105] R. Janu, V. Mrlik, D. Ribitsch, J. Hofman, P. Sedláček, L. Bielská, G. Soja, Biochar surface functional groups as affected by biomass feedstock, biochar composition and pyrolysis

temperature, Carbon Resour. Convers. 4 (2021) 36–46. https://doi.org/10.1016/j.crcon.2021.01.003.

[106] K. Jindo, H. Mizumoto, Y. Sawada, M.A. Sanchez-Monedero, T. Sonoki, Physical and chemical characterization of biochars derived from different agricultural residues, Biogeosciences 11 (2014) 6613–6621. https://doi.org/10.5194/bg-11-6613-2014.

[107] A. Enders, N. North, C. Fensore, J. Velez-Alvarez, H. Allen, Functional Group Identification for FTIR Spectra Using Image-Based Machine Learning Models, (2021). https://doi.org/10.26434/chemrxiv.14188679.v1.

[108] R. Wahab, M. Mustafa, N. Fauzi, H. Samsi, Thermal Degradation Analysis on 4-year-old Culms of Cultivated Tropical Bamboo Bambusa Vulgaris, J. Agric. Stud. 5 (2017) 50. https://doi.org/10.5296/jas.v5i3.11664.

[109] F. Fouchal, J.A.G. Knight, P.M. Dickens, Monitoring the polymerization of a diglycidyl ether bisphenol-A/2,2′-dimethyl-4,4′-methylenebis (cyclohexylamine) matrix with a Fourier transform infrared optical fibre sensor, Proc. Inst. Mech. Eng. Part L 218 (2004) 331–342. https://doi.org/10.1177/146442070421800407.

[110] L. Rinawati, R.E. Nugraha, R. Mahdia, I. Munifa, U. Chasanah, S. Wahyuningsih, A. Ramelan, Increasing the effectiveness of pesticides-based urea nanofertilizer encapsulatednanosilica with addition of rice husk TiO 2 additive substances, J. Chem. Pharm. Res. 2015 (2015) 85–89.

[111] FTIR Functional Group Database Table with Search - InstaNANO,. https://instanano.com/all/characterization/ftir/ftir-functional-group-search/.

[112] J. Černý, ALIPHATIC C-H BOND RESPONSES IN THE 900-700 cm−1 REGION OF THE FTIR SPECTRA OF COAL TARS, Fuel Sci. Technol. Int. 13 (1995) 807–818. https://doi.org/10.1080/08843759508947707.

Chapter 5. Cold plasma treated biochars and activated carbons for CH_4 adsorption: effects of raw material properties and plasma source gases[3]

This chapter is based on the article submitted to *Environmental Science and Technology*

Graphic abstract:

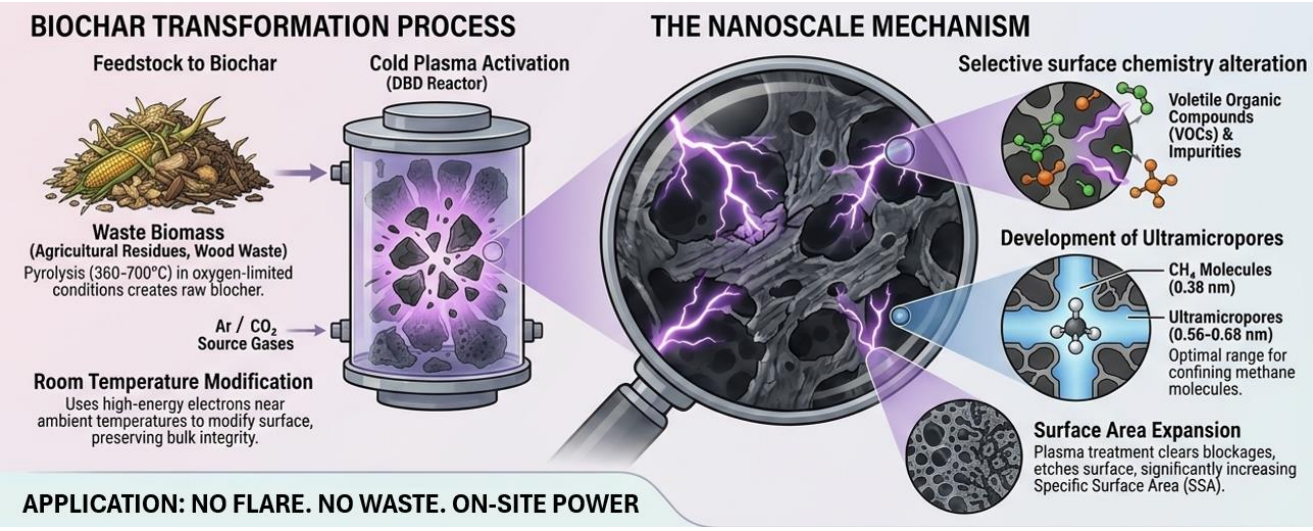

[3] V. Y. Ko, J. Wang, C. Lan, and D. Ryan, "Cold plasma treated biochars and activated carbons for CH4 adsorption: effects of raw material properties and plasma source gases" submitted to *Environmental Science and Technology*.

Abstract

The flaring of associated gas from oil fields motivates development of low-cost, distributed natural gas storage solutions. This study demonstrates that cold plasma treatment transforms waste biomass-derived biochars into effective methane (CH_4) adsorbents achieving up to 3.3 mmol/g at 75 bar and 298 K, representing enhancements of 23–73% driven by coupled volatile removal, ultramicropore development (0.56-0.68 nm), and feedstock-dependent surface chemistry. The enhancement mechanism operates through selective removal of volatile organic compounds that occlude micropore networks. Adsorption enhancement was dictated by material composition: the high-volatile biochar BC-D6 (waste-wood-derived) (17.4 wt%) achieved a 73% increase, whereas the low-volatile activated carbon AC-FB (commercial) showed only 1%, demonstrating that plasma effectiveness is constrained by the initial pore development and volatile content of the carbon framework. Alkaline minerals (CaO, MgO) in biochar neutralize plasma-generated acids, preserving hydrophobic surfaces consistent with maintaining a nonpolar surface environment favorable for CH_4 confinement. Effluent analysis quantified oxidation: non-oxidizing Ar/N_2 plasmas produced minimal CO_2 (0.03-0.04%) with maximum enhancements, while O_2/He generated 0.57% CO_2 (19-fold higher), indicating oxidizing plasma conditions associated with unfavorable surface modification for CH_4 adsorption. A composition-dependent framework was developed to guide treatment design, demonstrating that matching plasma source gas to feedstock enables predictive optimization. Plasma-enhanced biochars offer advantages over conventional adsorbents—utilizing waste feedstocks, requiring simple processing, and enabling modular adsorbed natural gas systems operating safely at <60 bar for distributed oil field applications. This approach transforms flared gas into capturable energy while valorizing agricultural residues, addressing energy security and sustainability.

Keywords:

CH_4 adsorption, natural gas storage, biochar, cold plasma, surface modification, plasma source gas

Highlights:

- Cold plasma treatment enhances biochar CH_4 adsorption by 23-73% through ultramicropore development
- Initial volatile matter strongly correlates with plasma-induced surface area gain
- Oxidizing plasmas with air or O_2/He reduces plasma effectiveness
- Ar and CO_2 were most effective as plasma source gases, but CO_2 is more appealing practically

5.1 Introduction

Natural gas (NG), predominantly composed of CH_4, is a promising fuel due to its lower carbon footprint compared to other fossil fuels such as coal, delivering approximately twice the energy per unit of CO_2 emitted [1,2]. While the majority of natural gas is produced from dedicated gas fields, oil fields also generate large quantities of "associated gas" as a by-product of oil extraction. This associated gas is often flared because capturing it is economically impractical given the lack of infrastructure for gas handling [2]. Moreover, as a by-product of oil extraction, continuous production and sale of NG are impractical due to variable output and economic constraints [3,4].

Utilizing associated gas for on-site power and heat generation at oil fields could therefore offer an environmentally viable solution, provided that economically feasible technologies for its capture, storage, and utilization are developed. NG requires storage systems that can accommodate production fluctuations and meet variable on-site supply demands. Conventional storage methods rely on compressed natural gas (CNG) [5] or liquefied natural gas (LNG) [6], which require high-pressure vessels or cryogenic handling, posing safety and operational challenges [7].

Adsorbed natural gas (ANG) has emerged as a safer and more energy-efficient alternative, storing NG at lower pressures in porous materials [8]. By confining CH_4 molecules within micropores and ultramicropores of the adsorbent, ANG systems reduce both the compression energy required and the operational risks compared with CNG and LNG. ANG can achieve up to 80% of the volumetric energy density of CNG stored at 3,000 psi (20.7 MPa), while operating at pressures as low as 500 psi (3.4 MPa) [9]. This makes ANG particularly suitable for oil field applications, where safety, operational simplicity, and the handling of intermittent associated gas streams are critical [10–12]. While real-world applications of ANG in oil and gas operations are currently limited, this study represents a first attempt to capture and store associated gas using ANG, enabling efficient on-site CH_4 storage and its subsequent use for power generation and local energy supply.

The choice of adsorbent is critical to the performance of ANG systems, which must balance capacity, scalability, and cost [13]. Porous materials such as activated carbons, metal-organic frameworks (MOFs), porous organic polymers (POPs), and covalent organic frameworks (COFs) are widely studied for ANG due to their high surface areas and tunable pore structures [14–16]. Activated carbons typically deliver 130–220 v/v at 35-65 bar and 298 K, while MOFs can exceed 260 v/v [8] though cost and scalability limit their practical use. In this study, a sustainable, low-cost alternative, biochar is introduced as an adsorbent. Engineered biochars with abundant

ultramicropores (<0.7 nm) achieve CH_4 uptakes of 1.5–2.5 mmol/g at 35 bar and 298 K [17], competitive with activated carbons. Beyond its adsorption performance, biochar offers broader sustainability advantages, including the beneficial use of waste biomass feedstocks, long-term carbon sequestration potential, and a lower environmental footprint than many conventional adsorbents [18]. For oil field operations, where associated gas is frequently flared due to economic and infrastructural barriers, ANG systems based on low-cost, locally produced biochars offer a practical solution. By enabling safe, low-pressure storage (<60 bar) in modular vessels, biochar-based ANG systems can capture, and store associated CH_4 for on-site use in power generation, heating, or local energy supply, transforming a waste by-product into a valuable energy resource.

Biochar is a pyrogenic carbon material produced from diverse biomass residues, including agricultural and forestry byproducts, manures, and biosolids, through thermochemical conversion under O_2-limited conditions, typically through slow or intermediate pyrolysis at 350–700 °C [19]. The physicochemical properties of biochar, including aromaticity, porosity, and ash composition, are strongly influenced by both feedstock composition and pyrolysis temperature [20]. Unlike activated carbon, which undergoes costly activation processes [21–23], biochar is produced through simple pyrolysis. Traditionally, biochar has been used in soil amendment and environmental remediation from landfill or water [24–26]. However, with minimal and inexpensive modifications, such as cold plasma treatment, biochar's adsorption capacity can be significantly enhanced, making it a viable and scalable solution for ANG applications.

Cold plasma, also referred to as non-thermal or non-equilibrium plasma, is a partially ionized gas in which electrons reach temperatures of around 10,000 K, while the overall gas temperature remains near ambient levels [27,28]. This allows cold plasma to operate at near-ambient temperatures while maintaining high electron energies, offering notable advantages over

conventional modification techniques [29–31]. Cold plasma treatment is widely recognized for its ability to functionalize surfaces, enhancing properties such as adhesion, wettability, chemical decontamination, membrane polymerization, wastewater purification, and food preservation [32–41]. This technique induces physical alterations, such as surface etching and cleaning, while increasing the content of surface functional groups (e.g., O_2- or N_2-containing), without altering the bulk properties of the material or introducing solvents and chemical contaminants, making it an environmentally friendly modification method [42,43]. Cold plasma has also gained attention for modifying carbon materials, such as activated carbons and graphene, due to its ability to enhance gas adsorption and catalytic properties [42,44–46]. In this study, we investigated how cold plasma treatment can enhance CH_4 storage by modifying the surface chemistry and porosity of three biochars and three commercial activated carbons, while assessing associated changes in their physical and chemical properties. Adsorbents were treated in a dielectric barrier discharge (DBD) reactor using five plasma source gases-argon (Ar), carbon dioxide (CO_2), nitrogen (N_2), an oxygen/helium (O_2/He) mixture, and air. Effluent gases were analyzed to identify reactive species generated during treatment and their influence on the adsorbent surface chemistry.

Surface pore structure was characterized using a BET instrument with CO_2 as the probe gas, specifically selected to probe porosity changes in the 0.4–0.7 nm range, critical for CH_4 adsorption due to CH_4's kinetic diameter (0.38 nm). Surface area and pore volume were determined using the Horváth–Kawazoe (HK) model, while density functional theory (DFT) pore size distribution was applied to account for the complex pore types and structures inherent in biochars and activated carbons. To comprehensively characterize the adsorbents pre- and post-plasma treatment, a suite of analytical techniques was employed: scanning electron microscopy (SEM) to examine surface morphology, zeta potential to assess surface charge, pH measurements to evaluate surface acidity,

attenuated total reflectance-Fourier transform infrared spectroscopy (ATR-FTIR) to identify changes in surface functional groups, and effluent gas analysis to understand plasma-induced chemical reactions.

5.2 Materials and methods

5.2.1 Materials

In this study, six porous carbon materials were evaluated as adsorbents: three biochars (BC-AT, BC-BL, and BC-D6) and three activated carbons (AC-CS, AC-DC, and AC-FB). BC-AT (AirTerra Inc.) was produced from pinewood; BC-BL (Bella Biochar Co.) was derived from landfill-diverted waste wood; and BC-D6 was prepared in-house from railway waste wood via pyrolysis at 600 °C for 15 min under a N_2 flow of 15 L/min at CanmetENERGY. The activated carbons included AC-CS from coconut shell, AC-DC procured from Sigma-Aldrich, and AC-FB from Fisher Scientific Ltd. The Ar gas (99.999 vol.%) was provided by Air Liquide Ltd. (Ottawa, Canada).

5.2.2 Structural property analyses

Physical, textural, and compositional properties of raw biochars and activated carbons were characterized prior to plasma treatment. The specific surface area (m^2/g) of each sample was measured using the Brunauer–Emmett–Teller (BET) method. Typically, N_2 is employed as the adsorbate gas in BET measurements. Biochar often contains abundant ultramicropores, and N_2 adsorption at 77 K can underestimate surface area due to diffusion limitations [47]. Therefore, CO_2 adsorption at 273 K over low relative pressures (P/P_0 = 0.001–0.03) was used to more reliably probe pores <0.7 nm and quantify ultramicroporosity. Physisorption isotherms for N_2 and CO_2

were measured using a BET instrument (ASAP2020 V3.00G, Micromeritics, USA) at 77 K and 273 K, respectively.

CO_2 adsorption data were analyzed using the HK method to calculate maximum pore volume and average pore width for pores smaller than 1 nm. Additionally, the DFT model was applied to derive pore size distributions within the 0.5–1 nm range, using a heterogeneous surface analysis approach. For evaluation purposes, this methodology was also applied to commercial activated carbons. Micropore characteristics, including specific surface area and pore volume within this range, were further estimated using the Dubinin–Astakhov (DA) method [47–50]. Based on our previous experimental experience [51], surface structural modifications induced by plasma treatment predominantly affect the micropore range (<2 nm). Accordingly, CO_2 adsorption at 273 K was employed in this study to probe microporous structural changes. CO_2 isotherms were analyzed over a P/P_0 range of 0.001–0.03. Using these data, the HK method was applied to calculate the maximum pore volume and median pore width for pores smaller than 1 nm, while the DFT model was used to derive the pore size distribution across the same range, employing a heterogeneous surface analysis approach for comprehensive characterization. For comparison, the same methodology was applied to activated carbons. Additionally, the DA method [52,53] was used to estimate specific surface area and pore volume in the micropore range (0.5–1 nm). Prior to measurements, all samples were degassed at 300 °C under vacuum for 600 min to eliminate strongly bound water from narrow micropores.

Specific pore volume (cm^3/g) and average pore width (nm) were determined using Horváth–Kawazoe (HK) method via MicroActive V.7 software. The HK method is a semi-empirical model commonly used for assessing pore size distributions in microporous materials, as it accounts for adsorbate–adsorbent interactions within slit-shaped pores.

Particle sizes (mm) were determined using sieve mesh sizes.

Skeletal density (g/mL) was measured using Helium pycnometer (Micromeritics AccuPyc II 1340) determining the volume of solid material excluding all pores and voids by measuring the pressure change of He gas in a calibrated chamber. Skeletal density was calculated as the ratio of sample mass to skeletal volume.

Bulk density was determined gravimetrically using a 5 mL sample reservoir, expressed as the mass of sample per unit volume (g/mL). A known mass of biochar or activated carbon was loaded into the graduated cylinder without compression to preserve the natural packing arrangement.

Porosity was calculated from the skeletal and bulk density measurements using the following equation:

$$\text{Porosity}\ (\%) = \left(1 - \frac{\text{bulk density}}{\text{skeletal density}}\right) \times 100 \tag{5.1}$$

Compositional analyses were performed on the raw materials prior to plasma treatment, including proximate analysis (moisture, ash, volatile matter, fixed carbon), ultimate analysis (C, H, N, O, S), and X-ray fluorescence (XRF) spectroscopy for metal oxides.

Proximate analysis was conducted following ASTM D3172 standards. Moisture content was determined by heating samples at 105–110 °C to constant weight. Ash content was measured by combustion at 750 °C for 3 hours under oxidizing conditions. Volatile matter was quantified by heating at 950 °C for 7 minutes under inert atmosphere, with mass loss (excluding moisture) representing the volatile fraction. Fixed carbon was calculated by difference: 100 − (moisture + ash + volatile matter).

Ultimate analysis was performed using an elemental analyzer (vario MACRO cube, Elementar). Samples (2–3 mg) were combusted at >900 °C in pure O_2, with resulting gases separated by gas chromatography and quantified by thermal conductivity detection. C, H, N, and S were directly measured; O content was calculated by difference: O (%) = 100 − (C + H + N + S + Ash). Atomic ratios H/C and O/C were calculated to characterize carbonization degree and surface oxidation state.

XRF spectroscopy (ZSX Primus IV, Rigaku) was employed to quantify metal oxide composition of the ash fraction. Major and minor oxide components (SiO_2, Al_2O_3, Fe_2O_3, CaO, MgO, K_2O, Na_2O, TiO_2, P_2O_5, SO_3) were determined and expressed as weight percentages of total ash.

5.2.3 Cold plasma treatment

The modification of biochar adsorbents was carried out using a parallel plate-type Dielectric Barrier Discharge (DBD) plasma reactor (CTP-2000K, ACS Material LLC) (Fig.5. 1a). As shown in Fig. 5.1b, the reactor consists of two parallel electrodes separated by a dielectric barrier, housed within a disc-shaped quartz glass chamber. The chamber measures 90 mm in diameter and 8 mm in depth, providing a controlled environment for plasma generation. Integrated gas inlet and outlet ports are incorporated into the reactor design to facilitate the flow of plasma-forming gas at a constant rate of 500 mL/min during operation.

Plasma was generated by applying a high-voltage sine wave across the electrodes, ionizing the gas within the chamber. The plasma generator operates at a discharge voltage range of 9–12 kV and a frequency range of 8–9 kHz, optimized by a step-up voltage transformer and a variable voltage controller. The power consumption of the system was maintained at approximately 200 W, as measured using a Tektronix TBS1102C-NEW oscilloscope and a P6015A-NEW passive high-

voltage probe. These parameters were selected to ensure stable and efficient plasma generation for biochar modification.

To monitor the electrical performance of the reactor, an oscilloscope probe was connected to the test port of the system. Real-time measurements of voltage amplitude, frequency, and current were recorded to ensure consistent plasma generation and to optimize the treatment process. The integration of the oscilloscope and high-voltage probe allowed for precise control and adjustment of the operational parameters during the experiment.

Adsorbent samples were placed within the quartz glass chamber and exposed to the plasma generated under the specified conditions. The treatment duration and gas flow rate (500 mL/min) were carefully controlled to ensure uniform modification of the biochar surface. The use of a dielectric barrier ensured that the discharge remained stable and prevented arcing, which could otherwise damage the samples or the reactor.

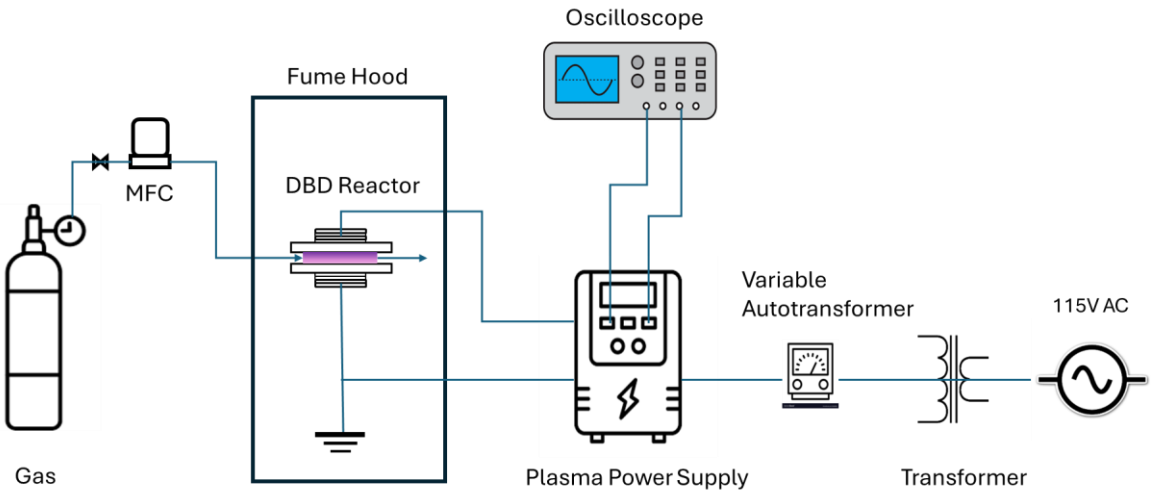

a

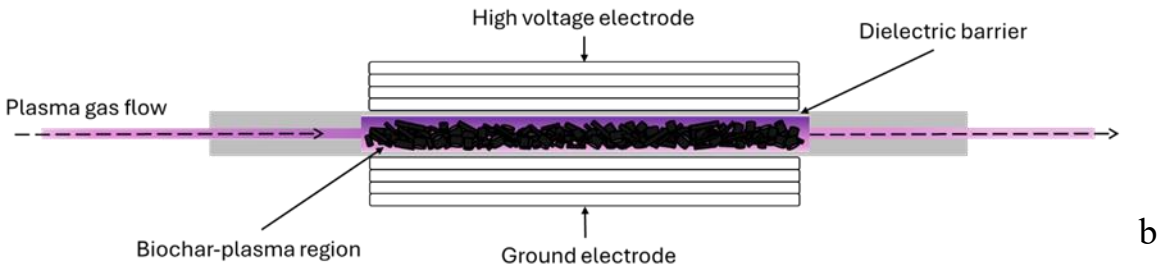

Fig. 5.1 Schematic diagram of the dielectric barrier discharge (DBD) experimental system (a) and the DBD reactor (b) for biochar modification

The plasma treatment was performed inside a fume hood to mitigate the risk of exposure to hazardous gases, such as ozone (O_3), which can form as a byproduct of parasitic discharges during plasma generation. Before initiating the treatment, a 2.8-3.4 g sample was loaded into the DBD reactor which had an internal volume of 51 mL (see Fig. 1b). To ensure an inert environment, the reactor chamber was purged with plasma-forming gas for 5 min, effectively displacing any residual air that could interfere with the plasma process. A step-up transformer was used to increase the input voltage from 110 V to 220 V, while a variable autotransformer (also known as a Variac) was employed to fine-tune and supply the high voltage required for the plasma power supply. This configuration allowed for precise control over the voltage delivered to the plasma reactor, ensuring stable and adjustable plasma generation. The experimental conditions, including voltage, frequency, gas flow rate, and treatment duration, are detailed in Table 5.1.

Once stable plasma discharge conditions were achieved within the reaction zone, the system parameters were further fine-tuned to optimize performance. Throughout the experiments, key electrical parameters, such as voltage, current, and frequency, were continuously monitored using an oscilloscope and a high-voltage probe.

Table 5.1 Variables tested in plasma modification at 500 mL/min, 11 kV, 8.2 kHz, 200 W, and 30 min

Sample	Precursor	Plasma source gas	Product
BC-AT-Raw	Waste wood	Ar	BC-AT-Ar
		Air	BC-AT-Air
		CO_2	BC-AT-CO_2
		N_2	BC-AT-N_2
		O_2-/He (23/77)	BC-AT-O_2He
BC-BL-Raw		Ar	BC-BL-Ar
BC-D6-Raw			BC-D6-Ar
AC-CS-Raw	Coconut shell		AC-CS-Ar
AC-DC-Raw	Petroleum coke		AC-DC-Ar
AC-FB-Raw	not specified by supplier		AC-FB-Ar

5.2.4 CH_4 adsorption measurements and isotherms

CH_4 adsorption measurements were performed using the PCTPro-2000 system (Setaram Inc.), based on the Sievert apparatus, a widely used volumetric instrument for measuring gas adsorption properties of materials, as schematically represented in Fig. 5.2. The instrument consists of two calibrated-volume reservoirs connected by an isolation valve. The adsorbent sample is loaded into the sample reservoir, and the initial pressure is recorded. The reference reservoir is then filled with CH_4 to a predetermined pressure. Upon opening the isolation valve, the gas equilibrates between the reference and sample reservoir. By knowing the initial gas pressures and the volumes of the system, the quantities of adsorbed or desorbed CH_4 can be determined. Adsorption isotherms were obtained by monitoring gas uptake through pressure changes within a calibrated volume. CH_4 was introduced into a 5 mL sample reservoir at pressures up to 75 bar in predetermined steps, maintaining a constant temperature of 25 °C with fluctuations controlled within ±0.5 °C to ensure precise measurements.

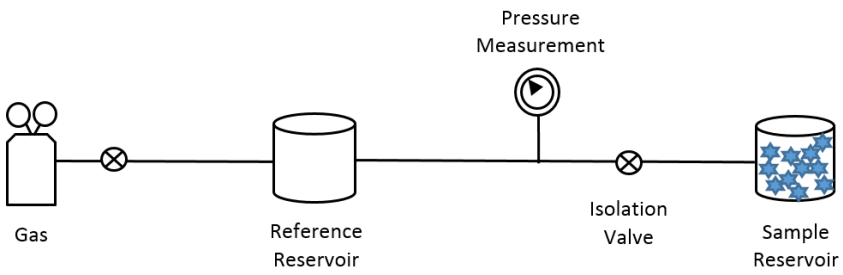

Fig. 5.2 A schematic of the Sievert measurement system

Prior to each experiment, the free volume of the sample reservoir was calibrated using He gas at the experimental temperature. Subsequently, CH_4 was pressurized in the reference reservoir and then released into the sample reservoir to facilitate adsorption. The amount of CH_4 adsorbed was calculated from the difference between the moles of gas introduced and the moles remaining in the gas phase at equilibrium, determined from pressure measurements. An automated computer program integrated into the analyzer incrementally increased the pressure to generate an adsorption isotherm. The program calculated the molar amounts of gas admitted into the reference reservoir and remaining at adsorption equilibrium by applying pressure-volume-temperature relations, utilizing non-ideal gas equations. At each pressure step, the program determined the difference in adsorption based on pressure variations between equilibrium states. The reduction in CH_4 gas pressure within the sample reservoir corresponded to the amount adsorbed by the sample. Gas quantities were correlated to pressure using the gas law, with compressibility factors determined under various pressure and temperature conditions, referencing the National Institute of Standards and Technology (NIST) database. All adsorption measurements were performed in duplicate, with results showing <5% variation between runs. Reported values represent the mean of replicate measurements.

The adsorption isotherms were analyzed using the Langmuir isotherm model to determine the CH_4 adsorption capacities of various adsorbents. The Langmuir equation is expressed as:

$$N = \frac{N_m * BP}{1+BP} \tag{5.2}$$

where N (mmol/g) is the amount of gas adsorbed at equilibrium, P (bar) is the gas pressure, N_m (mmol/g) represents the maximum adsorption capacity, and B (bar^{-1}) is the Langmuir constant. The parameters N_m and B are fitted parameters for a given adsorbent–adsorbate system at a given temperature and are independent of pressure. The Langmuir constant B reflects the affinity of CH_4 molecules for the surface of the adsorbents and can be interpreted as an apparent equilibrium constant within the Langmuir framework.

5.2.5 CH_4 adsorption performance metrics: plasma effectiveness (η) and surface concentration (γ)

To evaluate the performance of plasma treatment for enhancement of CH_4 adsorption, the plasma effectiveness (η) was calculated using Eq. 5.3:

$$\eta\ (\%) = \frac{A - A_0}{A_0} \times 100 \tag{5.3}$$

Here, A_o and A represent the CH_4 adsorption capacities of biochar or activated carbon (mmol/g) before and after plasma treatment, respectively.

η quantifies the relative improvement in CH_4 adsorption capacity induced by plasma treatment, defined as the fractional increase in CH_4 uptake of the treated material compared with its untreated

baseline. It provides a normalized measure of how responsive a given adsorbent is to plasma activation.

Additionally, to assess the effectiveness of the adsorbent surface in adsorbing CH_4, the surface concentration (γ) of CH_4 was defined by Eq. 5.4:

$$\gamma \left(\frac{\text{mol}}{\text{m}^2}\right) = \frac{\text{CH}_4 \text{ Adsorption capacity } \left(\frac{\text{mmol}}{\text{g}}\right)}{\text{Specific surface area } \left(\frac{\text{m}^2}{\text{g}}\right)} \times 1000 \tag{5.4}$$

γ describes the amount of additional CH_4 adsorbed per unit increase in specific surface area produced by plasma treatment. It serves as a metric of surface utilization efficiency, indicating how effectively generated surface contributes to CH_4 adsorption, and therefore reflects the fraction of plasma-created surface area that is adsorption-active.

While η and γ correlate positively across most samples, this correlation holds within a specific framework: cases where plasma predominantly generates new surface area. In practice, high γ can also arise from mechanisms that do not create new surface but instead make existing surface accessible, for example by widening narrow pore mouth constrictions to improve CH_4 diffusion, or useable, by tuning the internal pore width toward the optimal confinement range or by modifying pore wall chemistry to enhance instantaneous polarizability and strengthen London dispersion interactions with CH_4. These pathways contribute to increased CH_4 uptake per unit plasma energy without proportional increases in SSA, and their relative contribution depends on the starting material's pore structure and surface chemistry. The η–γ correlation reported here should therefore be interpreted as material-specific rather than universal.

5.2.6 Scanning electron microscopy (SEM)

SEM was utilized to investigate the surface morphology of adsorbents before and after plasma treatment. Samples were uniformly mounted onto conductive adhesive tape and examined using a Hitachi S-2500 SEM (Hitachi High-Technologies, Japan) at magnifications of ×100 and ×1,000, with a working distance of 10 mm and an accelerating voltage of 20 kV.

5.2.7 Suspension pH

The suspension pH of an adsorbent was measured before and after plasma treatment to evaluate chemical changes associated with surface modification. For each measurement, 0.01 g of sample was ground to <250 μm particle size and suspended in 10 mL of deionized (DI) water. Suspensions were equilibrated under gentle agitation to allow sufficient contact between the solid and liquid phases. pH values were recorded using a Thermo Fisher Scientific Orion Star pH/electrochemistry meter. Measurements were considered stable when the pH variation was less than ±0.1 units over 1 min. All determinations were performed in duplicate, and averaged values are reported.

5.2.8 Zeta potential

Electrokinetic (zeta) potential was determined to investigate the influence of plasma activation on the electrical surface charge of adsorbents. Zeta potential is a key parameter for evaluating electrostatic surface interactions in adsorption processes [54]. In this study, it serves as a comparative indicator of plasma-induced changes in surface ionizability in aqueous media, reflecting variations in the presence and accessibility of ionizable surface sites. To estimate the zeta potential, 0.01 g of biochar or activated carbon was ground (<250 μm) and dispersed in 10 mL of DI water. To promote homogeneous dispersion, suspensions were sonicated for 12 hours.

The pH of each sample was adjusted to 6.7 using 0.001 M HCl. No background electrolyte was added to preserve plasma-induced surface chemistry and avoid masking charge differences by extrinsic ions. Although ionic strength influences absolute zeta potential values, all samples were measured under identical conditions, allowing zeta potential to be used here as a comparative indicator of plasma-induced changes in surface polarity. Measurements were conducted using a Malvern Panalytical zeta potential analyzer (UK). For statistical reliability, three replicates were recorded per sample, and mean values were used for analysis.

5.2.9 Attenuated total reflectance-Fourier transform infrared spectroscopy (ATR-FTIR)

ATR-FTIR spectroscopy was employed to characterize the chemical and molecular properties of the adsorbent biochars and activated carbons, and to evaluate surface modifications induced by plasma treatment. Particular attention was given to identifying changes in hydroxyl, carboxyl, carbonyl, and aromatic functional groups that may influence adsorption behavior.

Spectral measurements were performed using a benchtop Cary 630 FTIR spectrometer (Agilent Technologies, USA). A germanium (Ge) single-reflection ATR module was selected over diamond due to its higher refractive index (n = 4.0 vs. 2.4), which minimizes spectral distortions arising from the comparable refractive indices of diamond and carbonaceous materials, thereby improving spectral resolution and reducing baseline interferences. This methodology enabled the identification of functional groups, chemical bonds, and by-products generated during plasma activation. Spectra were collected over the effective spectral range of 5,100 to 600 cm^{-1}. Spectral processing included ATR correction, baseline correction, and normalization prior to band assignment. Prior to analysis, each adsorbent was ground to a 60-mesh size (250 μm) using a

mortar and pestle to ensure uniform particle size and reproducible contact with the ATR crystal. Background spectra were recorded under identical conditions and subtracted automatically to remove atmospheric H_2O and CO_2 contributions.

5.2.10 Plasma effluent gas

The analysis of the plasma effluent gas was conducted to identify and quantify gaseous by-products generated from the interaction between the plasma and the adsorbent materials. Gas-phase products exiting the DBD reactor during plasma treatment of adsorbent samples were collected in a gas sampling bag and later analyzed with an Agilent 7890 GC refinery gas analyzer (Agilent Technologies), featuring flame ionization and thermal conductivity detectors (RGA-FID/TCD). This method enabled the identification and quantification of gaseous by-products generated from the plasma-biochar interaction.

5.3 Results and Discussions

5.3.1 Source gas dependent plasma modification of BC-AT

5.3.1.1 CH_4 adsorption

During the adsorption experiments, pressure was incrementally increased in a stepwise manner. CH_4 uptake was calculated based on pressure changes in the sample holder, which was connected to a high-pressure reservoir. The equilibrium adsorption capacity (mmol/g) was determined by dividing the amount of CH_4 adsorbed (calculated from pressure–composition–temperature (PCT) data) by the sample mass in grams.

The CH_4 adsorption isotherms of the BC-AT after being treated via different plasma source gases (Ar, CO_2, N_2, O_2/He, Air) are presented in Fig. 5.3.

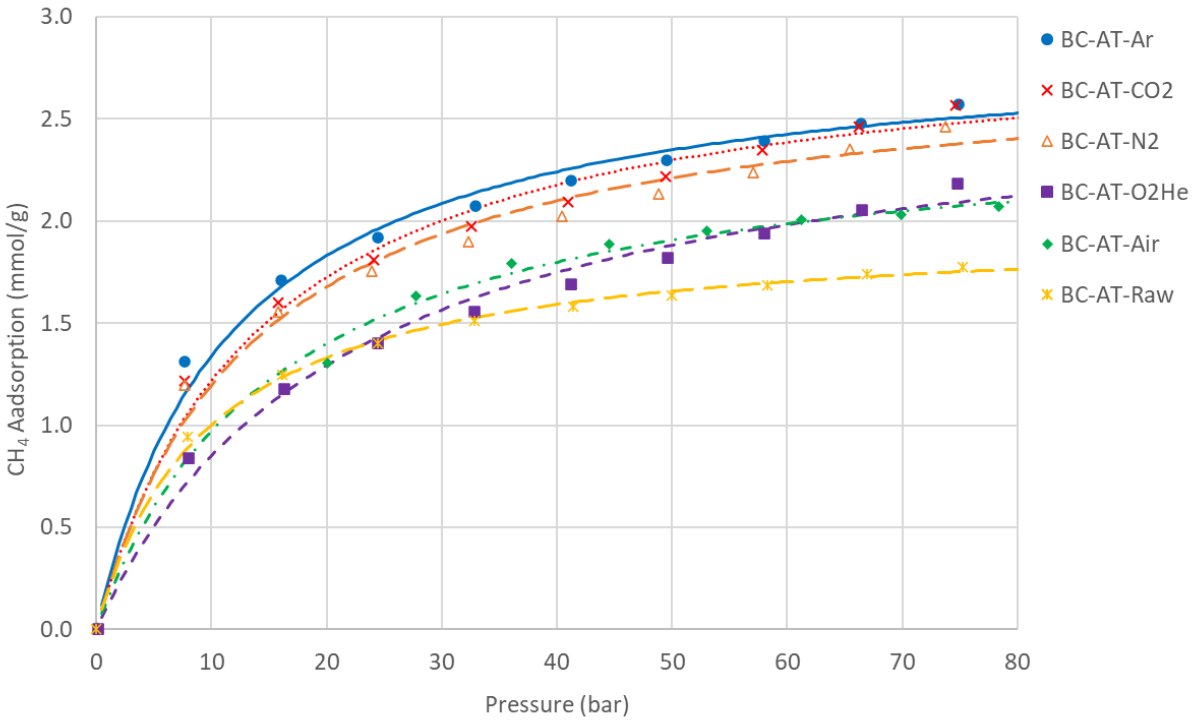

Fig. 5.3 Experimental CH_4 adsorption data and Langmuir adsorption isotherm of biochar (BC-AT) with different plasma source gases for 30 min

At low to moderate pressures, samples treated with Ar and CO_2 plasma consistently outperform others, showing steeper adsorption slopes and higher CH_4 uptakes due to dominant micropore filling mechanisms in ultramicropores typical of activated carbons and biochars [55]. At higher pressures (≥60 bar), the incremental uptake diminishes as micropores approach saturation and adsorption increasingly reflects surface excess on pore walls rather than additional micropore filling [56]. The Langmuir model provides an excellent empirical fit across the entire pressure range (R^2 = 0.9871–0.9958, Table 5.2), with the high-pressure plateau reflecting apparent

saturation associated with micropore filling and progressive densification of the adsorbed phase rather than a strict monolayer limit [57].

Table 5.2 Langmuir adsorption isotherm parameters of plasma source gases

Sample	Raw	BC-AT-Ar	BC-AT-CO_2	BC-AT-N_2	BC-AT-O_2/He	BC-AT-Air
R^2	0.9991	0.9958	0.9908	0.9916	0.9871	0.9955
N_m (mmol/g)	1.9794	2.90	2.95	2.81	2.70	2.52
B (bar^{-1})	0.1026	0.0859	0.0702	0.0743	0.0460	0.0627

5.3.1.2 Plasma effectiveness (η) and CH_4 surface concentration (γ) for BC-AT under different plasma gases

The isotherms in Figs. 5.3 and 5.6 demonstrate that all plasma treatments improve CH_4 uptake, but with varying degrees of success. To quantify these differences systematically and separate absolute capacity gains from surface utilization efficiency, two complementary metrics are introduced: η measuring relative adsorption improvement, and γ assessing CH_4 uptake per unit surface area.

Fig. 5.4 summarizes the coupled effects of plasma source gas on CH_4 adsorption enhancement, η, and γ for BC-AT after 30 min treatment. These metrics distinguish between absolute adsorption gains, surface utilization efficiency, and structural modification intensity. All percentage values represent changes relative to untreated BC-AT, enabling direct comparison of plasma source gas effects.

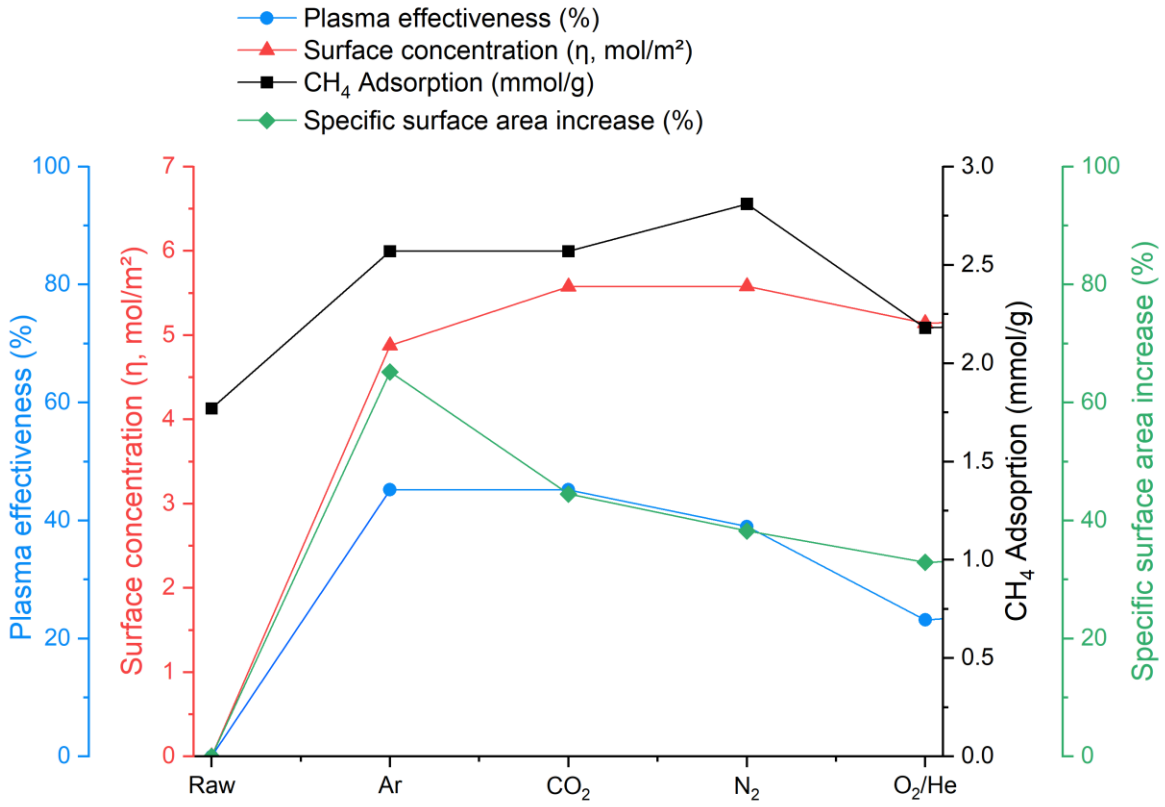

Fig. 5.4 Plasma effectiveness (η, %), surface concentration (γ, mmol CH_4/m2), CH_4 adsorption (mmol/g), and specific surface area increase (%) for BC-AT untreated (Raw) and treated for 30 min under different plasma source gases

All plasma treatments increase CH_4 uptake by 23–45%, with Ar and CO_2 producing the largest enhancements (η = 45%). These gains broadly follow the increase in specific surface area but with exceptions. Ar plasma produces the largest specific surface area increase (65%) but exhibits a relatively low γ (4.88 mol/m²), indicating that much of the newly generated surface is less adsorption-active, thereby limiting CH_4 uptake relative to its high specific surface area gain. Contrary to this, CO_2 plasma achieves a comparable CH_4 enhancement (45%) with a smaller specific surface area increase (45%) but higher γ, reflecting more effective generation of adsorption-relevant ultramicropores. Although Ar and CO_2 treatments produce identical absolute CH_4 uptakes (2.57 mmol/g) and equal η (45%), the higher γ associated with CO_2 indicates more

efficient utilization of accessible surface area, highlighting that CO_2 plasma preferentially generates adsorption-active ultramicropores rather than simply increasing total surface area. This divergence indicates that while specific surface area remains the primary driver of CH_4 adsorption, plasma source gas introduces secondary variations associated with pore accessibility and surface utilization efficiency. From an applicational perspective, since CO_2 is much cheaper and much more abundant than Ar, it would be a more favorable plasma source gas for large scale biochar plasma treatment.

Oxygen-containing plasmas (air and O_2/He) produce substantially smaller improvements in both specific surface area and CH_4 uptake, with O_2/He exhibiting the lowest η (23%). N_2 plasma shows intermediate behavior. Together, η and γ provide complementary metrics for distinguishing absolute adsorption enhancement from surface utilization efficiency across plasma environments, with CO_2 showing higher surface efficiency and Ar favoring surface area generation with comparatively lower adsorption efficiency per unit area.

5.3.2 Effect of raw material properties

5.3.2.1 Properties of raw biochars and activated carbons

The raw materials exhibit notable variations in textural and compositional properties (Tables 5.3 and 4). Among the biochars, BC-BL-Raw displays the highest specific surface area (506 m^2/g) and pore volume (0.128 cm^3/g), while BC-D6-Raw shows comparatively lower specific surface area (266 m^2/g) despite a moderate pore volume (0.116 cm^3/g). The activated carbons generally exhibited higher specific surface area, with AC-FB-Raw reaching 921 m^2/g, though its pore volume (0.053 cm^3/g) is lower than most other materials. Biochars generally contain higher

volatile matter compared with activated carbons. It is of great interest to observe that, although biochars and activated carbon have very diverse properties in many aspects, they exhibit certain common trends. For instance, all the three biochars, although of diverse skeletal densities, had very similar porosities ranging from 38-55%. On the other hand, the three activated carbons had porosities much smaller than the biochars but very similar to each other, in the range of 23-32% (Table 5.3).

Table 5.3 Physical, textural and bulk properties of raw biochars and activated carbons

Sample	Specific surface area (m^2/g)	Specific pore volume (cm^3/g)	Average pore width (nm)	Particle size (mm)	Bulk density (g/mL)	Skeletal density (g/mL)	Porosity (%)
BC-AT-Raw	319	0.085	0.6202	1.18 - 3.36	0.16	1.73	49
BC-BL-Raw	506	0.128	0.6227	1.60 - 6.40	0.23	2.03	38
BC-D6-Raw	266	0.116	0.6284	1.18 - 3.36	0.16	1.52	55
AC-CS-Raw	636	0.134	0.5550	0.71 - 1.68	0.50	2.15	23
AC-DC-Raw	443	0.108	0.5832	0.40 - 0.84	0.36	2.00	32
AC-FB-Raw	921	0.053	0.5575	1.41– 3.36	0.46	2.09	26

As listed in Table 5.4, while the ash content and moisture of different raw materials deviate from each other significantly without clear patterns, it can be observed that biochars generally contained higher volatile matter (11.4-17.4%) than activated carbons (2.58-6.59%). This is in accordance with the high H/C and O/C ratios of biochars versus those of activated carbons. Elemental compositions confirm the predominance of carbon in all samples (69–88 wt%), though with considerable variation in O_2 content. Notably, AC-FB-Raw contains the highest fixed carbon (87.7%) and lowest ash (2.62%). XRF analysis reveals significant differences in ash composition: AC samples contain elevated levels of SiO_2 and Al_2O_3, while biochars are richer in CaO, MgO,

and K_2O. These compositional features are likely to influence surface charge behavior, ionizable surface sites, and adsorbate–adsorbent interactions following plasma modification.

Table 5.4 Proximate, ultimate, and ash composition of the raw adsorbents

Sample	Moisture (%)	Ash (%)	Volatile matter (%)	Fixed carbon (%)	Elemental composition (wt%)							Ash composition (wt%)									
					C	H	N	S	O	H/C	O/C	SiO_2	Al_2O_3	Fe_2O_3	TiO	P_2O_5	CaO	MgO	SO_3	Na_2O	K_2O
BC-AT-Raw	8.5	4.6	11	76	82	1.3	0.4	<0.05	3.4	0.19	0.03	4.2	1.0	5.9	0.1	1.9	37	5.1	0.6	<0.20	14.1
BC-BL-Raw	3.8	18	12	66	69	0.7	0.5	<0.05	7.4	0.12	0.08	25	4.5	2.0	0.2	0.4	24	13	0.6	0.9	3.0
BC-D6-Raw	11	10	17	73	84	2.6	0.6	0.2	3.1	0.37	0.03	15	2.8	6.4	0.2	0.4	30	12	4.2	0.4	1.6
AC-CS-Raw	4.1	14	2.6	79	79	0.4	0.7	0.1	1.5	0.06	0.01	57	25	3.1	1.5	0.6	2.3	1.5	1.5	0.6	5.7
AC-DC-Raw	5.4	16	6.6	72	73	0.7	0.8	0.9	3.7	0.11	0.04	63	24	3.2	2.1	0.1	2.4	1.4	1.3	1.1	0.9
AC-FB-Raw	6.4	2.6	3.3	88	88	0.3	0.6	<0.05	2.5	0.04	0.02	23	0.5	1.4	0.0	1.8	2.0	1.8	4.1	2.8	27

Furthermore, as shown in Fig. 5.5, all the biochars and activated carbons show a near linear increase of moisture content with the volatile content, with BC-BL being the only outlier. This correlation is expected: the volatile fraction in biochars and activated carbons consists largely of oxygenated organic residues containing functional groups such as hydroxyl and carboxyl, which readily form hydrogen bonds with water and therefore attract moisture. BC-BL has a usually low moisture of 3.79% even though its volatile content is quite high (11.7%), which might be related to its unusually high ash content of 18.3% and the fact that its ash contains an unusually high portion of MgO (13.0%). Further studies are needed to confirm or disprove this hypothesis.

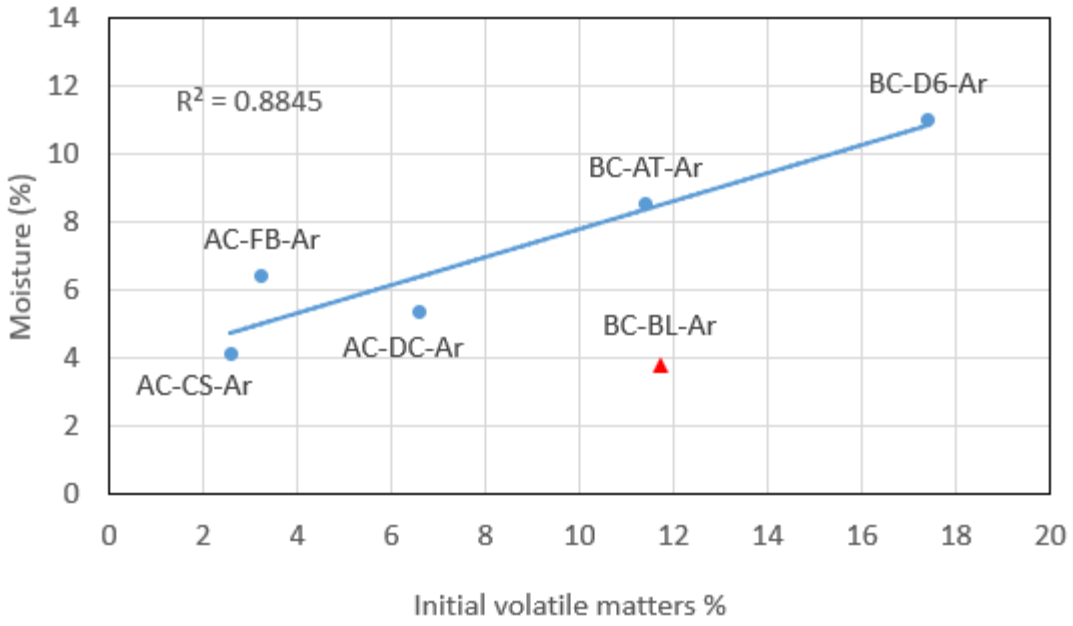

Fig. 5.5 Correlation between the moisture and volatile content of raw biochars and activated carbons

H/C and O/C denote atomic ratios calculated from ultimate analysis and are closely related to volatile matter in biochars and activated carbons. The H/C ratio is commonly used as an indicator of carbonization degree and aromatic condensation, whereas O/C reflects oxidation level and surface polarity [58,59]. As summarized in Table 5.4, activated carbons exhibit low H/C (0.04–0.11) and low O/C (0.01–0.04), consistent with highly carbonized and weakly oxygenated frameworks. By comparison, biochars span a wider compositional range, including BC-D6 with high O/C (0.56). The higher bulk O/C ratios of the biochars compared to the activated carbons imply intrinsically more O_2-rich and polar frameworks, and consequently more polar surfaces, provided that bulk and surface O/C ratios are correlated to each other.

5.3.2.2 CH_4 adsorption isotherms of Ar plasma treated biochars and activated carbons

Fig. 5.6 indicates that plasma treatment improves the CH_4 adsorption capacity of both the biochars and activated carbons: AC-FB-Ar has the highest capacity (5.80 mmol/g), followed by AC-CS and AC-DC. Although activated carbons significantly outperform biochars in CH_4 adsorption capacity, among biochars, BC-D6-Ar shows the best performance (3.33 mmol/g). Table 5.5 shows that all samples exhibit $R^2 > 0.98$, indicating excellent agreement with the Langmuir model.

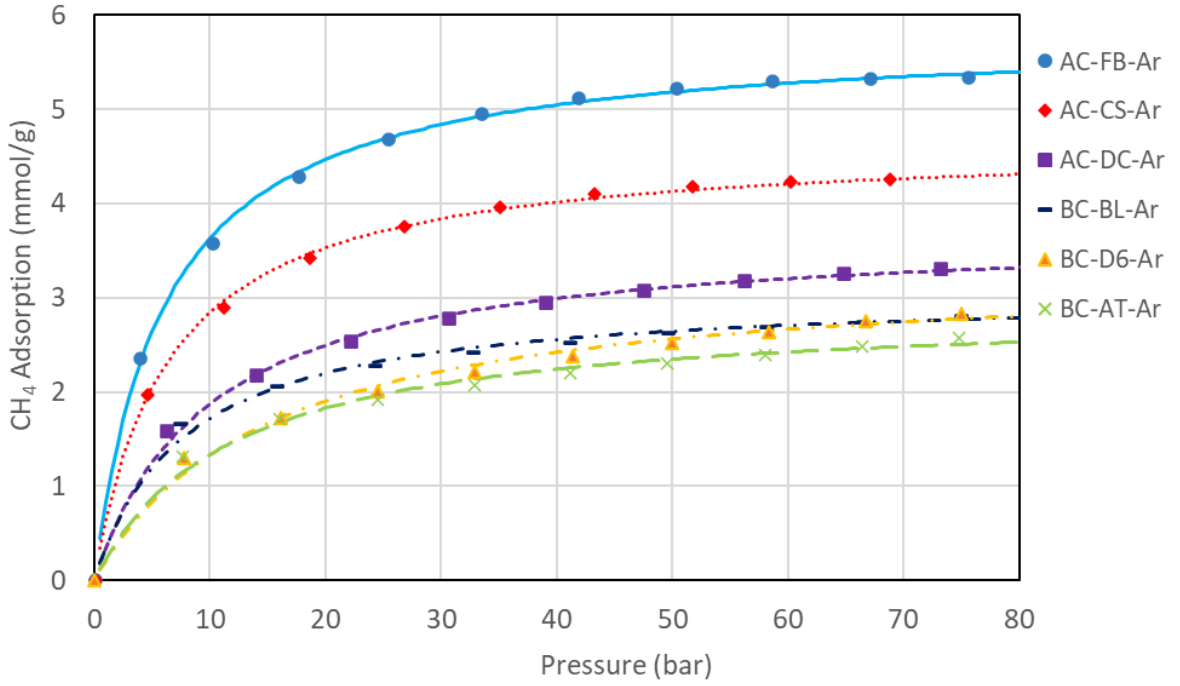

Fig. 5.6 CH_4 Adsorption data and Langmuir adsorption isotherm of biochars (BC-AT-Ar, BC-BL-Ar, BC-D6-Ar) and Ar-plasma treated activated carbons (AC-CS-Ar, AC-DC-Ar, AC-FB-Ar) after 30 min Ar-plasma treatment

Table 5.5 Langmuir adsorption isotherm parameters of biochars and activated carbons

Sample	BC-AT-Ar	BC-BL-Ar	BC-D6-Ar	AC-CS-Ar	AC-DC-Ar	AC-FB-Ar
R^2	0.9958	0.9986	0.9956	0.9997	0.9992	0.9998
N_m (mmol/g)	2.90	3.06	3.33	4.65	3.73	5.80
B (bar^{-1})	0.0859	0.1282	0.0664	0.1572	0.1010	0.1670

5.3.2.3 Plasma effectiveness (η) and CH_4 surface concentration (γ) of Ar plasma on biochars and activated carbons

Fig. 5.7 compares the increase in CH_4 adsorption capacity, specific surface area, and performance metrics (η, γ) induced by 30 min Ar plasma treatment across three biochars (BC-AT, BC-BL, BC-D6) and three commercial activated carbons (AC-CS, AC-DC, AC-FB). Values expressed as percentages represent changes relative to the corresponding untreated materials, enabling direct comparison of plasma response independent of large differences in initial properties.

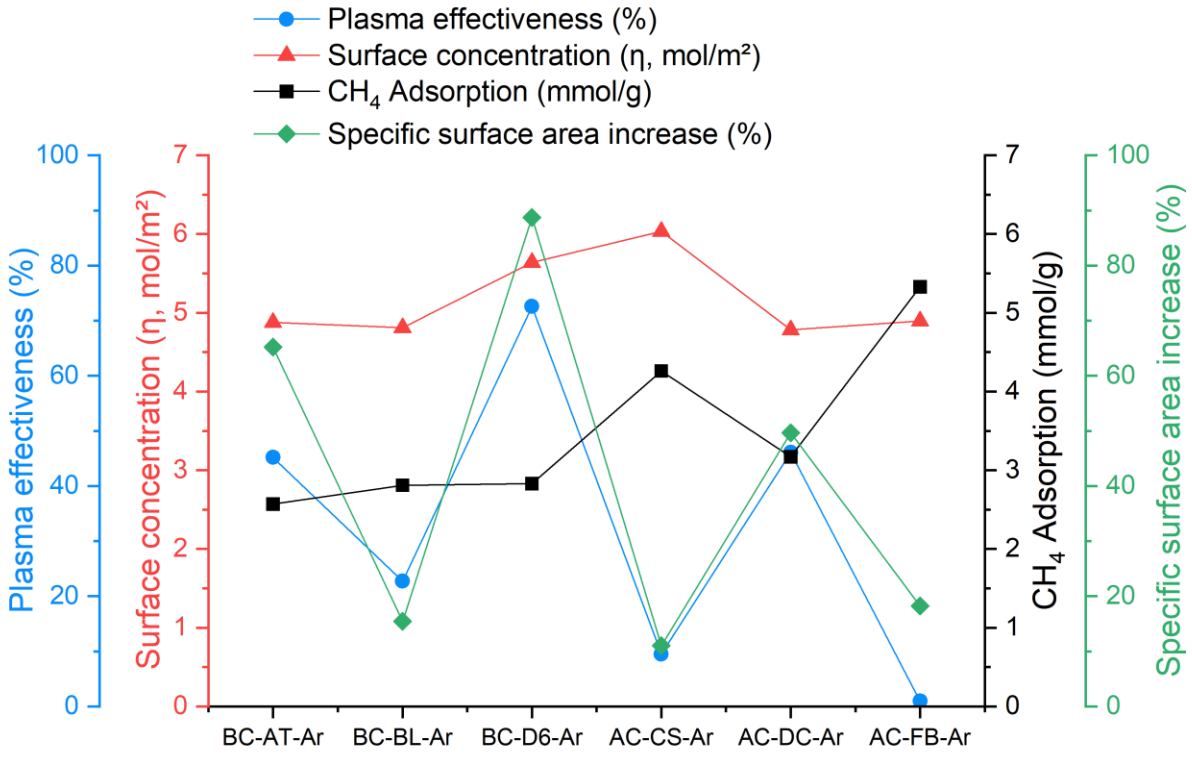

Fig. 5.7 Plasma effectiveness (η), surface concentration (γ), CH_4 adsorption (mmol/g), and specific surface area increase (%) after 30 min Ar-plasma treatment on biochars (AT, BL, D6) and activated carbons (CS, DC, FB)

Among the biochars, BC-D6 exhibits the highest η (73%) and the largest specific surface area increase (89%), accompanied by a high γ (5.6 mol/m²). BC-AT shows moderate η (45%) with a

substantial specific surface area increase (65%) and a slightly lower γ (4.9 mol/m²), suggesting effective but less optimal surface utilization relative to BC-D6. Despite its higher initial specific surface area, BC-BL exhibits a weaker plasma response than BC-D6. This behavior is consistent with the lower skeletal density of BC-D6 (1.52 vs. 2.03 g/mL for BC-BL) and comparable porosity (Table 5.3), indicating a more defective carbon structure that facilitates plasma-induced surface modifications.

Biochars and activated carbons, which start from lower baseline adsorption capacities, exhibit relatively higher η and γ values, indicating more efficient utilization of newly generated surface area following Ar plasma treatment. In contrast, BC-BL-Ar, AC-CS-Ar, AC-FB-Ar show lower η, γ and small specific surface increase rate, despite higher absolute specific surface area (Table 5.3), suggesting that their additional surface area contributes less effectively to CH_4 adsorption.

Among the three activated carbons, AC-FB, which has the largest initial specific surface area (921 m^2/g), shows the lowest and nearly negligible plasma effectiveness (0.9%) and specific surface area increase (18.2%), together with one of the smallest surface concentration (4.89 mol/m^2), indicating that its adsorption performance is already near intrinsic saturation and that additional plasma exposure yields limited benefit. This seems to be related to its low volatile content of 3.25%. This observation is to an extent confirmed by the response of AC-CS, which also has a low initial volatile matter (2.58%) and small η. The other activated carbon, i.e., AC-DC displayed the highest η (46%) and specific surface area increase (50%) among the three activated carbons, correlating well to the fact that it had the smallest initial specific surface area (443 m^2/g) and the highest volatile content among the three. These behaviors confirm that materials with highly

developed initial pore structures and low volatile content derive minimal benefit from further plasma activation.

While AC-DC and AC-FB achieve comparable absolute specific surface area gains, AC-DC show higher η and γ than AC-FB. AC-FB has very low pore volume (0.053 cm^3/g) and high skeletal density (2.09 g/mL), which indicate a dense pore network with limited capacity for further plasma-induced development (Table 5.3). In comparison, AC-DC, with larger average pore width (5.832 Å) but higher pore volume (0.108 cm^3/g), exhibits higher adsorption enhancement and specific surface area growth, reflecting greater structural adaptability under Ar plasma.

5.3.3 Drivers of CH_4 adsorption enhancement

5.3.3.1 Specific surface area

The plot in Fig. 5.8 demonstrates a strong linear relationship between specific surface area and CH_4 adsorption (R^2=0.9244) indicating that surface areas significantly drive adsorption capacity. Adsorbents with higher surface area likely offer more adsorption sites, directly contributing to enhanced CH_4 uptake. While deviations from the regression line reflect variations in pore geometry, surface chemistry, and material properties, surface area emerges as the primary predictor of CH_4 adsorption capacity across all materials tested. Consequently, evaluating plasma treatment effectiveness requires understanding how process conditions influence pore development and surface area generation. While surface area is a key predictor, optimal CH_4 adsorption requires a combination of high surface area, focused ultra-micropore distribution, and hydrophobic surface chemistry. This result supports the importance of pore development

(especially micropores and narrow mesopores) or surface roughness through activation processes (e.g., plasma treatment or chemical activation).

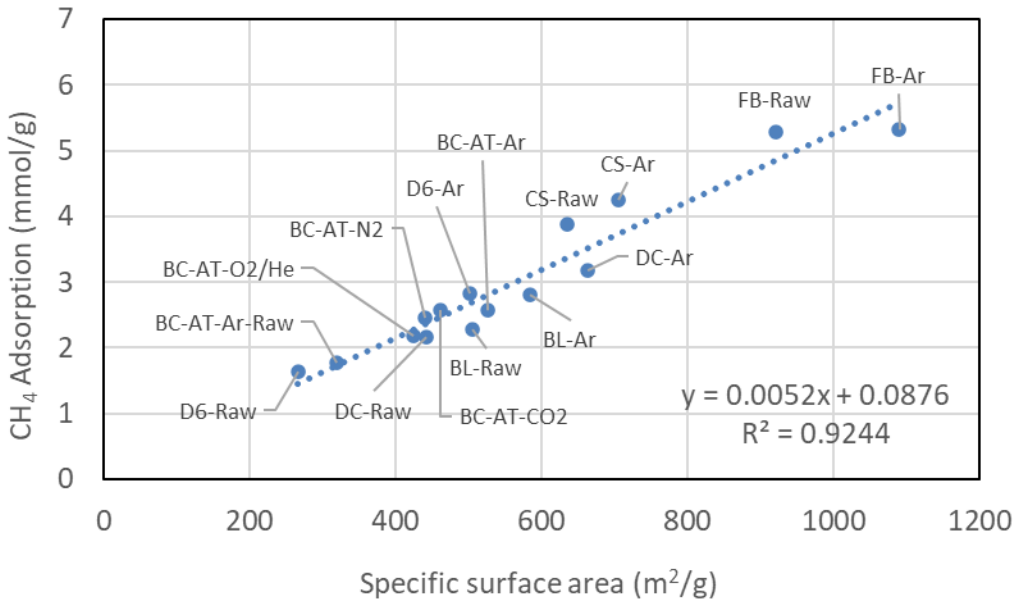

Fig. 5.8 CH_4 adsorption capacity and surface area of treated and untreated biochars and activated carbons

5.3.3.2 Pore size distributions

Fig. 5.9 compares the DFT pore size distributions of BC-AT before (BC-AT-Raw) and after plasma treatment using different plasma source gases. Below approximately 0.7 nm, all plasma treated samples show a pronounced increase in pore volume in this region. Ar and CO_2 were the most effective, generating pores at 0.58 nm through efficient physical (Ar) and chemical/physical (CO_2) etching, maximizing surface area (527 m^2/g, 461 m^2/g) and CH_4 adsorption (2.57 mmol/g). N_2 and Air are moderately effective, with pore volumes (0.08-0.12 $cm^3/g \cdot nm$), reflecting efficient physical (N_2) and balanced (Air) etching, with surface areas of 441 m^2/g and 427 m^2/g, respectively. O_2/He is the least effective, with the lowest pore volume (0.05-0.08 $cm^3/g \cdot nm$),

despite generating small pores (<0.55 nm), resulting in the lowest surface area (424 m^2/g) and CH_4 adsorption (2.18 mmol/g).

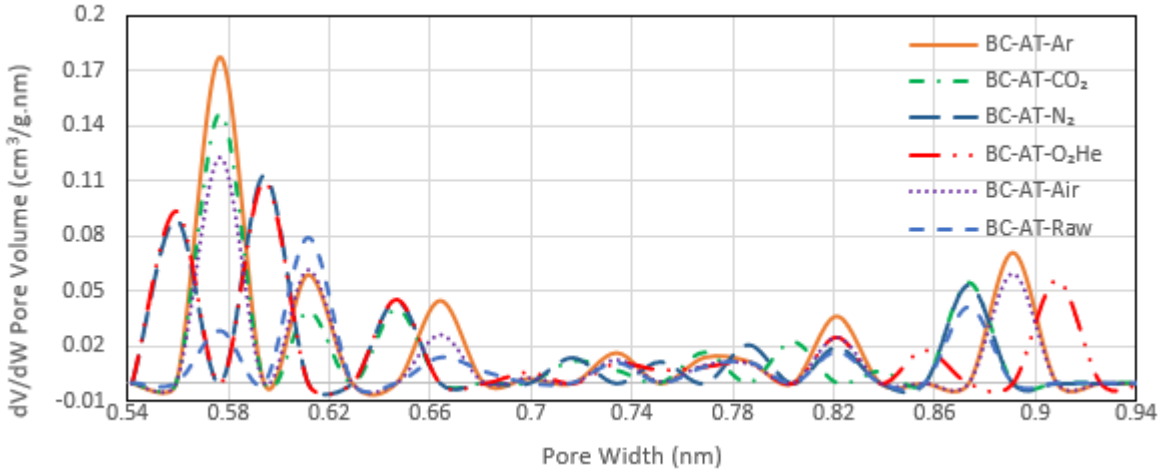

Fig. 5.9 DFT pore size distributions derived from CO_2 physisorption at 273 K for BC-AT biochar before and after 30 min plasma treatment with different plasma source gases (Ar, CO_2, N_2, O_2/He, Air)

The specific surface area of absorbent are determined by two factors, the specific pore volume and the pore size distribution. Since the ratio of specific surface area vs. specific pore volume is reversely proportional to pore diameter for spheric particles, micro- (< 2.0 nm), supermicro (0.7-2.0 nm) and ultramicropores (<0.7 nm) [60], often dominate the specific surface area of particles for the adsorption of CH_4, which has a kinetic diameter of approximately 0.38 nm. Fig. 5.10 shows the pore size distribution of untreated and Ar plasma treated biochars and activated carbons by plotting differential pore volume against pore width. Notably, two raw biochars (i.e., BC-BL and BC-D6) and two raw activated carbons (i.e., AC-CS and AC-FB) did not have ultramicropores at 0.56 nm pore width. For all these four absorbents, new ultramicropores were developed with the peak at 0.56 nm and with the existing pore peaks shifted towards the right, probably due to the enlargement of existing pores. The enlargement of existing pores could be attributed to the enlargement of the entrance of pores, which are usually ink-bottle shaped [51].

On the other hand, one biochar, i.e., BC-AT, and one activated carbon, i.e., AC-DC, already possessed ultramicropores peaking at 0.56 nm in their pristine states. Ar plasma treatment produces a substantial increase in the 0.56 nm ultramicropore population for BC-AT but only negligible change for AC-DC.

Interestingly, BC-AT and AC-DC are the biochar and activated carbon, respectively, that showed the least plasma efficiency in terms of both specific area and CH_4 adsorption capacity increases. These results suggest that the development of ultramicro pores peaked at around 0.56 nm was a major factor leading to the increase in specific surface and CH_4 adsorption capacity of Ar plasma treated biochar and activated carbons. This is physically reasonable given that the kinetic diameter of CH_4 (0.38 nm) is significantly smaller than 0.56 nm and can therefore access the internal surfaces of these pores. It should be noted that effective surfaces of smaller pores might be generated as well. These pores, however, are too small to be detected using the technique adapted in this study.

Taken together, these observations confirm that, across both biochars and activated carbons, Ar plasma treatment clearly alters microporosity, indicating significant pore restructuring. Specifically, the formation of ultramicropores smaller than 0.64 nm and enlargement of existing pores occur in most, if not all, Ar plasma treated samples.

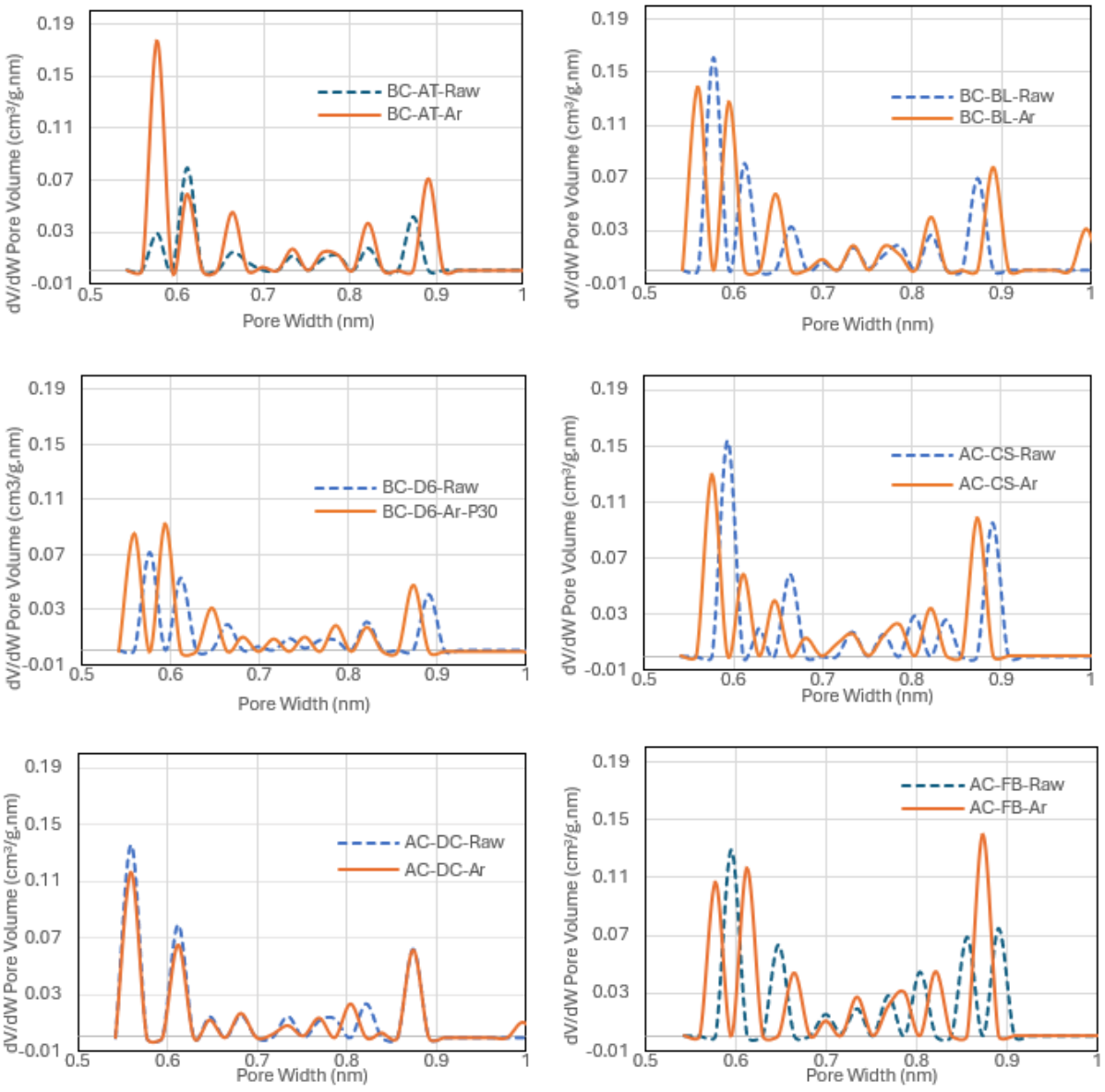

Fig. 5.10 DFT pore size distributions (0.5–1.0 nm range) derived from CO_2 physisorption at 273 K for untreated biochars (BC-AT-Raw, BC-BL-Raw, BC-D6-Raw), Ar plasma-treated biochars (BC-AT-Ar, BC-BL-Ar, BC-D6-Ar), untreated activated carbons (AC-CS-Raw, AC-DC-Raw, AC-FB-Raw), and Ar plasma-treated activated carbons (AC-CS-Ar, AC-DC-Ar, AC-FB-Ar)

5.3.3.3 SEM evidence of surface etching

SEM analysis revealed plasma-induced changes in surface morphology and roughness. The SEM images (Figs. 5.11–5.12) provide a visual comparison of the surface morphology of biochars BC-AT, BC-BL, BC-D6) and activated carbons (AC-CS, AC-DC, AC-FB) before and after Ar plasma

treatment for 30 min. These observations can be combined with prior pore size distribution, surface area, and CH_4 adsorption data to understand how surface morphology changes correlate with porosity and adsorption performance.

Fig. 5.11 presents the SEM images of untreated biochars (BC-AT, BL, D6) and 30 min treated under Ar at ×1,000 magnifications. The images (a, b, c) show that the untreated surface and pores are more aligned, smoother, and less porous. Meanwhile, plasma treatment produces a noticeably rougher and more eroded biochar surface in Fig. 5.11 (d, e, f). This morphological change is significant, as one study reported that grooved slit-shaped pores exhibit a higher CH_4 adsorption capacity than uniform slit-shaped pores, with adsorption capacity increasing progressively as groove spacing widens [61]. BC-AT shows the most significant texturing, aligning with its high surface area (527 m^2/g), and best CH_4 adsorption improvement (45%). Detachment of loosely bound carbon fragments is evident, exposing more surface can be observed in plasma treated BC-BL. The fiber-like structures observed in untreated BC-D6 evolve into a more open porous morphology after Ar plasma treatment, indicating the opening and widening of pre-existing pores. This structural change is consistent with the substantial increase in specific surface area (Fig. 5.7), suggesting enhanced accessibility of internal pore networks. The pronounced response of BC-D6 is attributed to its high volatile matter content (17 wt%), which facilitates pore development during plasma-induced volatilization, thereby improving CH_4 adsorption performance.

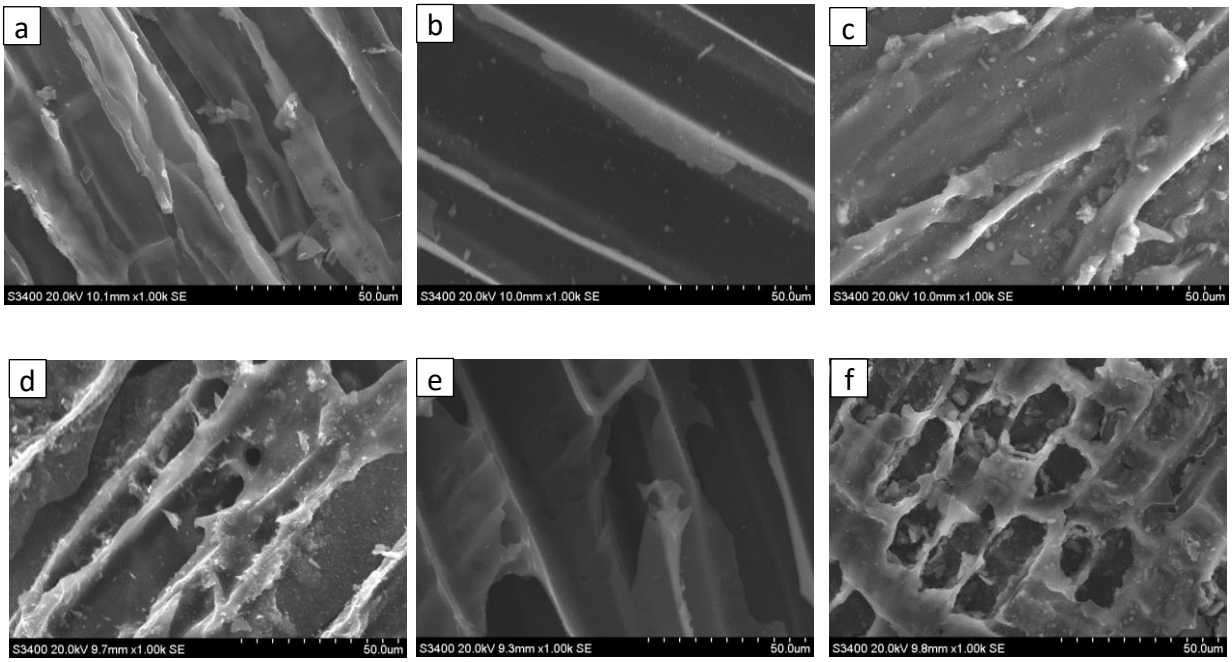

Fig. 5.11 SEM micrographs (×1,000) of raw BC-AT (a), BC-BL (b), and BC-D6 (c); as well as plasma-treated BC-AT-Ar (d), BC-BL-Ar (e), and BC-D6-Ar (f)

Fig. 5.12 shows SEM images (×1,000 magnification) of raw activated carbons (AC-CS, DC, FB) and Ar plasma treated activated carbons (AC-CS-Ar, AC-DC-Ar, and AC-FB-Ar). While the resolution of SEM is not sufficient to show the generation and restructuring of ultramicro-, micro-, or even mesopores, it is clear that the surfaces of activated carbons were deformed, showing the plasma etching effects. The AC-D6 surfaces exhibited significant erosion, with more irregular morphology.

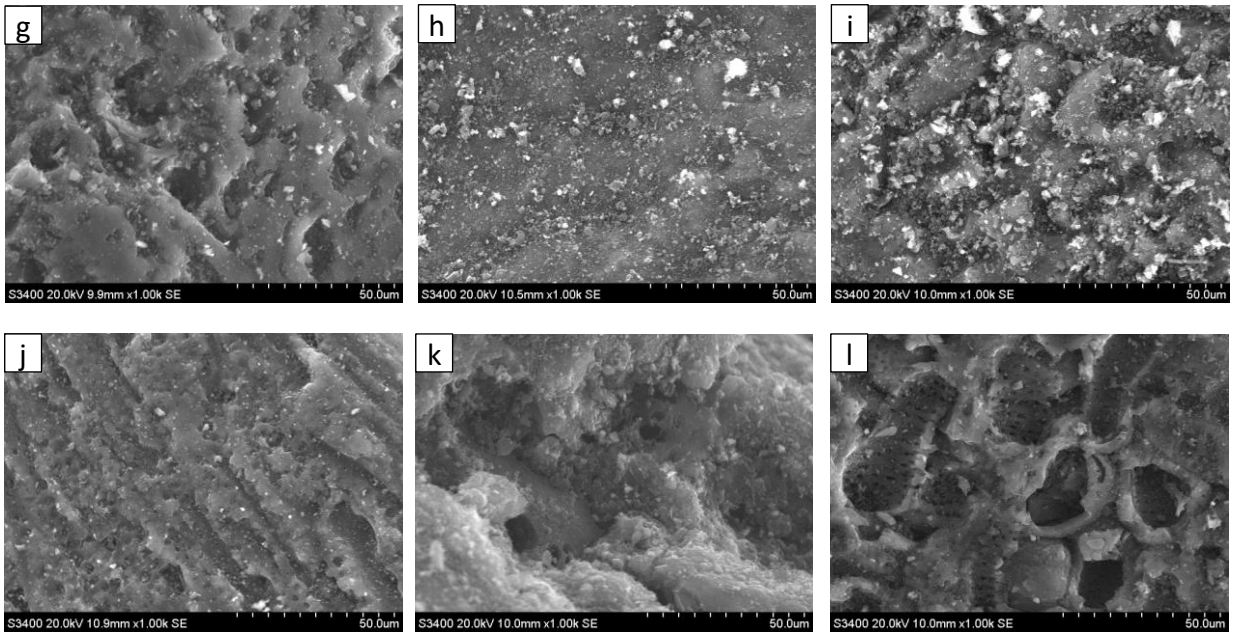

Fig. 5.12 SEM micrographs (×1,000) of raw AC-CS (g), AC-DC (h), and AC-FB (i); as well as plasma-treated AC-CS-Ar (j), AC-DC-Ar (k), and AC-FB-Ar (l)

Pore restructuring and surface morphological changes explain the wide variation in adsorption enhancement across materials and plasma gases, but cannot fully account for why different materials and plasma source gases produce vastly different results despite similar surface area gains. This disconnect indicates that chemical factors play a critical role. The following sections examine how feedstock composition governs η and how plasma source gas chemistry affects surface properties, particularly oxidation state, polarity, and functional group distributions that influence CH_4-surface affinity.

5.3.4 The chemistry of surface modification

While pore restructuring governs the dominant adsorption enhancement, plasma treatment also alters surface chemistry. The contribution of chemical modifications is therefore examined next, focusing on elemental composition and plasma source gas effects on surface polarity.

5.3.5 Effects of initial volatile matter content of raw materials

5.3.5.1 Correlation between initial volatile content and specific surface area increase

Tables 5.3 and 5.4 summarize the baseline properties of the raw biochars and activated carbons. The three biochars exhibit relatively high volatile matter contents (≥ 11.4 wt%), whereas all activated carbons contain ≤ 6.59 wt% volatiles. This contrast might be related to the more thorough treatment and activation steps used in commercial activated carbon production, which removed a larger fraction of volatile organic matters from source biomasses. The activated carbons also display higher initial specific surface areas (443-921 m^2/g) than the biochars (266-506 m^2/g), indicating a more developed pore network prior to plasma exposure.

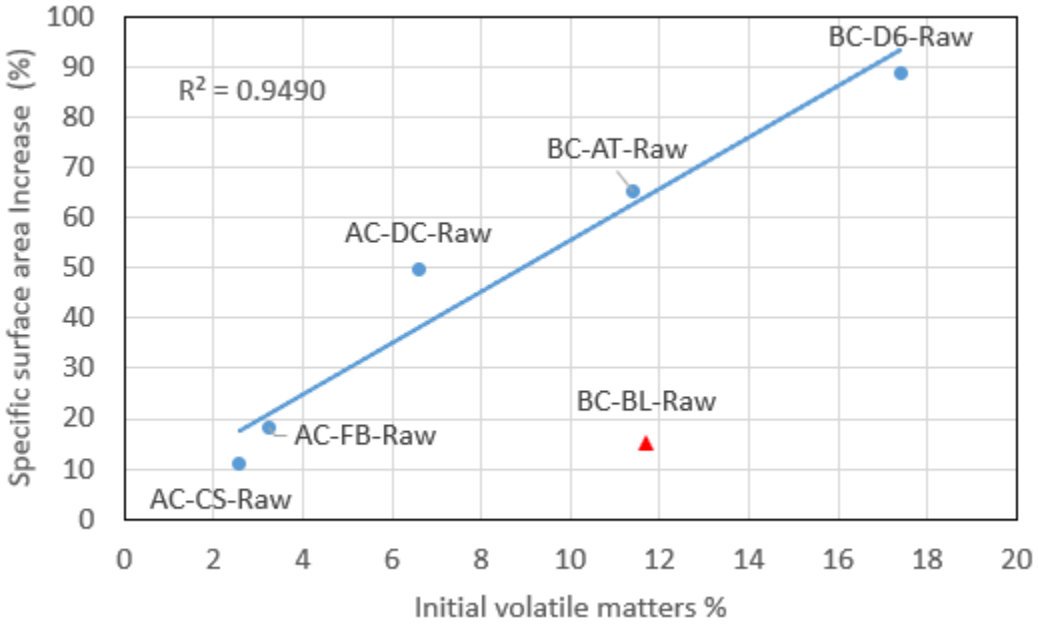

Fig. 5.13 Effect of initial volatile matter content on surface area increase (%) after Ar plasma treatment for three biochars and three activated carbons; linear fit excluding BC-BL-Raw

Fig. 5.13 shows a linear dependency of the percentage increase in specific surface area after Ar plasma treatment on the initial volatile matter content of the raw adsorbents, including both the biochars and the activated carbons, with BC-BL being the only exception. A strong correlation is observed across the five materials (R^2 = 0.949), demonstrating that volatile matter can be a predictor of plasma-induced surface development. In one of our previous works [62], we speculated that the removal of organic impurities was the predominate mechanism for the generation of ultramicropores in biochars according to the response of biochar to Ar plasma at different durations. The data in Fig. 5.13 provides direct evidence supporting that hypothesis. Note that volatile matter as reported in this paper are indeed organic impurities embedded in the matrices of biochars and activated carbons.

BC-BL deviates from this trend with a small specific surface area increase of 15.4% despite its relatively high volatile content (11.7 wt%), likely due to its unusually high ash content (18.3 wt%). The metal ions at the surface of biochars and activated carbons may interfere with the cold plasma process. Further, the minerals can occupy pore volume, block pore entrances, and partially shield the carbon framework from ion bombardment, thereby suppressing plasma-driven pore opening and limiting specific surface area development. However, systematic studies are needed to understand the effects of metal ions on plasma, if such effects are substantial.

5.3.5.2 Correlation between initial volatile content and zeta potential shift

Fig. 5.14 depicts the relationship between initial volatile content and zeta potential before and after Ar plasma treatment. Two distinct behaviors are observed. Activated carbons contain much less volatile matter than biochars. Activated carbons show a strong dependence of zeta potential on volatile matter and shift to more negative values (moving down), after Ar plasma, whereas

biochars show weak dependence and shift slightly toward the reduction of the negative values (moving up).

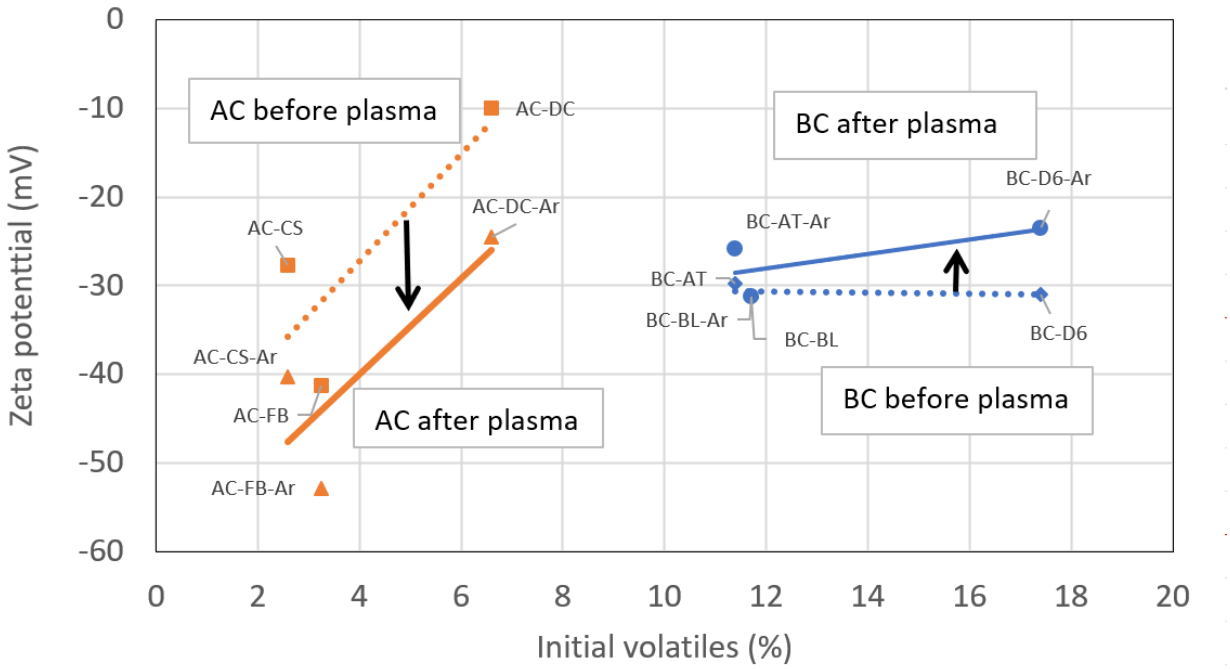

Fig. 5.14 Relationship between initial volatile matter content and zeta potential for biochars (BC-AT-Ar, BC-BL-Ar, BC-D6-Ar) and activated carbons (AC-CS-Ar, AC-DC-Ar, AC-FB-Ar) before and after Ar plasma treatment

The steep activated carbon slope in Fig. 5.14 further indicates that higher volatile matter yields less negative zeta potentials, consistent with partial masking of ionizable sites by residual organic layers [63, 64]. Their fixed carbon atoms are therefore much less protected by the shielding of volatile matter, which are more reactive than the fixed carbons, in cold plasma. Hypothetically, the fixed carbons of biochars are protected by their rich volatile matter, which are the primary subject bombarded by high temperature electrons and other reactive species in cold plasma, causing their removal from the affected layer on biochar surface and leaving ultramicro- and micropore in the layer as a result. Since volatile matter are rich in acidic functional groups such as -COOH, their removal would make the particle surface less negative and less acidic. Ar plasma

therefore drives larger negative shifts in zeta potential for low-volatile activated carbons (2.6–6.6 wt% volatiles, Table 5.4), with changes in the magnitude of Δ Zeta potential on the order of 11–14 mV, reflecting increased exposure of ionizable edge sites following plasma cleaning [65–67].

In contrast, biochars show smaller and opposite-direction shifts, indicating that volatile removal is coupled with activation of alkaline minerals (CaO, MgO) which carry positive surface charge at the measurement pH of 6.7. Volatile matter removal therefore exposes these alkaline phases, driving zeta potential less negative. Time-resolved measurements in our previous study show that BC-AT reaches an apparent equilibrium within 30 min, with both pH and zeta potential increasing during this period as volatile removal exposes alkaline minerals. Beyond 30 min, pH decreases slightly while zeta potential stabilizes, indicating volatile removal completion [51]. Activated carbons, which start with very low volatile matter (2.58-6.59 wt%), are therefore comparable to biochars in this post volatile removal state. This behavior mirrors the condition of activated carbons, which have already undergone extensive volatile removal during their production process and thus start in this volatile-depleted state.

5.3.6 Effects of plasma source gas

5.3.6.1 Effects of plasma source gas on zeta potential and suspension pH

Zeta potential and suspension pH were measured to assess plasma-induced surface modifications of biochar BC-AT with different plasma source gases. When carbon particles are dispersed in water, surface functional groups such as carboxyl, phenolic, and lactonic groups dissociate and interact with solution ions, forming an electric double layer. The zeta potential quantifies the electrostatic potential at the hydrodynamic shear plane, representing the boundary between ions moving with the particle and those in bulk solution [67]. Research on oxidized carbons

demonstrates that more negative zeta potentials arise from oxygen-containing surface groups, with surface charge determined by dissociation of oxygenated functionalities and water-mineral interactions [68]. Similarly, studies on plasma oxidation of carbon materials show that O_2 plasma treatment lowers the isoelectric point of carbon fibers, shifting it to more acidic pH values and indicating increased surface acidity [63,69]. They provide a useful comparative metric for assessing plasma-induced changes in surface polarity and chargeability [68,69]. More negative zeta potential values, which correspond to higher suspension pH, indicate higher concentrations of acidic oxygenated groups at particle surface [59,70,71]. Zeta potential and pH therefore reflect the degree of oxidation [72–74], serving as strong indicators marking the change of surface chemistry in plasma treatments. Critically, zeta potential measurements were conducted at a standardized pH of 6.7 (adjusted) to enable direct comparison of surface chemistry modifications, while the pH values shown represent the natural equilibrium pH of biochar suspensions in deionized water without adjustment. This methodological distinction is essential for proper interpretation: variations in zeta potential at fixed pH primarily reflect plasma-induced changes in the density and chemical nature of ionizable surface sites rather than pH-driven deprotonation effects. Zeta potential and suspension pH are therefore used here as a comparative indicator of plasma-induced surface polarity rather than a direct predictor of CH_4 adsorption.

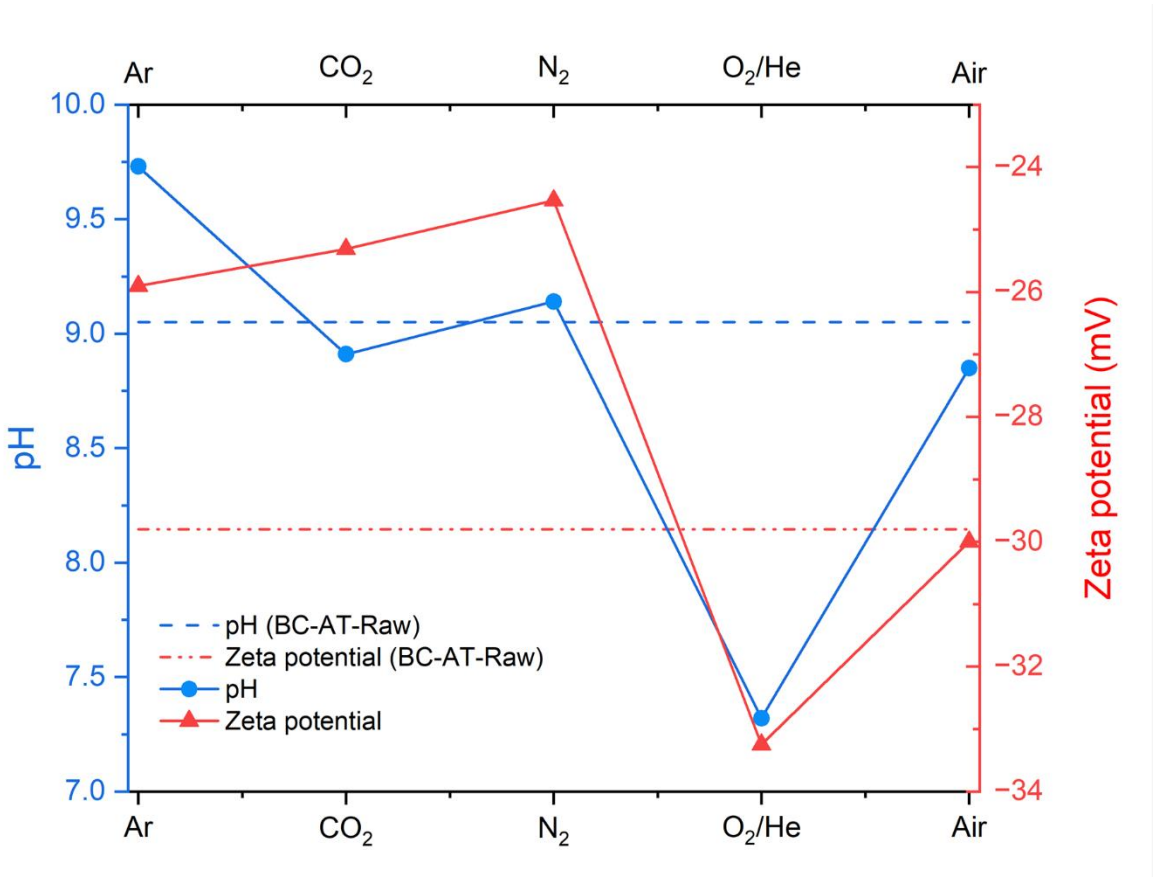

Fig. 5.15 Variations of suspension pH and zeta potential (at pH 6.7) for BC-AT biochar after plasma treatment with different plasma source gases

Fig. 5.15 synthesizes the interplay of structural and chemical responses of BC-AT biochar to plasma source gas chemistry. Non-oxidizing plasmas with Ar, N_2, or CO_2 produced larger CH_4 uptakes (2.46-2.57 mmol/g) and the specific surface area increases than the oxidizing plasma with air (2.22 mmol/g) and O_2/He plasma (2.18 mmol/g). These treatments also caused the increase of the suspension pH (8.9-9.7) and less negative zeta potentials (-24 to -26 mV), consistent with conditions that preferentially remove pore-blocking volatile matter residues and improve pore accessibility while largely preserving the nonpolar, hydrophobic character of the carbon surface that favors CH_4 confinement in ultramicropores [43]. The comparable CH_4 performance of Ar and CO_2, despite different plasma chemistries, indicates that both treatments can enhance adsorption-accessible porosity without generating excessive densities of strongly acidic surface sites [75].

By contrast, oxidizing plasma source gases, i.e., O_2/He and air, caused the decrease of suspension pH (7.32) and most negative zeta potential (−33.3 mV), indicating that O_2 plasma generate ionizable negative and carboxylate groups capable of deprotonation at near neutral pH, such as carboxylic- and phenolic-type sites ($R–COOH \rightleftharpoons R–COO^- + H^+$) [76,77].

It should be noted that air plasma exhibits a higher suspension pH and less negative zeta potential than O_2/He plasma. This difference can be rationalised by several contributing factors, namely, 1) the O_2 fraction in air (≈ 21%) which is slightly lower than that in the O_2/He mixture (23%); 2) the presence of N_2 (≈79% in air), which can reduce the effective oxidation strength relative to O_2/He through competitive O_2 consumption pathways, such as $N + O_2 \rightarrow NO + O$ and $N_2 + O \rightarrow N_2O$ [78,79]; and 3) He's low mass and minimal inelastic scattering, which allow electrons to retain higher kinetic energies (Te 3-5 eV) thereby maximizing O_2 dissociation ($O_2 + e^- \rightarrow 2O + e^-$) and generating highly reactive atomic oxygen radicals with strong surface reactivity [80,81]. This produces a 3.3 mV more negative zeta potential shift and 0.04 mmol/g lower CH_4 capacity compared to air, as N_2's efficient vibrational energy absorption reduces mean electron energy and thereby lowers the yield of oxidizing reactive species. Consistent with this interpretation, effluent gas analysis shows substantially higher CO_2 generation under O_2/He than under air (0.57 vs 0.22 mol%, Table 5.6), directly evidencing stronger oxidative carbon removal under O_2/He conditions.

Of particular interest is the effect of plasma source gas on suspension pH and zeta potential, as both are indicators of charged functional group density on particle surface. Biochars treated with Ar plasma generally exhibit neutral-to-positive pH shifts and less negative zeta potential, consistent with the volatile removal which reduces the density of carboxylate groups inherently concentrated in volatile matter. In the meantime, air and O_2/He plasma treatment produces the opposite trend: a decrease in suspension pH and a more negative zeta potential. This is attributed

to the generation of reactive oxygen radicals at the surface, which drive the formation of carboxyl and phenolic groups, acidic, proton-donating functionalities that deprotonate under the measurement conditions (pH 6.7), producing anionic surface sites ($–COO^-$, $–O^-$) that increase negative surface charge density and shift both pH downward and zeta potential in the negative direction..

5.3.6.2 Chemical modifications as revealed by plasma effluent gas analysis

Effluent gas analysis was used to probe plasma–surface reactions during treatment and to distinguish physical cleaning from chemical oxidation/gasification pathways. The composition of the outlet stream reflects interactions between the plasma source gas and the carbon surface, including volatile removal, bond scission, and formation of oxidation products that can alter surface polarity and ultimately affect CH_4 adsorption [59,82]. Table 5.6 summarizes the effluent composition for BC-AT treated for 30 min under Ar, CO_2, N_2, O_2/He, and air. Because Ar–O_2 and H_2–He peaks partially co-eluted in gas chromatography, H_2, He, Ar, and O_2 concentrations were determined by peak-area differences. Trace VOCs (C1–C5/C6+) were detected for all treatments (<0.01 mol%), confirming that removal of residual volatiles occurs regardless of plasma source gas [75,83–85].

Table 5.6 Composition of effluent gas after plasma treatment with different plasma source gases

Amount [mol %]

Gas Detected (mol %)	Plasma Source Gas				
	Ar	**CO_2**	**N_2**	**O_2/He (23/77)**	**Air**
H_2	**0.04**	**0.01**	**0.05**	**<0.01**	**0.01**
He	**< 0.01**	**<0.01**	**<0.01**	**76.0**	**<0.01**
CO_2	**0.03**	**97.7**	**0.04**	**0.57**	**0.22**
Ar	**99.8**	**< 0.01**	**<0.01**	**<0.01**	**<0.01**
O_2	**< 0.01**	**1.32**	**0.12**	**23.2**	**20.9**
N_2	**0.16**	**0.93**	**99.8**	**0.13**	**78.8**
CO	**0.01**	**1.77**	**0.01**	**0.07**	**0.06**
VOC C^1-C^5/C^{6+}	**Detected**	**Detected**	**Detected**	**Detected**	**Detected**
Sum	**100**	**100**	**100**	**100**	**100**

Due to co-elution of Ar-O_2 and H_2-He, H_2, He, Ar, O_2 are calculated by the difference of total

Inert plasmas (Ar, N_2) generated minimal reaction products, with only trace CO_2/CO (<0.04 mol%) and small amounts of H_2 (0.04–0.05 mol%). The low COx yields indicate negligible carbon oxidation, while the presence of H_2 suggests limited release of H-containing fragments [86]. These results support a predominantly physical modification mechanism (surface etching and pore cleaning), consistent with the high CH_4 adsorption capacities obtained after Ar and N_2 treatment (Fig. 5.3) [87].

CO_2 plasma produced a distinct effluent composition, characterized by elevated CO (1.77 mol%) and measurable O_2 (1.32 mol%), indicating both carbon–CO_2 reactions and CO_2 dissociation. It should be noted that the detected CO originates from two concurrent pathways: i) mild gasification of surface carbon (e.g., $C + CO_2 \rightarrow 2CO$), and ii) direct plasma-induced dissociation of the CO_2 feed ($CO_2 \rightarrow CO + O$). Therefore, the total CO concentration reflects the combined contribution

of these mechanisms rather than carbon consumption alone. The relatively high CO yield compared to Ar and N_2 plasmas suggests enhanced reactivity under CO_2 conditions, although the extent of surface carbon removal cannot be quantified solely from CO evolution. The low H_2 concentration (0.01 mol%) indicates that reactive pathways preferentially favor CO_2 conversion over H_2 evolution [88,89].

In addition, the N_2 concentration in the CO_2 plasma effluent (0.93 mol%) was 5.8 times higher than that measured under Ar plasma, suggesting possible involvement of N_2-containing surface species in redox processes during CO_2 reduction, although physical desorption of weakly bound N_2 species cannot be excluded. Despite this increased chemical activity, CO_2 treatment maintained strong CH_4 uptake, consistent with selective removal of amorphous or pore-blocking carbon without extensive surface oxidation [90].

Oxidizing plasmas (O_2/He and air) increased COx formation, with the strongest oxidation observed for O_2/He. O_2/He produced 0.57 mol% CO_2 and 0.07 mol% CO, indicating extensive oxidation with a low CO/CO_2 ratio consistent with near-complete conversion to CO_2. In contrast, air produced lower CO_2 (0.22 mol%) and comparable CO (0.06 mol%), demonstrating milder oxidation despite similar O_2 fractions in the feed. This difference highlights the importance of balance-gas identity: He sustains higher electron energies and enhances O_2 dissociation, whereas N_2 moderates electron temperature through energy transfer pathways and competes for reactive O_2 via NOx-forming reactions, thereby limiting the steady-state abundance of atomic O [91,92]. The higher CO_2 yield under O_2/He is consistent with the most negative zeta potential, lowest suspension pH, and poorest CH_4 adsorption observed for oxidizing conditions (Fig. 5.16), supporting oxidation-driven loss of hydrophobic adsorption character [82].

5.3.6.3 ATR-FTIR evidence for oxidation and surface polarity changes

Effluent gas composition provides a quantitative measure of oxidation severity during plasma treatment, with CO_2 generation serving as a direct indicator of carbon removal and O_2 incorporation. To confirm these gas-phase observations translate to surface chemical changes, ATR-FTIR spectroscopy was employed to identify oxygen-containing functional groups introduced by plasma treatment and correlate spectroscopic signatures with the electrochemical and adsorption trends observed across different plasma source gases. ATR-FTIR was used to confirm trends observed in electrochemical indicators (pH, zeta potential) by identifying changes in oxygen containing functional groups and aromatic framework signatures following plasma treatment. Fig. 5.16 shows the ATR-FTIR spectra illustrating the chemical changes on the surface of untreated biochar (BC-AT-Raw) and biochar treated with plasma source gases (Air, CO_2, O_2/He, N_2, Ar) at wavenumbers corresponding to O-H (3630 cm^{-1}), C=C (1566 cm^{-1}), C-O (1130 cm^{-1}), and C-H (873 cm^{-1}).

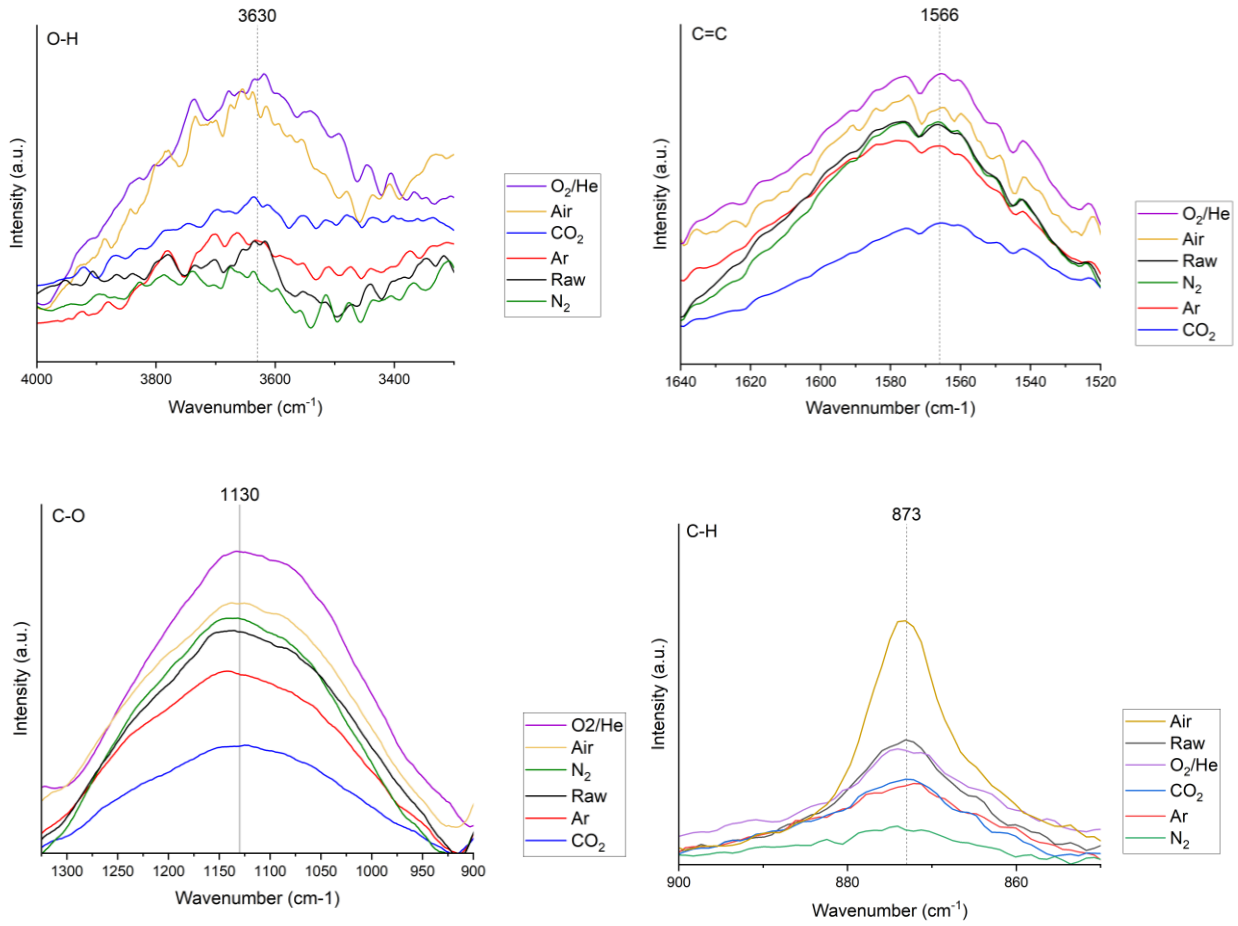

Fig. 5.16 ATR-FTIR spectra of BC-AT biochar before and after plasma treatment with different plasma source gases (Ar, N_2, CO_2, Air, O_2/He), highlighting O-H (3630 cm^{-1}), C=C (1566 cm^{-1}), C-O (1130 cm^{-1}), and C-H (873 cm^{-1}) bands

Baseline subtraction and normalization were conducted using OriginPro software. The asymmetric least squares (ALS) method was applied for baseline correction, followed by both peak height and peak area normalization. These processed spectra were used to qualitatively assess relative changes in the O-H, C=C, C-O, and C-H bands, and the functional groups are summarized in Table 5.7.

The ATR-FTIR spectra clearly indicates chemical modifications of the biochar surface after plasma treatment. In particular, O_2/He plasma treatments enhanced the intensities of O-H, C=O, and C=C bands, suggesting the introduction of oxygen-containing functional groups. These modifications are consistent with increased surface charge density, as the introduction of acidic

oxygen-containing functional groups promotes proton donation in aqueous suspension, reflected in the decreased pH measurements (Fig. 5.15). Ar and N_2 treatments show minimal polarity increase, causing physical changes (e.g., etching) rather than chemical functionalization. These observations are consistent with prior studies demonstrating that plasma treatments can substantially alter surface chemistry [58,65,76,77]. Introducing oxygen functionalities enhances hydrophilicity and metal affinity of biochars [93]. O_2/He causes chemical etching, removing amorphous carbon and exposing aromatic C=C sites, giving the highest C=C peak intensity (1566 cm^{-1}). However, this oxidation is too aggressive, leading to carbon loss (high CO_2/CO in the plasma gas effluent in Section 3.4.2.2), pore widening (Fig. 5.9), and a limited specific surface area gain (424 m^2/g), which reduces CH_4 adsorption. In contrast, Ar mainly produces non-selective physical etching, generating more microporosity and a higher surface area (527 m^2/g), improving CH_4 uptake. Although O_2/He and N_2 yield similar ultramicropore size ranges (0.56–0.68 nm), N_2 forms pores more efficiently via physical activation, minimal CO_2/CO formation, and higher surface area (441 m^2/g).

Table 5.7 Surface functional groups as identified by ATR-FTIR spectra

FTIR Wavenumber (cm^{-1})	Group	Class	Indicator	References
3580-3650	O-H stretching	hydroxyl groups	surface polarity	[94,64,95,96]
1566-1650	C=C Stretching	aromatic structures	biochar's carbon framework	[65,97,98]
1087-1124	C-O stretching	Alcohol	surface polarity	[99,100]
870-900	C-H bending	1,2,4-trisubstituted, 1,3-disubstituted, aromatic benzene rings	structural features of aromatic carbon domains	[100,101]

Ar plasma treatment can cause physical etching of the material's surface due to the ion bombardment and the presence of energetic electrons. This can break down unsaturated bonds,

such as C=C bonds, because the plasma's high energy can induce radical formation and bond scission. Thus, the Ar plasma treatment may reduce the density of C=C bonds on the surface. The surface can undergo reorganization, where highly reactive species (like C• radicals) may cause bond breakage or rearrangement, further reducing C=C bonds. CO_2 plasma is moderately effective, likely because it provides both oxidative (O radicals) and etching (CO formation) effects, enhancing functional groups while modifying surface morphology.

At 873 cm^{-1}, the C–H peak intensity is higher for Air plasma compared to Ar treatment. While Ar plasma primarily induces physical etching through ion bombardment and energetic electrons, leading to bond scission and reduction of surface C=C density as discussed above, Air plasma introduces a different mechanism. The increase in C–H intensity under Air plasma is attributed to the hydrogenation and reduction of aromatic C=C bonds on the biochar surface. Reactive hydrogen-containing species generated in the plasma partially hydrogenate exposed C=C double bonds, converting sp^2 carbon sites to sp^3 C–H. This hydrogenation does not produce a corresponding decrease in C=C peak intensity because Air plasma simultaneously removes the volatile matter layer and uncovers new graphitic C=C domains, compensating for the partial conversion.

Additionally, the greater surface area developed under Ar plasma (527 m^2/g vs. 427 m^2/g) dilutes the relative concentration of C–H groups per unit surface. The higher C–H intensity observed under Air plasma therefore arises from hydrogenation combined with moderated oxidation, whereas Ar treatment is dominated by physical surface development. These differences are consistent with the comparatively lower CH_4 adsorption enhancement observed for Air plasma relative to Ar-treated samples.

5.4 Conclusions

Cold plasma treatment improved CH_4 adsorption in biochars and activated carbons primarily by selective removal of volatile matter and the associated development of ultramicropores (0.56-0.68 nm). Performance gains ranged from 1–73%, depending on feedstock composition and plasma source gas. The enhancement of CH_4 adsorption by plasma treatment was mainly achieved by increasing the specific surface area of biochar or activated carbon as CH_4 adsorption capacity was shown to be proportional to the specific surface area of particles, regardless of their source biomass, pre-plasma processing, and plasma treatment conditions. Furthermore, it was shown that the percentage of specific surface area increase after plasma was proportional to the initial volatile contents of the raw materials, no matter it was biochar or activated carbon but with one exception. There are evidence showing the creation of ultramicropores after plasma treatment, which are considered to be the major mechanism of specific surface area increase during plasma treatment. Other elements, including minerals as reflected by the possible impact of ash content, may also have impacted the plasma treatment but systematic studies are needed to better understand this phenomenon and the mechanisms. Plasma source gas also showed significant impact on plasma effectiveness. While Ar was shown to be the best plasma source gas that led to the largest CH_4 adsorption enhancement, CO_2 demonstrated similar plasma effectiveness and might be the best source for practical application since it is much cheaper and more abundant than Ar. Having O_2 in the plasma source gas mixture, including both in air and in O_2/He, resulted in CH_4 adsorption enhancement but at plasma effectiveness much lower than that of plasma source gases without O_2, including Ar, CO_2, and N_2. Finally, data on the zeta potential, suspension pH, FTIR, and effluent gas composition all point to the change of particle surface chemistry during plasma, which could

have been caused by evaporation of volatile matter and the reactions of these molecules under cold plasma conditions.

Declarations

All related data are included in this article or available upon request.

Competing interests

The authors have no competing interests to declare that they are relevant to the content of this article.

Funding

This work is supported by the Program of Energy Research Development of Canada and a NSERC Discovery Grant to Dr. Christopher Lan.

Author contributions

Vivien Yoonhee Ko: Writing – original draft, Visualization, Validation, Resources, Project administration, Methodology, Investigation, Formal analysis, Data curation, Conceptualization. Jinsheng Wang: Supervision, Resources, Project administration, Conceptualization. Christopher Lan: Writing – review & editing, Supervision. David Ryan: Supervision, Resources, Project administration, Funding acquisition.

Acknowledgment

The authors gratefully acknowledge the Characterization Laboratory at CanmetENERGY Ottawa, Natural Resources Canada, for providing the ATR-FTIR spectra and valuable analytical insights.

References

[1] World Energy Outlook 2020 – Analysis - IEA, (2020). https://www.iea.org/reports/world-energy-outlook-2020 (accessed March 30, 2025).

[2] A. Pollard, Zero Routine Flaring by 2030 (ZRF), (n.d.). https://www.worldbank.org/en/programs/zero-routine-flaring-by-2030 (accessed September 2, 2025).

[3] R. Schulz, C. McGlade, P. Zeniewski, Putting gas flaring in the spotlight – Analysis, IEA (2020). https://www.iea.org/commentaries/putting-gas-flaring-in-the-spotlight (accessed September 8, 2025).

[4] M. Moosazadeh, A.S.T. Charmchi, P. Ifaei, V. Taghikhani, R.G. Moghanloo, C. Yoo, Flare-to-hydrogen in oil and gas industries: Techno-economic feasibility of a net-negative alternative, Energy Conversion and Management 300 (2024) 117926. https://doi.org/10.1016/j.enconman.2023.117926.

[5] Pipeline safety trust, Pipeline Basics & Specifics About Natural Gas Pipelines, Pipeline Safety (2015). http://pstrust.org/wp-content/uploads/2015/09/2015-PST-Briefing-Paper-02-NatGasBasics.pdf (accessed May 28, 2020).

[6] H. Lun, F. Filippone, D.C. Roger, M. Poser, Design and Construction Aspects of Post-Tensioned LNG Storage Tanks in Europe and Australasia, (2006) 6.

[7] J.E. Sinor, Comparison of CNG and LNG Technologies for Transportation Applications, Final Subcontract Report, June 1991 - December 1991, (1992). https://doi.org/10.2172/10110802.

[8] B. Li, H.-M. Wen, W. Zhou, J.Q. Xu, B. Chen, Porous Metal-Organic Frameworks: Promising Materials for Methane Storage, Chem 1 (2016) 557–580. https://doi.org/10.1016/j.chempr.2016.09.009.

[9] Z. Nie, Y. Lin, X. Jin, Research on the theory and application of adsorbed natural gas used in new energy vehicles: A review, Front. Mech. Eng. 11 (2016) 258–274. https://doi.org/10.1007/s11465-016-0381-2.

[10] J. Wegrzyn, M. Gurevich, Adsorbent storage of natural gas, Applied Energy 55 (1996) 71–83. https://doi.org/10.1016/S0306-2619(96)00015-3.

[11] Z. Zakaria, T. George, THE PERFORMANCE OF COMMERCIAL ACTIVATED CARBON ABSORBENT FOR ADSORBED NATURAL GAS STORAGE, (2011) 7.

[12] A. Arora, A. Bachle, Storage of Natural Gas by Adsorption Process, in: SPE/IATMI Asia Pacific Oil & Gas Conference and Exhibition, Society of Petroleum Engineers, Nusa Dua, Bali, Indonesia, 2015. https://doi.org/10.2118/176129-MS.

[13] M. Vashishtha, S. Gadipelli, K.V. Kumar, Deliverable Capacity of Methane: Required Material Property Levels for the Ideal “Holy Grail” Adsorbent, Chem Bio Eng 2 (2024) 64–67. https://doi.org/10.1021/cbe.4c00127.

[14] S. Alhasan, R. Carriveau, D. S.-K. Ting, A review of adsorbed natural gas storage technologies, International Journal of Environmental Studies 73 (2016) 343–356. https://doi.org/10.1080/00207233.2016.1165476.

[15] A.Y. Tsivadze, O.E. Aksyutin, A.G. Ishkov, I.E. Men’shchikov, A.A. Fomkin, A.V. Shkolin, E.V. Khozina, V.A. Grachev, Porous carbon-based adsorption systems for natural gas (methane) storage, Russ. Chem. Rev. 87 (2018) 950–983. https://doi.org/10.1070/RCR4807.

[16] X. Zhang, M. Yan, P. Chen, J. Li, Y. Li, H. Li, X. Liu, Z. Chen, H. Yang, S. Wang, J. Wang, Z. Tang, Q. Huang, J. Lei, T. Hayat, Z. Liu, L. Mao, T. Duan, X. Wang, Emerging MOFs, COFs, and their derivatives for energy and environmental applications, Innovation (Camb) 6 (2025) 100778. https://doi.org/10.1016/j.xinn.2024.100778.

[17] V.Y. Ko, J. Wang, I. He, D. Ryan, X. Zhang, C. Lan, Adsorption of methane on biochar for emission reduction in oil and gas fields, Biochar 5 (2023) 15. https://doi.org/10.1007/s42773-023-00209-x.

[18] S. Panić, N. Đurišić-Mladenović, M. Petronijević, I. Stijepović, M. Milanović, G. Kozma, Á. Kukovecz, Valorization of waste biomass towards biochar production – Characterization and perspectives for sustainable applications in Serbia, Environmental Technology & Innovation 37 (2025) 104043. https://doi.org/10.1016/j.eti.2025.104043.

[19] A. Al-Rumaihi, M. Shahbaz, G. Mckay, H. Mackey, T. Al-Ansari, A review of pyrolysis technologies and feedstock: A blending approach for plastic and biomass towards optimum biochar yield, Renewable and Sustainable Energy Reviews 167 (2022) 112715. https://doi.org/10.1016/j.rser.2022.112715.

[20] K. Kumar V, N.L. Panwar, Pyrolysis technologies for biochar production in waste management: a review, Clean Energy 8 (2024) 61–78. https://doi.org/10.1093/ce/zkae036.

[21] Z. Heidarinejad, M.H. Dehghani, M. Heidari, G. Javedan, I. Ali, M. Sillanpää, Methods for preparation and activation of activated carbon: a review, Environ Chem Lett 18 (2020) 393–415. https://doi.org/10.1007/s10311-019-00955-0.

[22] H. Marsh, F. Rodríguez-Reinoso, CHAPTER 5 - Activation Processes (Thermal or Physical), in: H. Marsh, F. Rodríguez-Reinoso (Eds.), Activated Carbon, Elsevier Science Ltd, Oxford, 2006: pp. 243–321. https://doi.org/10.1016/B978-008044463-5/50019-4.

[23] H. Marsh, F. Rodríguez-Reinoso, CHAPTER 6 - Activation Processes (Chemical), in: H. Marsh, F. Rodríguez-Reinoso (Eds.), Activated Carbon, Elsevier Science Ltd, Oxford, 2006: pp. 322–365. https://doi.org/10.1016/B978-008044463-5/50020-0.

[24] M. Ahmad, A.U. Rajapaksha, J.E. Lim, M. Zhang, N. Bolan, D. Mohan, M. Vithanage, S.S. Lee, Y.S. Ok, Biochar as a sorbent for contaminant management in soil and water: A review, Chemosphere 99 (2014) 19–33. https://doi.org/10.1016/j.chemosphere.2013.10.071.

[25] B.Y. Sadasivam, K.R. Reddy, Adsorption and transport of methane in biochars derived from waste wood, Waste Management 43 (2015) 218–229. https://doi.org/10.1016/j.wasman.2015.04.025.

[26] B.Y. Sadasivam, K.R. Reddy, Study of Methane Adsorption by Biochar in Landfill Cover, (n.d.).

[27] Voltage-Enhanced Processing of Biomass and Biochar, in: Voltage-Enhanced Processing of Biomass and Biochar, John Wiley & Sons, Ltd, 2022: pp. 33–57. https://doi.org/10.1002/9781119739777.ch3.

[28] M. Mozetič, A. Vesel, G. Primc, R. Zaplotnik, Introduction to Plasma and Plasma Diagnostics, in: Non-Thermal Plasma Technology for Polymeric Materials, Elsevier, 2019: pp. 23–65. https://doi.org/10.1016/B978-0-12-813152-7.00002-0.

[29] K. Jedynak, B. Charmas, Adsorption properties of biochars obtained by KOH activation, Adsorption (2023). https://doi.org/10.1007/s10450-023-00399-7.

[30] R. Azargohar, A. Dalai, Steam and KOH activation of biochar: Experimental and modeling studies, Microporous and Mesoporous Materials, 110 (2008) 413–421. https://doi.org/10.1016/j.micromeso.2007.06.047.

[31] E.M. Mistar, T. Alfatah, M.D. Supardan, Synthesis and characterization of activated carbon from Bambusa vulgaris striata using two-step KOH activation, Journal of Materials Research and Technology 9 (2020) 6278–6286. https://doi.org/10.1016/j.jmrt.2020.03.041.

[32] K. Vijayaraghavan, Recent advancements in biochar preparation, feedstocks, modification, characterization and future applications, Environmental Technology Reviews 8 (2019) 47–64. https://doi.org/10.1080/21622515.2019.1631393.

[33] A. Arpanaei, B. Winther-Jensen, E. Theodosiou, P. Kingshott, T.J. Hobley, O.R.T. Thomas, Surface modification of chromatography adsorbents by low temperature low pressure plasma, Journal of Chromatography A 1217 (2010) 6905–6916. https://doi.org/10.1016/j.chroma.2010.08.069.

[34] D. Thiry, A. Chauvin, A.-A. El Mel, C. Cardinaud, J. Hamon, E. Gautron, N. Stephant, A. Granier, P.-Y. Tessier, Tailoring the chemistry and the nano-architecture of organic thin films using cold plasma processes, Plasma Processes and Polymers 14 (2017) 1700042. https://doi.org/10.1002/ppap.201700042.

[35] S. Mujin, H. Baorong, W. Yisheng, T. Ying, H. Weiqiu, D. Youxian, The surface of carbon fibres continuously treated by cold plasma, Composites Science and Technology 34 (1989) 353–364. https://doi.org/10.1016/0266-3538(89)90004-3.

[36] J. López-García, Wettability Analysis and Water Absorption Studies of Plasma Activated Polymeric Materials, in: Non-Thermal Plasma Technology for Polymeric Materials, Elsevier, 2019: pp. 261–285. https://doi.org/10.1016/B978-0-12-813152-7.00010-X.

[37] V. Damideh, O.H. Chin, H.A. Gabbar, S.J. Ch'ng, C.Y. Tan, Study of ozone concentration from CO_2 decomposition in a water cooled coaxial dielectric barrier discharge, Vacuum 177 (2020) 109370. https://doi.org/10.1016/j.vacuum.2020.109370.

[38] K.M. Praveen, C.V. Pious, S. Thomas, Y. Grohens, Relevance of Plasma Processing on Polymeric Materials and Interfaces, in: Non-Thermal Plasma Technology for Polymeric Materials, Elsevier, 2019: pp. 1–21. https://doi.org/10.1016/B978-0-12-813152-7.00001-9.

[39] J. Fennila, K.A. Vijayalakshmi, Renewable cold plasma exposed activated carbon-derived eucalyptus leaves (EL) as electrode in fabricating low-cost energy storage devices, Energy Sources, Part A: Recovery, Utilization and Environmental Effects 46 (2024) 6743–6760. https://doi.org/10.1080/15567036.2024.2353179.

[40] S. Kulkarni, Plasma Assisted Polymer Synthesis and Processing, in: Non-Thermal Plasma Technology for Polymeric Materials, Elsevier, 2019: pp. 67–93. https://doi.org/10.1016/B978-0-12-813152-7.00003-2.

[41] Y. Che, J. Zhou, Z. Wang, Plasma Modification of Activated Carbon Fibers for Adsorption of SO_2, Plasma Sci. Technol. 15 (2013) 1047–1052. https://doi.org/10.1088/1009-0630/15/10/16.

[42] M. Bidaei, R. Yarahmadi, M. Azadfallah, Effect of surface modification of activated carbon by cold plasma on the adsorption capacity of Rhodamine B, Iran Occupational Health 17 (2020).

[43] I.H. Loh, R.E. Cohen, R.F. Baddour, Modification of carbon surfaces in cold plasmas, J Mater Sci 22 (1987) 2937–2947. https://doi.org/10.1007/BF01086494.

[44] L. Hui, S.F. Kong, Y.S. Liu, H. Zeng, Application of Plasma Technology in Surface Modification of Carbon Materials, Applied Mechanics and Materials 319 (2013) 102–106. https://doi.org/10.4028/www.scientific.net/AMM.319.102.

[45] R.K. Gupta, M. Dubey, P. Kharel, Z. Gu, Q.H. Fan, Biochar activated by oxygen plasma for supercapacitors, Journal of Power Sources 274 (2015) 1300–1305. https://doi.org/10.1016/j.jpowsour.2014.10.169.

[46] S. Corujeira-Gallo, H. Dong, Effect of microstructure on the plasma surface treatment of carbon fibres, Journal of Composite Materials 51 (2017) 3239–3256. https://doi.org/10.1177/0021998316684935.

[47] D. Lozano-Castelló, D. Cazorla-Amorós, A. Linares-Solano, Usefulness of CO_2 adsorption at 273 K for the characterization of porous carbons, Carbon 42 (2004) 1233–1242. https://doi.org/10.1016/j.carbon.2004.01.037.

[48] K. Skic, A. Adamczuk, A. Gryta, P. Boguta, T. Tóth, G. Jozefaciuk, Surface areas and adsorption energies of biochars estimated from nitrogen and water vapour adsorption isotherms, Sci Rep 14 (2024) 30362. https://doi.org/10.1038/s41598-024-81030-9.

[49] A. Mukhtar, N. Mellon, S. Saqib, S.-P. Lee, M.A. Bustam, Extension of BET theory to CO_2 adsorption isotherms for ultra-microporosity of covalent organic polymers, SN Appl. Sci. 2 (2020) 1232. https://doi.org/10.1007/s42452-020-2968-9.

[50] P. Maziarka, C. Wurzer, P.J. Arauzo, A. Dieguez-Alonso, O. Mašek, F. Ronsse, Do you BET on routine? The reliability of N2 physisorption for the quantitative assessment of biochar's surface area, Chemical Engineering Journal 418 (2021) 129234. https://doi.org/10.1016/j.cej.2021.129234.

[51] V.Y. Ko, J. Wang, C. Lan, D. Ryan, Enhanced CH_4 adsorption through ultramicropores development in cold plasma-activated biochar, Chemical Engineering Journal 524 (2025) 169286. https://doi.org/10.1016/j.cej.2025.169286.

[52] Y. Sun, S. Li, R. Sun, S. Yang, X. Liu, Modified Dubinin–Astakhov Model for the Accurate Estimation of Supercritical Methane Sorption on Shales, ACS Omega 5 (2020) 16189–16199. https://doi.org/10.1021/acsomega.0c01675.

[53] N. Saeidi, M. Parvini, Accuracy of Dubinin-Astakhov and Dubinin-Radushkevich Adsorption Isotherm Models in Evaluating Micropore Volume of Bentonite, Periodica Polytechnica Chemical Engineering 60 (2016) 123–129. https://doi.org/10.3311/PPch.8374.

[54] B. Salopek, D. Krasi, S. Filipovi, MEASUREMENT AND APPLICATION OF ZETA-POTENTIAL, Rudarsko-geoloSko-Naftni Zbornik, 4 (1992).

[55] J. Alcañiz-Monge, D. Lozano-Castelló, D. Cazorla-Amorós, A. Linares-Solano, Fundamentals of methane adsorption in microporous carbons, Microporous and Mesoporous Materials 124 (2009) 110–116. https://doi.org/10.1016/j.micromeso.2009.04.041.

[56] S. Himeno, T. Komatsu, S. Fujita, High-Pressure Adsorption Equilibria of Methane and Carbon Dioxide on Several Activated Carbons, J. Chem. Eng. Data 50 (2005) 369–376. https://doi.org/10.1021/je049786x.

[57] H. Swenson, N.P. Stadie, Langmuir's Theory of Adsorption: A Centennial Review, Langmuir 35 (2019) 5409–5426. https://doi.org/10.1021/acs.langmuir.9b00154.

[58] L. Qian, B. Chen, Interactions of Aluminum with Biochars and Oxidized Biochars: Implications for the Biochar Aging Process, J. Agric. Food Chem. 62 (2014) 373–380. https://doi.org/10.1021/jf404624h.

[59] Z. Ghanbarpour Mamaghani, K.A. Hawboldt, S. MacQuarrie, Adsorption of CO_2 using biochar - Review of the impact of gas mixtures and water on adsorption, Journal of

Environmental Chemical Engineering 11 (2023) 109643. https://doi.org/10.1016/j.jece.2023.109643.

[60] M. Thommes, K. Kaneko, A.V. Neimark, J.P. Olivier, F. Rodriguez-Reinoso, J. Rouquerol, K.S.W. Sing, Physisorption of gases, with special reference to the evaluation of surface area and pore size distribution (IUPAC Technical Report), Pure and Applied Chemistry 87 (2015) 1051–1069. https://doi.org/10.1515/pac-2014-1117.

[61] S. Chen, C. Zhang, X. Li, Y. Zhang, X. Wang, Simulation of methane adsorption in diverse organic pores in shale reservoirs with multi-period geological evolution, Int J Coal Sci Technol 8 (2021) 844–855. https://doi.org/10.1007/s40789-021-00431-7.

[62] V.Y. Ko, J. Wang, C. Lan, D. Ryan, Enhanced CH_4 adsorption through ultramicropores development in cold plasma-activated biochar, Chemical Engineering Journal (2025) 169286. https://doi.org/10.1016/j.cej.2025.169286.

[63] J.P. Boudou, J.I. Paredes, A. Cuesta, A. Martínez-Alonso, J.M.D. Tascón, Oxygen plasma modification of pitch-based isotropic carbon fibres, Carbon 41 (2003) 41–56. https://doi.org/10.1016/S0008-6223(02)00270-1.

[64] M.C. Almazán-Almazán, M. Pérez-Mendoza, M. Domingo-García, I. Fernández-Morales, F. del Rey-Bueno, A. García-Rodríguez, F.J. López-Garzón, The role of the porosity and oxygen groups on the adsorption of *n*-alkanes, benzene, trichloroethylene and 1,2-dichloroethane on active carbons at zero surface coverage, Carbon 45 (2007) 1777–1785. https://doi.org/10.1016/j.carbon.2007.05.003.

[65] C. Saka, Overview on the Surface Functionalization Mechanism and Determination of Surface Functional Groups of Plasma Treated Carbon Nanotubes., Critical Reviews in Analytical Chemistry 48 (2018) 1–14. https://doi.org/10.1080/10408347.2017.1356699.

[66] I.H. Loh, R.E. Cohen, R.F. Baddour, Modification of carbon surfaces in cold plasmas, J Mater Sci 22 (1987) 2937–2947. https://doi.org/10.1007/BF01086494.

[67] A.V. Delgado, F. González-Caballero, R.J. Hunter, L.K. Koopal, J. Lyklema, Measurement and interpretation of electrokinetic phenomena, Journal of Colloid and Interface Science 309 (2007) 194–224. https://doi.org/10.1016/j.jcis.2006.12.075.

[68] D.W. Fuerstenau, J.M. Rosenbaum, Y.S. You, Electrokinetic behavior of coal, Energy Fuels 2 (1988) 241–245. https://doi.org/10.1021/ef00009a002.

[69] A.B. García, A. Cuesta, M.A. Montes-Morán, A. Martínez-Alonso, J.M.D. Tascón, Zeta Potential as a Tool to Characterize Plasma Oxidation of Carbon Fibers, Journal of Colloid and Interface Science 192 (1997) 363–367. https://doi.org/10.1006/jcis.1997.5007.

[70] H. Pan, Y. Yi, Q. Lin, G. Xiang, Y. Zhang, F. Liu, Effect of Surface Chemistry and Textural Properties of Activated Carbons for CH_4 Selective Adsorption through Low-Concentration Coal Bed Methane, J. Chem. Eng. Data 61 (2016) 2120–2127. https://doi.org/10.1021/acs.jced.6b00066.

[71] M. Ahmad, S.S. Lee, X. Dou, D. Mohan, J.-K. Sung, J.E. Yang, Y.S. Ok, Effects of pyrolysis temperature on soybean stover- and peanut shell-derived biochar properties and TCE adsorption in water, Bioresource Technology 118 (2012) 536–544. https://doi.org/10.1016/j.biortech.2012.05.042.

[72] M. Karimi, G. Parsafar, H. Samouei, Polarizing Perspectives: Ion- and Dipole-Induced Dipole Interactions Dictate Bulk Nanobubble Stability, J. Phys. Chem. B 128 (2024) 7263–7270. https://doi.org/10.1021/acs.jpcb.4c03973.

[73] R. Asiain-Mira, P. Zamora, V. Monsalvo, L. Torrente-Murciano, Effect of functional groups on the adsorption of urea on activated carbon, Carbon 228 (2024) 119361. https://doi.org/10.1016/j.carbon.2024.119361.

[74] M. Dai, The Effect of Zeta Potential of Activated Carbon on the Adsorption of Dyes from Aqueous Solution: I. The Adsorption of Cationic Dyes: Methyl Green and Methyl Violet, Journal of Colloid and Interface Science 164 (1994) 223–228. https://doi.org/10.1006/jcis.1994.1160.

[75] G. Mogildea, C. Popa, G. Chiritoi, The Assessment of Carbon Dioxide Dissociation Using a Single-Mode Microwave Plasma Generator, Molecules 25 (2020). https://doi.org/10.3390/molecules25071558.

[76] G.-Q. Wu, X. Zhang, H. Hui, J. Yan, Q.-S. Zhang, J.-L. Wan, Y. Dai, Adsorptive removal of aniline from aqueous solution by oxygen plasma irradiated bamboo based activated carbon, Chemical Engineering Journal 185–186 (2012) 201–210. https://doi.org/10.1016/j.cej.2012.01.084.

[77] H. Zhang, T. Wang, Z. Sui, Y. Zhang, B. Sun, W.-P. Pan, Enhanced mercury removal by transplanting sulfur-containing functional groups to biochar through plasma, Fuel 253 (2019) 703–712. https://doi.org/10.1016/j.fuel.2019.05.068.

[78] A. Sakudo, M. Higa, K. Maeda, N. Shimizu, Y. Imanishi, H. Shintani, Sterilization mechanism of nitrogen gas plasma: induction of secondary structural change in protein, Microbiology and Immunology 57 (2013) 536–542. https://doi.org/10.1111/1348-0421.12061.

[79] D. Kong, P. Zhu, F. He, R. Han, B. Yang, M. Wang, J. Ouyang, Influence of nitrogen and oxygen admixture on the development of helium atmospheric-pressure plasma jet, Journal of Applied Physics 129 (2021) 103303. https://doi.org/10.1063/5.0031345.

[80] J. Dutton, F. Llewellyn-Jones, D.B. Rees, Ionization Coefficients in Helium at High Pressures, Nature 200 (1963) 58–59. https://doi.org/10.1038/200058a0.

[81] Y.V. Ralchenko, R.K. Janev, T. Kato, D.V. Fursa, I. Bray, F.J. de Heer, Y.V. Ralchenko, R.K. Janev, Cross section database for collision processes of helium atom with charged particles. 1. Electron impact processes, (2000). https://inis.iaea.org/records/ytpg7-5hs02 (accessed January 20, 2026).

[82] S. Samukawa, M. Hori, S. Rauf, K. Tachibana, P. Bruggeman, G. Kroesen, J.C. Whitehead, A.B. Murphy, A.F. Gutsol, S. Starikovskaia, U. Kortshagen, J.-P. Boeuf, T.J. Sommerer, M.J. Kushner, U. Czarnetzki, N. Mason, The 2012 Plasma Roadmap, J. Phys. D: Appl. Phys. 45 (2012) 253001. https://doi.org/10.1088/0022-3727/45/25/253001.

[83] S. Kantharaju, J. Vinodhini, G. M, S. Bhowmik, An investigation to enhance the mechanical property of high-performance thermoplastic composite through different plasma treatment, Polymer Composites 44 (2023) 178–189. https://doi.org/10.1002/pc.27037.

[84] M. Laroussi, Low Temperature Plasma-Based Sterilization: Overview and State-of-the-Art, Plasma Processes and Polymers 2 (2005) 391–400. https://doi.org/10.1002/ppap.200400078.

[85] D. Hegemann, H. Brunner, C. Oehr, Plasma treatment of polymers for surface and adhesion improvement, Nuclear Instruments and Methods in Physics Research Section B: Beam Interactions with Materials and Atoms 208 (2003) 281–286. https://doi.org/10.1016/S0168-583X(03)00644-X.

[86] J. R. Roth, Industrial Plasma Engineering | Volume 2: Applications to N, (n.d.). https://www-taylorfrancis-com.proxy.bib.uottawa.ca/reader/download/e84bcc3a-7fe5-4e9f-89a6-f822bada3c9e/book/pdf?context=ubx (accessed January 21, 2026).

[87] X. Sun, J. Bao, K. Li, M.D. Argyle, G. Tan, H. Adidharma, K. Zhang, M. Fan, P. Ning, Advance in Using Plasma Technology for Modification or Fabrication of Carbon-Based Materials and Their Applications in Environmental, Material, and Energy Fields, Advanced Functional Materials 31 (2021) 2006287. https://doi.org/10.1002/adfm.202006287.

[88] R. Brandenburg, Dielectric barrier discharges: progress on plasma sources and on the understanding of regimes and single filaments, Plasma Sources Sci. Technol. 26 (2017) 053001. https://doi.org/10.1088/1361-6595/aa6426.

[89] A. Bogaerts, E. Neyts, R. Gijbels, J. van der Mullen, Gas discharge plasmas and their applications, Spectrochimica Acta Part B: Atomic Spectroscopy 57 (2002) 609–658. https://doi.org/10.1016/S0584-8547(01)00406-2.

[90] P. Bruggeman, D.C. Schram, On OH production in water containing atmospheric pressure plasmas, Plasma Sources Sci. Technol. 19 (2010) 045025. https://doi.org/10.1088/0963-0252/19/4/045025.

[91] M. A. Lieberman, A. J. Lightenberg, Principles of Plasma Discharges and Materials Processing, 2nd Edition | Wiley, n.d. https://www.wiley.com/en-us/Principles+of+Plasma+Discharges+and+Materials+Processing%2C+2nd+Edition-p-9780471724254 (accessed January 27, 2026).

[92] E.C. Neyts, K. (Ken) Ostrikov, M.K. Sunkara, A. Bogaerts, Plasma Catalysis: Synergistic Effects at the Nanoscale, Chem. Rev. 115 (2015) 13408–13446. https://doi.org/10.1021/acs.chemrev.5b00362.

[93] R. Zhou, X. Wang, R. Zhou, J. Weerasinghe, T. Zhang, Y. Xin, H. Wang, P. Cullen, H. Wang, K.K. Ostrikov, Non-thermal plasma enhances performances of biochar in wastewater treatment and energy storage applications, Front. Chem. Sci. Eng. 16 (2022) 475–483. https://doi.org/10.1007/s11705-021-2070-x.

[94] M. Keiluweit, P.S. Nico, M.G. Johnson, M. Kleber, Dynamic Molecular Structure of Plant Biomass-Derived Black Carbon (Biochar), Environ. Sci. Technol. 44 (2010) 1247–1253. https://doi.org/10.1021/es9031419.

[95] R. Janu, V. Mrlik, D. Ribitsch, J. Hofman, P. Sedláček, L. Bielská, G. Soja, Biochar surface functional groups as affected by biomass feedstock, biochar composition and pyrolysis temperature, Carbon Resources Conversion 4 (2021) 36–46. https://doi.org/10.1016/j.crcon.2021.01.003.

[96] K. Jindo, H. Mizumoto, Y. Sawada, M.A. Sanchez-Monedero, T. Sonoki, Physical and chemical characterization of biochars derived from different agricultural residues, Biogeosciences 11 (2014) 6613–6621. https://doi.org/10.5194/bg-11-6613-2014.

[97] K.A. Vijayalakshmi, K.C. Sowmiya, High capacitance sustainable low-cost cold plasma exposed activated carbon electrode derived from orange peel waste to eco-friendly technique, Carbon Lett. 34 (2024) 1737–1754. https://doi.org/10.1007/s42823-024-00722-4.

[98] A. Memetova, I. Tyagi, R. Rao Karri, Suhas, N. Memetov, A. Zelenin, R. Stolyarov, A. Babkin, V. Yagubov, I. Burmistrov, A. Tkachev, V. Bogoslovskiy, G. Shigabaeva, E. Galunin, High-Density Nanoporous carbon materials as storage material for Methane: A value-added solution, Chemical Engineering Journal 433 (2022) 134608. https://doi.org/10.1016/j.cej.2022.134608.

[99] A.B.D. Nandiyanto, R. Oktiani, R. Ragadhita, How to Read and Interpret FTIR Spectroscope of Organic Material, Indonesian J. Sci. Technol 4 (2019) 97. https://doi.org/10.17509/ijost.v4i1.15806.

[100] webpage, FTIR Functional Group Database Table with Search - InstaNANO, (n.d.). https://instanano.com/all/characterization/ftir/ftir-functional-group-search/ (accessed April 19, 2025).

[101] F. Fouchal, J.A.G. Knight, P.M. Dickens, Monitoring the polymerization of a diglycidyl ether bisphenol-A/2,2′-dimethyl-4,4′-methylenebis (cyclohexylamine) matrix with a Fourier transform infrared optical fibre sensor, Proceedings of the Institution of Mechanical Engineers, Part L: Journal of Materials: Design and Applications 218 (2004) 331–342. https://doi.org/10.1177/146442070421800407.

Chapter 6. Multicycle CH_4 Adsorption-Desorption in Biochar: Degradation Analysis and Value-Added Applications[4]

This chapter is based on a manuscript prepared for submission to a peer-reviewed journal.

Graphic abstract:

[4] V. Y. Ko, J. Wang, C. Lan, X. Huang and D. Ryan, "Multicycle CH_4 Adsorption-Desorption in Biochar: Degradation Analysis and Value-Added Applications" to be submitted to a peer-reviewed journal.

Abstract

To prevent venting and flaring natural gas in oil and gas fields where gas-recovery infrastructure is limited or unavailable, the use of low-cost biochars as adsorbents for methane (CH_4) capture and storage was investigated with particular focus on long-term adsorption performance. Four biochars derived from wood wastes were tested for CH_4 adsorption over more than 100 adsorption–desorption cycles. The adsorption capacities initially decreased rapidly during the first few cycles but subsequently approached stable values. The degradation of adsorption capacity was attributed to the accumulation of residual CH_4 within the pore structure of the biochar. Residual CH_4 retention was verified by infrared spectroscopy.

To utilize the degraded adsorbents containing residual CH_4, three potential utilization pathways were evaluated: 1) continued use for CH_4 adsorption; 2) use as a solid fuel for energy recovery; 3) use as a soil amendment to promote plant growth. The degraded biochars retain significant adsorption capacity for CH_4. It is shown that two of the biochars can store more CH_4 per unit volume than compressed-gas vessels at pressures up to 75 bar, which could eliminate the need for high-pressure compression and gas-gathering pipelines in oil and gas fields, thereby reducing associated costs. The other two biochars exceed compressed-gas storage capacity up to over 40 bar, which is above the typical operating pressure of adsorbed natural gas (ANG) systems for vehicles and could satisfy most storage requirements in oil and gas field applications operating at low-to-moderate pressures.

The degraded biochars exhibit higher calorific values and lower ignition temperatures, which are attributed to the presence of residual CH_4 within the pore structure. Moreover, the calorific values and ignition temperatures of the spent biochars compare favorably with those of lignite coal,

suggesting their potential use as solid fuels for energy recovery. Furthermore, residual CH_4 is gradually released from the biochar matrix, which may support plant growth if the spent biochars are applied as soil amendments. Such applications could contribute to cost-effective reduction of greenhouse-gas emissions while enabling value-added utilization of biochar in CH_4 adsorption systems.

Keywords:

CH_4 adsorption; Biochar; ANG; Multicycle degradation; Residual CH_4; Calorific value

Highlights:

- Multicycle CH_4 adsorption in biochars shows early-stage capacity loss followed by stabilization over extended cycling.
- Residual CH_4 accumulation increases calorific value (up to ~35%) and lowers ignition temperature relative to raw biochar.
- High-performing biochars (BL and AH) maintain volumetric CH_4 storage exceeding compressed gas up to 75 bar, even after degradation.
- FTIR and thermal analyses confirm gradual ambient release of retained CH_4, linking adsorption degradation to altered thermal behavior.
- Spent biochar exhibits lignite-comparable fuel properties and offers potential second-life pathways for energy recovery and soil amendment.

6.1 Introduction

Methane (CH_4) emissions represent one of the most urgent climate challenges associated with upstream oil and gas production. CH_4 is a powerful greenhouse gas, whose global warming potential is over 80 times greater than that of CO_2 over a 20-year period [1]. In Canada, CH_4 is the second-largest contributor to total GHG emissions, with the oil and gas sector accounting for 40–50% of national CH_4 releases, the single largest sectoral source [2], [3]. A substantial fraction of these emissions arises from intentional venting and flaring during routine operations or for safety purposes [4], [5].

In oil production, CH_4 is the principal component of the associated petroleum gas (APG) produced together with crude oil. This gas is frequently vented or flared when infrastructure for gas transport or utilization is unavailable [6]. Globally, flaring alone releases approximately 270–280 million tonnes of CO_2eq emissions annually, while venting contributes additional unburned CH_4 directly to the atmosphere [7]. On the other hand, CH_4 is a valuable fuel. It produces less CO_2 per unit energy during combustion than heavier fossil fuels and is often regarded as a transitional fuel in the global shift toward lower-carbon energy systems [8]. Utilizing the CH_4 as fuel instead of venting and flaring not only reduces greenhouse gas emissions but also reduces energy loss.

To utilize CH_4, effective capture and storage technologies are required. Current technologies include compressed natural gas (CNG) and liquefied natural gas (LNG). CNG requires compressing natural gas to high pressure and storing it in heavy vessels, whereas LNG requires cryogenic cooling and storage at very low temperatures [9]. Both technologies require substantial infrastructure and energy input, which may not be economically feasible for small-to-medium oil fields [10].

Adsorbed natural gas (ANG) has been used for natural gas vehicles, where the natural gas is adsorbed in activated carbons. ANG is under relatively low pressure (35-65 bar) and does not require large compressors and bulky high-pressure vessels. It is used under ambient temperature and does not require cooling facilities. If this technology is used in oil fields, it can enable substantial cost savings for handling the co-produced natural gas, as the gas is under pressure and large compressors and compression power can be saved. The storage does not require heavy vessels that are needed to stand high pressure of compressed gas and cooling that is needed to maintain the liquid phase of liquefied gas. The adsorbed gas can be released simply by lowering the pressure and the adsorbents can be reused.

In a previous study, biochar was evaluated as an adsorbent for CH_4 storage [11]. Biochar, a porous, carbon-rich material derived from biomass pyrolysis, has emerged as a promising adsorbent for CH_4 capture due to its high surface area, tunable porosity, and environmental sustainability [12], [13]. Biochar has properties similar to activated carbon such as high porosity and large surface area, but it is cheaper and more environmentally friendly. With increasing applications of biomass pyrolysis and gasification, biochar has high availability. The results of the previous study on CH_4 adsorption using biochar derived from forest waste are promising, showing that biochar could take more CH_4 per unit storage volume than gas vessels under low to moderate pressure, and using biochar for ANG in oil fields can have significant economic benefits. However, practical ANG deployment requires repeated adsorption-desorption cycles. Adsorbents are known to show decreasing adsorption capacity over many cycles [14]. The capacity degradation has been attributed to accumulation of residual hydrocarbons which reduce available adsorption sites [15]. Reactivation of degraded activated carbons may be achieved by thermal treatments under high temperatures, which can recover the adsorption capacity to over 90 percent [16], [17].

Nevertheless, a portion of the capacity is lost and eventually the spent adsorbent will need to be disposed of. Typical methods for disposal of spent activated carbons are landfill and incineration. At oil field scale, where large adsorbent inventories are required, the cumulative cost of reactivation and eventual disposal of spent adsorbent represents a significant economic burden.

Biochar has mostly been used for soil amendment. It may also be used as fuel for energy production [18]. These applications of biochar should also be feasible for spent biochars after they have reached their end life as CH_4 adsorbents.

The present work investigates the long-term CH_4 adsorption behavior of biochar. Further, the underlying mechanism for the observed behavior is elucidated and cost-effective applications for spent biochar adsorbents are evaluated. In particular, this study explores the potential of residual CH_4 in spent biochar for producing value-added solid fuel and soil conditioners. The results are expected to advance the understanding of biochar–CH_4 interactions and facilitate the application of biochar-based ANG toward maximizing environmental and economic benefits.

6.2 Materials and Methods

6.2.1 Materials

Four biochars (AH, AT, BL, and D6) were evaluated as adsorbents under multicycle conditions. AH is a non-commercial material produced from waste wood, with unspecified pyrolysis conditions. AT is derived from beetle-infested pinewood waste sourced from AirTerra Inc. BL was obtained from Bella Biochar Co. and originated from landfill-diverted waste wood. D6 was produced from railway waste wood via pyrolysis at 600 °C under a nitrogen atmosphere.

Table 6.1 presents the physical properties of the biochars including the specific surface area, pore volume, and average pore width determined by CO_2 adsorption at 273 K using a Brunauer–Emmett–Teller (BET) apparatus (ASAP2020 V3.00G, Micromeritics, USA). Prior to BET analysis, all samples (0.2–0.3 g) were degassed under vacuum at 300 °C for 10 hours to remove residual moisture and gases confined within micropores. Particle size (1.18–3.36 mm) was determined based on sieve mesh classification. Skeletal density was measured using a helium pycnometer (Accupyc II 1340, Micromeritics), while bulk density (g/mL) was obtained using a 5 mL sample reservoir. Compositional analyses including proximate analysis (moisture, ash, volatile matter, fixed carbon), ultimate analysis (C, H, N, O, S) and X-ray fluorescence (XRF) metal oxides analysis are shown in Table 6.2.

Table 6.1 Properties of adsorbent materials

Sample	Type	BET Surface Area (m^2/g)	Pore volume (cm^3/g)	Average Pore width (nm)	Particle Size (mm)	Bulk Density (g/ml)	Skeletal Density (g/ml)
AH	Non-commercial	404	0.250	0.6308	1.18 - 1.70	0.06	2.00
AT	Non-commercial	319	0.085	0.6202	1.18 - 3.36	0.16	1.73
BL	Commercial	506	0.128	0.6227	1.60 - 6.40	0.23	2.03
D6	Lab-made	266	0.116	0.6284	1.18 - 3.36	0.16	1.52

Table 6.2 Characteristic analysis of raw biochar (wt%)

Description	Moisture	Ash	Volatile Matter	Fixed Carbon	C	H	N	S	O	SiO_2	Al_2O_3	Fe_2O_3	TiO_2	P_2O_5	CaO	MgO	SO_3	Na_2O	K_2O
AH	8.68	12.0	12.9	66.4	72	0.6	0.3	<0.05	6.6	14	4.4	2.7	0.2	1.8	28	4.3	14	3.4	13
AT	8.52	4.56	11.4	75.5	82	1.3	0.4	<0.05	3.4	4.2	1.0	5.9	0.1	1.9	37	5.1	0.6	<0.2	14
BL	3.79	18.3	11.7	66.2	69	0.7	0.5	<0.05	7.4	25	4.5	2.0	0.2	0.4	24	13	0.6	0.9	3.0
D6	11.0	9.96	17.4	72.7	84	2.6	0.6	0.2	3.1	15	2.8	6.4	0.2	0.4	30	12	4.2	1.0	1.6

6.2.2 Adsorption measurements

Measurements for CH_4 adsorption by the biochars were conducted with a commercial sorption analyzer PCT-Pro from Setaram Inc. The analyzer is based on Sievert volumetric method, which is illustrated in Fig. 6.1. Measurements in the present work were under temperature of 25 ± 0.5 °C and pressure up to 75 bar.

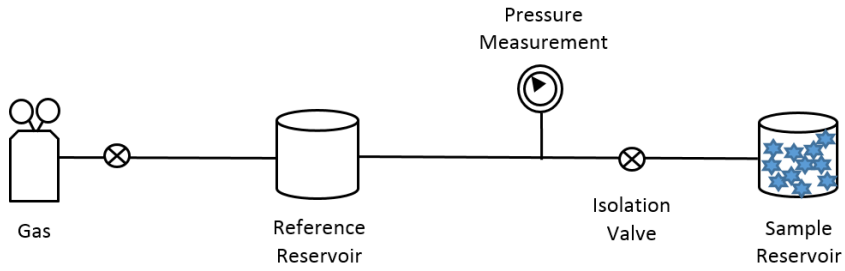

Fig. 6.1 A schematic of the Sievert measurement system

The volume of the sample reservoir is 5 mL. After the biochar sample was loaded, the free volume of the reservoir, i.e., the volume that was not occupied by the sample was determined using He at the measurement temperature. After this step an amount of pressurized CH_4 gas was introduced into the reference reservoir whose volume was known. Then the valve connecting the reference

reservoir to the sample reservoir was open to introduce the gas into the sample reservoir for adsorption measurement. The amount of CH_4 adsorbed was calculated based on the difference in equilibrium pressure measured before and after the gas transfer. To determine the molar quantity of CH_4 initially introduced and the amount remaining after equilibrium, pressure–volume–temperature (PVT) relationships were applied using non-ideal gas equations implemented in a computer program. This program calculated the incremental adsorption at each pressure step. After the highest equilibrium pressure was reached, adsorption measurement was stopped and desorption was performed by releasing the CH_4 gas in the sample and reference reservoirs and using a vacuum pump to degas the system. Then, a new adsorption and desorption cycle started. The same procedure repeated until the preset number of cycles was attained.

6.2.3 Calorific value and ignition temperature changes and CH_4 evolution after multicycle adsorption

Two important combustion properties, calorific value and ignition temperature, were evaluated to compare the biochars before and after multicycle adsorption of CH_4 to assess the potential for using spent biochar adsorbents as solid fuels. In addition, residual CH_4 evolution from biochar after multicycle adsorption of CH_4 was investigated to assess the potential for using biochar adsorbents for soil amendment. Differential scanning calorimetry (DSC), integrated with thermogravimetric analysis (TGA), quantified calorific values and ignition temperatures from exothermic peaks during heating. TGA-measured weight loss from ambient to 800–1000 °C at 10 °C/min under argon or air, identifying ignition temperatures at the onset of significant decomposition. Fourier Transform Infrared Spectroscopy (FTIR) was used to observe CH_4

evolution using a heated transfer line, capturing spectra (4000–400 cm^{-1}, 4 cm^{-1} resolution) with characteristic bands at 2990 cm^{-1}.

6.2.4 Biochar aging procedure

Biochar aging was performed by exposing the samples to ambient laboratory conditions (temperature ~25 °C, relative humidity ~60%) for a duration of 30 days. This approach was selected to simulate natural storage and handling conditions where biochar is exposed to air and moisture over time. After aging, the samples were dried under controlled conditions prior to analysis to ensure comparability with fresh samples.

6.3 Results and Discussions

6.3.1 Initial CH_4 adsorption capacity of biochars

CH_4 adsorption isotherms of the original biochars, i.e., the isotherms obtained from the first adsorption measurement are shown in Fig. 6.2. BL showed highest adsorption capacity, close to 2.5 mmol CH_4 per gram of biochar at 75 bar CH_4 gas pressure. The capacity of other biochars was lower in the decreasing order of AH, AT and D6. The CH_4 adsorption capacity of the biochars apparently correlates significantly with the specific surface area, as can be seen from the property data of Tables 6.1 and 6.2, whereas the other properties do not show clear influences on the adsorption performance.

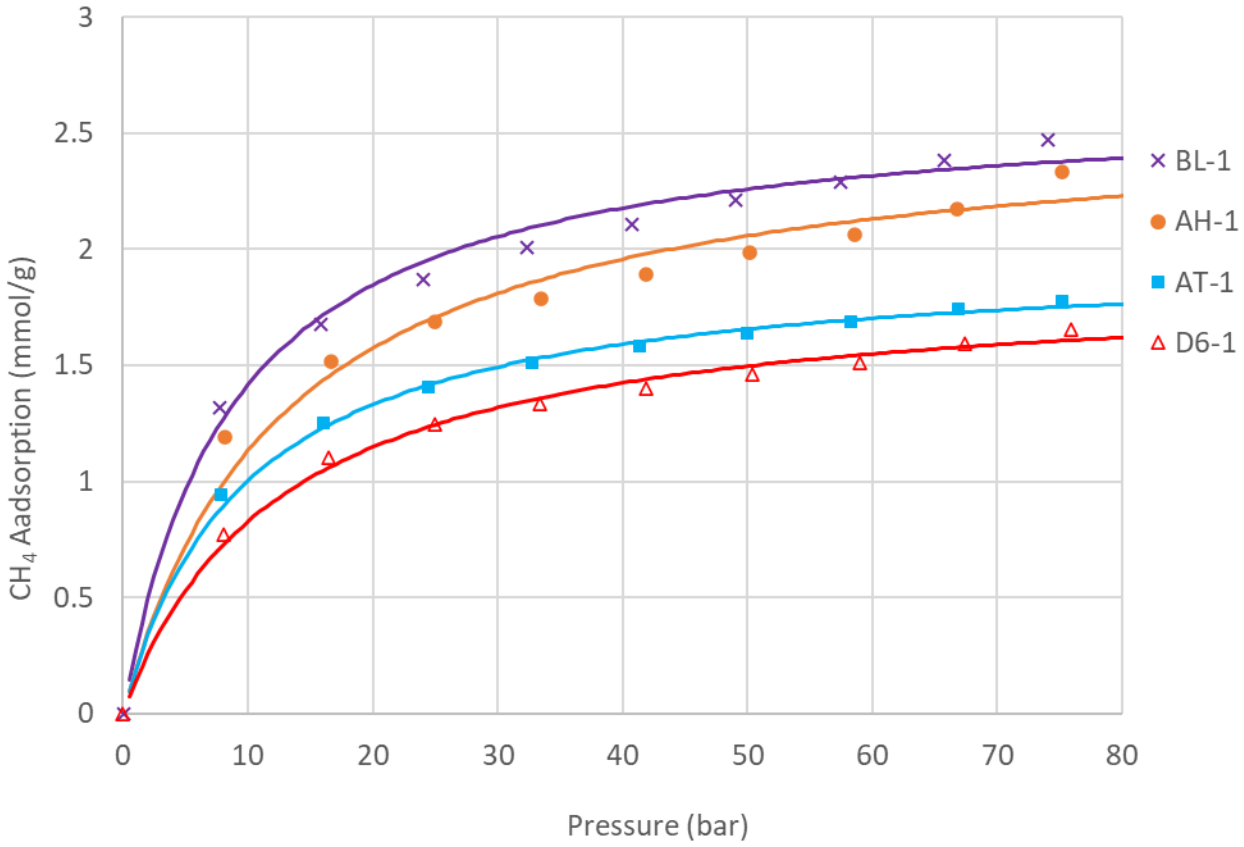

Fig. 6.2 Langmuir isotherms of CH_4 adsorption of biochars at the 1st cycle

The curves in Fig.6.2 represent the fitting to the CH_4 adsorption data by the Langmuir adsorption equation:

$$N = \frac{N_m BP}{1+BP} \tag{6.1}$$

where N is the number of millimoles of gas adsorbed by 1 gram of adsorbent; N_m is the maximum number of millimoles as the pressure increases infinitely. *B* is the Langmuir adsorption constant; *p* is the adsorption pressure. The Langmuir equation gave acceptable fittings to the experimental data. The square of the regression coefficient (R^2) for the fitting was between 0.9874 and 0.9991, as shown in Table 6.3. According to the Langmuir adsorption theory, the adsorbed molecules

form a monolayer on specific sites of the solid surface, with no further adsorption occurring once all sites are occupied.

Table 6.3 Langmuir adsorption isotherm parameters

	AH-1	**AT-1**	**BL-1**	**D6-1**
R^2	0.9874	0.9991	0.9957	0.9957
N_m (mmol/g)	2.5880	1.9794	2.6553	1.8776
B (bar^{-1})	0.0777	0.1026	0.1141	0.0786

6.3.2 Effects of multicycles on CH_4 adsorption capacity of biochars

Upon cyclic adsorption and desorption, the adsorption capacity of all four biochars decreased. This can be seen clearly in Fig. 6.3, which shows the adsorption isotherms of the last cycle of the biochars, respectively, in comparison with their initial (1^{st} cycle) isotherms. Notably, the patterns of the last-cycle isotherms of BL, AH and D6 are similar to those of their initial isotherms. By contrast, the adsorption capacity of AT showed a maximum at about 40 bar and then decreased with increasing pressure. This behavior is similar to the isotherms of two biochars at 30 °C, which were discussed in Chapter 3 and could be attributed to lower density of adsorbed CH_4.

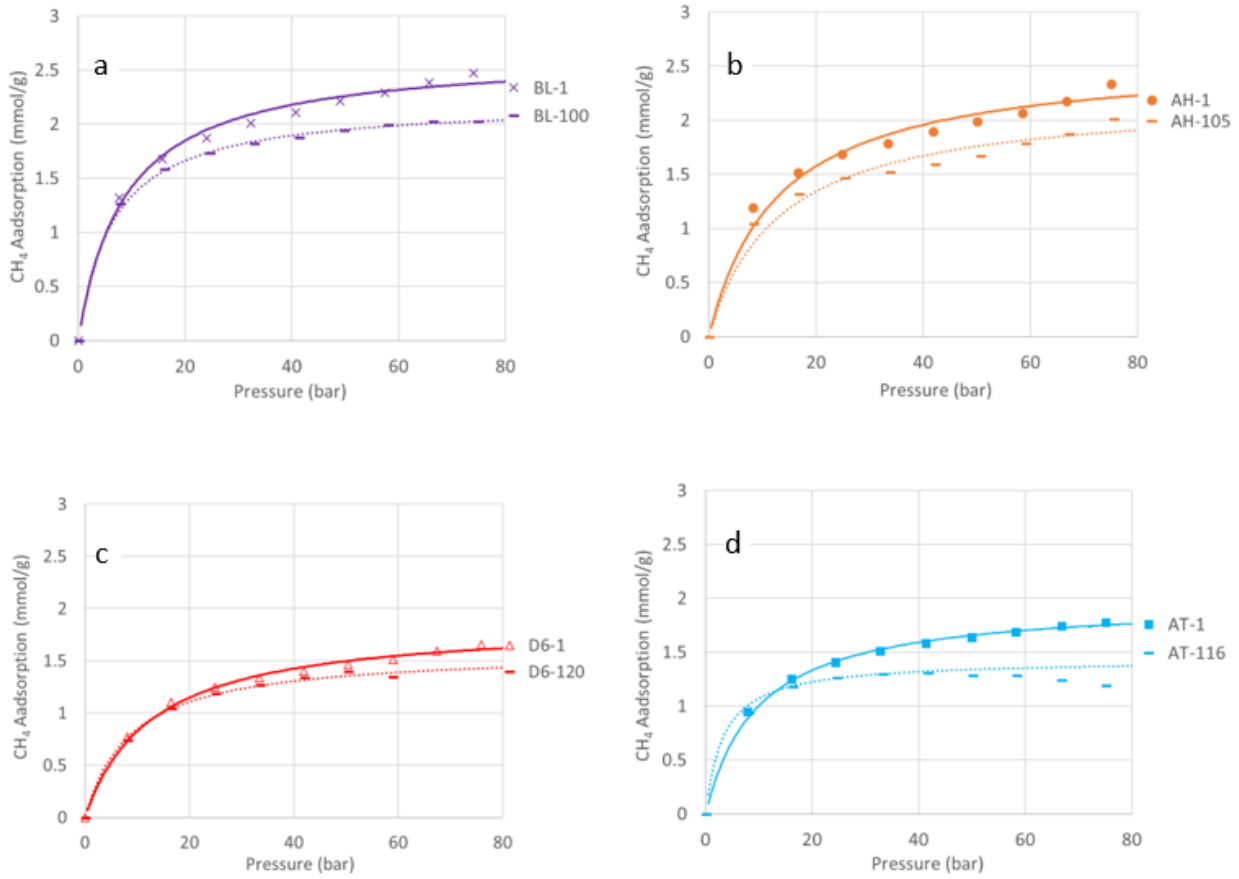

Fig. 6.3 Comparison of adsorption isotherms of biochars in the first cycle and the last cycle: a) BL; b) AH; c) D6; d) AT

Fig. 6.4 shows the dependence of adsorption capacity on the number of cycles at 75 bar, which is the highest pressure investigated in this study. The biochars show similar patterns of multicycle behavior. A notable feature is that the adsorption capacity does not decrease monotonically but instead exhibits periodic fluctuations, with alternating decreases and partial recoveries. In general, the adsorption capacity decreases with increasing number of cycles, with most of the decrease occurring in the first 10 cycles. Then the capacity fluctuates around a certain level which may be taken as stabilized. The drop in the adsorption capacity may be attributed to decreased adsorption sites due to undesorbed CH_4 molecules which occupy the adsorption sites. The rise may be

associated with the formation of microcracks in the biochar matrix caused by cyclic pressurization and depressurization, which create additional accessible surface area.

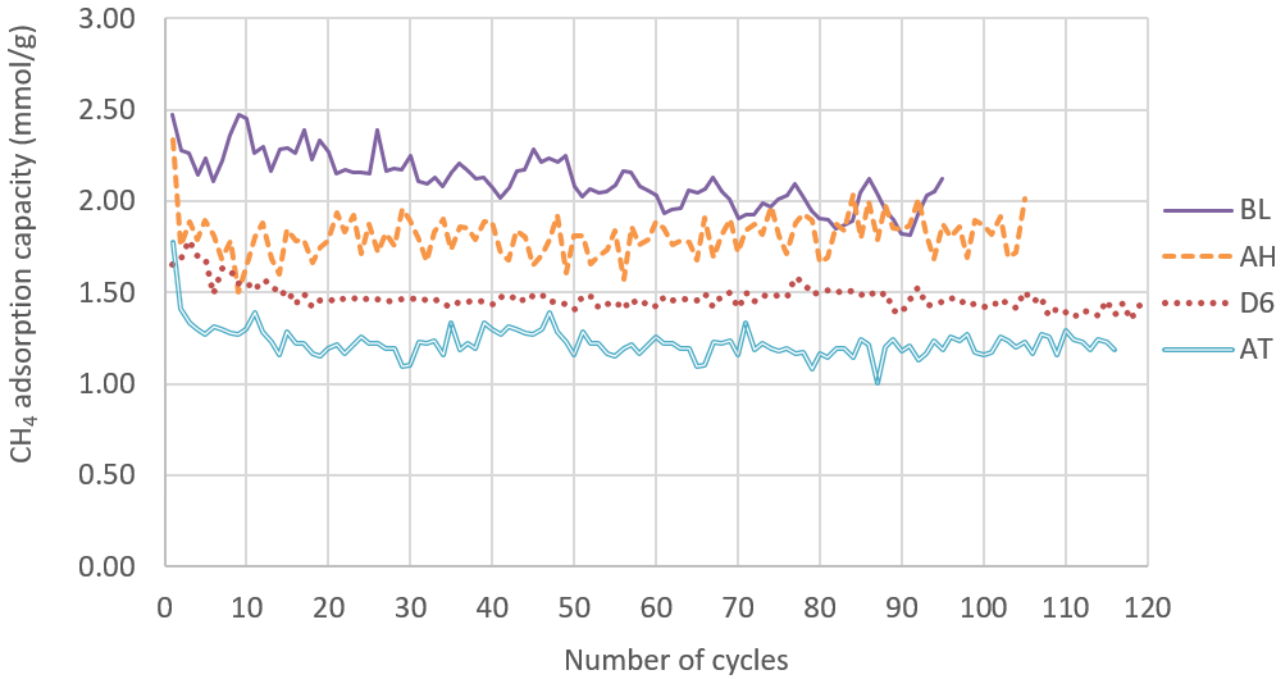

Fig. 6.4 CH_4 adsorption trend of biochars over multicycles

To evaluate the effect of residual CH_4 on the adsorption capacity, we first give a mathematical description of the adsorption capacity over multicycles [19]:

$$A_N = A_{N-1} - k(A_{N-1} - A_\infty) \tag{6.2}$$

where A_N is the activity of the adsorbent which is defined as the ratio of the adsorption level to the initial adsorption level. A_∞ is the stabilized activity value. k is a coefficient characterizing the rate of the degradation of adsorption capacity, which includes the effect of decreased adsorption sites by undesorbed CH_4 and the effect of newly created sites in the microcracks. The fitted curves obtained using Eq. 6.2 are shown in Fig. 6.5 and provide a reasonable representation of the experimental trends.

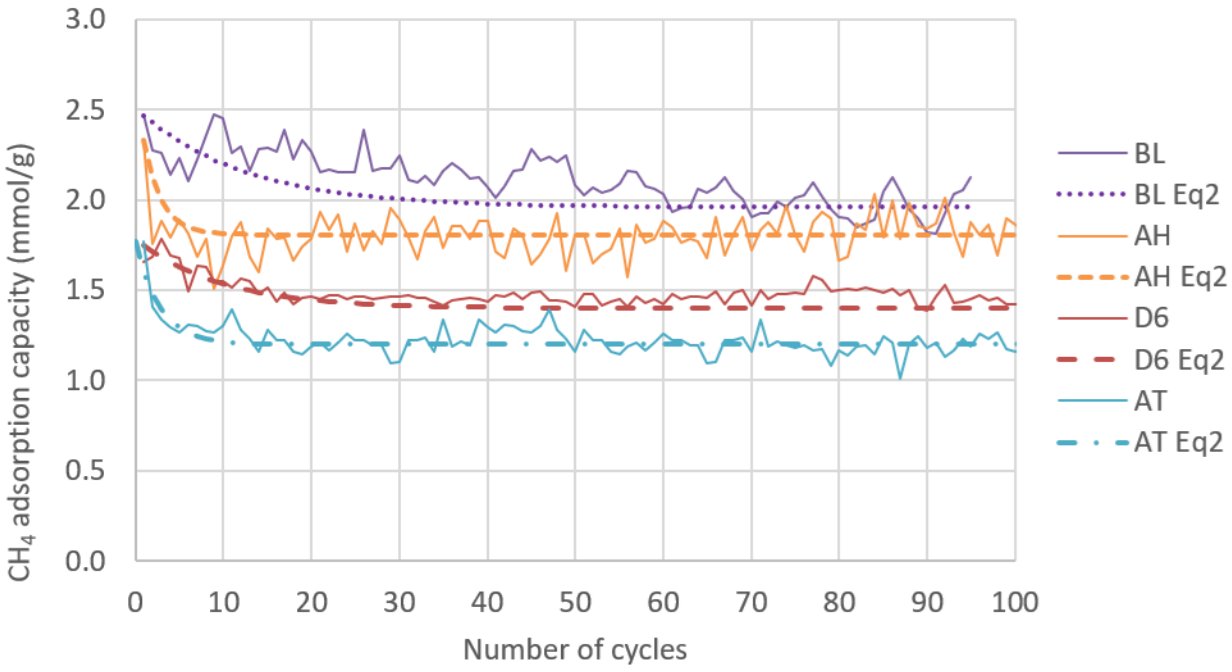

Fig. 6.5 Description of multicycle CH_4 adsorption behavior by Eq. 6.2

The above formula requires numerical computation for each previous cycle from the beginning, i.e., from the first cycle. To enable direct examination of the relationship between the adsorbent performance and number of cycles and better computational efficiency, the formula can be transformed into an explicit expression in the following way [19]:

$$\frac{A_N - A_{N-1}}{N-(N-1)} = \frac{\Delta A}{\Delta N} \tag{6.3}$$

When the number of cycles is large, $\frac{\Delta A}{\Delta N}$ may be approximated by $\frac{dA}{dN}$ and Eq. 6.2 be written into

$$\frac{dA}{dN} = -k(A - A_\infty) \tag{6.4}$$

where A is a continuous variable representing the activity. Eq. 6.5 results in

$$A_N = A_\infty + (1 - A_\infty)e^{-kN} \tag{6.5}$$

which can be directly calculated for any cycle number N without the need of determining the values of the preceding cycles. Fig. 6.6 compares exemplary calculation results of the two equations for BL and AH, which have high adsorption capacity. Even for small cycle numbers Eq. 6.5 results essentially in the same values as Eq. 6.2. Eq. 6.5 also shows that activity decreases exponentially with the number of cycles featured by a rapid initial drop followed by an asymptotic level. We use Eq. 6.5 to discuss long-term adsorption behavior and check the relationship between the apparent adsorption capacity and the residual CH_4.

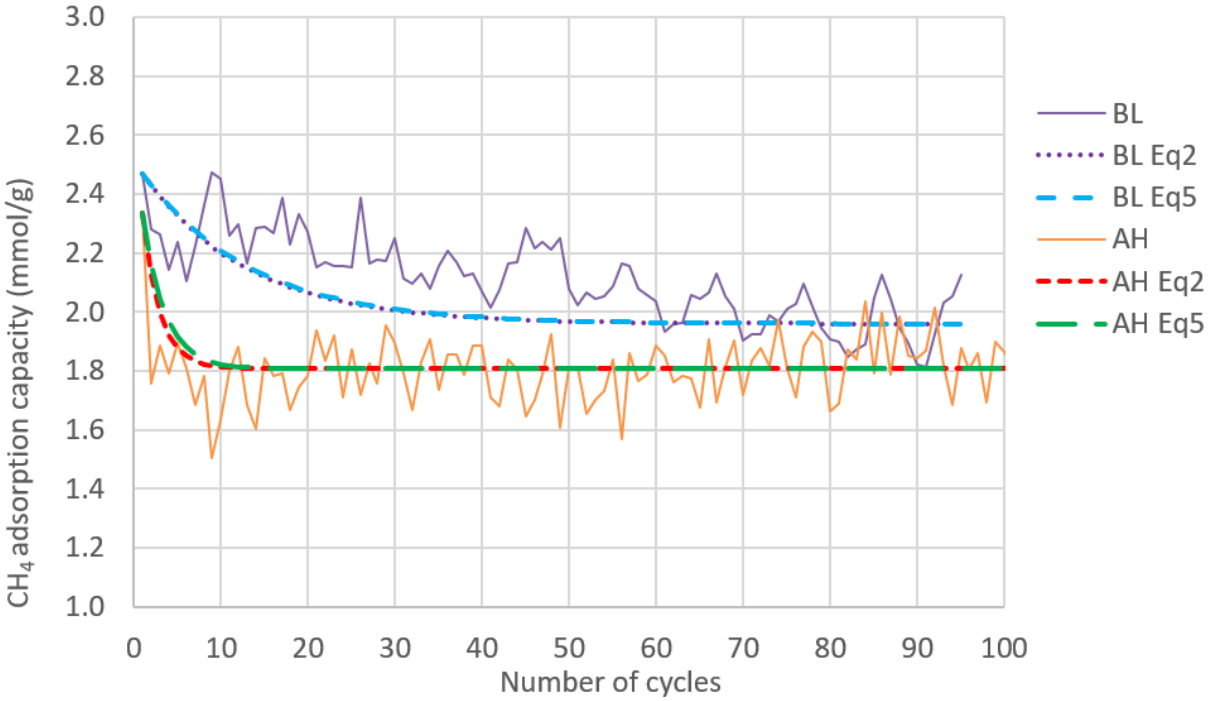

Fig. 6.6 Comparison of Eq. 6.2 and Eq. 6.5 for description of multicycle adsorption behavior for biochars BL and AH

It is worth noting that the two high adsorption-capacity biochars BL and AH can store more CH_4 than compressed gas in a given volume up to 75 bar. This comparison is discussed below.

The adsorption values obtained from the volumetric measurements correspond to Gibbs excess adsorption, which counts only the additional gas near the surface relative to the bulk gas density,

without accounting for the volume occupied by the adsorbed phase. Consequently, the adsorbed phase can be viewed as attached to the skeleton of adsorbents without taking any space whereas all the void volume which is not occupied by the skeleton is viewed as filled by the gas phase adsorbate. Thus, the amount of adsorption is related to the skeletal density volumetrically: a higher skeletal density yields a greater amount of adsorbed CH_4 per unit skeletal volume. The biochars BL and AH have relatively high skeletal densities (2.03 g/cm^3 for BL and 2.00 g/cm^3 for AH).

To compare the storage capacity of the biochars with that of compressed CH_4 in terms of volume, we just need to compare the excess adsorption of the solid portion of the biochars with the capacity of compressed gas which takes the space of the solid portion of the biochars. This is because by the definition of excess adsorption, the pore space of adsorbents is taken as filled with gas under the same pressure of compressed gas and therefore occupying the same space of compressed gas per unit pore volume. In this way, the storage capacity of the biochars on the volume basis can be calculated by multiplying the excess adsorption (i.e., the experimentally measured adsorption) with the skeletal density of the biochars.

The adsorption capacities determined this way for the four biochars are shown in Fig. 6.7, in comparison with the storage capacity of compressed CH_4 which is determined from the density of CH_4 gas under 75 bar and the same temperature 25 °C. As can be understood, even after the adsorption capacity drops to the asymptotic level, the ability for storing CH_4 by the skeletal volumes of the two biochars is still higher than compressed CH_4 that occupies the same volume under 75 bar.

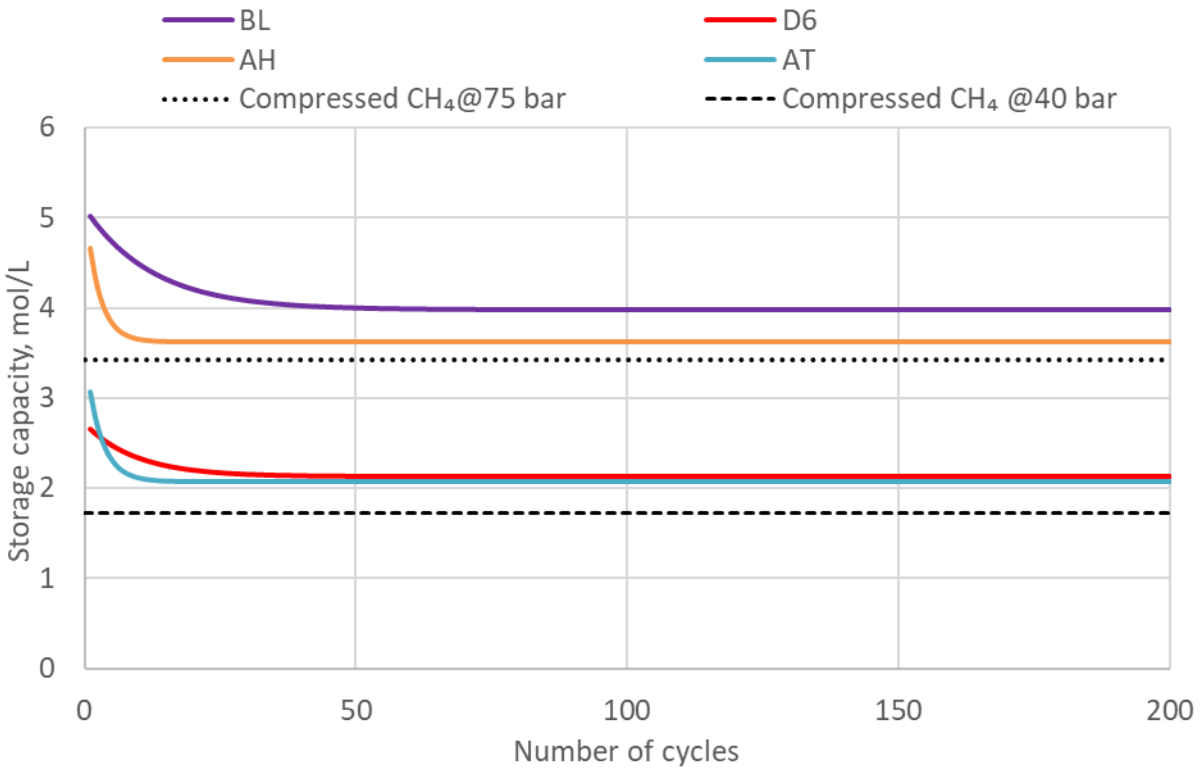

Fig. 6.7 Multicycle degradation and stabilization of volumetric CH_4 storage capacity of BL, AH, D6, and AT biochars compared with compressed CH_4 at 75 bar

Also shown in Fig. 6.7 are the predicted long-term adsorption performances for the two lower-capacity biochars AT and D6. As can be understood, after the degradation the unit-volume adsorption capacity of these two biochars is above the storage capacity of compressed CH_4 at 40 bar, which is above the 35 bar gas pressure for ANG vehicles and could meet most of the pressure requirements for CH_4 storage and utilization in oil and gas fields.

The results suggest that, with the same volume, the biochars could store more CH_4 than compressed gas vessels could do even after long-term use. Moreover, when the pressure is lower, the storage capacity of the biochars would be further higher than that of the compressed gas vessels, because the density of compressed CH_4 decreases faster with pressure.

This can be seen from Fig. 6.8. Near 20 bar, the two lower-capacity biochars can store twice or more CH_4 than compressed gas, while the two higher-capacity biochars can store over triple more CH_4 than compressed gas.

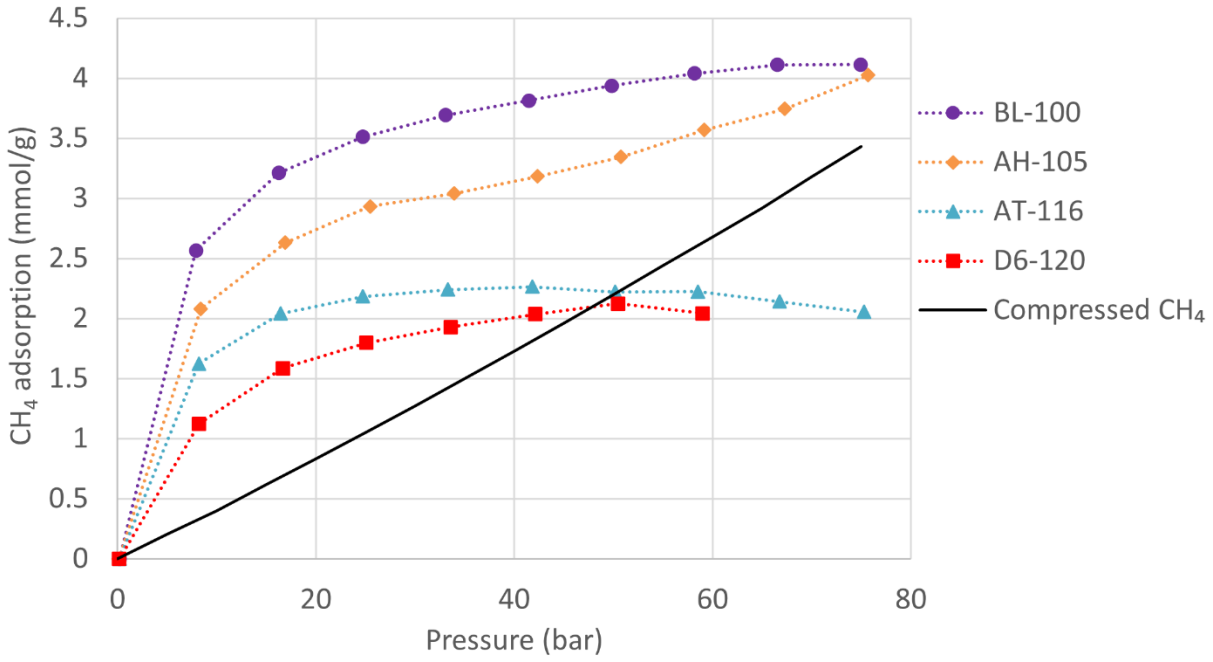

Fig. 6.8 Comparison of CH_4 storage capacity of degraded biochars with compressed gas

Furthermore, when the temperature decreases, the storage capacity of the biochars would be increasingly higher than compressed-gas vessels, as CH_4 adsorption increases with decreasing temperature whereas the density of compressed CH_4 has a weak temperature dependence. The temperature effect is illustrated in Fig. 6.9 by the results of a previous study [11]. This is advantageous for our targeted application in Canadian oil and gas fields, where ambient temperature is lower

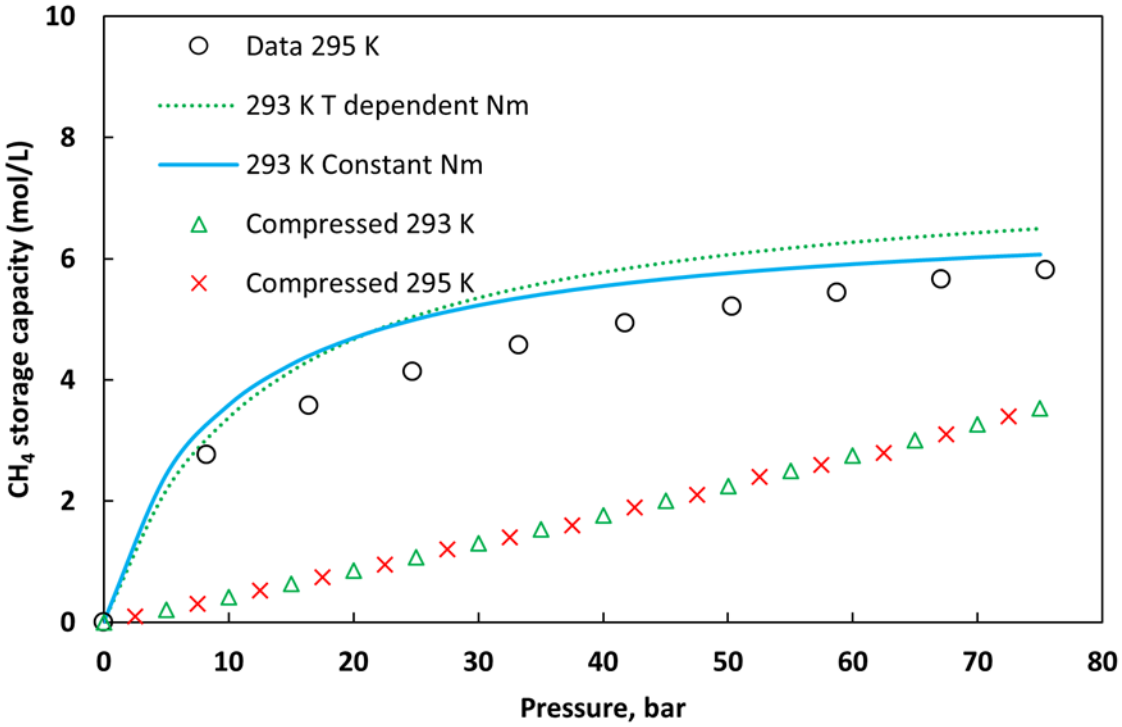

Fig. 6.9 Volumetric CH_4 storage performance of BC-Ash under varying temperature and pressure conditions compared with compressed gas storage. Reproduced from Fig. 3.3 (Chapter 3) [11]

6.3.3 Effects of multicycles on calorific values and ignition temperatures of biochars

The observed decrease in adsorption capacity following repeated adsorption-desorption cycles is attributed to residual CH_4 molecules occupying adsorption sites. If this interpretation is correct, the retained CH_4 should contribute to an increase in the calorific value of the biochar, since CH_4 is combustible. To examine this effect, the calorific values of the biochar samples before adsorption and after multicycle operation were evaluated using DSC.

Fig. 6.10 presents representative DSC curves of BL before adsorption (BL-0), after 100 adsorption–desorption cycles (BL-100), and after 100 cycles followed by 30 days of aging (BL-

100-30). The exothermic peak area, corresponding to the calorific value, increases markedly after multicycle adsorption. As summarized in Table 6.4, the calorific value of BL rises from 13.88 kJ/g (BL-0-0) to 18.62 kJ/g (BL-100-0), representing an increase of approximately 34%. If the spent biochar adsorption is used as a solid fuel, the calorific value can be substantially higher compared to the raw biochar.

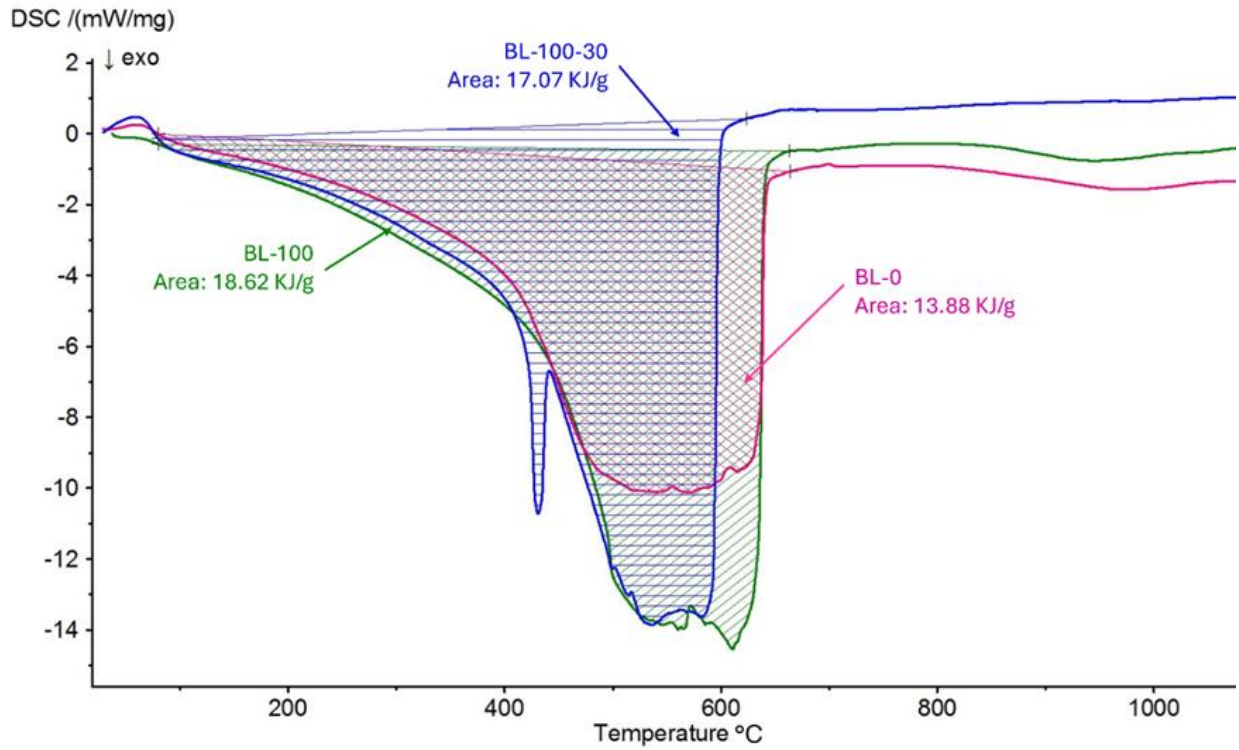

Fig. 6.10 Calorific values of BL biochar before adsorption (BL-0), after 100 CH_4 adsorption-desorption cycles (BL-100), and after 30 days of aging (BL-100-30)

After 30 days of exposure to air (BL-100-30), the calorific value decreases to 17.07 kJ/g from 18.62 kJ/g. Although higher than the raw biochar, the reduction relative to BL-100 suggests gradual desorption or diffusion of CH_4 from the pore network under ambient conditions. This interpretation is consistent with the observed decrease in CH_4 adsorption capacity over cycles and supports the hypothesis that retained CH_4 is responsible for the calorific enhancement.

The shift in ignition temperature shown in Table 6.4 provides complementary evidence. For BL, the ignition temperature decreases from 273 °C (BL-0-0) to 256 °C (BL-100-0), indicating enhanced combustibility after cycling. Following 30 days of aging, the ignition temperature increases to 285 °C, which is consistent with partial CH_4 loss and reduced reactivity. Notably, this increase occurs despite the calorific value of BL-100-30 remaining higher than that of BL-0. This divergence indicates that ignition behavior is not governed solely by residual CH_4 content. The increase in ignition temperature is attributed to moisture uptake during aging under ambient laboratory humidity, where adsorbed water requires additional energy for evaporation prior to combustion, thereby delaying ignition. In contrast, the elevated calorific value reflects retained residual CH_4 within the micropore structure. Therefore, while calorific value and ignition behavior generally reflect CH_4 retention and release, ignition temperature is also sensitive to environmental effects introduced during aging.

For a solid fuel, ignition temperature is a key parameter governing combustion behavior. Understanding how residual CH_4 retained within the pore structure of biochar influences ignition characteristics is therefore of particular interest. The ignition temperatures of the biochars were determined using thermogravimetric analysis (TGA) in the present study.

A representative TGA result is shown in Fig. 6.11 for AH biochar, where sample mass loss is plotted as a function of temperature. Ignition temperature was determined using the deviation method, defined as the temperature at which the combustion curve obtained under oxidizing conditions (air) begins to deviate from the inert pyrolysis baseline (Ar), indicating the onset of oxidative mass loss [20-22]. The two curves in Fig. 6.11 represent the results of raw AH (denoted by AH-0) and AH after 105 cycles of adsorption of CH_4 (denoted by AH-105), respectively. It can

be seen that the ignition temperature of AH decreased from 320 °C to 250 °C after multicycle adsorption of CH_4.

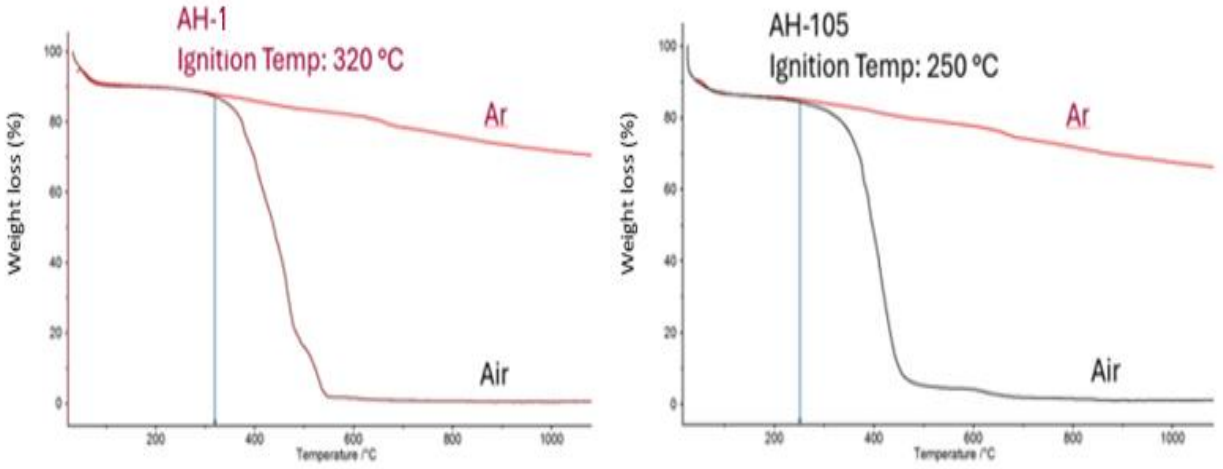

Fig. 6.11 Shift in ignition temperature of AH biochar (AH-0) after 105 cycles (AH-105)

The calorific value and ignition temperature of other biochar samples were evaluated and summarized in Table 6.4. Similar trends are observed for AT and D6. For AT, calorific value increases from 14.12 to 15.06 kJ/g, accompanied by a reduction in ignition temperature from 300 °C to 250 °C. For D6, calorific value increases progressively with cycle number (10.39→12.72 kJ/g from 0 to 120 cycles), while ignition temperature decreases moderately (312→300 °C). However, the magnitude of change for D6 remains smaller than that of BL, consistent with its lower adsorption capacity.

In general, the calorific value increased and ignition temperature decreased after the biochars underwent multicycle adsorption of CH_4. The slightly reduced calorific value and increased ignition temperature observed for BL-100-30 relative to BL-100 suggest partial release of residual CH_4 during ambient aging. This release may also influence non-combustion applications of spent biochar, such as soil amendment. The accumulation and subsequent loss of residual CH_4, and their

relationship to changes in calorific value and ignition temperature, are further examined in conjunction with the infrared spectroscopy results discussed.

Table 6.4 Calorific values and ignition temperatures of biochars before and after multicycles of CH_4 adsorption

Sample-Cycles-Aging (days)	Ignition Temperature (°C)	Calorific value (kJ/g)
AH-0	320	14.95
AH-105	250	15.16
AT-0	300	14.12
AT-116	250	15.06
BL-0	273	13.88
BL-100	256	18.62
BL-100-30*	285	17.07
D6-0	312	10.39
D6-49	301	11.33
D6-120	300	12.72

***BL after 100 CH_4 adsorption cycles and then exposed to air for 30 days.**

6.3.4 Evidence of residual CH_4 in biochar after multicycle adsorption

Fig. 6.12 presents infrared spectroscopy results providing qualitative evidence for residual CH_4 retained in biochar following multicycle adsorption. The absorption bands near 2990 cm^{-1} correspond to C–H stretching vibrations characteristic of CH_4 and are observed in cycled BL samples (BL-100) and in samples exposed to air for 7 and 30 days following cycling, but are absent in the uncycled BL-0 sample. After multicycle operation, a discernible CH_4 signal appears in the biochar, indicating CH_4 retention within the pore structure. Upon exposure to ambient air, the intensity of this band decreases progressively with time, demonstrating gradual CH_4 release. This

behavior is consistent with the calorific values trends summarized in Table 6.4, where the calorific value of BL increases after 100 cycles, and subsequently decreases following 30 days of air exposure.

If the spent biochar adsorbents are repurposed as soil amendments, their contribution extends beyond the gradual release of retained CH_4. Biochar itself is widely recognized for improving soil health by enhancing water retention, increasing nutrient-holding capacity, improving soil structure, and supporting microbial activity. These properties can promote root development and overall plant growth, particularly in degraded or low-fertility soils.

In addition, the gradual release of retained CH_4 may provide auxiliary functional benefits. CH_4 has been reported to act as a signaling molecule in plants, promoting root development and enhancing tolerance to abiotic stresses. Soil microorganisms can also utilize CH_4 as a carbon and energy source, potentially supporting plant growth through microbe–plant interactions [23]. These effects suggest that CH_4-retaining biochar may offer combined benefits in soil systems, where the intrinsic properties of biochar provide the primary contribution, while retained CH_4 plays a secondary, supportive role. However, direct biological validation is required to confirm these interactions.

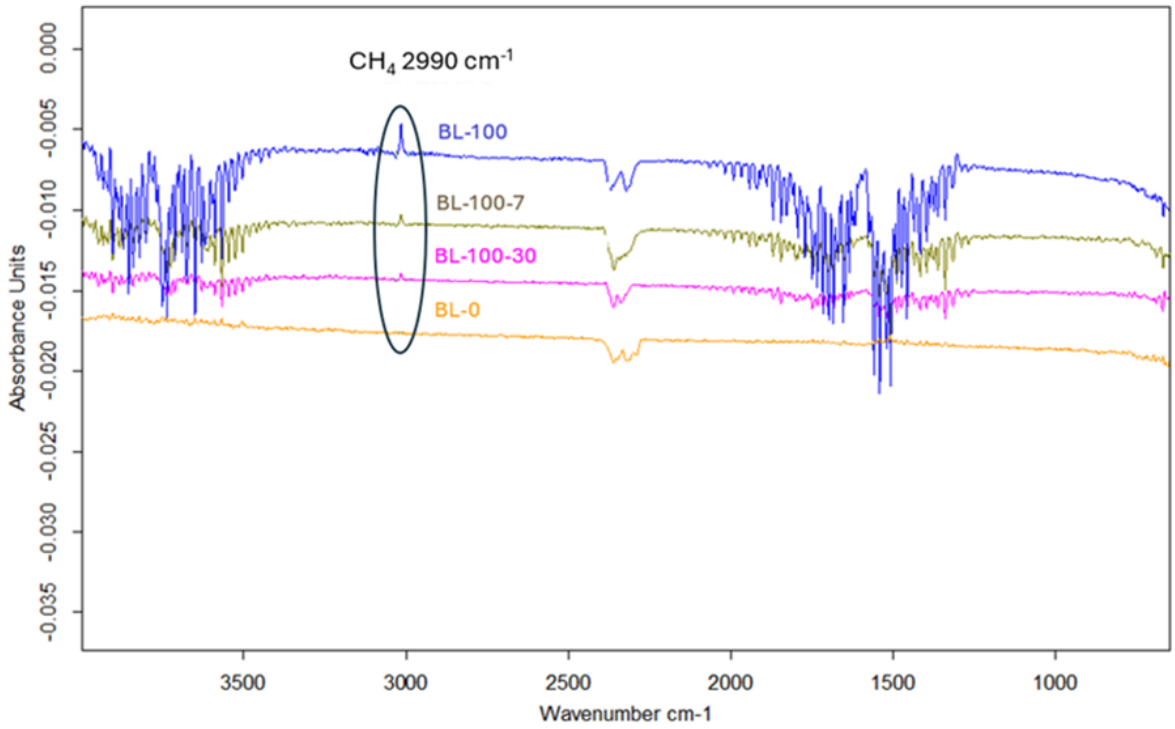

Fig. 6.12 Infrared spectroscopy for BL samples, where BL-0 denotes fresh BL, BL-100 denotes BL-0 subjected to 100 CH_4 adsorption cycles, and BL-100-7 and BL-100-30 denote BL-100 exposed to air for 7 days and 30 days, respectively

6.3.5 The relationship of changed calorific value and ignition temperature with respect to decreased CH_4 adsorption capacity

Since the increased calorific value and decreased ignition temperature of the biochars could be related to the residual methane, and the residual methane could be the cause of the decrease in the CH_4 adsorption capacity of the biochars, the change in the calorific value and ignition temperature could be connected to the decrease in the CH_4 adsorption capacity.

CH_4 is a combustible gas. If the calorific values of raw biochar and adsorbed CH_4 are additive, the increased calorific value of the biochar after multicycle CH_4 adsorption may be calculated from the calorific value of adsorbed CH_4. Table 6.5 compares measured calorific value changes (ΔH) with the calculated calorific values of residual CH_4 ($\Delta Hcal$) based on the reduction in adsorption

capacity (ΔA), assuming the amount of the residual CH_4 is equal to the decreased amount of adsorbed CH_4 and the calorific value of adsorbed CH_4 is equal to that of CH_4 gas.

For AH, the measured calorific-value increase (0.42 kJ/g) is close to the calculated result (0.40 kJ/g) based on the adsorption capacity drop. However, for BL, AT, and D6, the measured calorific-value increases are substantially higher than the predicted values based on the apparent adsorption-capacity reduction. This discrepancy indicates that the actual amount of retained CH_4 is larger than expected from the apparent adsorption capacity drop.

One possible explanation is that microcracks formed in the biochars due to repeated compression and decompression, similar to the phenomenon of material fatigue under cyclic loading. The microcracks lead to new surface area for adsorption which compensated for the adsorption capacity drop caused by undesorbed CH_4 molecules. As a result, the actual contents of CH_4 residue in the biochars are higher, leading to higher calorific value.

Table 6.5 Measured and predicted changes in calorific value based on adsorption capacity reduction

	A_0 (mmol/g)	**A_∞ (mmol/g)**	**ΔA (mmol/g)**	**ΔH (kJ/g)**	**ΔHcal (kJ/g)**
BL-100	2.41	1.96	0.45	4.74	0.36
AH-105	2.30	1.80	0.50	0.42	0.40
AT-116	1.77	1.20	0.57	0.94	0.46
D6-120	1.75	1.40	0.35	2.33	0.28

The multicycled biochars consistently show lower ignition temperatures compared with their raw biochars. This could be attributed to residual CH_4 accumulation within the pore network. It is worth noting that the autoignition temperature of CH_4 gas is 537 °C, which is much higher than the ignition temperature of the raw biochars in this study. The lower ignition temperature of the

biochars after multicycle adsorption of CH_4 could be the result of fixation of adsorbed CH_4 molecules on the pore surfaces. In addition to the higher surface concentration of CH_4 which enables higher frequency of collisions with reactive species such as O_2 and O-H radical, favorable orientations of adsorbed molecules may increase the efficiency of the collisions and lower the activation energy for CH_4 oxidation. The overall outcome is lower ignition temperature compared to both raw biochar and pure CH_4 gas. Low ignition temperature allows easy and stable burning and reduces pollutant emissions. These are desirable if the spent biochar is used as a solid fuel.

For natural gas, the degradation of the adsorbent would be more significant because of the presence of higher hydrocarbons C_2 and above which can contribute to pore blocking or stronger adsorption. In conventional activated carbon adsorption systems, regeneration at elevated temperatures is commonly practiced and may be economically viable. However, for low-cost biochars, replacement with fresh material and repurposing of spent biochar for secondary applications may be more cost-effective than thermal regeneration.

The results show that, although the apparent adsorption capacity of the biochars declines only moderately with cycling, residual CH_4 accumulates and enhances the calorific value while reducing ignition temperature. Notably, the calorific values and ignition temperatures of the multicycled biochars compare favorably with those of lignite coal [24], indicating that spent biochar adsorbents possess potential as solid fuels for energy recovery.

6.4 Conclusions

Degradation of CH_4 adsorption capacity was observed for all biochar adsorbents during repeated adsorption–desorption cycles. This degradation follows an exponential trend with cycle number and is attributed to the accumulation of residual CH_4 in biochar, as confirmed by infrared

spectroscopy. The degraded biochars exhibit increased calorific values and reduced ignition temperatures, which could be related to the residual CH_4.

Despite capacity degradation, the high-performing biochars BL and AH maintain volumetric CH_4 storage capacities exceeding those of compressed gas at pressures up to 75 bar. In addition, all multicycled biochars exhibit calorific values and ignition temperatures comparable to those of lignite coal, indicating that spent adsorbents may be repurposed as solid fuels for energy recovery.

Residual CH_4 was observed to decrease gradually during ambient aging, suggesting slow release from the biochar matrix. This behavior may enable secondary non-combustion applications, such as soil amendment, where retained CH_4 may promote plant growth. Such applications of spent biochar adsorbents can support cost effective reduction of CH_4 emissions and value-added utilization of biochar by the adsorption process.

Declarations

Availability of data and material

All related data are included in this article or available upon request.

Competing interests

The authors have no competing interest in declaring that they are relevant to the content of this article.

Funding

This work is supported by the Program of Energy Research Development of Canada.

Author contributions

All authors contributed to this work.

Acknowledgment

References

[1] Environmental Defense Fund, “Methane: A crucial opportunity in the climate fight - Environmental Defense Fund.” Accessed: Feb. 23, 2026. [Online]. Available: https://www.edf.org/climate/methane-crucial-opportunity-climate-fight

[2] K. MacKay, S. P. Seymour, H. Z. Li, D. Zavala-Araiza, and D. Xie, “A Comprehensive Integration and Synthesis of Methane Emissions from Canada’s Oil and Gas Value Chain,” *Environ. Sci. Technol.*, vol. 58, no. 32, pp. 14203–14213, Aug. 2024, doi: 10.1021/acs.est.4c03651.

[3] B. M. Conrad, D. R. Tyner, H. Z. Li, D. Xie, and M. R. Johnson, “A measurement-based upstream oil and gas methane inventory for Alberta, Canada reveals higher emissions and different sources than official estimates,” *Commun Earth Environ*, vol. 4, no. 1, p. 416, Nov. 2023, doi: 10.1038/s43247-023-01081-0.

[4] ECCC, “Reducing methane emissions from Canada’s oil and gas sector: discussion paper.” Accessed: Feb. 23, 2026. [Online]. Available: https://www.canada.ca/en/environment-climate-change/services/canadian-environmental-protection-act-registry/consultation-reducing-methane-emissions-oil-gas-sector.html

[5] Alison Bailie, “Finalizing Canada’s oil and gas methane regulations,” 440 Megatonnes: Tracking Canada’s path to net zero. Accessed: Feb. 23, 2026. [Online]. Available: https://440megatonnes.ca/insight/finalizing-canada-oil-gas-methane-regulations-easy-win-climate-progress/

[6] E. Chan *et al.*, “Hybrid bottom-up and top-down framework resolves discrepancies in Canada’s oil and gas methane inventories,” *Commun Earth Environ*, vol. 5, no. 1, p. 566, Oct. 2024, doi: 10.1038/s43247-024-01728-6.

[7] J. Hu, H. Gao, X. Wang, and B. Tan, “High-Capacity Volumetric Methane Storage in Hyper-Cross-Linked Porous Polymers via Flexibility Engineering of Building Units,” *Advanced Materials*, vol. 37, no. 16, p. n/a-n/a, 2025, doi: 10.1002/adma.202418005.

[8] Tom Green and Ian Hanington, “Burning-Bridge-Debunking-LNG-as-a-Climate-Solution-Report.” © 2023 David Suzuki Foundation.

[9] T. He, I. A. Karimi, and Y. Ju, “Review on the design and optimization of natural gas liquefaction processes for onshore and offshore applications,” *Chemical Engineering Research and Design*, vol. 132, pp. 89–114, Apr. 2018, doi: 10.1016/j.cherd.2018.01.002.

[10] D. Lozano-Castelló, J. Alcañiz-Monge, M. A. de la Casa-Lillo, D. Cazorla-Amorós, and A. Linares-Solano, “Advances in the study of methane storage in porous carbonaceous materials,” *Fuel*, vol. 81, no. 14, pp. 1777–1803, Sep. 2002, doi: 10.1016/S0016-2361(02)00124-2.

[11] V. Y. Ko, J. Wang, I. He, D. Ryan, X. Zhang, and C. Lan, “Adsorption of methane on biochar for emission reduction in oil and gas fields,” *Biochar*, vol. 5, no. 1, p. 15, Mar. 2023, doi: 10.1007/s42773-023-00209-x.

[12] P. Brassard *et al.*, “4 - Biochar for soil amendment,” in *Char and Carbon Materials Derived from Biomass*, M. Jeguirim and L. Limousy, Eds., Elsevier, 2019, pp. 109–146. doi: 10.1016/B978-0-12-814893-8.00004-3.

[13] M. Jeguirim *et al.*, “12 - Sustainability assessment for biomass-derived char production and applications,” in *Char and Carbon Materials Derived from Biomass*, M. Jeguirim and L. Limousy, Eds., Elsevier, 2019, pp. 447–479. doi: 10.1016/B978-0-12-814893-8.00012-2.

[14] M. Bastos-Neto, A. E. B. Torres, D. C. S. Azevedo, and C. L. Cavalcante, “A Theoretical and Experimental Study of Charge and Discharge Cycles in a Storage Vessel for Adsorbed Natural Gas,” *Adsorption*, vol. 11, no. 2, pp. 147–157, 2005, doi: 10.1007/s10450-005-4906-y.

[15] J. Zheng, G. Huang, Q. Cheng, L. Zhen, Y. Cai, and W. Wang, “Degradation of mechanical and microporous properties of coal subjected to long-term sorption,” *Fuel*, vol. 315, p. 123245, May 2022, doi: 10.1016/j.fuel.2022.123245.

[16] B. Ledesma, S. Román, A. Álvarez-Murillo, E. Sabio, and J. F. González, “Cyclic adsorption/thermal regeneration of activated carbons,” *Journal of Analytical and Applied Pyrolysis*, vol. 106, pp. 112–117, Mar. 2014, doi: 10.1016/j.jaap.2014.01.007.

[17] F. Salvador, N. Martin-Sanchez, R. Sanchez-Hernandez, M. J. Sanchez-Montero, and C. Izquierdo, “Regeneration of carbonaceous adsorbents. Part I: Thermal Regeneration,” *Microporous and Mesoporous Materials*, vol. 202, pp. 259–276, Jan. 2015, doi: 10.1016/j.micromeso.2014.02.045.

[18] H.-P. Schmidt, Novel Uses of Biochar, p. 106.

[19] J. Wang and Edward J. Anthony, “A common decay behavior in cyclic processes,” *Chemical Engineering Communications*, vol. 194, no. 11, pp. 1409–1420, Nov. 2007, doi: 10.1080/00986440701401594.

[20] L. C. de Morais, A. A. Maia, P. R. Resende, A. H. Rosa, and L. J. R. Nunes, “Thermochemical Conversion of Sugarcane Bagasse: A Comprehensive Analysis of Ignition and Burnout Temperatures,” *Clean Technologies*, vol. 4, no. 4, pp. 1127–1137, Oct. 2022, doi: 10.3390/cleantechnol4040068.

[21] I. Ávila, P. M. Crnkovic, F. E. Milioli, and J. D. Pagliuso, “Kinetic Interpretation of the Ignition Temperature for Coals,” 2008.

[22] W. Cao, J. Li, and L. Lue, “Study on the ignition behavior and kinetics of combustion of biomass,” *Energy Procedia*, vol. 142, pp. 136–141, Dec. 2017, doi: 10.1016/j.egypro.2017.12.022.

[23] L. Li, S. Wei, and W. Shen, “The role of methane in plant physiology: a review,” *Plant Cell Reports*, vol. 39, no. 2, pp. 171–179, 2019, doi: 10.1007/s00299-019-02478-y.

[24] C. Sensogut, H. Ozsen, and A. Demirbas, “Combustion Characteristics of 24 Lignite Samples,” *Energy Sources, Part A: Recovery, Utilization, and Environmental Effects*, vol. 30, no. 5, pp. 420–428, 2008, doi: 10.1080/00908310600712224.

Chapter 7. Conclusions and Future Directions

7.1 Summary of research

This thesis evaluates biochar ANG and a novel approach, i.e., cold plasma, for enhancing the CH_4 adsorption capacity of biochars in the context of ANG storage as a field-deployable strategy to mitigate flaring of APG in remote oil field operations.

The study pursued three interconnected objectives. The first objective was to establish biochar as a viable adsorbent of ANG under oil field-relevant pressures and temperatures. The second objective systematically investigated the effects of three key parameters on plasma modification efficiency, i.e., 1) plasma treatment duration, 2) feedstock properties with emphasis on initial volatile matter content, and 3) plasma source gas composition. The third objective aimed to assess multicycle durability of biochars and identify potential end-of-life pathways for spent biochar as value-added products.

7.2 Key findings

The results of this research indicate that biochars are potentially viable adsorbents of ANG for on-site CH_4 storage and energy recovery in remote oil fields, where transporting associated gases to markets is uneconomic. The CH_4 adsorption isotherms and kinetics of four biochars derived from forestry wastes was compared with those of three commercial activated carbons. It was shown that biochar-based ANG can volumetrically store more CH_4 than CNG for a pressure up to 75 bar, suggesting the possibility of avoiding extremely high-pressure gas compression and heavy storage vessels, which may lead to substantial cost savings in oil and gas field applications.

Furthermore, although the adsorption capacity of the biochars was more than 50% lower than that of the activated carbons, their low-cost, renewability, and potential environmental benefits provide strong motivation for further investigation.

Cold plasma surface treatment was investigated as a room-temperature, solvent-free modification strategy to enhance biochar performance without compromising its economic or environmental advantages. Optimized plasma treatment significantly increased CH_4 adsorption capacity, with non-oxidizing plasmas such as Ar and N_2 producing the most pronounced improvements. Results indicate that CH_4 adsorption enhancement increased with plasma treatment duration up to approximately 30 minutes under the investigated conditions; beyond this point, both plasma effectiveness (η) and surface concentration of adsorbed CH_4 (γ) declined, indicating that excessive plasma exposure damages the pore network and reduces effective adsorption capacity.

It was also found that, when three biochars and three activated carbons were subjected to identical plasma conditions, the increase in CH_4 adsorption capacity was proportional to the initial volatile matter content of the raw materials. In parallel, when five different plasma source gases (Ar, N_2, CO_2, O_2/He and air) were tested under identical conditions for the same biochar, oxidizing plasmas (O_2/He and air) were less effective than non-oxidizing plasmas. While Ar and CO_2 plasma produced comparable CH_4 adsorption enhancement, CO_2 plasma is more attractive for practical applications due to its low cost and wide availability.

From a mechanistic perspective, the results indicate that cold plasma enhances CH_4 adsorption primarily through physical restructuring of the pore network, leading to increased specific surface area and formation of micro- and ultramicropores. It was further demonstrated that these pores are generated mainly through removal of volatile organic impurities embedded within the biochar

matrix, which unblocks previously inaccessible pore structures. Evidence supporting this mechanism includes CH_4 adsorption measurements, elemental and proximate analyses, pore structure characterization, surface chemistry analysis (zeta potential, suspension pH, and FTIR), and effluent gas composition measurements.

The durability of biochars was evaluated through multicycle adsorption–desorption experiments, which revealed predictable declines in CH_4 capacity during repeated cycling. Adopting a lifecycle perspective, this work demonstrates that spent biochar retains significant capacity for storing CH_4 and value as a solid fuel with enhanced calorific content due to retained hydrocarbons. This pathway transforms adsorbent replacement from a disposal burden into a recoverable energy resource, thereby strengthening the overall feasibility of biochar-based ANG systems.

Collectively, the results demonstrate that biochars function as a technically viable, economically credible, and lifecycle-compatible adsorbent for on-site CH_4 storage and utilization in oil field environments.

7.3 Contribution to the field

This research makes several contributions to gas adsorption science, porous carbon materials research, and CH_4 mitigation in the oil and gas sector. The primary contribution is a comprehensive evaluation of biochar for high-pressure, cyclic CH_4 storage under conditions relevant to the ANG systems, extending ANG research beyond its traditional focus on vehicular fuel storage and premium engineered adsorbents. By establishing baseline adsorption performance and operational behavior for biochar, this thesis positions low-cost biomass-derived carbon materials as credible candidates for stationary CH_4 storage applications.

A second key contribution is the mechanistic clarification of cold plasma effects on CH_4 adsorption in porous carbons. The results demonstrate that plasma treatment effectiveness is dominated by physical restructuring processes, including volatile matter removal, pore unblocking, and ultramicropore development. This finding explains why non-oxidizing plasmas enhance CH_4 uptake, whereas oxidizing plasma may reduce CH_4 adsorption affinity despite structural changes. The identification of initial volatile matter content as a predictor of plasma effectiveness further provides a practical descriptor for feedstock selection and plasma process optimization.

The thesis also contributes conceptually by reframing evaluation criteria for ANG adsorbents intended for field deployment. Rather than prioritizing maximum adsorption capacity, the analysis presented in this thesis emphasizes deliverable capacity, cyclic stability, operational tolerance, and end-of-life utility. This perspective aligns adsorbent assessment with the practical constraints of stationary oil field systems, where cost, durability, and logistical simplicity dominate design considerations.

Finally, by integrating adsorption performance, plasma modification, multicycle durability, and post-use material utilization within a single framework, this research advances a lifecycle-oriented perspective on solid adsorbents. Demonstrating that degraded biochar can transition from a gas storage medium to a value-added solid fuel or, prospectively, to a soil amendment distinguishes biochar from many engineered adsorbents and strengthens its role within circular carbon management strategies.

7.4 Unsolved issues and future directions

Despite the advances presented in this thesis, several important issues remain open. The adsorption experiments focus primarily on CH_4 as a single component, whereas real APG streams contain

CO_2, higher hydrocarbons, water vapor, and trace contaminants. Competitive adsorption effects, pore blocking, and long-term exposure to mixed gas compositions may influence both storage capacity and durability. Future work should therefore extend the present framework to multicomponent adsorption systems under dynamic operating conditions. This thesis provides the first empirical evidence for plasma-induced pore development in biochar as a CH_4 adsorbent. Whether this mechanism is distinct from thermal or chemical activation requires explicit comparison, which lies outside the scope of the present work.

Scale-up of plasma treatment also remains a critical engineering challenge. Although dielectric barrier discharge plasma proved effective at laboratory scale, further investigation is required to assess energy efficiency, throughput, and reactor configurations suitable for continuous processing or fluidized bed treatment of large biochar inventories. In addition, longer-term cycling studies would also help clarify the structural evolution of ultramicropores and refine degradation models over extended service lifetimes.

At the system level, the case study presented here demonstrates technical feasibility but does not constitute a full techno-economic optimization. Future research should integrate adsorbent performance with detailed economic modeling, including plasma treatment energy demand, adsorbent replacement frequency, diesel displacement potential, and carbon credit revenues, in order to define deployment thresholds across different field sizes and regulatory contexts.

Beyond oil field APG mitigation, the principles developed in this thesis may also apply to other distributed CH_4 sources such as biogas facilities, landfills, and remote energy systems, offering opportunities to extend the impact of biochar-based ANG technologies to broader CH_4 mitigation strategies.

Appendix A: Excess adsorption

Decreasing CH_4 adsorption with increasing pressure after a peak value has been reported for coal, shale and activated carbon. The behavior is related to the decrease of the free space that is occupied by the gas phase because of the increase of adsorbed phase. For volumetric and gravimetrical measurement of adsorption, the observed adsorption can be expressed by

$$M = M_a(1 - \frac{\rho_g}{\rho_a}) \quad \text{(A-1)}$$

where M is the observed adsorption or excess adsorption; Ma is the actual adsorption; ρ_g and ρ_a are the density of the gas phase and the adsorbed phase, respectively. The observed adsorption is lower than the actual adsorption. The difference between M and Ma increases with increasing gas pressure as a result of increasing ρ_g . When ρg equals ρa the observed adsorption becomes zero. In the present work, other two biochars (BC Biocarb and BC Birch) also show the trend of decreasing adsorption with increasing pressure at 303 K after a peak value, but the activated carbons do not show such a behavior. This may be reconciled with the lower adsorption level of the biochars at 303 K. Lower adsorption may suggest weaker attraction force between the adsorbents and the adsorbate, resulting in a larger distance between the surface of the adsorbents and the center of the adsorbed molecules. In consequence, the density of the adsorbed phase ρ_a is lower and results in the observed maximums.

What makes n_{ex} negative?

In Fig. 3.2, BC-Elkem at 303 K exhibits negative excess adsorption at elevated pressures. This appendix explains the physical origin of this observation with reference to Table 3.1.

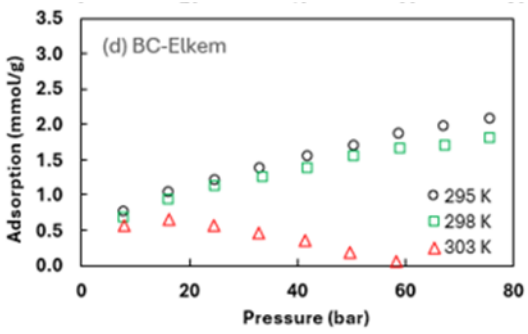

Sample*	BET Surface Area ($m^2 g^{-1}$)	Pore volume ($cm^3 g^{-1}$)	Average Pore width (Å)
BC-Ash	490	0.25	19.98
BC-Birch	34	0.02	24.07
BC-Biocarb	525	0.29	22.26
BC-Elkem	3.72	0.06	646.4
AC-FW	970	0.65	26.66
AC-CABOT*	551	0.54	39.44
AC-F400	907	0.52	22.80

Definition of excess adsorption:

$$\boldsymbol{n_{ex}} = n_{abs}\left(1 - \frac{\rho_g}{\rho_a}\right), \quad \boldsymbol{n_{ex}} = n_{abs} - \rho_{bulk} \cdot V_{ads}$$

n_{ex}: excess (observed) adsorption

n_{abs}: actual adsorption

ρ_g: density of gas phase (NIST)

ρ_a: density of adsorbed phase

ρ_{bulk}: bulk gas density at the same P, T (NIST)

V_{ads}: adsorption-phase volume

n_{ex} <0 because:

- Weak CH_4 affinity: limited CH_4–surface interaction.
- Higher temperature: 303 K suppresses exothermic adsorption.
- Under high pressure, ρ_g or ρ_{bulk} becomes large.
- Extremely low surface area: 3.72 m^2/g, pore volume: 0.06 cm^3/g, large pore width (64.6 nm)

Physical interpretation. Negative n_{ex} does not mean CH_4 is repelled from the surface. It means the density of CH_4 inside BC-Elkem's macropores is lower than the free-gas density at the same pressure — the material displaces gas rather than concentrating it. BC-Elkem acts as dead volume, not as an adsorbent.

Sievert (Volumetric) Apparatus: How Δn Becomes Negative?

The Sievert apparatus measures excess adsorption directly via pressure–volume balance. Each dosing step records the moles of gas before and after valve opening, using the real-gas equation of state n = PV/ZRT, where Z is the compressibility factor. The incremental moles adsorbed per dose are:

$$n_{ex} = \text{Sievert}, n = \frac{PV}{ZRT}$$

$$\Delta n = \left(\frac{P_d V_d}{Z_d RT} + \frac{P_i V_s}{Z_i RT}\right) - \left(\frac{P_f (V_d + V_s)}{Z_f RT}\right)$$

$$\Delta n < 0, \text{ when } \left(\frac{P_d V_d}{Z_d RT} + \frac{P_i V_s}{Z_i RT}\right) < \left(\frac{P_f (V_d + V_s)}{Z_f RT}\right)$$

$$\Delta n = \frac{1}{RT}\left[V_d\left(\frac{P_d}{Z_d} - \frac{P_f}{Z_f}\right) + V_s\left(\frac{P_i}{Z_i} - \frac{P_f}{Z_f}\right)\right]$$

since $V_d, V_s, R,$ Tare constant, $V_d\left(\frac{P_d}{Z_d} - \frac{P_f}{Z_f}\right) + V_s\left(\frac{P_i}{Z_i} - \frac{P_f}{Z_f}\right) < 0$

Usually in a dosing step: $P_d > P_f > P_i$

$$\frac{P_d}{Z_d} - \frac{P_f}{Z_f} \gtrsim 0, \quad \frac{P_i}{Z_i} - \frac{P_f}{Z_f} < 0$$

At high pressure, if $\frac{P_f}{Z_f}$ becomes large enough, $\boldsymbol{\Delta n < 0}$.

$\mathbf{n_{ex,\,j} = \sum_{i=1}^{j} \Delta n_i < 0}$ at pressure j

Negative excess adsorption in the Sievert apparatus is not an instrumental artifact. It is the physically correct measurement for a material whose adsorbed-phase density cannot exceed the free-gas density at the same conditions. For BC-Elkem, the combination of negligible microporosity, macroporous pore structure, weak CH_4–surface affinity, and high-pressure non-ideal gas behavior produces this result. The material offers no thermodynamic advantage over free compression and is effectively inert as a CH_4 adsorbent.

Appendix B: Equations and parameters of adsorption isotherm models

The adsorption models that have been used to analyze the data are shown in Table below.

Table Equations and parameters of adsorption isotherm models

Model	Equations	Parameters
Langmuir	$N = \frac{N_m * BP}{1 + BP}$	N_m (mmol/g) B (bar $^{-1}$)
Freundlich	$N_m = KP^{1/n}$	K (mmol/g*bar $^{-1/n}$) N_m (mmol/g)
Sips	$N = \frac{N_m * (BP)^{1/n}}{1 + (BP)^{\frac{1}{n}}}$	N_m (mmol/g) B (bar $^{-1}$) n (dimensionless)
BET	$\frac{P}{N * (P_0 - P)} = \frac{1}{N_m * C} + \frac{C - 1}{N_m * C} * \frac{P}{P_0}$	N_m (mmol/g) C (dimensionless)
Toth	$N = \frac{Ns * BP}{(1 + (BP)^t)^{1/t}}$ $B = B_0 * \exp\{\frac{Q}{RT_0} * \left(\frac{T_0}{T} - 1\right)\}$ $t = t_0 + \alpha(1 - \frac{T_0}{T})$ $Ns = Ns_0 * \exp\{\chi\,(1 - \frac{T}{T_0})\}$	N, Ns, Ns_0 (mmol/g) B, B_0 (bar $^{-1}$) Q/RT_0 (dimensionless) T_0 (K) t, t_0 (dimensionless) α (dimensionless) χ (dimensionless)

Appendix C: "Cold plasma-modified biochar for CH_4 capture and utilization on oil fields" - CanCH_4 symposium